



UNIVERSITY OF IOANNINA

SCHOOL OF SCIENCES

DEPARTMENT OF PHYSICS

**PHOTOPHYSICAL AND CATALYTIC STUDY OF PLASMONIC-
SEMICONDUCTING NANOMATERIALS DEVELOPED BY FLAME
SPRAY PYROLYSIS TECHNOLOGY**

CONSTANTINOS MOULARAS

PhD THESIS

IOANNINA 2023



ΠΑΝΕΠΙΣΤΗΜΙΟ ΙΩΑΝΝΙΝΩΝ
ΣΧΟΛΗ ΘΕΤΙΚΩΝ ΕΠΙΣΤΗΜΩΝ
ΤΜΗΜΑ ΦΥΣΙΚΗΣ

**ΜΕΛΕΤΗ ΦΩΤΟΦΥΣΙΚΩΝ ΚΑΙ ΚΑΤΑΛΥΤΙΚΩΝ ΙΔΙΟΤΗΤΩΝ
ΠΛΑΣΜΟΝΙΚΩΝ-ΗΜΙΑΓΩΓΙΜΩΝ ΝΑΝΟΎΛΙΚΩΝ ΠΟΥ
ΑΝΑΠΤΥΧΘΗΚΑΝ ΜΕ ΤΕΧΝΟΛΟΓΙΑ ΨΕΚΑΣΜΟΥ ΠΥΡΟΛΥΣΗΣ
ΦΛΟΓΑΣ**

ΚΩΝΣΤΑΝΤΙΝΟΣ ΜΟΥΛΑΡΑΣ

ΔΙΔΑΚΤΟΡΙΚΗ ΔΙΑΤΡΙΒΗ

ΙΩΑΝΝΙΝΑ 2023

Three-member advisory committee

1. Yiannis Deligiannakis (supervisor), Professor, Department of Physics, University of Ioannina, Greece
2. Georgios Evangelakis, Professor Emeritus, Department of Physics, University of Ioannina, Greece
3. Athanasios Bourlinos, Associate Professor, Department of Physics, University of Ioannina, Greece

Seven-member assessment committee

1. Yiannis Deligiannakis (supervisor), Professor, Department of Physics, University of Ioannina, Greece
2. Georgios Evangelakis, Professor Emeritus, Department of Physics, University of Ioannina, Greece
3. Athanasios Bourlinos, Associate Professor, Department of Physics, University of Ioannina, Greece
4. Alexios Douvalis, Professor, Department of Physics, University of Ioannina, Greece
5. Maria Louloudi, Professor, Department of Chemistry, University of Ioannina, Greece
6. Michael Karakassides, Professor, Department of Materials Science and Engineering, University of Ioannina, Greece
7. Anastasios Markou, Assistant Professor, Department of Physics, University of Ioannina, Greece

Acknowledgments

During my PhD journey these past years, I have been grateful to many people for their contribution both in the scientific and the rest of life aspects.

I think it is fair to start by expressing my sincere gratitude to **Prof. Yiannis Deligiannakis**, Head of the Lab of Physical Chemistry of Materials and Environment, my supervisor and mentor. 6 years ago, he provided me the opportunity to begin my academic track and explore further my limits as a young physicist. The endless, deep conversations in his office about science, passion and motivation has been the inner motor for my drive and personal development and I will always be grateful to him.

I feel much appreciation towards the other two members of my 3-member advisor committee:

Prof. Georgios Evangelakis, the insightful and fruitful conversations have always been a pleasure and his expertise in the electronic behavior of metals has been very useful. Moreover, he kindly provided me free access to his lab and, specifically, to operate the X-ray Photoelectron Spectroscopy equipment installed there.

Assoc. Prof. Athanasios Bourlinos, or simply **Thanasis** to me, his office and lab doors have been always open to me and my questions about carbon materials, and his deep knowledge he provided to me without hesitation, was something I will always carry to my future career.

Special thanks should go to the rest members of my 7-member examiner committee:

Prof. Maria Louloudi, her vast expertise in catalysis has been at times, of paramount importance to my PhD research, specially the plasmon-driven phenomena in such complex chemical reactions we thoroughly studied.

Prof. Alexios Douvalis, his presence during my undergraduate and graduate studies have been very important to my personal evolution as a physicist and the great atmosphere in our neighboring labs made the tough PhD routine endurable.

Prof. Michail Karakasides and **Assist. Prof. Anastasios Markou**, we did not have the chance to get familiar until now, however I am grateful for their valuable time and expertise devoted for evaluating my thesis and research.

Obviously, many thanks go to all the members of Lab of Physical Chemistry of Materials and Environment I encountered so far:

Dr. Yiannis Georgiou, he has been the co-mentor through my journey. He taught me fundamentals of physicochemical mechanisms and lab routine and has been, since then, a true friend to me.

Dr. Panagiota Stathi, the first post-doc I met upon my arrival on the group. Thank you for the vivid atmosphere and the all-around assistance in all aspects.

On this regard, I would like to thank **Pavlos Psathas**, my PhD and office companion since our common start, has always been a dear collaborator and friend, **Areti Zindrou**, for the excellent communication in challenging projects and lab routine, **Christos Dimitriou**, for his invaluable contribution in major aspects of my PhD study and the fruitful discussions, **Loukas Belles**, for the great collaborations we had and the vital electrochemical expertise he provided, and last but not least, **Dr. Maria Solakidou**, for the great communication and answering any chemical questions came up. Also, many thanks go to the newest lab members, **Sokratis Soutzios** and **Christos Sidiropoulos** for the scientific help and friendly environment. All the aforementioned, they made me feel welcomed, like a member of a family, and I cannot thank every one of them enough for that.

Special thanks go to all members of the Head Lab of Biomimetic Catalysis and Hybrid Materials, specially to **Aikaterini Gemenetzi**, for the many years of collaboration on the fascinating field of plasmonic photocatalysts and **Marinos Theodorakopoulos**, a guy who has been a moving chemistry encyclopedia answering all my questions and a dear friend providing moral support of paramount importance through my PhD journey.

Finally, my dearest gratitude is devoted to all my loved ones for their tremendous faith upon me, and specially, **Angela Kaloudi**, my life partner, for her limitless patience and enduring support through these tough periods. Lastly, I dedicate my deepest emotions to my parents, **Thanasis** and **Lamprini**, for just being there and following me in every choice with their absolute trust and unconditional love, despite the difficult moments. Their sacrifices have made my dreams possible to be chased, and for this, they will always be my role models.

“The most beautiful experience we can have is the mysterious. It is the fundamental emotion which stands at the cradle of true art and true science”

Albert Einstein

For those who seek the answers...

Abstract

Local surface plasmon resonance (LSPR) in metallic nanostructures gives birth to a collection of optical and electronic phenomena, stemming from processes that occur during the excitation and subsequent damping of the plasmon energy, stored in the oscillating electron cloud. Plasmonic effects are attributed to *radiative* and *non-radiative* effects. In the latter case, the plasmon-induced local electric fields and high-energy “hot” electrons create new pathways in the context of energy transfer and utilization, such as photocatalysis. In this context, a photoexcited plasmonic nanoparticle can change the landscape of a chemical process and initiate reactions that would otherwise be thermodynamically and/or kinetically blocked, using visible- or ultraviolet light. This opens up new possibilities for tuning the selectivity and efficiency of photoinduced processes, e.g., such as photocatalysis and photothermal phenomena. In hybrid systems {plasmonic/semiconducting interface}, the multidimensional degrees of freedom, raise challenges on the understanding and control of the photophysical processes. To this front, the desired properties can -in principle- be controlled by engineering the nanostructure’s characteristics and environment.

In the present PhD thesis, three particle configurations were developed and studied:

- (i) core@shell Ag@SiO₂ nanoaggregates, where the Ag core particles of controlled size were encapsulated in an amorphous SiO₂ layer of controlled thickness.
- (ii) Visible-light active Ag/TiO₂ nanocomposites, where TiO_x Magneli suboxides (Ti₃O₅, Ti₄O₇) are formed in the Ag/TiO₂ interface.
- (iii) NaTaO₃ and Ag/NaTaO₃ nanostructures of controlled phase composition and particle size.

All the aforementioned nanostructures have been produced by Flame Spray Pyrolysis (FSP), a single-step synthesis technology with industrial scalability. For the case of Ag@SiO₂ nanoaggregates, the fundamental plasmon-driven mechanisms were disentangled and studied. Firstly, the temperature rise due to plasmon-driven photothermal mechanism was monitored and correlated to the interparticle distance of Ag core particles. Then, we used Mie theory for the theoretical analysis, where we suggest the use of the fractal dimension of the Ag@SiO₂ nanoaggregates as a geometrical parameter, determining the dominant photothermal mechanism (local or collective thermal effects).

In the following, a novel method has been developed for *in-situ* monitoring of the hot-electrons transferred from photoexcited Ag@SiO₂ nanoaggregates, based on the use of Electron Paramagnetic Resonance (EPR) spectroscopy. Cr⁶⁺-ions were used as multi-electron acceptors, resulting in EPR-detectable Cr⁵⁺ and Cr³⁺ species. Moreover, the plasmon-enhanced Cr⁶⁺ photo-reduction in the presence of Ag@SiO₂ renders the plasmonic hot electrons beneficial for environmental remediation using sunlight. The optimal performance was parametrized, in terms of SiO₂-shell thickness, excitation wavelength and the underlying plasmon mechanism was investigated.

To study the {plasmon-semiconductor} interface, two types of nanocomposites have been engineered using FSP: {Ag/TiO₂} and {Ag/NaTaO₃}. For the {Ag/TiO₂} case, the effect of Ag-TiO₂ association was studied in detail varying Ag and TiO₂ particle size. In addition, black {Ag/TiO_x/TiO₂} nanocomposites were studied. We found that black, visible-light active {Ag/TiO_x/TiO₂} can act as an electron-storage nanodevice, under post-illumination dark conditions. The photoinduced and post-illumination electron-transfer events were investigated in the context of “dark catalysis”. The efficient storage of surface electrons was attributed to the presence of the distorted TiO_x suboxide nano-islands in the Ag/TiO₂ interface, thus the improved dark photo-reduction of Cr⁶⁺, which was used again as a chemical probe. Lastly, NaTaO₃ and Ag/NaTaO₃ nanoparticles were successfully produced using FSP in a single-step process, thus engineering the smallest NaTaO₃ particle size, reported so far (14 nm). The dynamics of photo-stimulated electron/hole pairs was thoroughly explored using EPR spectroscopy. Larger NaTaO₃ particles (26 nm) yield significantly lower photo-induced carriers due to rapid recombination phenomena. The interplay of size effect and detection of photo-excited carriers by EPR (i.e., improved carrier migration) is inherently related to high photocatalytic performance in H₂ production from water splitting.

Overall, the present PhD research provides new insights in the plasmonic photophysics of FSP-made Ag nanoparticles and the {Ag/TiO₂} and {Ag/NaTaO₃} nanocomposites. This study provides key-understanding on the synergy between plasmon-driven mechanisms and interfacial carrier dynamics, with a special focus on the utilization of plasmonic catalysis for efficient sunlight energy conversion to chemical activity.

Περίληψη

Ο συντονισμός τοπικού επιφανειακού πλασμονίου (LSPR) σε μεταλλικές νανοδομές, είναι ευρέως γνωστό πως παρέχει μια συλλογή νέων οπτικών και ηλεκτρονικών φαινομένων, μία διαδικασία που απορρέει από τη διέγερση και την επακόλουθη απόσβεση της πλασμονικής ενέργειας που είναι αποθηκευμένη στη συλλογική ταλάντωση του ηλεκτρονιακού νέφους στο εκάστοτε μεταλλικό σωματίδιο. Τα πλασμονικά φαινόμενα κατηγοριοποιούνται σε ακτινοβολητικά και μη-ακτινοβολητικά. Στη δεύτερη περίπτωση, τα πλασμονικά επαγόμενα ηλεκτρικά πεδία και τα ηλεκτρόνια υψηλής ενέργειας (γνωστά ως hot ηλεκτρόνια) δημιουργούν νέες οδούς για την μεταφορά και εκμετάλλευση ενέργειας, όπως στην περίπτωση της φωτοκατάλυσης. Σε αυτό το πλαίσιο, ένα πλασμονικό νανοσωματίδιο υπό φωτισμό, είναι ικανό να μεταβάλλει την πορεία μίας χημικής διεργασίας και να επιταχύνει αντιδράσεις με αποδόσεις, που θερμοδυναμικά είναι μη εφικτές, αξιοποιώντας το το υπεριώδες και ορατό φάσμα. Έτσι προκύπτουν νέες πιθανότητες για την επαρκή ρύθμιση της εκλεκτικότητας και αποτελεσματικότητας φωτοεπαγόμενων διεργασιών. Σε υβριδικά συστήματα (διεπιφάνεια πλασμονίου/ημιαγωγού), οι πολυδιάστατοι βαθμοί ελευθερίας, καθιστούν απαιτητική την κατανόηση και τον έλεγχο των φωτοφυσικών διεργασιών. Σε αυτό το μέτωπο, οι επιθυμητές ιδιότητες μπορούν να ελεγχθούν με ακρίβεια, επεξεργάζοντας τα χαρακτηριστικά και το περιβάλλον της εκάστοτε νανοδομής.

Στην παρούσα διατριβή, τρεις διαφορετικές νανο-ετεροδομές αναπτύχθηκαν και μελετήθηκαν:

- I. Νανосуσωματώματα Ag@SiO_2 σε μορφολογία πυρήνα@κελύφους, όπου τα σωματίδια Αργύρου ελεγχόμενου μεγέθους ενθυλακώθηκαν σε ένα άμορφο στρώμα Πυριτίας ελεγχόμενου πάχους.
- II. Νανοσύνολα Ag/TiO_2 ενεργά στο ορατό φάσμα, λόγω του σχηματισμού υποξειδίων Τιτανίου, γνωστά ως φάσεις Magneli (Ti_3O_5 , Ti_4O_7) στη διεπιφάνεια Ag/TiO_2 .
- III. Περοβσκιτικές νανοδομές NaTaO_3 και Ag/NaTaO_3 ελεγχόμενης σύστασης και μεγέθους.

Όλες οι προαναφερθείσες νανοδομές παρήχθησαν με την τεχνολογία πυρόλυση ψεκασμού φλόγας (Flame Spray Pyrolysis - FSP), μία ενός βήματος τεχνολογία σύνθεσης με δυνατότητα βιομηχανικής αναβάθμισης. Για την περίπτωση των Ag@SiO_2 συσσωματωμάτων,

οι πλασμονικοί μηχανισμοί μελετήθηκαν ξεχωριστά. Πρώτον, η θερμοκρασιακή αύξηση λόγω φωτοθερμικού μηχανισμού μετρήθηκε και συσχετίστηκε με την απόσταση μεταξύ των νανοσωματιδίων Αργύρου. Για τη θεωρητική ανάλυση, χρησιμοποιήσαμε τη θεωρία Mie, όπου προτείνουμε τη χρήση της φράκταλ διάστασης των νανοςυσσωματωμάτων ως μία γεωμετρική παράμετρο, που καθορίζει τον κυρίαρχο φωτοθερμικό μηχανισμό (τοπικά ή συλλογικά θερμικά φαινόμενα).

Στη συνέχεια, μία πρωτότυπη μέθοδος αναπτύχθηκε για την *in situ* καταμέτρηση των «hot» ηλεκτρονίων που παράγονται και μεταφέρονται από τα φωτοδιεγερμένα Ag@SiO_2 νανοςυσσωματώματα, που βασίζεται στη φασματοσκοπία ηλεκτρονικού παραμαγνητικού συντονισμού ηλεκτρονίων (EPR). Συγκεκριμένα, χρησιμοποιήσαμε ιόντα εξασθενούς Χρωμίου (Cr^{6+}) ως αποδέκτες ηλεκτρονίων με αποτέλεσμα τα EPR-ενεργά Cr^{5+} και Cr^{3+} species. Επιπλέον, η πλασμονικά ενισχυμένη φωτοαναγωγή του Cr^{6+} παρουσία των Ag@SiO_2 σωματιδίων, καθιστά τα hot ηλεκτρόνια ωφέλιμα για περιβαλλοντικές εφαρμογές με χρήση ηλιακού φωτός. Η βέλτιστη απόδοση παραμετροποιήθηκε αναφορικά με το πάχος του κελύφους SiO_2 , το μήκος κύματος διέγερσης και διερευνήθηκε ο υποκείμενος μηχανισμός πλασμονίου.

Για την μελέτη της διεπιφάνειας {πλασμονίου/ημιαγωγού}, δύο είδη νανοςύνθετων δομών παρήχθησαν με χρήση FSP, Ag/TiO_2 και Ag/NaTaO_3 . Στην περίπτωση των νανοςύνθετων $\text{Ag/TiO}_x/\text{TiO}_2$, μελετήθηκε η αλληλεπίδραση Ag-TiO_2 για μεταβαλλόμενο μέγεθος σωματιδίων. Επιπλέον, μελετήθηκαν «μαύρες» $\{ \text{Ag/TiO}_x/\text{TiO}_2 \}$ νανοςύνθετες δομές, όπου μπορούν να λειτουργήσουν ως συσκευή αποθήκευσης ηλεκτρονίων, υπό συνθήκες σκοταδιού αφού έχει προηγηθεί φωτισμός. Τα φωτοεπαγόμενα φαινόμενα μεταφοράς ηλεκτρονίων διερευνήθηκαν στο πλαίσιο της «σκοτεινής φωτοκατάλυσης». Η αποτελεσματική αποθήκευση των επιφανειακών ηλεκτρονίων αποδόθηκε στην παρουσία των νανο-πλειάδων υποξειδίου του TiO_x στην παραμορφωμένη διεπιφάνεια Ag/TiO_2 , με αποτέλεσμα τη βελτιωμένη αναγωγή του Cr^{6+} , το οποίο χρησιμοποιήθηκε ξανά ως χημικός ανιχνευτής. Τέλος, τα περοβσκιτικά νανοςωματίδια NaTaO_3 και Ag/NaTaO_3 παρήχθησαν με επιτυχία χρησιμοποιώντας την τεχνολογία FSP, σε ενός βήματος σύνθεση, κατασκευάζοντας το μικρότερο μέγεθος σωματιδίων NaTaO_3 , που έχει αναφερθεί μέχρι στιγμής βιβλιογραφικά (14 nm). Η δυναμική των φωτοδιεγερμένων ζευγών ηλεκτρονίων/οπών διερευνήθηκε διεξοδικά χρησιμοποιώντας φασματοσκοπία EPR. Τα μεγαλύτερα σωματίδια NaTaO_3 (26 nm) παρέχουν σημαντικά χαμηλότερους φωτοεπαγόμενους φορείς λόγω των φαινομένων ταχείας επανασύνδεσης. Η αλληλεπίδραση του μεγέθους και της ανίχνευσης φωτοδιεγερμένων

φορέων με EPR (δηλαδή βελτιωμένη μετανάστευση φορέα στην επιφάνεια του σωματιδίου) σχετίζεται εγγενώς με την υψηλή φωτοκαταλυτική απόδοση στην παραγωγή H_2 από τη διάσπαση του νερού.

Συμπερασματικά, η παρούσα διδακτορική έρευνα παρέχει νέα γνώση στους πλασμονικούς φωτοφυσικούς μηχανισμούς για νανοσωματίδια Αργύρου και διεπιφάνειες πλασμονίου/ημιαγωγού παραχθέντα σε φλόγες. Σε αυτό το πλαίσιο, διερευνάται διεξοδικά η συνέργεια μεταξύ των πλασμονικά επαγόμενων μηχανισμών και της δυναμικής των διεπιφανειακών φορέων, με ιδιαίτερη έμφαση, στην εκμετάλλευση της πλασμονικής κατάλυσης για αποτελεσματική μετατροπή της ηλιακής ενέργειας σε ωφέλιμη χημική δραστηριότητα.

Acknowledgments	i
Abstract	iv
Περίληψη	vi
Chapter 1	1
<i>Introduction</i>	1
1.1. Nanoplasmonics	1
1.1.1 Local Surface Plasmon Resonance.....	1
1.2 Plasmon-driven Phenomena in Nanoscale	4
1.2.1 Phenomena Outside the Particle (Light Scattering – Mie Theory)	4
1.2.1.1 The General Concept of Light Scattering.....	4
1.2.1.2 Dielectric function.....	6
1.2.1.3 Mie equations.....	8
1.2.1.4 Dipole Approximation	10
1.2.1.5 Effect of Particle Size and Surrounding Medium.....	12
1.2.1.6 Mie Theory Limitations.....	14
1.2.2 Phenomena Inside the Particle.....	16
1.2.2.1 Hot Carriers	17
1.2.3 Phenomena in the Particle-Particle Interface {Metal-Metal}.....	23
1.2.3.1 Near-field Enhancement (Hot Spots)	23
1.2.3.2 Thermoplasmonics.....	24
1.2.3.2.1 Fundamental Physics of Plasmonic Heating.....	25
1.2.3.2.2 Sample Geometry.....	27
1.2.3.2.3 Collective Thermal Effects	28
1.2.4 Phenomena in the Particle-Particle Interface {Plasmonic Metal/Semiconductor Junction}	32
1.3 Plasmonics in Interface: Indirect/Direct Electron Migration in Metal/Adsorbate & Metal/Semiconductor Systems	35

1.3.1	Plasmon-assisted Catalysis by Near-Field Enhancement	36
1.3.2	Catalysis by Electron-Transfer in Plasmonic Metal/Adsorbate Interface 38	
1.3.3	An Overview of Plasmonic Catalysis.....	42
1.3.4	Disentangling the Plasmon-mediated Mechanisms - Currently Standing Challenges.....	44
1.4	Why Ag?.....	50
1.5	Synthesis of Plasmonic/Semiconducting Nanostructures by Flame Spray Pyrolysis.....	51
1.5.1	Traditional synthesis of Ag nanostructures	51
1.5.2	Flame Spray Pyrolysis	52
1.5.2.1	Fundamentals of Flame Spray Pyrolysis Process	53
1.5.2.2	Flame Spray Pyrolysis as a Versatile Nanoparticle Synthesis Technology ...	56
1.5.2.3	Flame-made Plasmonic Nanoaggregates.....	59
1.6	Motivation and Scope of the Thesis	59
1.7	Thesis Outline.....	60
1.8	Bibliography.....	63
Chapter 2	95
	<i>Experimental Methods</i>	95
2.1	Flame Spray Pyrolysis (FSP) Apparatus	95
2.2	Synthesis of Flame-made Plasmonic Nanomaterials.....	96
2.2.1	Single-step Synthesis of Core@Shell Ag@SiO ₂ Nanoaggregates	97
2.2.2.	Synthesis of Flame-made Visible-light Active Black Ag/TiO ₂	98
2.2.2	Synthesis of NaTaO ₃ and Ag/NaTaO ₃	99
2.3	Electron Paramagnetic Resonance (EPR) Spectroscopy	100

2.3.1	Fundamentals Principles.....	100
2.3.2	Quantitative EPR.....	103
2.3.3	Method Development of Detection of Hot Electrons in Plasmon-enhanced Cr ⁶⁺ Reduction.....	105
2.3.4	Spin Trapping.....	114
2.4	Characterization Techniques	116
2.5	Light Irradiation Set-up	117
2.6	References	119
Chapter 3	121
	<i>Photothermal Effects by Flame-made Core@Shell Plasmonic Nanoaggregates</i>	121
3.1	Introduction	121
3.2	Materials & Methods	123
3.3	Results/Discussion	128
3.3.1	Core-shell Quality and Control of Interparticle Distance	128
3.3.2	Regulation of Local Surface Plasmon Resonance	132
3.3.3	Thermoplasmonic Performance.....	133
3.3.3.1	Particles in liquid suspension irradiated by Simulated Solar Light	133
3.3.3.2	Particles on a Glass Film	135
3.4	Conclusions	142
Chapter 4	149
	<i>Detection and Harvesting of Hot Electrons in Plasmon-driven Redox Reactions</i>	149
4.1	Introduction	149
4.2	Materials & Methods	152
4.3	Results/Discussion	158
4.3.1	Ag@SiO ₂ Characterization	158

4.3.2	Plasmon-mediated hot carriers vs direct electron transfer in dark (DETD): Evaluation of Ag ⁺ leaching	161
4.3.3	Quantitative monitoring of hot-electron transfer to {Cr-oxalate} species by EPR spectra	162
4.3.4	Monitoring hot-electron transfer to Cr ⁶⁺ /Cr ⁵⁺ /Cr ³⁺	164
4.3.5	Quantitative analysis of hot-electron transfer	166
4.3.6	Disentangling the role of hot-electron transfer and thermal effects on plasmon-enhanced Cr-reduction mechanism.....	169
4.4	Conclusions	175
Chapter 5	185
	<i>Photo-induced Electron/Hole Dynamics in Flame-made NaTaO₃ Nanoparticles</i>	185
5.1	Introduction	185
5.2	Materials & Methods	186
5.3	Results & Discussion	189
5.3.1	Photo-excitation of electron/hole pairs in NaTaO ₃	189
5.3.2	Synthesis and Characterization of Ag/NaTaO ₃	197
5.4	Conclusions	198
5.5	Supplementary Information	199
Chapter 6	207
	<i>Understanding the Electron Storage in Interfacial Magnéli Islands on Flame-made Black Ag/TiO₂ Nanostructures</i>	207
6.1	Introduction	207
6.2	Materials & Methods	209
6.3	Results/Discussion	213

6.3.1	Structural Characterization of Black Ag/TiO ₂ @TiO _x nanocomposites ..	213
6.3.2	Storage and Transfer of Photo-generated Carriers in Distorted Suboxide Interface	218
6.3.3	Dark photocatalysis in Cr ⁶⁺ reduction.....	223
6.4	Conclusions	224
6.5	Supporting Information	225
Chapter 7	232
	<i>Concluding Remarks & Future Research Perspectives</i>	232
	<i>Appendix A: Evaluation of Ag⁺ Leaching and UV-Vis/EPR Analysis of Ag@SiO₂/Cr system</i>	235
	<i>Curriculum Vitae</i>	244

Chapter 1

Introduction

1.1. Nanoplasmonics

Periods in history have been given names based on the primary materials employed by those civilizations. We can safely assume that 20th century prefaces the "Nano" Age. With "nano" deriving from a Greek prefix signifying something very small, Richard Feynman's renowned speech -in December 1959- provided the groundwork for the scientific field today known as *nanotechnology* and fueled man's elation to understand and control matter in the nanoscale (10^{-9} nm).¹ It took over three decades for the scientific community to realize Feynman's dream due to the lack of appropriate characterization instruments and methodologies. Phenomena like the quantum-size-effect and surface-confinement, can change the classically anticipated bulk properties.^{2,3} Nowadays, these properties have been extensively utilized in a wide range of novel applications in numerous scientific fields, correlating the usage of sophisticated nanostructures with civilization's technological progress.^{4,5}

1.1.1 Local Surface Plasmon Resonance

Metallic nanostructures display vivid optical qualities steaming from their nanoscale features. Silver (Ag) and gold (Au) colloids have been employed extensively from ancient times for their color-hues, such as in stained glass or the renowned Lycurgus cup, where the color shift is based on the type of incident-light, as seen in Figure 1.1.^{6,7} When light is transmitted through the glass, it looks red, while when light is scattered on the surface, it

appears opaque green. This behavior in metals is triggered by the collective oscillation of the free electrons stimulated by incident electromagnetic waves. In the electrodynamic picture, the Coulomb forces induced by external electric fields and the restoring forces induced by positive ions in the metallic lattice compel electrons to oscillate.

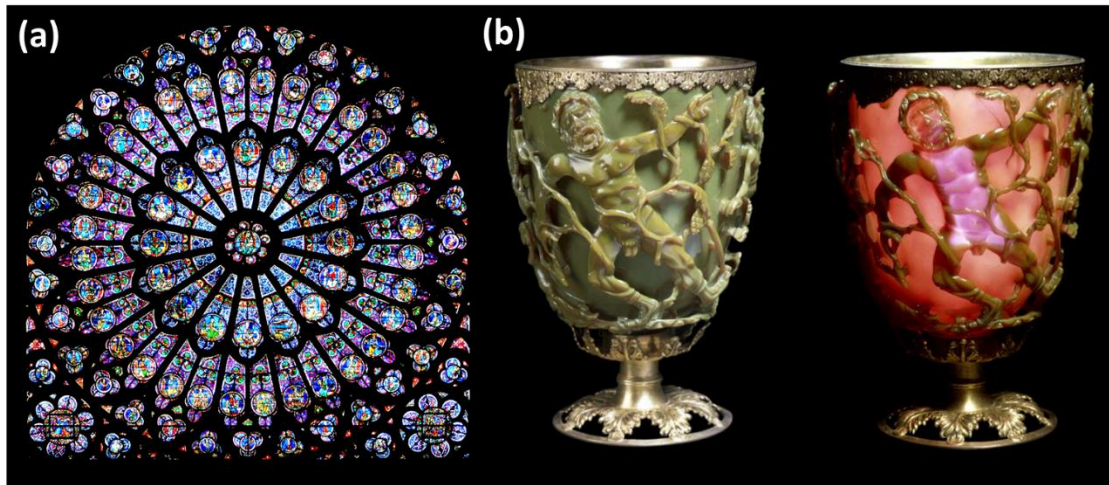


Figure 1.1. (a) Stained glass in Notre Dame Cathedral, Paris. (b) Lycurgus cup displaying the transmitted (green) and reflected (red) light. Copyrights belong to British Museum.

Energy is stored in this coherent oscillation in the form of quanta known as *plasmons*.⁸ The highest energy gained occurs when the *plasmon frequency* is in resonance with the frequency of the incident's electric field.⁸ This mode is known as *surface plasmon* when it occurs at the interface between a metallic surface and a dielectric surrounding medium. Changes in oscillation frequencies are caused by factors that alter these boundary conditions, such as metal size, shape, and dielectric constants. To avoid misunderstanding, in the case of a *bulk plasmon* the electronic excitation occurs over the whole 3D volume of the metal, while a *surface plasmon* refers in the 2D interface.⁹ When the electric-charge displacement is restricted to the nanoscale, however, other phenomena emerge such as concentrated photons, which are defined by the term **Local Surface Plasmon Resonance (LSPR)**. Figure 1.2 exemplifies a LSPR scheme, where the metallic nanostructures that exhibit these phenomena are referred to as **Plasmonic NanoParticles (PNPs)**.^{10,11} When the particle size is smaller than the mean free path of the material.

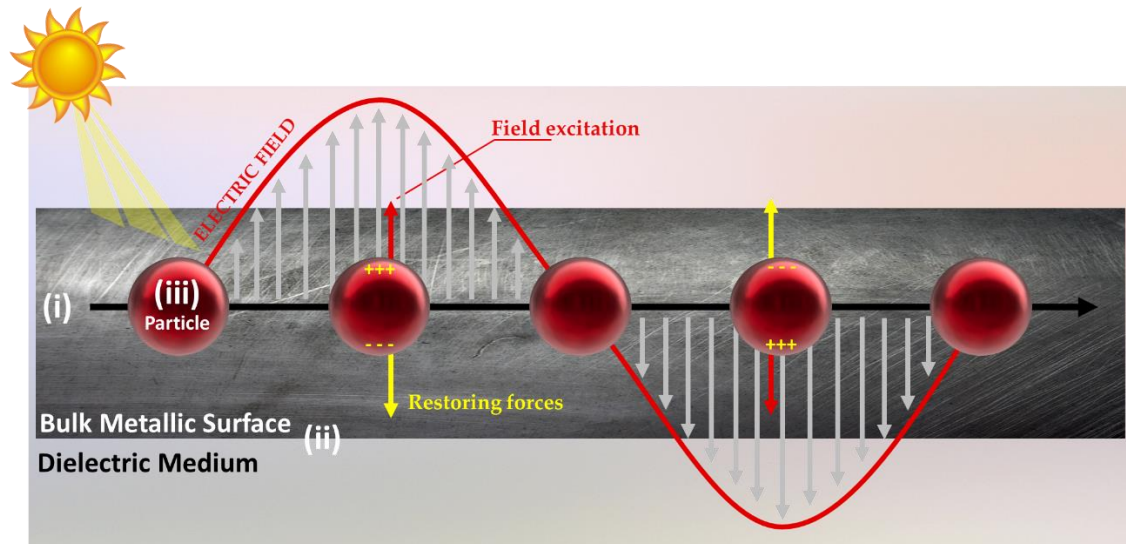


Figure 1.2. LSPR scheme depicting the 3 plasmon cases: (i) the bulk plasmon (3D) in a metal. (ii) the surface plasmon (2D) confined in a metal/dielectric interface. (iii) The local plasmon resonance (0D), where the metallic particle’s dimensions are much smaller than the incident wave’s wavelength.

To describe each LSPR-induced phenomenon, a description of the fundamental physics is required to fully comprehend the reason for these extraordinary optical capabilities exhibited by metallic nanoparticles.

Among existing theories, Mie theory is, so far, the most successful in describing the plasmonic photoexcitation and response by a single metallic nanosphere, thus, hereafter we focus on Mie theory.

1.2 Plasmon-driven Phenomena in Nanoscale

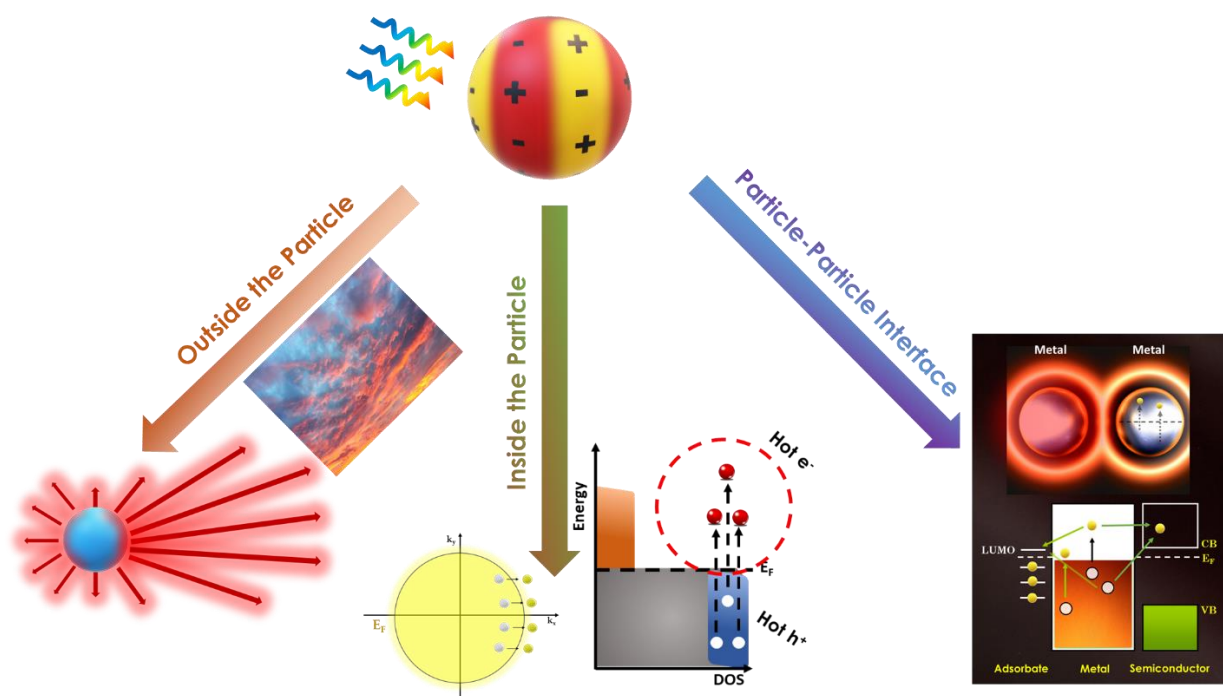


Figure 1.3. A schematic depicting the plasmon-driven mechanisms regarding the scale they occur. The LSPR-induced energy dampens through radiative phenomena outside the particle (light scattering) and non-radiative phenomena inside the particle (hot-carrier generation) and on the particle-particle interface (thermal effects, electric fields, and charge transfer to near acceptors).

1.2.1 Phenomena Outside the Particle (Light Scattering – Mie Theory)

1.2.1.1 The General Concept of Light Scattering

Scattering is the phenomenon according to which, light interacts with particles and changes its direction of propagation. The amount and type of scattering depend on the size and composition of the particles, as well as the wavelength of the light. Two well-known types of scattering are Rayleigh scattering and Mie scattering, which are named after their respective discoverers, Lord Rayleigh and Gustav Mie.

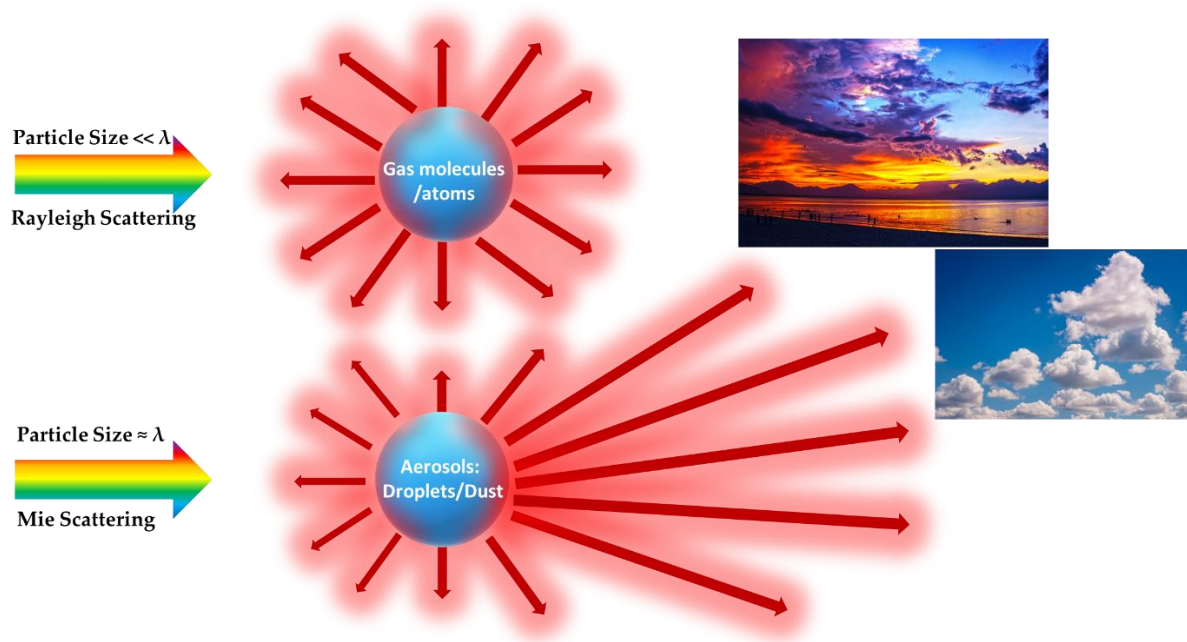


Figure 1.4. Schematic depicting the light scattering upon a homogeneous sphere varying size. The Rayleigh and Mie scattering are dependent on particle's size and wavelength of incident light. These phenomena explain the blue color of sky and the sunset colors.

Rayleigh scattering occurs when the size of the scattering particle is much smaller than the wavelength of the incident light. This type of scattering is responsible for the blue color of the sky during the daytime. When sunlight enters the Earth's atmosphere, the shorter blue wavelengths are scattered more than the longer red wavelengths. This scattering causes the blue light to spread out in all directions, giving the sky its characteristic blue color. At sunrise and sunset, the Sun's light has to travel through more of the atmosphere, which causes more scattering of the blue light, and leaves the longer red and orange wavelengths to dominate, thus leading to the warm hues we associate with those times of day, as shown in Figure 1.4.

Mie scattering, on the other hand, occurs when the size of the scattering particle is comparable to or larger than the wavelength of the incident light. This type of scattering is responsible for the white appearance of clouds and the blurring of images when viewed through fog. In Mie scattering, the scattered light is more evenly distributed across all wavelengths, resulting in a diffuse and uniform appearance. The degree of scattering also depends on the size and concentration of the scattering particles. During a sunset, the atmosphere also contains particles such as dust, pollution, and aerosols, which can scatter light, further enhancing the colors of the sunset. These particles are generally larger than the air molecules and can cause Mie scattering, which scatters all colors of light equally, leading to a more vibrant and colorful

sunset, combined with Rayleigh scattering. Mie theory is also important in other fields such as atmospheric science, where it is used to study the properties of aerosols, and in biology, where it plays a role in understanding the scattering of light in cells and tissues.

In summary, Rayleigh and Mie scattering are two important types of scattering that occur when light interacts with particles of different sizes. Rayleigh scattering occurs when the particle size is much smaller than the wavelength of the incident light, while Mie scattering occurs when the particle size is comparable to or larger than the wavelength. Understanding these phenomena is important in a range of fields, from atmospheric science to biology. In this thesis, we focus on scattering phenomena described by Mie theory.

1.2.1.2 Dielectric function

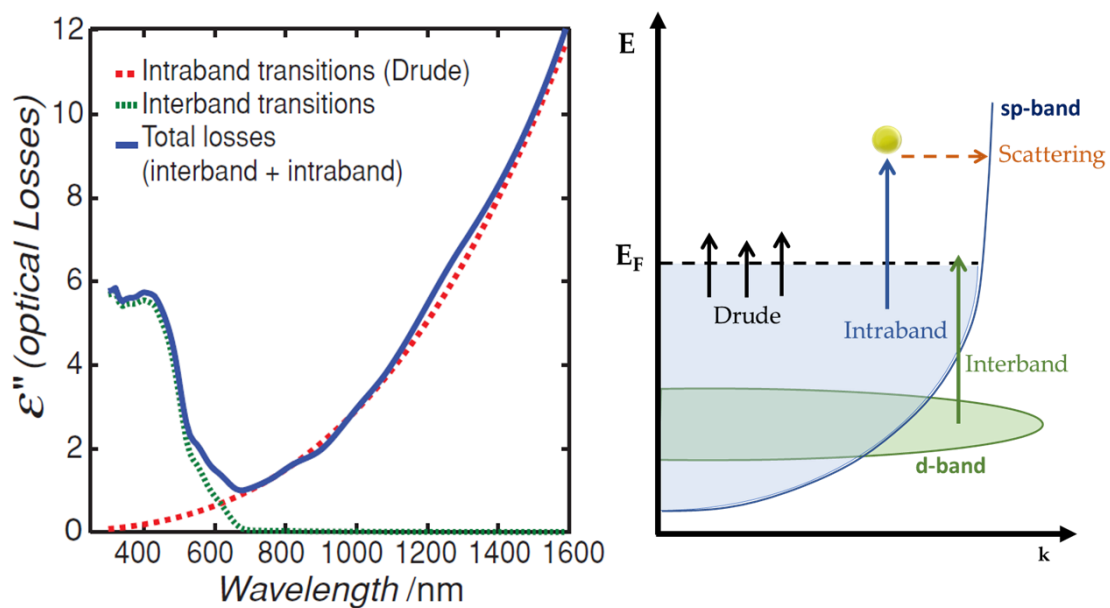


Figure 1.5. (left) The imaginary part of dielectric function of Au, depicting the losses in the visible region due to interband transitions. (right) The electron motion in a metallic lattice: Drude motion due to LSPR and interband/intraband transitions due to photon absorption.

Metals are essential in the study of plasmonics, mainly due their "free" electron density in their valence bands. Their response to incident electromagnetic waves can be described by the dielectric function. In bulk metals, the Drude model entails that the optical response can be approximated by evaluating the influence of an external electromagnetic-stimulus on a single free electron and then multiplying by the total number of electrons.¹² Assuming the external force could be expressed by a simple electric field, Newton's law is applied:

$$m_e \frac{d^2 r}{dt^2} = e \bar{E} - m_e \gamma_0 \bar{u} \quad (1.1)$$

$$\text{, where } \bar{E} = E_0 e^{-i\omega t}$$

γ_0 is the so-called Drude damping constant. Then, the dielectric function can be written as:

$$\varepsilon(\omega) = \varepsilon(re) + i\varepsilon(im) = 1 - \frac{\omega_p^2}{\omega^2 + i\gamma_0\omega} \quad (1.2)$$

, where $\omega_p^2 = ne^2/\varepsilon_0 m_e$ is the plasma frequency of the electrons inside the metal structure, n is the free electron density, e is the electron charge, ε_0 is the vacuum permittivity, m_e is the electron effective mass and γ_0 is the damping constant.¹³ For the case of the free electron gas in the limit $\gamma_0 < \omega$, γ_0 equals to the plasmon bandwidth Γ . Characteristic values for the common plasmonic metals are listed in Table 1.1.

Table 1.1. Characteristic parameters of plasmonic metals.

Material	Plasmon frequency ω_p (eV)	Work function (eV)	Damping constant γ (eV)	Interband transition energy (eV)
Silver	9.01	4.26	0.05	3.3
Gold	8.93	5.10	0.14	2.4
Aluminum	14.98	4.28	0.10	1.5
Copper	11.01	4.65	0.06	3.5

The damping term in the dielectric function (eq. 1.2), as described by the imaginary part, is attributed to interband transitions and scattering losses (Figure 1.5), mainly due to the presence of crystal impurities and relaxation events.¹⁴ These damping mechanisms are described by the damping constant γ_0 and expressed via Matthiessen's rule as

$$\gamma_0 = \sum_i \frac{1}{t_i} = \frac{1}{t_{e-e}} + \frac{1}{t_{e-ph}} + \frac{1}{t_{e-d}} \quad (1.3),$$

where t_{e-e} , t_{e-ph} , and t_{e-d} are the relaxation times of electron-electron, electron-phonon, and electron-defect¹⁵, respectively. When the particle size is smaller than the mean free path of the

material, the electron-surface backscattering dampens LSPR because the particle boundaries confine the electron mobility. As a result, the damping constant has a radial dependence:

$$\gamma(r) = \gamma_0 + A \frac{u_F}{r} \quad (1.4),$$

where r is the particle radius and A is a dimensionless empirical constant on the order of unity.¹⁶

1.2.1.3 Mie equations

When the dielectric constants of a given particle and its environment are known, the phenomena of light scattering must be analyzed to calculate the plasmonic response. Faraday was the first -in 1857AD- to use Maxwell's electrodynamic theory, to explain how light interacts with the gold particles, resulting in a vivid ruby red color¹⁷, see for example Figure 1.1. However, an analytical solution remained elusive until 1908 when Gustav Mie solved the Maxwell equations with the appropriate boundary conditions for a single, homogeneous, dielectric sphere.¹⁸ Mie theory calculates size-dependent scattering and absorption cross-sections, and has numerous applications in fields such as nanotechnology, meteorology, astrophysics, and biology.¹⁹ As seen in Figure 1.4 when the particle size is much smaller than the wavelength of the incident wave ($d = 5$ nm), the scattered light distribution corresponds to electric dipole radiation. The Mie effect manifests itself in changes in light distribution as particle size increases.

Mie equations for a spherical particle: for the case of a spherical particle, the wave equation in spherical coordinates

$$(\nabla^2 + k^2)\Phi = 0 \quad (1.5)$$

has several independent scalar potential solutions:

$$\Phi_{enm}^o(r, \theta, \phi) = \zeta_n(kr) P_{nm}(\cos \theta) \quad (1.6)$$

Where $n = 1, 2, \dots, \infty$ and $m = 0, \pm 1, \dots, \pm n$. ζ_n represents either spherical Bessel functions j_n or spherical Neumann functions y_n or spherical Hankel functions h_n . $P_{nm}(\cos \theta)$ are the Legendre polynomials.

Assuming the radial vector $\vec{r} = r\hat{r}$, we consider a pair of spherical harmonics M_{enm} and N_{enm} associated with Φ as:

$$M_{enm} = \nabla \times (\Phi_{enm} r) \quad (1.7)$$

$$N_{enm} = k^{-1} \nabla \times M_{enm} \quad (1.8)$$

Then, the incident and scattered waves propagating on the z-axis and polarized on the x-axis can be calculated in terms of spherical harmonics:

$$E_{inc} = E_0 \sum_{n=1}^{\infty} \frac{i^n (2n+1)}{n(n+1)} [M_{on1}^{(1)}(k_M) - iN_{en1}^{(1)}(k_M)] \quad (1.9)$$

$$H_{inc} = \frac{-k_M E_0}{\omega \mu_0} \sum_{n=1}^{\infty} \frac{i^n (2n+1)}{n(n+1)} [M_{en1}^{(1)}(k_M) + iN_{on1}^{(1)}(k_M)] \quad (1.10)$$

$$E_{sca} = E_0 \sum_{n=1}^{\infty} \frac{i^n (2n+1)}{n(n+1)} [M_{on1}^{(3)}(k_M) - ia_n N_{en1}^{(1)}(k_M)] \quad (1.11)$$

$$H_{sca} = \frac{k_M E_0}{\omega \mu_0} \sum_{n=1}^{\infty} \frac{i^n (2n+1)}{n(n+1)} [a_n M_{en1}^{(3)}(k_M) + ib_n N_{on1}^{(3)}(k_M)] \quad (1.12)$$

Then, applying Maxwell's boundary conditions at the particle surface considering the symmetry of a sphere, scattering coefficients a_n and b_n can be calculated as

$$a_n = \frac{\psi_n(\chi)\psi_n'(m\chi) - m\psi_n'(\chi)\psi_n(m\chi)}{\xi_n(\chi)\psi_n'(m\chi) - m\xi_n'(\chi)\psi_n(m\chi)} \quad (1.13)$$

$$b_n = \frac{m\psi_n(\chi)\psi_n'(m\chi) - \psi_n'(\chi)\psi_n(m\chi)}{m\xi_n(\chi)\psi_n'(m\chi) - \xi_n'(\chi)\psi_n(m\chi)} \quad (1.14)$$

where $\psi_n(x) = xj_n(x)$, $\chi_n(x) = x\gamma_n(x)$ and $\xi_n(x) = xh_n(x)$ are Riccati-Bessel, Riccati-Neumann and Riccati-Hankel function respectively as shown in eq 1.6.

The parameter $m = n_p/n_M$ includes the complex refractive index of the particle and the refractive index of the surrounding medium.

x is the size parameter $x = k_M R$, where k_M is the wavenumber of the incident wave.

Bessel functions ensure the electric field's continuity at the origin of the reference frame centered in the spherical particle and Hankel functions represent the outgoing spherical waves.

The infinite sum over n corresponds to the radiating multipolar field expansion of order n , with $n = 1$ being the dipole mode. The extinction, scattering and absorption cross sections are calculated as:

$$\sigma_{ext} = \frac{2\pi}{k^2} \sum_{n=1}^{\infty} (2n+1) \Re(a_n + b_n) \quad (1.15)$$

$$\sigma_{sca} = \frac{2\pi}{k^2} \sum_{n=1}^{\infty} (2n+1) (|a_n|^2 + |b_n|^2) \quad (1.16)$$

$$\sigma_{abs} = \sigma_{ext} - \sigma_{sca} \quad (1.17)$$

Expressions 1.15, 1.16, 1.17 are the Mie equations that connect the light-matter interactions for the case of an isolated nanosphere.

In the present thesis, Mie equations have been implemented in MATLAB package MNPBEM and the computer code is presented in Appendix A.

1.2.1.4 Dipole Approximation

The electric field is assumed to be constant for particle sizes much smaller than the wavelength of the incident light, and retardation effects are ignored. In this case, the particle is thought of as an electric dipole, and its polarizability scales with particle diameter d as follows:

$$a(\omega) = d^3 \frac{\varepsilon_{re}(\omega) - \varepsilon_{im}}{\varepsilon_{re}(\omega) + 2\varepsilon_{im}} \quad (1.18)$$

In the dipole approximation, $\sigma_{abs} \sim \sigma_{ext} \propto I[a(\omega)]$ and scattering events are negligible since the particle size is small. The multipolar excitations are restricted only to dipole mode ($n=1$), thus the exact solutions of eqs 1.15-1.17 are:

$$\sigma_{ext} = \frac{24\pi^2 d^3 \epsilon_2^{3/2}}{\lambda} \frac{\epsilon_{im}(\omega)}{(\epsilon_{re}(\omega) + 2\epsilon_M)^2 + \epsilon_{im}(\omega)^2} \quad (1.19)$$

$$\sigma_{sca} = \frac{16\pi^2 d^6 \epsilon_2^{1/2}}{3\lambda} \frac{(\epsilon_{re}(\omega) - \epsilon_M)^2 + \epsilon_{im}(\omega)^2}{(\epsilon_{re}(\omega) + 2\epsilon_M)^2 + \epsilon_{im}(\omega)^2} \quad (1.20)$$

A Mie resonance occurs when the denominator of eqs 1.19-1.20 takes the lowest value, thus

$$\epsilon_{re}(\omega) = -2\epsilon_M \quad (1.21)$$

This means that at a given wavelength, the Mie cross sections are maximum. This results in a spectral response, as shown in Figure 1.6.

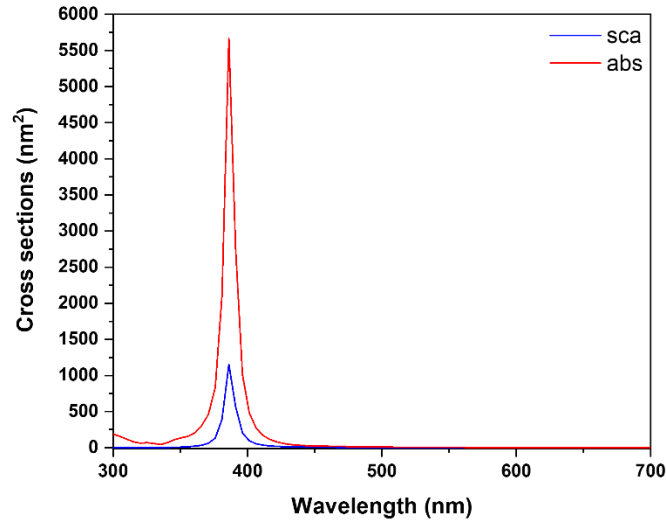


Figure 1.6. Absorption and scattering cross sections varying wavelength. The wavelength where the peak is observed, corresponds to plasmon resonance wavelength.

Thus, according to Mie theory, LSPR is affected by particle size as well as the dielectric properties of both the particle and the surrounding medium.

1.2.1.5 Effect of Particle Size and Surrounding Medium

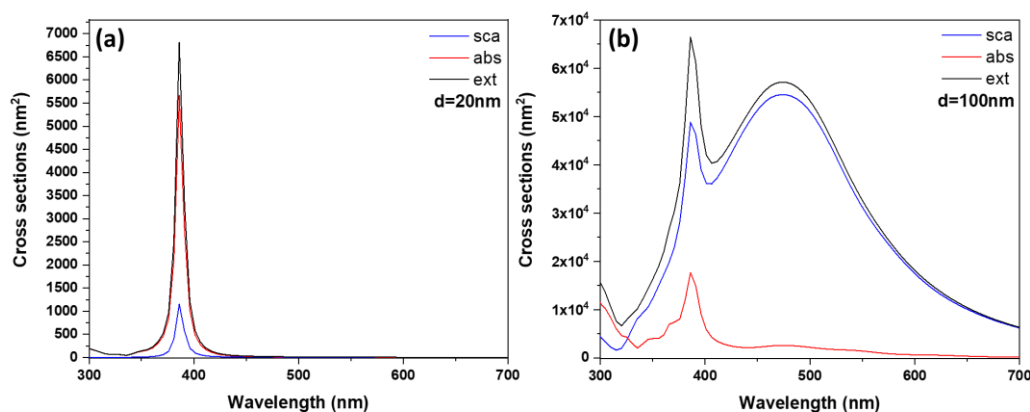


Figure 1.7. Cross sections for a single (a) 20 nm and (b) 100 nm Ag particle. The spectra are simulated by MNPBEM Matlab package and the optical data sets for silver, shown in Appendix A.

Figure 1.7 depicts the absorption of 20 nm Ag particles versus 100 nm particles. The larger the particle size, the higher the scattering cross section of light. Furthermore, losses are reduced when particle dimensions exceed the electron mean free path (for example, 40nm for silver, see Table 1.1). Another effect of increasing size is a red-shift of the plasmon resonance, as shown in Figure 1.7. Particles that have grown in size can no longer be considered dipoles.

The electric field's phase may differ across the particle volume, resulting in nonuniformities in charge distribution on the particle surface; thus, retardation effects must be considered.^{20,21} Aside from the resonance red-shift, Figure 1.9a shows that increasing particle size induces additional plasmon bands, because multipolar modes of higher order arise (dipolar and quadrupolar).²²

Dipole term: The electric field around a spherical particle can be expressed as a series of spherical harmonics, which are solutions to the Laplace equation. The first term in the series corresponds to the monopole, which represents the total intensity of the field. The second term corresponds to the dipole, which represents the directional component of the field. The third term corresponds to the quadrupole, which represents the variation of the field intensity with direction. The dipole term is the dominant term in the field expansion for small particles, where the size of the particle is much smaller than the wavelength of light, shown in Figure 1.8a. This is because the dipole term is proportional to the size of the particle, while the quadrupole term

is proportional to the square of the particle size. The dipole term is also dominant for particles that are highly polarizable, such as metallic particles.

Quadrupolar term: The quadrupole mode becomes increasingly important as the size of the particle approaches the wavelength of light, see Figure 1.8b. This is because the variation in the intensity of the field becomes more significant as the particle size increases. The quadrupole term is also dominant for particles that have an anisotropic shape, such as prolate or oblate spheroids. In summary, the dipole and quadrupole terms in Mie theory describe the directional and intensity components of the electric field around a spherical particle, respectively. The dominance of each term depends on the size and shape of the particle, as well as its polarizability.

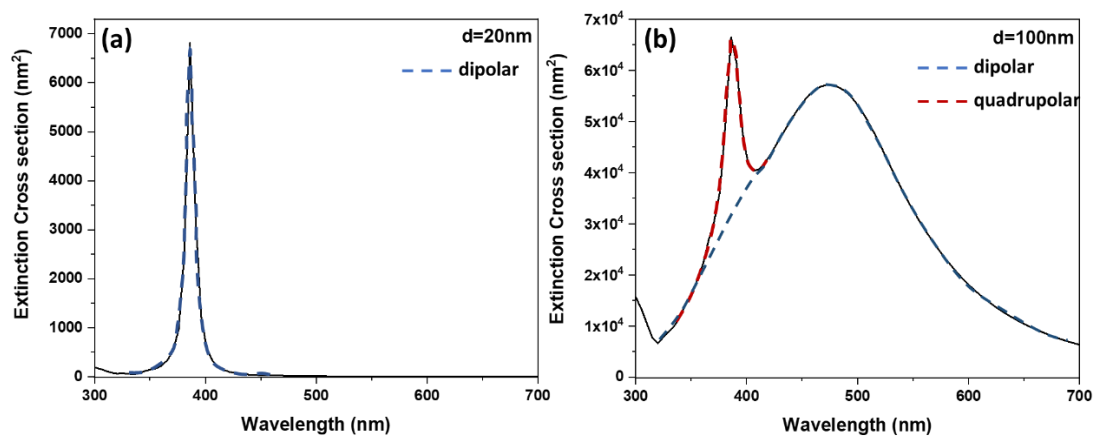


Figure 1.8. Extinction cross section of single Ag nanoparticle of (a) 20 nm and (b) 100 nm. The spectrums are deconvoluted in dipolar and quadrupolar modes.

When the refractive index of the surrounding medium is increased, redshifts of LSPR peaks are also expected, as shown in Figure 1.9b.^{23,24} As previously stated, cross sections reach their maximum value under the resonance condition of eq 1.21, demonstrating the effect of the dielectric medium on interfacial electronic oscillations.

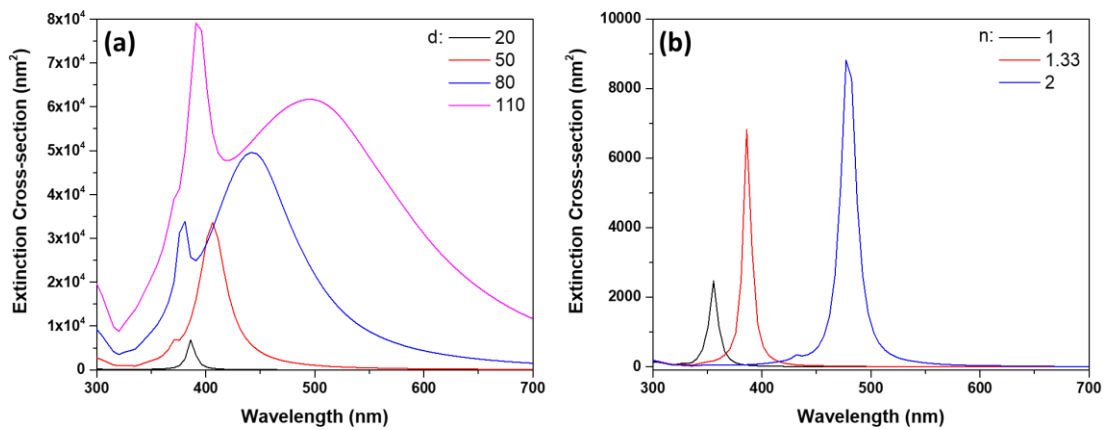


Figure 1.9. (a) Extinction cross sections of Ag particles varying in diameter (d) of the particle. (b) Extinction cross sections of Ag particles, for varying refractive index (n) of the surrounding medium.

1.2.1.6 Mie Theory Limitations

Particle Shape: Although Mie solutions to Maxwell's equations give satisfactory interpretation of plasmon resonance, for an isolated homogeneous spherical particle. Many practical applications require deviation from the spherical shape since the particle morphology displays higher sensitivity in resonance tuning than the particle size engineering.

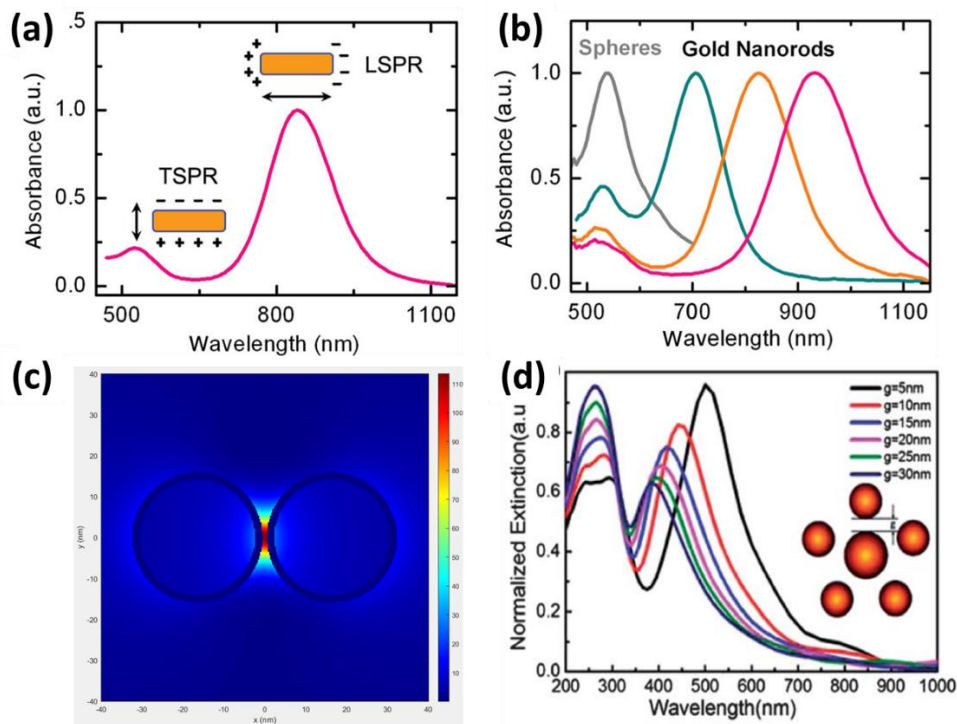


Figure 1.10. (a) Extinction spectra of a gold nanorod, displaying the transverse and longitudinal modes. (b) Extinction spectra of gold nanorod varying aspect ratio. Increasing aspect ratio, the resonance peak is red-shifted. (Taken from this work²⁵). (c) Electric field contour for a plasmonic dimer consisted of Ag nanospheres of 30nm. Hot spots are observed in the interparticle nanogap. (d) Extinction spectra of aggregated Ag nanoparticles. (Taken from this work²⁶).

Because the elongated shape induces plasmon-resonance tuning to the near-infrared region where human tissues are transparent, gold nanorods are a well-known plasmonic system in biomedical applications, as shown in Figure 1.10a-b.^{27,28}

Nanoparticle Aggregates: Furthermore, because of the trapped scattered photons in close proximity, plasmonic dimers (two neighboring metallic particles) generate enhanced electric fields confined in the interparticle nanogaps.²⁹ These fields concentrated in "hot spots," are the reason that PNPs are used as "antennas" in a variety of applications to enhance incoming electromagnetic waves and accelerate chemical transformations, as presented in Figure 1.10c. Mie theory, aside from the dimer ideal, cannot explain the plasmonic response of plasmonic aggregates, where intense plasmonic coupling between PNPs strengthens LSPR phenomena. Figure 1.10d depicts the plasmonic spectra of Ag aggregates with varying particle size. When

the interparticle nanogap is decreased, nonuniformities in charge oscillation induce additional red-shifted plasmon bands, in a similar way by increasing particle size.²⁶ When the nanogap is increased until each particle is considered isolated, the plasmon resonance is similar to that predicted by Mie theory.

1.2.2 Phenomena Inside the Particle

LSPR in metal nanostructures give rise to a collection of optical and electronic phenomena, processes that occur during the excitation and subsequent damping of the plasmon energy stored in the oscillating electron cloud. Plasmonic effects are attributed to radiative and non-radiative effects.³⁰ In the case of the former, LSPR relaxes and re-radiates light into the far-field and/or the metal nanostructures act as a secondary light source (antenna) that concentrates light in particle surface and enhances local electric fields in close proximity. In the case of the latter, the plasmon dephasing causes photon absorption that deposits electronic energy and results to highly energetic electrons with energy above the Fermi level, the so-called “hot” electrons.^{31,32} In this context, all the possible pathways of these hot carriers and routes of the plasmon-energy dissipation will be distinguished in the following sections.

1.2.2.1 Hot Carriers

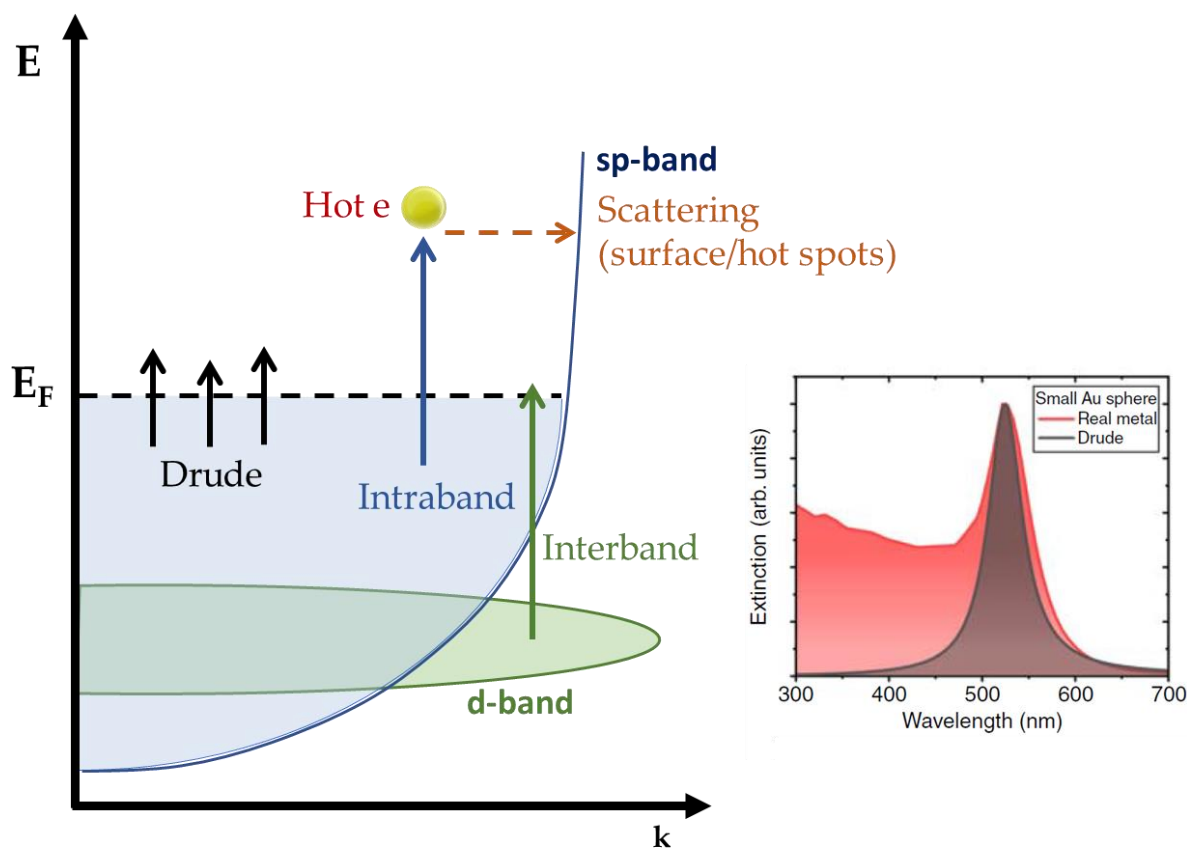


Figure 1.11. A schematic depicting the allowed electronic transitions in Ag, i.e., the plasmon-energy damping channels

Considering an electron cloud following Fermi-Dirac distribution, Figure 1.11 depicts the carrier dynamics and plasmon decay pathways when an external electric field interacts with a PNP. Because LSPR decay is a multi-step non-radiative event, a detailed step-by-step explanation of the plasmon energy transfer is necessary to comprehend the plasmon-driven mechanisms. In classical picture, the charge displacement results to a coherent oscillation of the electron cloud following Drude model. However, in the quantum mechanical picture, the quantization of the electric field must also be considered.³³ Under such perspective, the PNPs are illuminated by discrete photons with energy $\hbar\omega$. Furthermore, photon absorption in this light-matter interaction is impossible because such transitions require additional momentum through inelastic scattering (eg. with a defect or a phonon) or occur in a confined system with boundaries (back-scattering events), as shown in Figure 1.11.^{34,35}

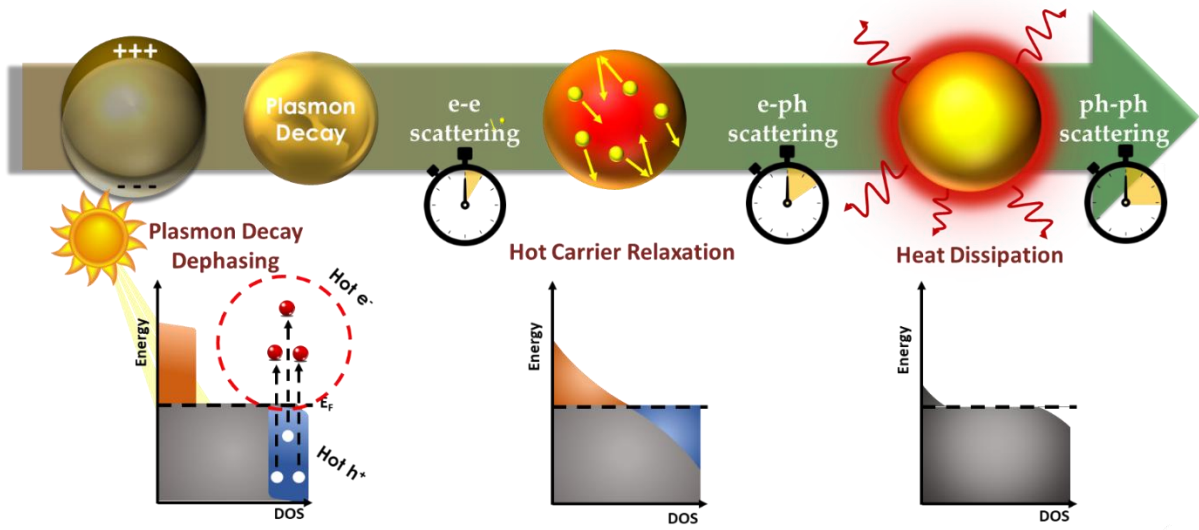


Figure 1.12. Hot Carrier Relaxation Events. (from left to right): The absorption of light photons deposits energy into electronic distribution and stimulates electron-holes pairs above the Fermi level. Subsequently, the hot carriers relax and equalize their temperature with the lattice vibrations in a few ps. The relaxation of hot lattice is achieved via phonon-phonon interactions, where stored energy in the vibrational modes is dissipated from the nanoparticle to the surrounding medium as generated heat leading to temperature rise.

After this introduction to the dynamics of charge carriers in a metal, the effects of quantum confinement in small particles should be introduced. The first immediate consequence of this transition is that the current created by the driving field will accumulate electric charge at the surface of the particle. In the classical picture, these charges would accumulate solely at the surface of the particle, but in realistic systems the charges at the interface extend into a non-zero volume inside the metal, screened and in interaction with other mobile charges. Therefore, decreasing the particle size, the quantum effects at the surfaces become more relevant over the plasmon dynamics.³⁶ Specifically, they contribute to plasmon dephasing, with the coherent collective oscillation of the carriers in the metal decaying into incoherent electronic excitations. This is observable through the broadening of the plasmonic peak in small NPs, with an increased plasmon decay rate scaling as the inverse of the size, expressed by eq 1.4³⁷

$$\gamma_{surf} = A \frac{u_F}{R}$$

Regarding the classical description, the surface-induced damping arises from the collisions of electrons with the boundaries of the particle, while quantum-mechanically speaking, the boundary discretizes the electronic states inside the metal. Then, the surface allows a breaking of the momentum conservation by discretizing the electronic states in the particle, a process known as surface-assisted plasmon decay or Landau damping.^{38,39} This anelastic scattering allows the excitation of nonthermal hot electrons with energies ranging in the interval $E_F < E_{HE} < E_F + \hbar\omega$, even in crystals with no defects and assuming an absence of electron–phonon interaction.⁴⁰ Thus, the generation of hot carriers can be controlled by modifying the size and shape of the metallic particle.^{41–43} Another factor that correlates to surface confinement, and hence the stimulation of hot carriers is the presence of intense electric fields in particle’s boundary vicinity, also known as hot spots (will be explained in further details in the next section).⁴⁴ When this local field distribution is concentrated in sharp features the nanostructure may have or in nanogaps for the case of coupled PNPs, the plasmonic fields amplifies significantly the population of nonthermal carriers.^{45–47}

The excitation of hot carriers in metallic nanoparticles depends on the lossy nature of LSPR process. Hence, one should comprehend all the non-radiative decay mechanisms expressed by the plasmon lifetime in similar fashion with eq 1.3:⁴⁸

$$\gamma_{plasmon} = \gamma_{Drude} + \gamma_{interband} + \gamma_{surf} + \gamma_{HotSpots} + \gamma_{rad} \quad (1.22)$$

γ_{Drude} is the term for the electron-electron and electron-phonon interaction following the classical electrodynamic picture of coherent charge oscillation. $\gamma_{interband}$ is the term for the direct optical transitions (typically from the d to sp band for the case of noble Ag & Au), which is not included in the classical model. The previously described surface and hot spots effects are included in γ_{surf} and $\gamma_{HotSpots}$ respectively. Contrary to the other terms, γ_{rad} is the term for radiative losses, where light is re-emitted in the far-field.

When this stored plasmon energy is not shared to other systems with any of the aforementioned pathways, the following relaxation events dampens the plasmon resonance until the energy is dissipated as heat (shown in Figure 1.12):^{49,50}

- Electronic thermalization

The free electrons in the metal's valence band can be thought of as an electronic gas with a Fermi-Dirac distribution ($T_e = 0$ K). The absorption of light photons deposits energy into

electronic distribution and stimulates electron-holes pairs above the Fermi level (see Fig. 1.9). Because the generated hot electrons and holes are highly energetic, the initial electron and hole distribution is non-thermal and far from the Fermi-Dirac distribution anticipated for charge carriers at a given temperature. As a result, electron-electron interactions redistribute the extra energy, bringing the electronic plasma to an equilibrium state at a high temperature within some hundreds of fs.⁵¹ Silver and gold exhibit relaxation times of 350 fs and 350 fs, respectively, in the case of noble metals.

- Hot carrier relaxation

The following stage involves the conversion of electronic energy to vibrational energy via electron-phonon interactions.⁵² The two-temperature model (TTM) may represent the hot electron-phonon coupling, in which the electronic gas and the crystal lattice are two connected subsystems with distinct temperature distributions. TTM is valid owing to the difference in heat capacity between the systems. According to conventional electron-phonon relaxation times, the hot carriers relax and equalize their temperature with the lattice vibrations in few ps. As a result, the equilibrium inside the particle has been restored, as the electron gas temperature matches the crystal lattice temperature, and internal thermal homogeneity has been achieved.⁵³ When entering the quantum size domain, it is fascinating to investigate the hot carrier interactions under the size confinement. The particle size influence in the timescale of electron-phonon interactions was demonstrated by Hartland et al.⁴⁹ and Link et al.⁵⁴ Furthermore, Nordlander et al. demonstrated that the hot electron generation rate is particle-size dependent as well.

- Heat dissipation

The relaxation of hot lattice is achieved via phonon-phonon interactions, where stored energy in the vibrational modes is dissipated from the nanoparticle to the surrounding medium as generated heat leading to temperature rise in particle vicinity. The timescale of heat dissipation is on order of a few hundred ps and will be further elaborated in “Thermoplasmonics” Section. During the external thermalization, the temperature of the electron gas and the lattice gradually decreases and the whole system recovers to its original (ground) state prior to the excitation. For a long time, the absorption and this subsequent temperature rise were considered to be side effects in the LSPR, however this optical loss can be utilized giving birth to a subfield called thermoplasmonics.⁵⁵ The purpose of this field is to employ metal nanostructures under illumination as controlled nano-sources of heat, leveraging the quick conversion of light energy

into heat and opening the door to new emergent applications. As a result, understanding the dynamics of plasmon-induced hot carriers and energy transfer via carrier interactions is critical, in order to utilize the full potential of PNPs.

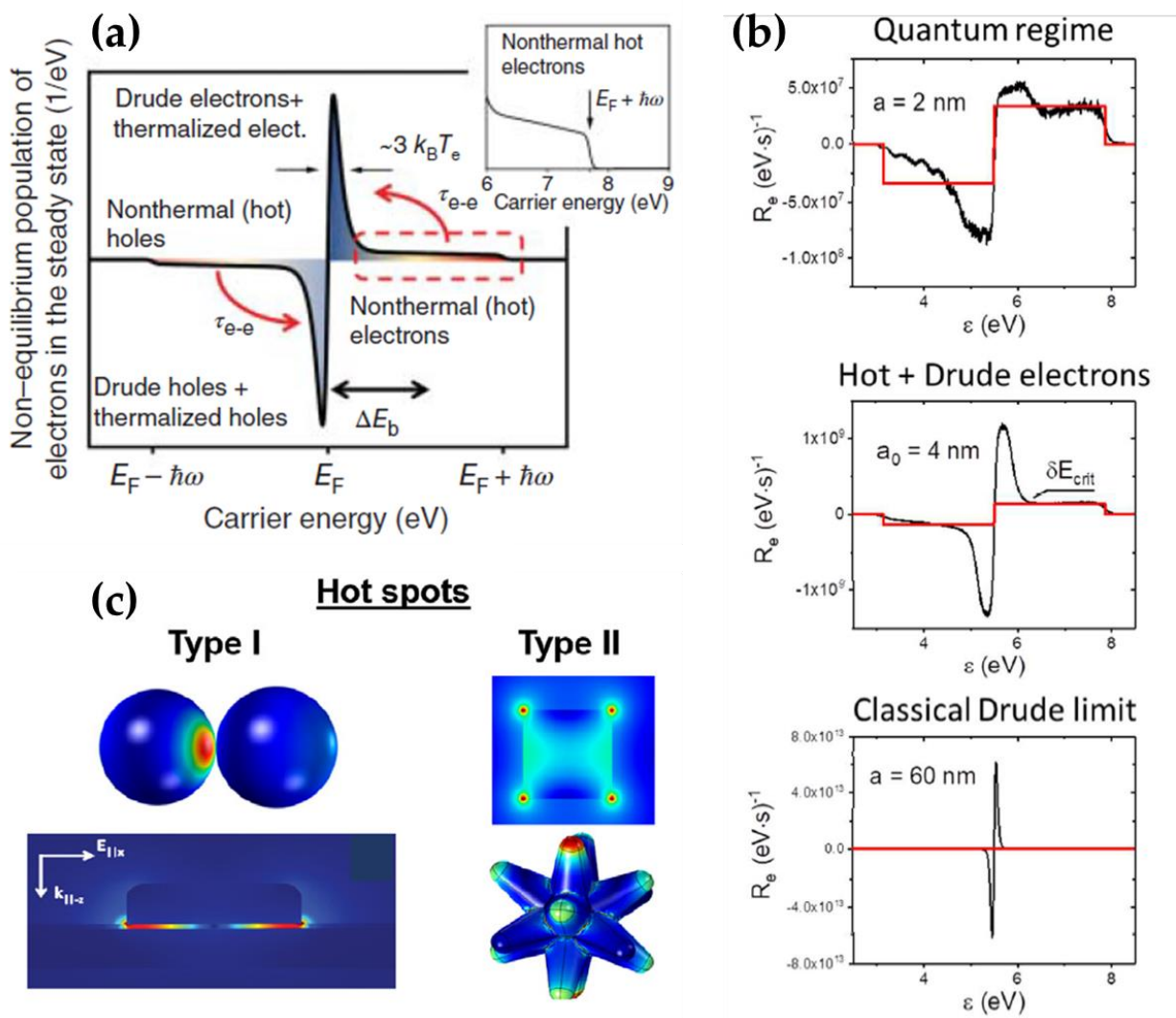


Figure 1.13. Illustration scheme hot carrier excitation and transfer. (a) was adapted from this work⁵⁶. (b) was adapted from this work.⁴⁸

During the plasmon non-radiative decay several types of excited electrons coexist inside the particle, characterized mainly by the energy distribution. The common kind are the electrons that carry the current of the plasmonic oscillation and have small energies above the Fermi level, known as Drude electrons, while the counterpart holes reside below Fermi level, as shown in Figure 1.13a. The carrier population that extends to energies up to the total photon energy $\hbar\omega$ above/below Fermi level is attributed to hot electrons/holes respectively, i.e. the

surface-induced nonthermal carriers that cannot be described by Fermi-Dirac behavior of the electron cloud.⁵⁷ The origin of these energetic carriers in metallic nanostructures is typically encountered in intraband transitions, where electron-surface scattering events allow photon absorption.⁵⁸ If left unexploited, the nonthermal hot carriers rapidly relax back to Drude electrons while raising the electron cloud to a higher electronic temperature, as explained above. In this context, Govorov et al. calculated the generation of nonthermal carriers as:⁴⁸

$$P_{hot-e} \approx \frac{1}{2\pi^2} \times \frac{e^2 E_F^2}{\hbar} \frac{1}{(\hbar\omega)^2} \int_{S_{NP}} |E(r)|^2 ds \quad (1.23)$$

where $E(r)$ is the electric field inside the metallic particle.

This work alongside Manjavacas et al., highlighted the influence the particle size has in the hot-carrier generation rate and energy distribution. Specifically, Figure 1.13b demonstrates that despite larger Ag particles excite more electrons, they are low-energy, Drude-like carriers. By decreasing particle size, surface effects dominate and plasmon decays into high-energy electrons, although the population of hot carriers remain low compared to Drude carriers.^{41,48} In the case of 2 nm particles, the overall carrier population is lower than that of the larger particles but the relative concentration of hot and Drude carriers is almost equal. Moreover, eq 1.23 reveals that hot-carrier generation depends on the electric fields on the particle surface.⁴⁸ Specifically, hot spots formed in coupled PNPs and/or sharp features in PNP shape, increase the number of hot electrons drastically.^{45,59-61}

Despite the engineering of the PNP characteristics for higher generation of hot carriers, they must be transferred to the immediate environment so that this stored energy can contribute to chemical reactions. Thus, other important parameters to the successful charge transfer is the carrier migration and injection to a near electron acceptor.⁶² The latter can be consisted of (i) a molecule adsorbed in the metal's surface and/or (ii) a semiconductor in contact with metal. In this context, two major distinct routes have been established for harvesting these hot carriers: the (i) indirect electron transfer and the (ii) direct electron transfer to the desired adsorbate/semiconductor (will be further described in the following section).

1.2.3 Phenomena in the Particle-Particle Interface {Metal-Metal}

1.2.3.1 Near-field Enhancement (Hot Spots)

As mentioned above, the conduction electrons in a metallic nanoparticle collectively behave as a coherent electronic cloud when stimulated by an incident electromagnetic wave. The Coulomb-induced charge displacement causes the polarization of the particle, with charges accumulating at the opposite ends of its structure. This oscillating behavior is maximum at resonance, resulting in a near-field amplification near the charged area, i.e., the particle's surface. Thus, the capacity of PNPs to efficiently concentrate light is required for these localized high electric fields in the particle proximity. As a direct LSPR-induced mechanism, near-field enhancement is highly sensitive on particle morphology and plasmonic coupling. As the shape becomes more intricate, the local fields around sharp features are remarkably enhanced, as shown in Figure 1.14a.^{63,64} Nanostars exhibit intense electric fields even in the single-particle level, because the curvature of these features increase the surface charge density in this region. The local fields in the nanogaps between coupled particles, the so-called "hot spots", are significant because they result in significant increases of the near-field enhancement.⁴⁴ Based on this, plasmonics has evolved into a distinct study area in which nanoparticle shapes may be built and modified to achieve the required field augmentation at specific sites, using the plasmon hybridization principle.⁶⁵

Regarding plasmonic nanoensembles, the first experimental evidence of these enhanced fields was when Raman scattering was greatly amplified by the presence of a metallic substrate,⁶⁶ which later attributed to LSPR giving birth to Surface-Enhanced Raman Scattering (SERS).⁶⁷ For the case of spherical particles, the analytical solution for the magnitude of the electric field outside the particle, is given by:⁶⁸

$$E_{out}(x, y, z) = E_0 \hat{z} - \alpha E_0 \left[\frac{\hat{z}}{r^3} - \frac{3z}{r^5} (x\hat{x} + y\hat{y} + z\hat{z}) \right] \quad (1.24)$$

where α is the polarizability in eq 1.18. In Raman scattering, the applied field induces an oscillating dipole in the molecule on the surface. When this dipole radiates, there is a probability for a vibrational transition to occur resulting to a different re-emitted frequency. Because the initial photon absorption is proportional to the electric field intensity near the

molecule, LSPR-induced enhanced local fields can greatly amplify this process. Thus, the SERS enhancement is relative to the initial intensity of the incident wave as:⁶⁹

$$EF = \frac{|E_{out}|^2 |E'_{out}|^2}{|E_0|^4} \quad (1.25)$$

EF factor directly correlates to hot spots intensity (Figure 1.14b), establishing SERS as an excellent tool to study and quantify the plasmon-induced near-field enhancement in the PNPs surface.⁷⁰

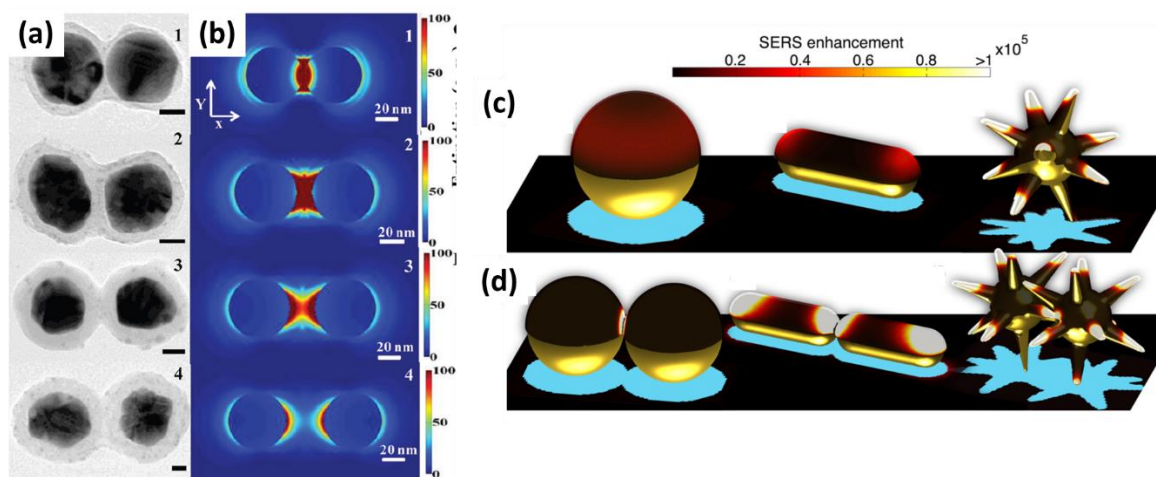


Figure 1.14. (a-b) Hot spots mapping varying SiO₂ shell thickness of Ag@SiO₂ particles (taken from this work⁷¹). (c-d) SERS enhancement for the case of a sphere, rod, star and the dimer.

1.2.3.2 Thermoplasmonics

Until the early 2000s, photothermal effects were regarded as undesirable side effects in the plasmonics field. The pioneering work of Halas group at photothermal cancer therapy established thermal effects as a beneficial plasmon-induced mechanism.^{72,73} It is already mentioned that when the 'free' electrons are excited on resonance, the part of the plasmon energy that is not radiated through light scattering is dissipated through Landau damping (non-radiatively), causing a dramatic temperature rise in particle's vicinity and making possible heat control in nanoscale.⁷⁴ Even in resonance, metals are not ideal optical conductors, so due to their lossy nature the imaginary part of their dielectric function implies the generation of

resistive heat (photon-electron interactions) and its dissipation through lattice oscillations (electron-phonon interactions).⁷⁵ This mechanism gave birth to the new sub-field of Thermoplasmonics, where Guillaume Baffou established the fundamental physics.^{55,76,77}

1.2.3.2.1 Fundamental Physics of Plasmonic Heating

To understand better this process, let's consider a metal nanoparticle of complex dielectric function $\varepsilon(\omega)$, that is illuminated by monochromatic light at a frequency $\omega = 2\pi c/\lambda$ where $E(r,\omega)$ is the complex amplitude of the incident electric field. Since the electronic excitation resembles a current in the metal, heat is generated by Joule mechanisms, the heat power density is proportional to distance r and time t and given by:

$$\vec{q}(r) = \frac{1}{2} \Re[\vec{J}^*(r) * \vec{E}(r)] \quad (1.26)$$

where $J(r)$ is the generated complex current density inside the nanoparticle. Using the relations $J^*(r) = -i\omega P(r)$ and $P = \varepsilon_0 \varepsilon(\omega) E$, eq 1.26 can be rewritten as:

$$q(r) = \frac{\omega \varepsilon_0}{2} \Im[\varepsilon(\omega)] |E|^2 \quad (1.27)$$

Then, the total generated heat delivered by a nanoparticle, is simply the integrated heat density over a specific volume and given by:

$$Q = \frac{\omega \varepsilon_0}{2} \Im[\varepsilon(\omega)] \int dr |E| \quad (1.28)$$

It is clear that heat generation is proportional to the square of the electric field outside the particle, emphasizing the significance of Mie's hot spot distribution and intensity. The problem of heat calculations is primarily geometrical in nature. Mie equations simplify the calculation for simple geometries such as spherical nanostructures, and the heat power can be expressed:

$$Q = \sigma_{abs} I \quad (1.29)$$

where σ_{abs} is the Mie-derived absorption cross section and I is the irradiance of the incident radiation $I = n_m c \varepsilon_0 |E_0|^2 / 2$.

The temperature profile under continuous-wave illumination can be investigated once the heat power originating from the Joule mechanism is determined. Supposing a uniform medium, the resolution of the heat diffusion equation is used to determine the temperature distribution $T(r)$:

$$p c_p dT(\vec{r}, t) - k \nabla^2 T(\vec{r}, t) = q(\vec{r}, t) \quad (1.30)$$

where p is the density of the material, c_p is the heat capacity at constant pressure, k is the constant thermal conductivity and $T(r, t)$ is the equilibrium temperature as a function of space and time. Eq 1.30 indicates that the generated heat is highly dependent on the heat capacity and the thermal conductivity of the material. In the case of metal nanostructures, the thermal characteristics are defined by the 'free' electrons according to the Fermi-Dirac distribution. As a result, a part of the absorbed photon energy can be stored in the lattice as vibrational energy known as phonon. Although this work focuses on continuous-wave illumination that simulates solar irradiance, pulsed illumination allows for the study of hot electron dynamics because the time scale of pulsed energy is in the same range as the time scale of electron-electron and electron-phonon relaxations. Except of diffusion, convection is a heat transfer mechanism as well. Convection takes place when the plasmonic nanoparticles are dissolved in a liquid medium causing thermal-induced fluid convection. However, this kind of convection cannot distort the temperature homogeneity due to its weak Rayleigh number.

Under continuous illumination, eq 1.30 is expressed by the Poisson (Laplace) equation inside(outside) the metallic nanoparticle:

$$\nabla^2 T(\vec{r}) = \begin{cases} -q(\vec{r}) / k, & r < R \\ 0, & r > R \end{cases} \quad (1.31)$$

For the case of a spherical particle of radius R , simple calculations lead to this temperature profile:

$$\Delta T(r) = \begin{cases} \Delta T_{NP} + T_{\infty}, & r < R \\ \Delta T_{NP} \frac{R}{r} + T_{\infty}, & r > R \end{cases} \quad (1.32)$$

where $\Delta T(r)$ is the temperature rise, T_{∞} is the ambient temperature and

$$\Delta T_{NP} = \frac{Q}{4\pi kR} = \frac{\sigma_{abs} I}{4\pi kR} \quad (1.33)$$

Despite heat density can be non-uniform within a metallic particle, in this case the temperature is constant because of the much larger thermal conductivity of metal compared to that of the surrounding medium.⁵⁵ Excluding the thermal properties of the metal, the temperature rise is highly dependent on the absorption cross-section, particle morphology and the illumination wavelength and intensity.

1.2.3.2.2 Sample Geometry

In thermoplasmonics, the PNPs are usually utilized in two geometries:

- NPs dispersed in liquid mediums, representing a 3D geometry.
- NPs deposited/attached on a substrate, representing a 2D geometry.

Eqs 1.33 can be applied in the former case, as the solution resembles a uniform medium of constant thermal conductivity k_s . The latter case is more complex because of the two surrounding media adding non-uniformity in the system. According to Figure 1.15, applying the image method and replacing the temperature and the generated heat power with the electric potential and the electric charges respectively, the elevated temperature equals as follows:

$$T(\vec{r}) = \frac{Q}{4\pi K |\vec{r}|} \quad (1.34)$$

where K is the average thermal conductivity

$$K = \frac{k_1 + k_2}{2} \quad (1.35)$$

The key-assumption is that the embedded particles are not exactly at the interface, but rather they are exposed to the upper medium and not within the substrate, simplifying the analytical calculations.

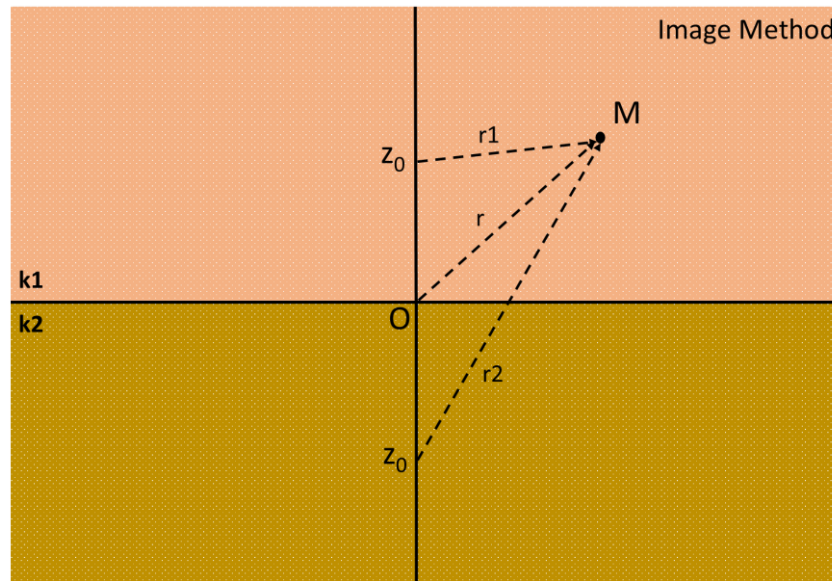


Figure 1.15. Temperature estimation using the image method.

1.2.3.2.3 Collective Thermal Effects

Aside from the metal's thermal characteristics, temperature rise is greatly reliant on absorption cross-section, particle shape, and light wavelength and intensity. However, in the practical case of a plasmonic nanoparticle ensemble, photothermal efficiency takes into account the influence of particle interactions. The pioneering independent works of Govorov and Baffou established the contribution of collective heating when an ensemble of PNPs are illuminated.⁷⁸⁻⁸² The temperature rise of N nanoparticles of radius R is estimated as:

$$\Delta T_j = \frac{Q_j}{4\pi k_m R} + \sum_{k=1}^N \frac{Q_k}{4\pi k_m |\vec{r}_j - \vec{r}_k|} \quad (1.36)$$

Eq. 1.36 interprets that the temperature variation arises from two contributions: [i] a self-contribution and [ii] a neighboring contribution from the $N-1$ particles.⁸¹ Assuming, a

uniform irradiation beam, the total ΔT for such an ensemble of NPs deposited in a planar substrate is given by a closed expression:

$$\Delta T(\rho) = \Delta T_{self} + \Delta T_{coll} = \frac{Q}{4\pi k_m r} + \frac{\sigma_{abs} I}{k_m} \frac{1}{\pi D \rho^2} \left(1 - \frac{2\sqrt{\rho^2}}{\sqrt{\pi D}}\right) \quad (1.37)$$

where k_m is the thermal conductivity ($\text{W}/\text{m}^{-1}\text{K}^{-1}$) of the medium surrounding the particle, ρ the interparticle distance (m), $I(\lambda)$ the irradiance of the illumination, D beam's diameter (m) and r the distance from the heat source.

A way to predict which regime is dominant, Baffou inserted a dimensionless factor

$$\zeta = \frac{\rho}{RN^{(m-1)/m}} \quad (1.38)$$

where N is the number of particles in the illuminated area, R the particle radius and m the dimensionality of the sample geometry (eg. $m=2$ for deposited particles in planar substrate, $m=3$ for dispersed particles in solution). If $\zeta \gg 1$, the temperature rise is locally confined around the particle, which is acting as an isolated heat source, thus the first term of eq 1.38 dominates. If $\zeta \ll 1$, thermal collective effects arise where neighboring contribution takes place, resulting in a uniform heat density and temperature homogenization despite the discrete nature of the heat nanosources.⁸¹ In this case, a bulk heating of the surrounding medium occurs and can be measured by a macroscopic observer. The usage of ζ parameter is exemplified in Figure 1.16.

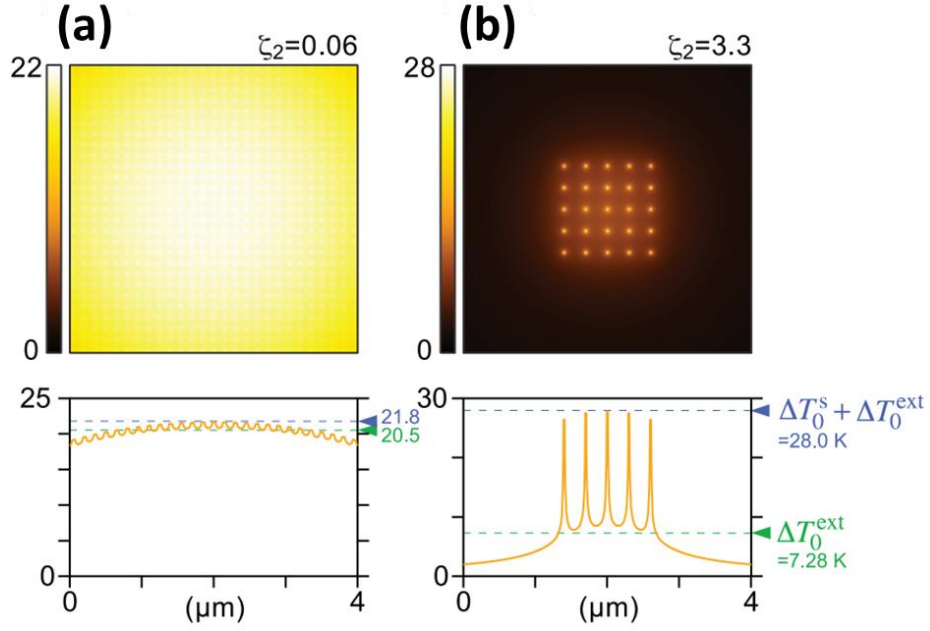


Figure 1.16. Temperature distribution of a 2D periodic lattice of PNPs of (a) $\zeta = 0.06$ and (b) $\zeta = 3.3$. (Taken from this work).⁸¹

Considering the kinetics of the temperature variation, the time-temperature profile of a point source in surrounding medium of thermal diffusivity D_s can be expressed using a Green's function formalism:

$$T(r, t) = \frac{Q_0}{c_p \rho} \int_0^t \frac{1}{(4\pi D_s t')^{3/2}} \exp\left(-\frac{r^2}{4D_s t'}\right) dt' \quad (1.39)$$

Inserting the error function

$$\text{erf}(x) = \frac{2}{\sqrt{\pi}} \int_0^x e^{-u^2} du \quad (1.40)$$

the temperature profile can be expressed in a packed form as:

$$\Delta T(r, \rho, t) = \Delta T(r, \rho) \left[1 - \text{erf}\left(\frac{r}{\sqrt{4D_s t}}\right)\right] \quad (1.41)$$

where $\Delta T(r, \rho)$ is given by eq. 1.37, D_s is the medium's thermal diffusivity $D_s = \kappa / (\rho c_p)$ (m^2/s), ρ is the material's density and c_p is the specific heat capacity. As $\text{erf}(1) = 0.84$, the parameter

$$\tau = \frac{r^2}{4D_s} \quad (1.42)$$

corresponds to the time when the temperature rise is 84% of the equilibrium temperature, thus is the timescale of the temperature evolution.^{83,84} Notice that according to eq. 1.41-42, the distance from the heat source r and the surrounding medium's thermal properties determine the macroscopically observed ΔT kinetics. For instance, nanoscale heating equilibrates during 100 ns, while in the case of significant collective thermal effects, bulk heating timescale is $\tau \sim \text{min}$, as shown in Figure 1.17.

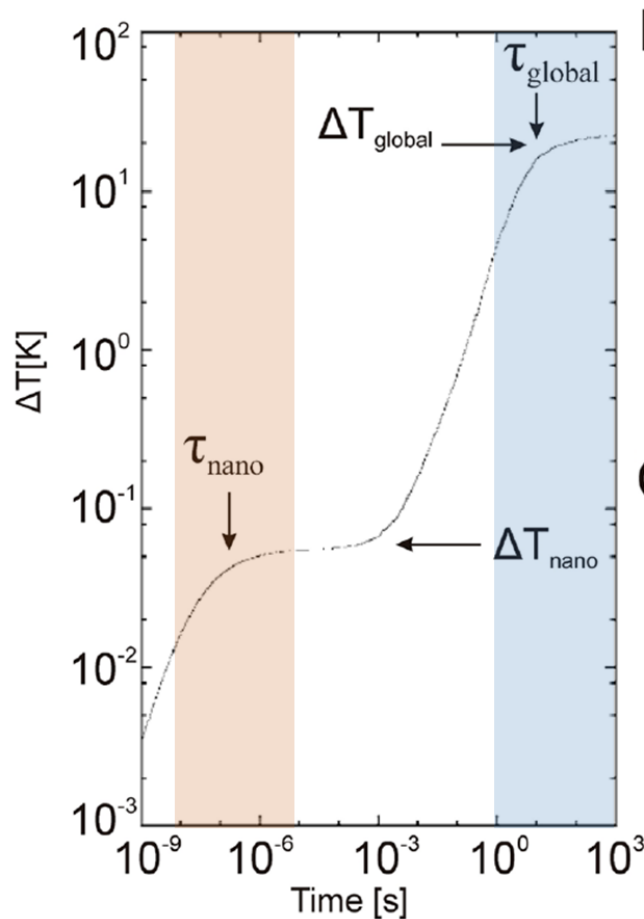


Figure 1.17. Timescale of temperature evolution depending on the distance from the heat source. The orange and blue zones correspond to the temperature rise occurring in nanoscale and bulk environment respectively (Adapted from this work⁸⁵).

1.2.4 Phenomena in the Particle-Particle Interface {Plasmonic Metal/Semiconductor Junction}

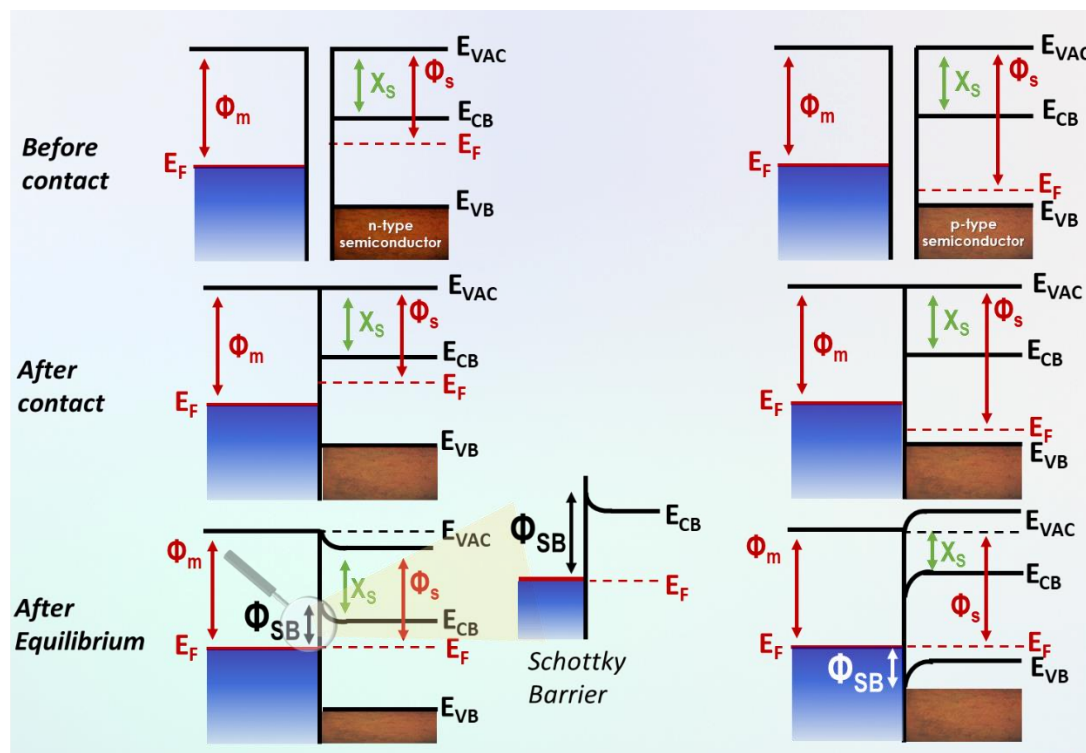


Figure 1.18. Band bending of n- (left) and p- (right) type semiconductor conduction and valence bands in contact with a metal and the associated formation of Schottky barrier after equilibrium in the interface.

When a PNP and semiconductor come into contact, an energy barrier, namely Schottky barrier, is formed in the metal/semiconductor interface and the nonthermal hot carriers can be injected in the semiconductor via a new pathway. In the context of plasmonic catalysis, the Schottky barrier facilitates the electron/hole separation prolonging each carrier lifetime and preventing back-transfer events. At the same time, the active sites on the semiconductor surface operate as charge carrier traps and contribute to chemical activity.⁸⁶ Figure 1.18 illustrates a metallic and semiconducting structure before contact under equilibrium. The metal/semiconductor coupling induces a Fermi level alignment depending on the type of semiconductor (n- or p- type), as depicted in Figure 1.18.

Specifically, the electrons in the CB and VB of a n-type semiconductor (eg. TiO_2) near the interface are forced to be transferred in the metal (eg. Ag). This charge flow depletes the electron density of the semiconductor near the interface and negatively charges the metallic surface until equilibrium (aligned Fermi levels), activating an electric field due to the induced

voltage. The space charge region where semiconductor's electron density is decreased is called depletion layer.⁸⁷ In the depletion layer, the charge flow induces a distortion of the surface states, i.e. an upward band bending arise, compensating for the electron loss. For the case of Ag/TiO₂ heterostructure, the band bending causes an energy threshold in the interface known as Schottky barrier. Using Mott-Schottky equation, the Schottky barrier can be estimated as:

$$\Phi_{SB} = W_m - \chi_s \quad (1.43)$$

where W_m is the metal's work function and χ_s the semiconductor's electron affinity.⁸⁷ This barrier is a parameter of paramount importance for using efficiently metal/semiconducting nanohybrids in plasmonic catalysis. Schottky barrier acts as a filtering frontier where only the highly energetic electrons can overcome and provides a selectivity depending on the excitation wavelength. Moreover, Schottky barrier hinders recombination events, as there is not any available hole in semiconductor's VB for the injected electron.^{88,89} On a similar note, a charge flow is induced in the case where a plasmonic metal comes in contact with a p-type semiconductor, however the electrons flow from the metal to semiconductor, increasing electron density in CB near the interface. This space charge region is called accumulation layer and the generated interfacial electric field causes a downward band bending until Fermi level alignment, as illustrated in Figure 1.18. An important note in this case is the formation of an energy barrier for the hot-hole transfer. For instance, the hot holes that reside in the deep d-band, excited by interband transitions, possess the sufficient energy to overcome this barrier and accumulate the semiconductor's VB, contributing to oxidizing reactions.⁹⁰

Thus, the engineering of Schottky barrier height is pivotal so that efficient hot-carrier transfer is allowed but with limited back-transfer probability.⁹¹ Numerous studies demonstrated the successful generation of nonthermal hot electrons, stimulated with the proper energy via Landau damping, to overcome the interface barrier and be "trapped" in the semiconductor's CB, driving chemical reactions.⁹²⁻¹⁰⁵ The pioneering observation of successful hot electron transfer from a PNP to a semiconductor was reported by Tian and Tatsuma, where Au nanoparticles generated hot electrons that were injected in TiO₂ CB with efficiency ~ 12%.¹⁰⁶ Among following works, Wei and co-workers demonstrated a superior performance in visible-light-driven H₂ evolution using Au/TiO₂ heterostructure, attributing the enhanced activity to the beneficial Schottky barrier (~ 1.1 eV).¹⁰⁷ This charge transfer involves a sequential two-step process: (i) the generation of high-energy electrons, stimulated by the dissipation of the plasmon energy via Landau damping and (ii) the efficient injection to the coupled

semiconductor before recombination. Although the process namely plasmon-induced indirect electron transfer (PIIET), generates a large number of nonthermal carriers, the injection efficiency is deficient. Rapid electron-electron interactions thermalize the hot electrons and diminish the transfer probability to a near acceptor, thus it is essential more transition pathways to be utilized.

As mentioned in the section 1.3.1, the limitations of conventional plasmon-induced indirect electron transfer (PIIET) require further optimization of the electron injection route. In light of this, an analogous process as CID provides a more efficient one-step transfer channel bypassing the energy loss via carrier interactions.¹⁰⁸ In this case, plasmon decay induces a direct excitation of an electron to the semiconductor's CB, indicating the overlap of metal and semiconductor's energy states.¹⁰⁹ In the same way with PIIET, band bending provides the separation of electron-hole pairs and since there are no holes in the semiconductor's VB under visible light, the electron's lifetime is prolonged significantly.

Wu et al. reported the first experimental evidence of plasmon-induced direct electron transfer (PIDET), by modifying a Au/CdSe interface.¹¹⁰ The broadening of Au LSPR to infrared region indicated the coupling of Au and CdSe electronic states. They highlighted that the LSPR-independent high QY values up to 24%, revealed that electrons are directly excited to CdSe CB, thus PIDET being the dominant plasmon-driven mechanism. However, the rapid back-transfer of these electrons back to metal reveals the insufficient height of Schottky barrier. On a similar note, Camargo et al. provided a complete carrier-kinetic landscape for the case Au/CdSe and confirmed the mixing of energy levels.¹¹¹

Theoretical studies predicted PIDET as the dominant plasmon-driven process using Ag-based nanosystems as well, such as Ag/CdSe and Ag/TiO₂ by modifying the metal/semiconductor interface.¹¹²⁻¹¹⁴ Furthermore, Song et al. reported hot-electron transfer efficiency up to 54% for Ag/TiO₂ heterostructure. They revealed that by decreasing Ag particle size, the injection efficiency is mitigated with both PIIET and PIDET contributing to the beneficial carrier migration to TiO₂ CB.¹¹⁵ Moreover, Collado et al. explored the CO₂ reduction selectivity towards CH₄/CH₃OH under UV and visible wavelength respectively and attributed the performance on the formation of hybridized Ag-O orbitals in the Ag/TiO₂ interface.¹¹⁶

Therefore, the recently utilized PIDET mechanism is already established as a solid way to enhance electron interfacial transfer in metal/semiconductor junctions. However, despite the constantly increasing literature,^{114,117,118} the comprehension of plasmon-mediated hot carrier

generation and charge transfer kinetic in such interfaces remains a complex task, requiring a thorough distinguishment of the involved mechanisms in order to optimize the performance of plasmonic photocatalysts.¹⁰⁹

1.3 Plasmonics in Interface: Indirect/Direct Electron Migration in Metal/Adsorbate & Metal/Semiconductor Systems

Despite engineering the PNP characteristics for higher generation of hot carriers, they must be transferred to the immediate environment so that this stored energy can contribute to chemical reactions. Thus, another important parameters to the successful charge transfer is the carrier migration and injection to a near electron acceptor.⁶² The latter can be consisted by (i) a molecule adsorbed in the metal's surface and/or (ii) a semiconductor in contact with metal. In this context, two major distinct routes have been established for harvesting the hot carriers: the (i) indirect electron transfer and the (ii) direct electron transfer to the desired adsorbate/semiconductor.

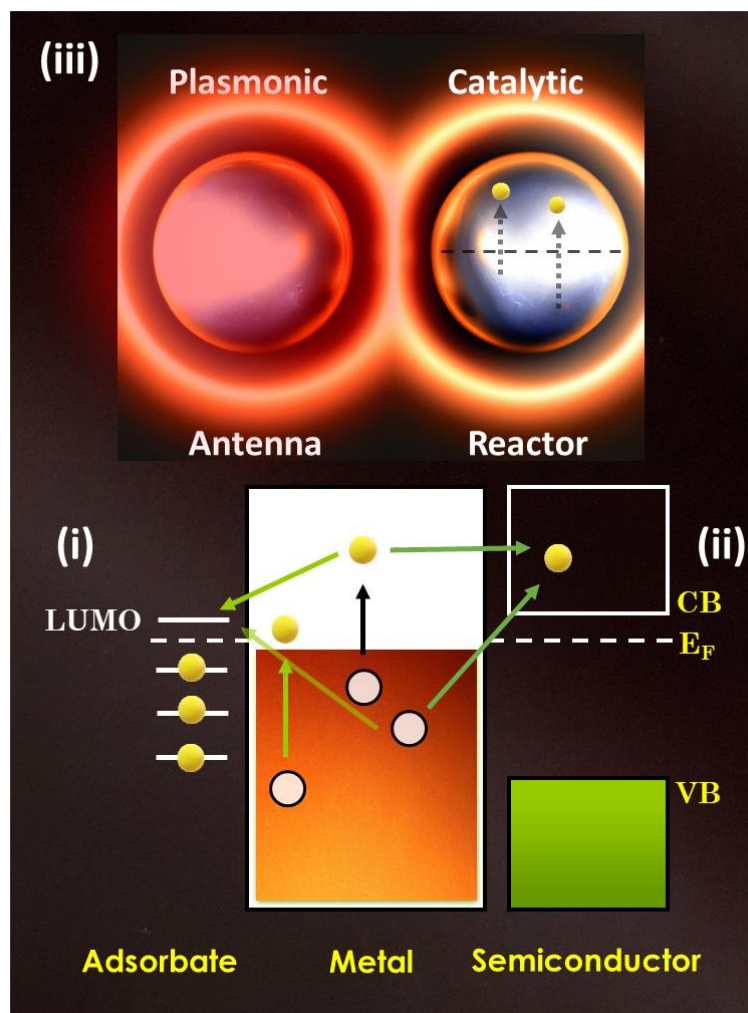


Figure 1.19. Type of plasmon-induced mechanism regarding the attached species. Indirect and direct electron transfer in (i) a metal/molecule interface and (ii) a metal/semiconductor interface. (iii) Plasmon-induced resonant energy transfer (PIRET) in antenna-reactor interface where the intense electric fields drive self-excitation of the catalytic metal.

1.3.1 Plasmon-assisted Catalysis by Near-Field Enhancement

The excitation of a PNP by light at the suitable wavelength alters the surrounding electromagnetic environment significantly. A PNP collects energy from incident radiation and transmits this energy, localized in the form of an augmented electric field, to other material systems near the PNP's surface. Plasmonic nanostructures can therefore connect and transmit with surrounding molecules or structures via near-field enhancement. Excited nanostructures that interact with their environment are referred to as nanoantennae, serving as a light

controller. In the same fashion with SERS, near-field enhancement can induce chemical transformations and accelerate catalytic reactions.

As mentioned above, these amplified electric fields have an impact in the hot-carrier generation rate as well.⁴⁵ Additionally, near-field enhancement facilitates the successful direct electron transfer to near acceptors such as adsorbates and semiconductors.¹¹⁹ In this context, Seemala et al. demonstrated improved O₂ dissociation using Ag nanoparticles, where LSPR-induced electric fields promotes the direct excitation to the adsorbed O₂.¹²⁰ Similarly, Linic group used SERS to demonstrate the decomposition of methylene blue (MB) employing Ag nanocubes. Again, the hot spots drive the direct transition to LUMO of MB.¹²¹ Similar selectivity in electronic transitions has been verified in other systems as well, using near-field enhancement to control the chemical pathway.^{122–126} On the other hand, Tesema et al. observed that electric fields alone do not induce demethylation of MB, but excitation of the MB absorption band is required. Thus, the local fields supports the self-excitation of MB from HOMO to LUMO, driving the demethylation.¹²⁷ Sotiriou et al. utilized core@shell Ag@SiO₂ nanoaggregates to accelerate proton-coupled electron transfer (PCET) for the first time.¹²⁸ In the presence of locally intense hot spots, the plasmon energy is dissipated to the vibrational modes of gallic acid (GA), distorting the GA-OH bond and amplifying the PCET via bond dissociation.

However, conventional plasmonic metals, such as Ag, Au and Cu display poor catalytic activity. By combining plasmonic and catalytic metals, the plasmonic “antenna” can couple light to catalytic “reactor”. In this antenna-reactor complex, the LSPR-induced local fields drive a plasmon to the catalytic metal resulting to enhanced optical absorption of the nonplasmonic particles in the hot spot vicinity.¹²⁹ The first successful design of Al-Pd nanodisks as an antenna-reactor system was provided by Halas’ group and demonstrated enhanced H₂ dissociation rate due to the concentrated energy in the Pd proximity. The same group studied the optimal design of antenna-reactor structures, as well as the influence the PNP size, geometry and the distance of catalytic metal from the hot spots region have on the enhanced light harvesting.¹³⁰ The innovative concept of harvesting light for catalytic metals utilizing PNPs led to more sophisticated designs of antenna-reactor complexes and more challenging chemical reactions, such as formic acid dehydrogenation^{131–134} and carbon dioxide conversion.^{135,136}

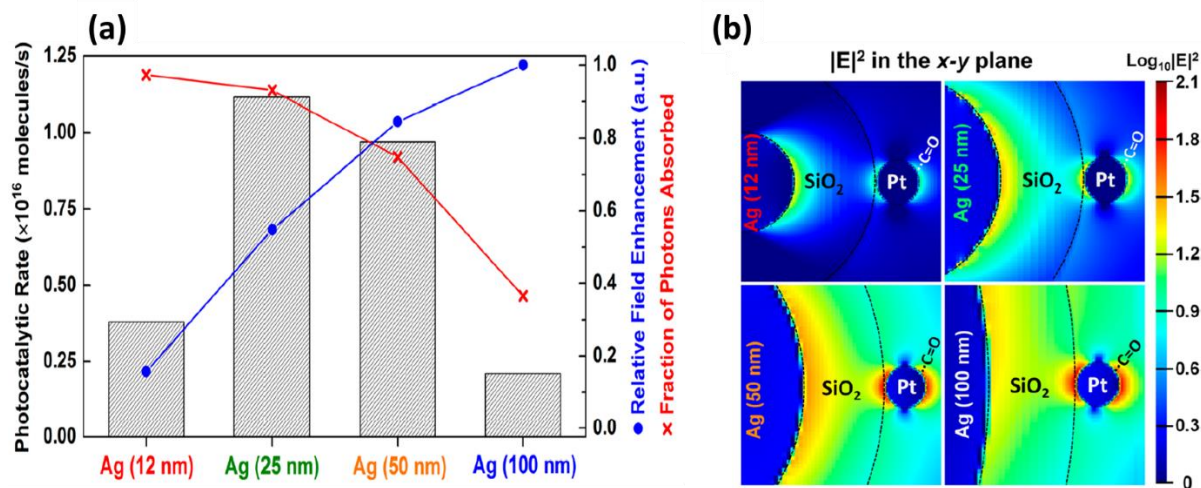


Figure 1.20. (a) Photocatalytic rate dependence on particle size and field enhancement. (b) Electric field distribution in the Ag@SiO₂-Pt proximity. The larger Ag particles promote enhanced local fields in Pt surface but scatter more photons, inaccessible for reactions. Taken from this work.¹³⁰

1.3.2 Catalysis by Electron-Transfer in Plasmonic Metal/Adsorbate Interface

Despite the poor catalytic activity of plasmonic metals such as Ag and Au, PNPs can act as the light controller and electron supplier to adsorbate molecules accelerating chemical transformations.^{137,138} The surface-assisted plasmon dephasing results in the stimulation and transfer of high-energy nonthermal electrons that induce the activation of the adsorbed species via vibrational excitation. When the kinetic energy is sufficient, these hot electrons are injected to lower unoccupied orbital of the adsorbate (LUMO). It is important to highlight that low-energy Drude electrons cannot overcome the interfacial barrier, thus they are transferred to the adsorbate. A constantly expanding literature has showcased the enhanced chemical activity in adsorbed species, induced by the excitation of hot holes^{139–144} and hot electrons.^{145–159}

Among them, the pioneering work of Halas group demonstrated the plasmon-mediated dissociation of adsorbed H₂ species.¹⁶⁰ Using Au nanoparticles under visible light, the kinetic energy of the excited nonthermal carriers overcomes the large activation energies and drives the catalytic process at room temperature. Initially, the nonthermal hot electrons are injected into antibonding orbitals of H₂ molecule, however due to the short lifetime, they are transferred back to Au. The H-H bond stretching induced by the accumulated vibrational energy leads to H₂ dissociation. Furthermore, the same group provided evidence that the dissociation occurs on Au surface by changing the substrate (TiO₂, SiO₂)¹⁶¹, normalizing any charge transfer between Au and substrate.¹⁶² Also, the fact that H₂ species adsorb weakly on Au surface

indicates that the dominant charge-transfer mechanism is the indirect interfacial transfer mechanism.

On a similar note, another prominent plasmon-driven reaction is O_2 dissociation, as demonstrated for the first time by Christopher and co-workers.¹⁶³ They reported enhanced performance in the oxidation of ethylene utilizing Ag nanocubes. In the same way to H_2 dissociation, the hot electrons with the sufficient energy to be transferred to LUMO, dissipate energy into the vibrational modes stretching O_2 bonds and activates the dissociation process.

On a different note, Deligiannakis and co-workers revealed an unorthodox reversible process where hot electrons hinders a catalytic alkene oxidation by a Mn complex using plasmonic Ag@SiO₂ nanoparticles.¹⁶⁴ They demonstrated that high-energy nonthermal electrons, assisted by LSPR-induced electric fields as well, act as reductive agents that provide a selective “pause” in the catalytic reaction on demand.

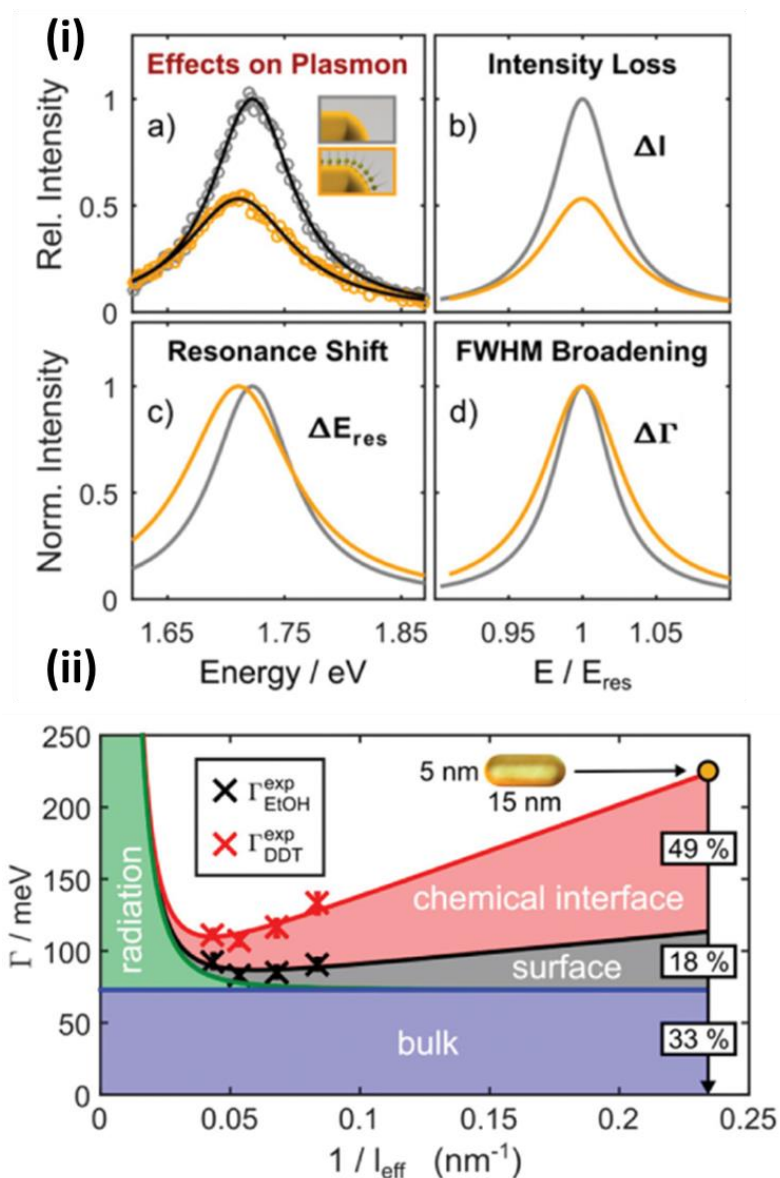


Figure 1.21. (i) Spectrum of dark-field spectroscopy (DFS) of a Au NR where the associated effects of chemical interface damping (CID) are displayed. (ii) Line width contribution for each damping mechanism as a function of effective path length. (Taken from this work).¹⁶⁵

Despite the promising potential of the highly energetic charge carriers to drive challenging chemical reactions, the most studied indirect charge transfer mechanism exhibits insufficient yields because of the short carrier lifetime and rapid recombination.⁵⁶ Recently, a broadening of plasmon bands in single-particle systems in contact with adsorbed/semiconducting species is attributed to a new damping process, called chemical interface damping (CID).¹⁶⁶ CID arises from the hybridization between the electronic states of the metal and the molecular orbitals of the attached species, providing a novel pathway for direct electron injection in the adsorbate.¹⁶⁵ The conventional indirect electron transfer is a

lossy two-step mechanism, where Landau damping triggers the generation of nonthermal hot electrons with energies up to $E_F + \hbar\omega$ and then are injected into the LUMO of adsorbate. However, the direct electron transfer is completed during the plasmon decay via CID, where the electron is transferred through the hybridized states. Thus, CID can be inserted in eq 1.22 as a damping term with a similar size dependence as the surface-induced damping.^{166,167} This pathway is considered far more efficient and overcomes limitations such as short carrier lifetime and e-e interactions. Despite the superior electron transfer efficiency, the engineering of direct transfer is challenging since the overlap of LSPR resonance and the HOMO-LUMO transition of hybridized states is required.

Linic group demonstrated that degradation of methylene blue (MB) adsorbed on Ag nanocubes aggregates is induced by direct charge transfer.¹²¹ Employing SERS, they evidenced that MB decomposition occur under illumination at 785 nm and not 532 nm. One would expect increased efficiency for high-energy photons (532 nm), because they excite more energetic hot electrons that overcome the energy gap between Fermi level and LUMO of MB. These findings suggest that the electrons follow a CID route via Ag-MB hybridized electronic states, providing selectivity for particular chemical pathways activated exclusively by CID-induced direct electron transfer.¹⁶⁸

Furthermore, Seemala et al. correlated enhanced O_2 dissociation using Ag nanoparticles to CID phenomena assisted by surface electric fields. The yield trend does not correspond to the calculated hot carrier density indicating that the preferred mechanism is the direct electron transfer induced by CID.¹²⁰ In both aforementioned works, the direct-transfer route is ostensibly promoted by the local fields that mitigate the energy dissipation in the vibrational modes of the attached species and alleviates the dissociation process.

Moreover, Christopher and co-workers demonstrated that hybridized metal-adsorbate electronic states between CO and Pt surface can selectively control CO oxidation via direct electron transfer to CO-Pt bonds.¹⁶⁹ Thus, CID is an auspicious plasmon-induced pathway for highly efficient electron transfer that drives chemical activity in the PNP vicinity, overcoming the bottleneck of the rapidly relaxed non thermal hot carriers. Nonetheless, the verified evidence of plasmon-driven direct-transfer events in literature remains surprisingly limited, possibly due to the complexity of the formation of resonant hybridized states and the strong chemisorption on chemically inert surfaces of plasmonic metals such as Ag and Au.

1.3.3 An Overview of Plasmonic Catalysis

Despite the exhaustive research photocatalysis have enjoyed this century so far, the groundwork of its industrial potential is not realized yet, because the cost-to-benefit ratio of triggering a light-driven chemical reaction usually pales in comparison to a thermal-mediated process. So far, although the highest efficiency of sunlight energy conversion into chemical activity was almost exclusively confined to the utilization of UV-absorber TiO₂-based nanomaterials. In order to truly mimic nature's superior performance, the visible and near-infrared spectrum has to be utilized as well.

In light of this, the extraordinary optical properties of metal nanoparticles aroused the interest of scientific community in the context of light harvesting. Such plasmonic nanostructures act as "antenna": they can concentrate light in nanoscale volumes, thus arising locally intense electric fields, an ideal active site for chemical processes to occur. Moreover, the stored quanta energy in the oscillating charge density during LSPR, can be dissipated via several mechanisms (as described above) and utilized in different ways.¹⁷⁰ The plasmon-induced nonthermal hot electrons, if efficiently injected from the metal, can reduce the activation barrier of a chemical reaction by exciting the chemically attached adsorbates, either electronically or vibrationally, unlocking the rate-limiting step for challenging chemical reactions.^{171,172} Using an illuminated plasmonic nanoparticle to change the landscape of a chemical process can initiate reactions that would otherwise be thermodynamically and/or kinetically blocked. This opens up new possibilities for tuning the selectivity and efficiency of heterogeneous photocatalytic processes. Regarding selectivity, the metal/adsorbate strong interactions enable new electron transfer channels through hybridization of metal's energy levels and adsorbate's orbitals, so that photon energies different than LSPR and/or optical absorption of adsorbates can be harvested, triggering unique chemical pathways.¹⁷³

Equivalently, a light-induced reduction in the activation barrier enables the use of the same reaction conditions between the light and the temperature driven process with far higher efficiencies for the illuminated case. In a simplified picture, part of the energy needed for the reaction to proceed has been provided by the plasmonic photocatalyst, which is capable of efficiently harvesting photons and injecting the energy into adsorbed molecules (the reactants), dissipating energy in the vibrational modes and thus inducing bond distortion/dissociation processes. Hence, beyond light absorption, the nonradiative surface-induced Landau damping of plasmon energy into electron/hole formation and the efficient carrier migration to the near

molecule-semiconductor are the key parameters for the plasmonic acceleration of a chemical reaction.

An alternative route is the coupling of common plasmonic materials (such as Au, Ag and Al) into catalytic metals (eg., Pt, Pd et al.) to promote the carrier excitation of catalytic metal in visible wavelengths via the LSPR-induced local electric fields in the PNP vicinity.¹⁷⁴ The interplay between both plasmonic and catalytic properties and the channeling of energy in hybrid photocatalysts has received considerable attention over the past few years. Although, these hybrid plasmon-assisted photocatalysts, also known as “antenna-reactors”, have received considerable scientific interest, the design of novel hybrid nanostructure’s geometry is required for optimizing the plasmon-assisted activity. The question of whether the selectivity of these processes can be externally controlled with the illumination wavelength, i.e. different electronic transitions, is still in their exciting early stages.

Furthermore, the efficient light absorption in traditional catalysts is an open challenge and it can be considered the current bottleneck for photocatalysis at industrial levels. The ability of plasmonic nanostructures to concentrate light in the proximity where chemical reactions occur and to manipulate the reaction selectivity via controlled photon absorption, might provide new avenues for driving chemical processes and establish the plasmonic photocatalysis as the new frontier in catalysis. Transferring this information into traditional catalytic materials and methods has the potential to completely transform the chemical pathways that we have discovered thus far. It is noteworthy to mention that the thorough comprehension of such complex energy conversion pathways and the several degrees of freedom the control of plasmonic properties induce, necessitates the coalescence of research fields such as heterogeneous catalysis, physical chemistry, solid-state physics and material science.

In this context, plasmonic catalysis has seen of tremendous interest in the past decade with numerous interdisciplinary reviews focusing on the implementation of the plasmon-mediated mechanisms in solar to energy conversion in various fields, such as solar cells¹⁷⁵, environmental remediation¹⁷⁶, H₂O splitting¹⁷⁷, NH₃ production¹⁷⁸ and photocatalysis in general^{179–181}, as well as the design of the proper plasmonic nanostructures for the given chemical reaction.¹⁸² However, despite the bold advancements in plasmonic catalysis, moving from the “optical” hot spots (hot carriers, field enhancement, energy transfer) to the “chemical” hot spots (reactant adsorption, CID, reaction activity and selectivity), some critical bottlenecks need to be tackled. In particular, Cortez and co-workers¹⁸³ provided a comprehensive summary

of the present challenges in the field with the most important being: [i] the creation of a theoretical model with a general description of all the possible plasmon mechanisms in photocatalysis. [ii] the complex degrees of freedom in plasmonic catalysis require the diligent control of numerous experimental parameters such as plasmonic photocatalyst characteristics (size, shape, composition, surface chemistry) and illumination settings (excitation wavelength, absorbed optical power, reactor geometry). In this regard, the [iii] contribution of thermal effects should be carefully addressed on every occasion by measuring correctly the sample's temperature and simulating the illuminating setup under dark conditions considering thermal gradients, inhomogeneities and collective effects. Lastly, the [iv] development and implementation of such robust plasmonic systems at relevant industrial levels and [v] the design of highly efficient plasmonic devices (TRL 6-7) using abundant low-cost plasmonic materials (eg. Al).

1.3.4 Disentangling the Plasmon-mediated Mechanisms - Currently Standing Challenges

Driving chemical reactions with plasmonic nanoparticles is a rapidly growing research field of high economic and industrial impact. The complex plasmonic mechanisms derived by illuminating metallic nanoparticles as thoroughly described in section 1.2 lower the activation barriers and drive chemical reactions, which otherwise (in the absence of visible-light stimulation) are thermodynamically unfavorable, to be activated. However, the multiple degrees of freedom in these systems render the proper distinguishment of the relative contributions of each plasmonic mechanism, a challenging procedure. For instance, in the case of a hybrid plasmonic/semiconducting nanostructure, the contribution of the nonthermal hot carriers (surface-induced intraband transitions), high-energy interband transitions, resonant energy excitation and CID effects due to hybridized metal/semiconductor energy levels provide an intriguing landscape of charge/energy transfer reaction channels. Besides that, if we consider the contribution of near-field enhancement and thermal effects in these processes as well, the disentangling problem becomes even further burdensome to resolve.

For starters, the central dilemma can arguably be boiled down to whether the rate enhancement is caused by the action of these energetic hot carriers or by the plasmon-induced temperature rise. In this case, the actual involvement of hot carriers has been recently questioned and initiated a “hot” debate around hot-electron photochemistry and the proper measurement of the temperature in such experiments. Specifically, the work of Halas' group¹⁸⁴

reported a light-induced reduction of the apparent activation barrier for ammonia decomposition employing a plasmonic antenna-reactor morphology (Cu-Ru). They designed experiments under various light intensity, excitation wavelength and temperature and simulated control experiments in dark conditions at the same temperature obtained under light and they attributed the lower activation energy to excited Ru-N species, facilitating the N₂ desorption process. However, Sivan et al. found the claims invalid.¹⁸⁵ They considered that the temperature control was insufficient and that the default emissivity value (0.95) set in the thermal imager was inaccurate based on the employed photocatalyst. They estimated that such an error would inevitably lead to a temperature offset ~20%, and thus an underestimation of activation energy of 3 orders of magnitude. In response, the authors attributed the high emissivity in the porosity of catalyst bed and neglected thermal inhomogeneities due to the domination of collective thermal effects for the studied system.¹⁸⁶

However, due to the rapid development of hot-carrier photochemistry since 2011 and the interdisciplinary involvement of researchers of different scientific background, the establishment of a set of fundamental principles is hindered. Thus, such debates and discussions are usual to arise concerning the report of photocatalytic efficiencies, the origin of hot carriers and the proper disentangling of the plasmon-driven mechanisms.^{187–192} In the case of hot carriers vs thermal effects, the control experiment of measuring the reaction rate with no light excitation by simulating the steady-state temperature obtained under light, despite that in principle is correct, it is difficult to precisely measure the actual catalyst surface temperature. In light of these bottlenecks, a guide of the best practices has been reviewed in order to properly distinguish the plasmon-induced phenomena using simple experimental procedures and avoiding the common pitfalls.^{188,193–195}

Light Intensity: In plasmonic catalysis where near-field enhancement of photochemical reactions or hot-charge-carrier-assisted redox reactions at the nanoparticle surface occur, the reaction rate is proportional to the rate of incident photons and therefore to the incident light intensity. This assumption holds true for CW illumination under moderate light power and may deviate toward a super-linear dependence for increased power or under fs-pulsed laser illumination due to multiphoton absorption events. The case of a photothermal process is, however, different and should not feature such a linear dependence. Within a good approximation, the temperature rise of a system due to light absorption is also proportional to the optical power impinging onto the sample. However, the rate constant *K* of a chemical reaction typically follows an Arrhenius-type temperature dependence, thus in the case of a

photothermal process, the rate of chemical transformation follows an exponential dependence on the illumination power. These two different dependences of the reaction rate on the incident optical power offer a simple means to discriminate a hot-electron photochemical events from photothermal effects by plotting the measured chemical reaction rate as a function of the light source power. A linear dependence would indicate a charge-transfer-mediated process, whereas an exponential increase would rather be the signature of a photothermal effect.

However, this experimental practice determining the dominant plasmonic mechanism can be done only if the optical power is varied across a significant range, typically leading to variations of the reaction rate over several orders of magnitude. In the first observation of plasmon-enhanced photocatalysis in 2011 by Linic group, they attributed the observed O₂ dissociation to hot electrons using the same procedure.¹⁶³ Interestingly, Baffou showed that the same results can be fitted as purely thermal effects. In their study the laser power range leads to a temperature increase of ~20 K, a variation of 4%.¹⁹³ Ideally, an experimental data set should be large enough to be fitted with a superposition of exponential (photothermal) and linear (photochemical) terms. In practice, however, this is often difficult, as such large range of chemical rates would entail the use of extremely sensitive measurements of reaction rates at high powers. Specifically, at high optical irradiances, the mechanism of the chemical process under study might change due to the activation of alternative reaction pathways at high temperatures or to non-linear optical effects. Under high-intensity illumination and large temperature increases, convection effects in the gaseous or liquid surrounding medium could also occur. As convection favors heat removal, this condition could result in a sub-linear increase of the temperature and a non-exponential increase of the reaction rate with increasing illumination intensity, despite a purely photothermal mechanism. In addition, varying the rate of chemical reactions over multiple orders of magnitude may lead to additional complications due to changes in the catalyst surface coverage, and therefore its activity and selectivity or to saturation effects due to mass transport limitations. Note that a mass transport limitation would yield a damping of the chemical rate as a function of the illumination power, not an exponential increase, so this effect cannot be confused with a photothermal effect. For all the above reasons, this experimental practice can only be used to discriminate thermal effects from hot carriers for well-characterized catalytic reactions over stable plasmonic nanomaterials and preferably in conjunction with additional independent methods.

Excitation Wavelength: In the same spirit with varying incident light power, which is the absorbed photon energy, i.e. the excitation wavelength matters. A different rate

enhancement under different wavelengths would not directly imply a plasmonic hot-carrier driven process, but it would at least give strong evidence for the existence of a photochemical process. Specifically, it is possible to measure the reaction rate as a function of the optical power under two irradiation wavelengths, one with energetic photons that can give rise to nonthermal hot carriers via either interband absorption or plasmon-mediated Landau damping (surface-collision-induced intraband absorption), and one that cannot account for any hot carrier effect and which will necessarily only lead to photothermal effects induced by the carrier relaxation described in Section 1.2. As the absorbance of the sample is generally not the same for low- and high-energy photons, the line shapes of the “rate versus power” plots at the two wavelengths will not overlap in principle. However, if the process is purely thermally driven in both cases, then there should exist a constant factor for which the two plots perfectly overlap. Another approach that requires adjustable excitation wavelength is the acquisition of a spectrum of the chemical rate as a mean to possibly reveal a wavelength threshold for a sharp electronic transition, above which the reaction is drastically damped, by keeping the light intensity constant. This would be a typical feature of charge excitation/transfer process, which is the case for hot carriers and not thermal effects, where the chemical rate would typically follow the plasmonic resonance absorption spectrum. In this context, this procedure provides the means to distinguish the electron excitation/transfer pathway. Knowing the plasmon resonance wavelength and the excitation energy/band gap of any adsorbate/semiconductor attached in the surface of the plasmonic material, one can determine if the enhanced chemical activity comes from nonthermal hot carriers (surface-induced intraband transitions), interband transitions or resonance energy transfer to the attached species if LSPR overlaps with the excitation energy.

Temperature measurement: In thermoplasmonics, nanoscale temperature measurements are not always required to estimate the temperature increase in a plasmonic system. In most experimental conditions, where the illumination spot size is much larger than the average interparticle distance, the illumination of a large number of particles at the same time gives rise to collective thermal effects, effectively suppressing nanoscale temperature inhomogeneities, leading to a macroscopic temperature homogenization. Under these conditions, if the reactive surface is accessible to be imaged with an infrared camera, infrared thermal measurements are certainly an excellent approach to monitor temperature variations. However, as black body radiation depends not only on the temperature but also on the emissivity of the material, proper calibration of the reactive medium is critical for reliable

measurements, as mentioned above. In any case, care has to be taken in particular with plasmonic samples, as metals are IR reflective and have very low emissivity values, typically on the order of ~ 0.1 , making IR temperature measurements even less reliable. Additionally, seeking a given emissivity not only assumes its spatial but also its spectral uniformity, which is not always the case for such substrates. Also, it is important to emphasize that using an infrared camera is unsuitable for experiments where the photocatalyst is immersed in a liquid. In this case, the IR camera would probe the temperature of the surface of the liquid rather than the one at the reactive sites. More generally, the medium between the reactive area and the IR camera should not absorb IR light. Alternatively, thermal measurements on macroscopic systems can be performed using thermocouples, which are ideally suited to measure the temperature in macroscopic bulk samples. An excellent approach has been reported by Liu & Everitt.^{196,197} In general, [i] one must ensure that light does not directly impinge on the thermocouple to avoid heating it directly. [ii] Physically contacting the substrate to a thermocouple can affect the local heat dissipation, which can in turn prevent reliable temperature measurements. [iii] The thermocouple has to be placed as close as possible to the reactive medium and in good thermal contact with it; otherwise, the temperature increase may be largely underestimated. The problem here is that light-driven plasmonic heating generates a non-uniform temperature increase within the device, localized on the photocatalyst area. The temperature increase under illumination is thus underestimated by the remote thermocouple position.

Despite the plethora of papers that adopts the aforementioned procedures in the plasmon mechanism discrimination,^{195,198,199} some advanced methods have been reported as well. Everitt and Liu developed a novel indirect illumination technique, where they coated the photocatalyst with an inert photothermal Ti_2O_3 layer, that absorbs all the incident light and act as the heater, providing the same temperature profile as would occur without its presence. Moreover, Zhan et al. employed electrochemical methods and found that the plasmonic photocurrent for the case of an Au array can be separated in two components. Utilizing the procedures mentioned above, they managed to attribute each photocurrent component to photo-electron and photo-thermal contribution, inserting the photo-electrochemistry in this field as well.²⁰⁰ Furthermore, when the characteristics of a plasmonic nanoensemble are known (particle size, interparticle distance, absorption cross-section, light intensity, thermal conductivity), the theoretical estimation of the temperature increase can be reliably achieved using the eqs 1.33-1.34. Although this approach is risky, if it is done properly, i.e. considering

the collective thermal effects, the calculated temperature variation provides a useful estimation for every plasmon-enhanced photocatalytic reaction. Lastly, plasmonic photocatalysts are known to provide reaction selectivity, i.e. alter the chemical reaction pathway to one inaccessible via the conventional temperature increase. Specifically, in the case of multi-electron-transfer reactions (eg. artificial photosynthesis)^{157,201,202}, illumination of plasmonic nanomaterials influences the product selectivity, which implies that new electron transfer channels are unlocked, either indirectly (hot electrons) or directly (CID). These reaction pathways are not thermodynamically favored, thus cannot be accessed by heating the reactor. Hence, reaction selectivity can be another useful tool to distinguish plasmon-driven mechanisms in complex reactions. Nevertheless, both hot-charge-transfer and thermal effects are beneficial plasmonic mechanisms and synergistic events are more than welcome. In contrast to conventional heating, plasmonic heating provides localized heat in photocatalyst's active sites and the use of the abundant source of sunlight energy, while the hot carriers offer improved control over the preferential activation of reaction pathways, thus yielding outcomes inaccessible with thermal catalysis.

Following numerous proof-of-concept reaction demonstrations, the field of plasmonic photocatalysis is increasingly focusing on developing a fundamental understanding of the underlying mechanisms so that experimental results can be correctly interpreted and catalysts can be tailored for a wide range of chemical reactions. Despite the efforts to disentangle all conceivable plasmonic mechanisms, there is mounting evidence that a synergistic effect accelerates photocatalytic reaction rates even more. In recent works, Everitt and Liu recently reported that the dominant hot-carrier contribution in reactions such as CO₂ hydrogenation and methanation can be assisted by elevated temperatures under specific conditions by recording precisely the temperature variations and gradients in their reactor.^{196,197,201,203} Understanding and exploiting the synergistic temperature dependence of nonthermal plasmonic effects is of special interest since this constitutes a novel and exciting contribution to the well-established area of heterogeneous catalysis.^{200,204–207} Of course, the important photothermal contributions to a reaction should not be disregarded, since the benefits of illuminating plasmonic photocatalysts allow the localized heating and create favorable thermal gradients that cannot be readily achieved in traditional catalysts. However, the promise of plasmonic photocatalysis ultimately rests in its capability to regulate product selectivity beyond of what is possible, under the conventional thermal catalysis.

1.4 Why Ag?

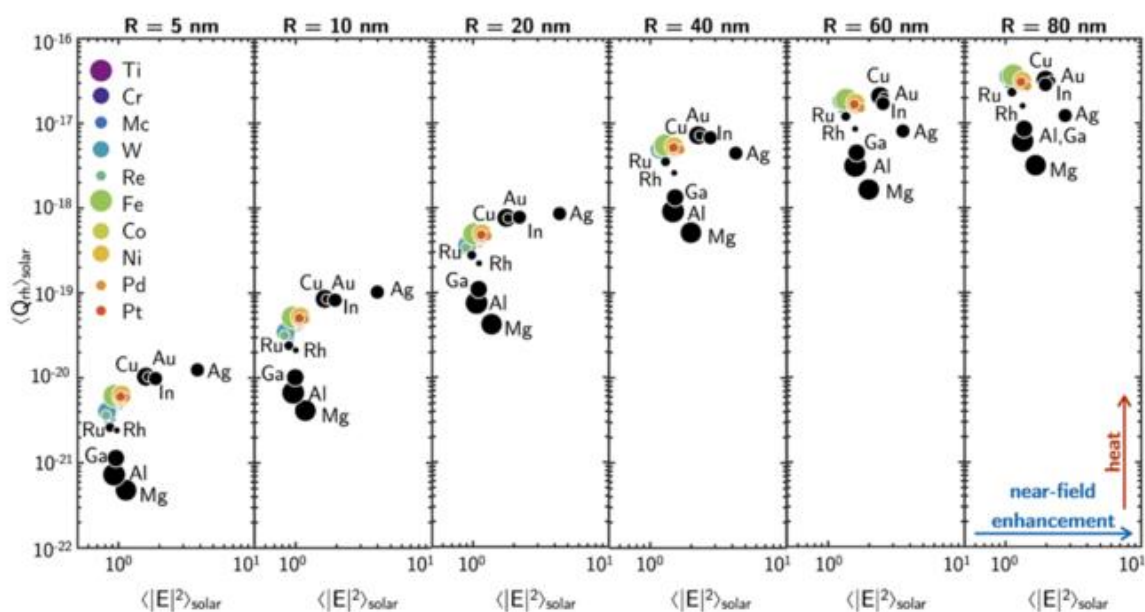


Figure 1.22. Comparison of thermal vs nonthermal effects in the solar-visible spectral range (1.7–4.1 eV) produced in nanospheres of each metal with radius R ranging from 5 to 80 nm. The size of each data point is proportional to the logarithm of that metal's natural abundance. (Taken from this work²⁰⁸).

Silver is probably the most important material in nanoplasmonics. In particular, exhaustive reviews of plasmonic materials survey and performance benchmark conclude to the notable superiority of silver in near-field enhancement, far-field scattering and photothermal effects, when the particle size is increased, for the latter case (see Figure 1.22).^{208–210} These LSPR-driven mechanisms are attributed to greater absorption and scattering cross-sections Ag displays compared to the other conventional choices. In particular, Al is a famous plasmonic candidate with high efficiency but limited in UV region, while Au and Cu suffer from high losses under visible light due to the presence of interband transitions (d to sp band), that take place at 2.6-2.7 eV, dampening LSRP.²¹⁰ Moreover, Ag possess the highest thermal and electrical conductivity among them and is almost 50 times cheaper than Au. However, the oxidation of Ag in aqueous environment causes Ag^+ leaching that hinders its integration in bioapplications.²¹¹ Sotiriou et al. demonstrated that the main reason of nanosilver toxicity comes from the oxidized layer Ag_2O surrounding the stable Ag core, thus the proper washing and the subsequent surface passivation removes the oxidized layer and decreases drastically the toxicity.²¹² Of course the search of meta-materials in plasmonics is still active, with metal

nitrides (TiN, ZrF) being the most promising candidates due to tunable plasmon resonance and low losses in visible and near-infrared region.^{15,213–215} Again, the main bottleneck is the lower performance compared to Ag and Au in all plasmon-derived phenomena, hence the implementation of these materials in functional devices is very beneficial with high technological impact but performance-wise, further optimization is required.¹⁴

1.5 Synthesis of Plasmonic/Semiconducting Nanostructures by Flame Spray Pyrolysis

1.5.1 Traditional synthesis of Ag nanostructures

Nowadays, a wealth of methods is available for the synthesis of Ag nanostructures of controlled size and morphology. One successful route is the chemical reduction of dissolved Ag^+ ions to Ag atoms using the proper reducing agents. Numerous reactions such as citrate reduction, silver mirror reaction, the usage of growth seeds and/or light provide a useful toolbox for controlling size distribution and shape.²¹⁶ Moreover, Ag characteristics can be controlled utilizing a suitable substrate, however this technique comes with limitations such as anisotropic growth and the presence of impurities. Another one famous synthetic approach is the nanosphere lithography, a technique aligned to SERS. Widely used by Van Duyne group, nanosphere lithography allows a well-ordered 2D nanoparticle array of tunable interparticle distance and particle size, two crucial parameters for SERS phenomena.^{217,218} Another one colloidal approach, known mainly for deposition of metals on photocatalytic semiconductors, is the photo-deposition.²¹⁹ Photo-excited electrons generated on the common semiconductor's CB, have energy levels above the reduction potential of Ag^+ ions (0.7996 vs. NHE) and drive the reduction to Ag nanoparticles. Despite the user-friendly procedure, photo-deposition is unable to control particle size, which is increased during continuous illumination, and the co-existence of Ag and Ag_2O species.^{220,221}

1.5.2 Flame Spray Pyrolysis

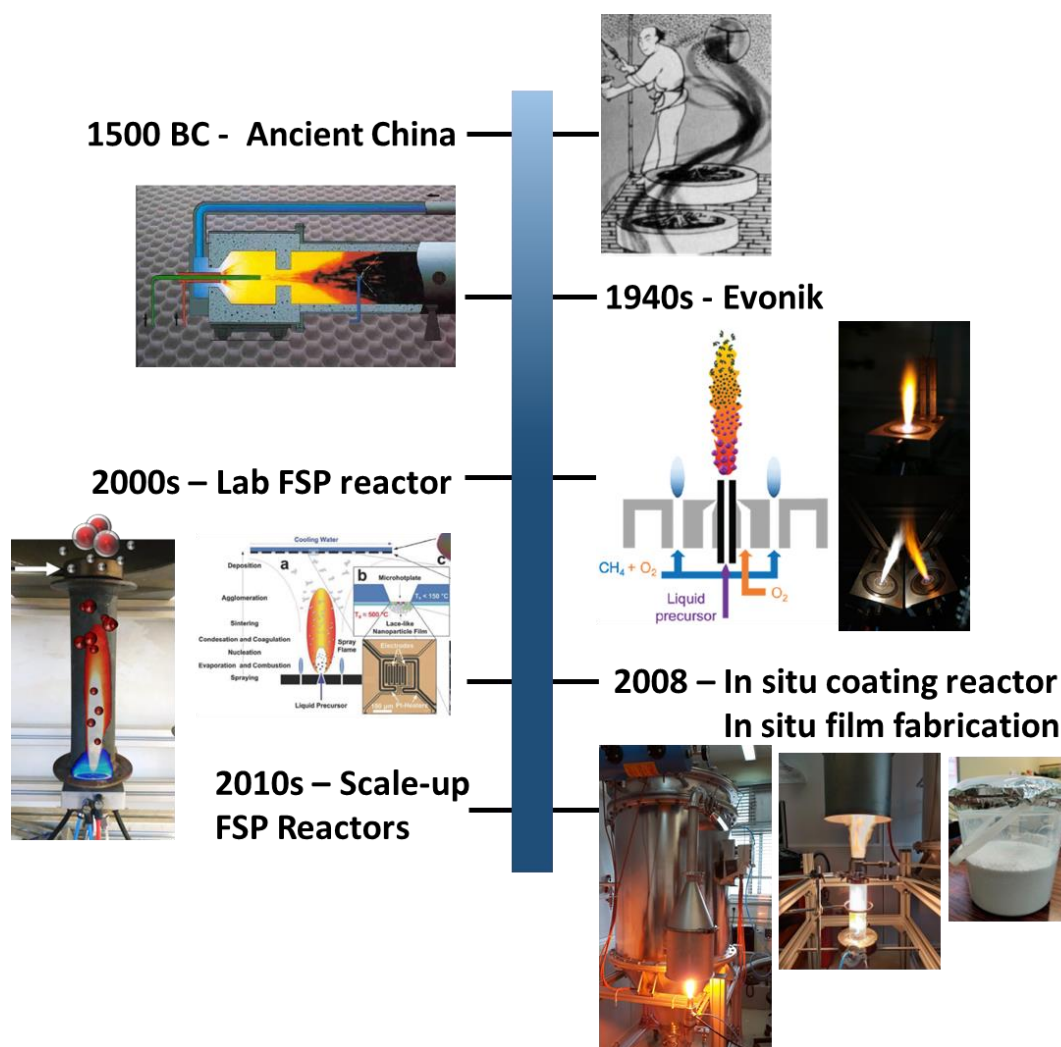


Figure 1.23. A brief timeline of flame aerosol processes in particle synthesis: From Ancient China, to industrial- and lab-scale reactors and flame spray pyrolysis technology (FSP).

To fully harness the promises of plasmonic catalysis, one can understand that the design and the fabrication of sophisticated robust nanostructures are required. Flame aerosol synthesis is a potential and versatile approach for engineering nanocatalysts of well-defined properties. Actually, this synthesis pathway can be traced way back in history timeline, shown in Figure 1.23, where the first flame-made carbon soot was produced in Ancient China.²²² In the early days, flame aerosol technology was utilized only on industrial level to manufacture tons of basic commodities such as carbon black, titania pigments and fumed silica and alumina, until the mid-20th century where its true potential as a novel method for nanoparticles synthesis was realized.^{223,224} Because of the transition from industry level to synthesis of more complex and sophisticated nanostructures, nowadays flame aerosol synthesis can be classified into two

categories: [i] vapor-fed aerosol flame synthesis (VAFS) is the gas-phase method employed by industry “giants” such as Evonik, Cabot and DuPont for the production of tons per year.²²⁴ According to particle formation pathways in flames, the chosen precursors in VAFS (eg. TiCl_4 , SiCl_4) do not meet the required volatility and combustion enthalpy for the synthesis of homogeneous multicomponent nanostructures, hindering the number of available materials.²²⁵ The improvement of VAFS resulted to the birth of the versatile and scalable flame spray pyrolysis (FSP), where the metal precursors of choice are mixed with the proper solvents, forming a liquid solution. On the early stage, the precursor solution (based on salts) did not provide a self-sustaining flame, a bottleneck that required an additional enthalpic source (H_2 supply),²²⁶ although the usage of organometallic precursors and combustible solvents at later stages, provided a precursor fuel of tunable combustion enthalpy and a self-sustaining process.²²⁷

1.5.2.1 Fundamentals of Flame Spray Pyrolysis Process

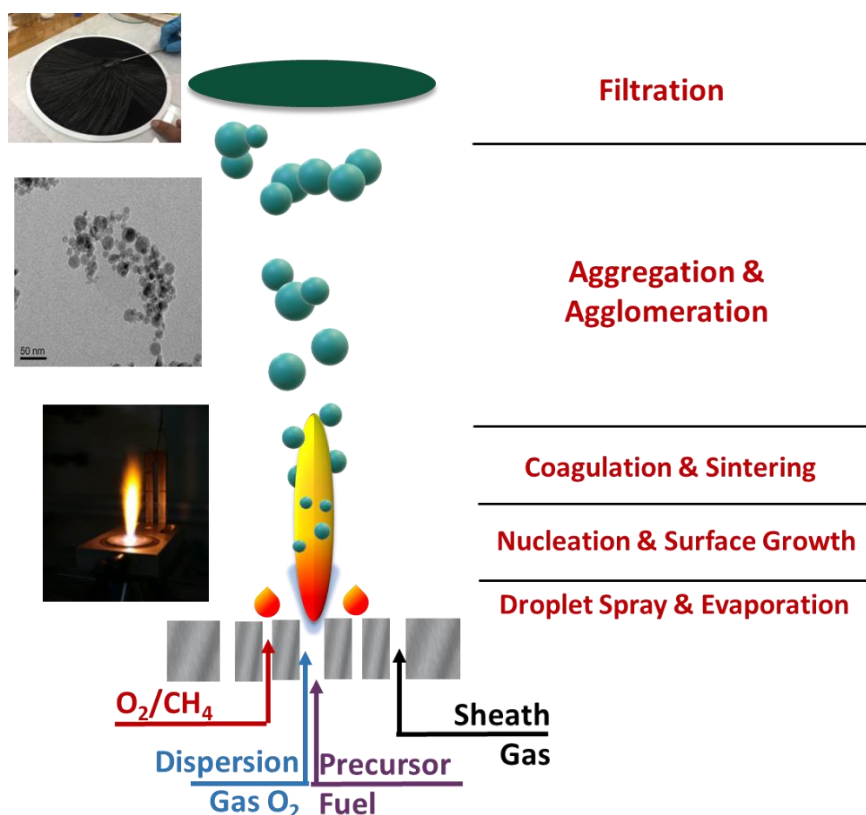


Figure 1.24. Modern FSP Configuration using a pressure-assisted gas nozzle & the associated particle formation process occurring in the jet flame. Insets: Photos of a jet flame, nanoaggregates and a filter with the collected product powder.

FSP synthesis enjoys more than two decades of successful cases of tailored nanostructures designed for catalysis, energy, environmental remediation, health and sensors since the development of the pilot gas-assisted nozzle by Pratsinis and Madler.^{228,229} However, the thorough theoretical landscape of particle formation in flames, despite the fundamental understanding^{230,231}, is still lacking due to the complex flame environment and the multi-parameter-dependent process requiring sophisticated in situ measurements.²³² In any case, a simplified mechanism of nanoparticle formation via FSP is depicted in Figure 1.24. The precursor fuel is atomized into droplets with a size distribution of a few of micrometers, assisted by a dispersion agent (usually O₂ gas). The history of the formed particles boils down to the future of these sprayed droplets. So far, two reaction pathways have been proposed: [i] the droplet-to-particle and [ii] the gas-to-particle formation route. In the latter case, the droplets undergo a complete evaporation, and the subsequent precursor decomposition triggers the nucleation of the exposed metallic vapor forming the first nuclei inside the hottest flame field. The ratio of the solvent's boiling point to the precursor decomposition point is an important parameter that defines the formation route.²³³

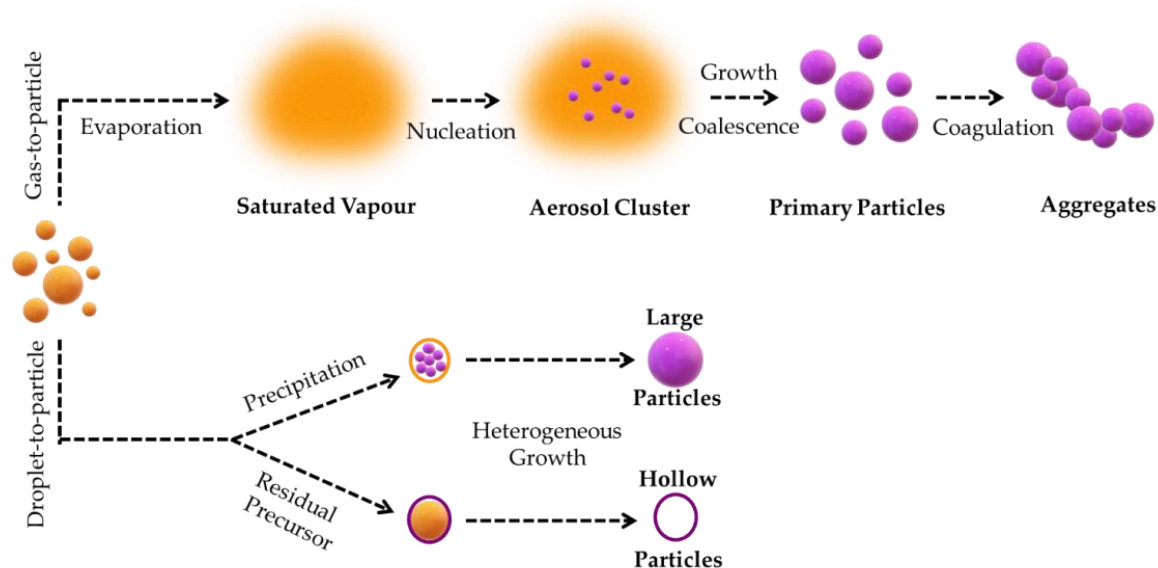


Figure 1.25. The formation pathways of nanoparticles during flame aerosol processes, consisted of gas-to-particle and droplet-to-particle formation.

When $T_{bp}/T_{mp} > 1$, the organic compounds are fully combusted exposing the metallic centers while the combustion of solvent provides the desired high temperature for homogeneous nucleation. When $T_{bp}/T_{mp} < 1$, the solvent is combusted before the complete

droplet burning, resulting to particles with inhomogeneous characteristics and the undesired droplet-to-particle formation route. In any case, if the combustion enthalpy provided by the precursor fuel is high enough ($> 4.7 \text{ kJ/g}_{\text{gas}}$) as reported by Jossen et al., the gas-to-particle formation can still be achieved.²³³ In general, the precursor chemistry should meet the criteria of high volatility, low viscosity and high combustion enthalpy in order to avoid disruptive droplet combustion and microexplosions resulting to heterogeneous nucleation.^{234–236}

Figure 1.25 depicts a schematic illustration of the mechanisms involved in the nanoparticle synthesis in a FSP reactor. Upon gas-to-particle route and the subsequent nucleation, the high temperatures in the flame center ($>1300 \text{ }^\circ\text{C}$) induce the ensuing surface growth (monomer condensation) and particle coalescence (also termed as sintering) and force the primary particles to fuse into a larger one. Coalescence events are extremely sensitive to temperature, so when the particles are inserted in colder thermal gradients in the flame field, things change. Coalescence takes longer time to occur, thus coagulation events (i.e. Brownian collisions) are dominating. These collisions force the particles to bind each other into aggregates (strong chemical bonds) and, when outside flame field, into agglomerates (weak physical bonds) until their collection/deposition.

Considering all the above, one can realize that engineering the properties of flame-made nanomaterials, although the experimental procedure seems rather simple and user-friendly, can be precarious if its multiparameter character is not considered thoroughly, as summarized in Figure 1.26. Notably, every researcher should implement every tunable parameter in the concept of high-temperature-residence-time zone (HTRT), that defines all the significant particle properties such as primary particle size distribution, aggregation degree, crystallinity, homogeneous morphology, phase composition, dispersion on a substrate and in general the reproducible synthesis of dense and robust nanomaterials.²³⁷ For instance, increasing precursor molarity and/or precursor fuel feed rate drastically affects HTRT and particle size and the specific surface area due to increased combustion enthalpy and increased nuclei population in the flame field.^{229,238} On the other hand, the dispersion oxidant rate defines the spraying angle and the particle in-flight velocity. Increasing dispersion oxidant gas triggers flame constriction and combustion acceleration, thus HTRT is reduced since the particles stay less in the more confined high temperature zones inside the flame, hence the particle size is decreased.^{239–241}

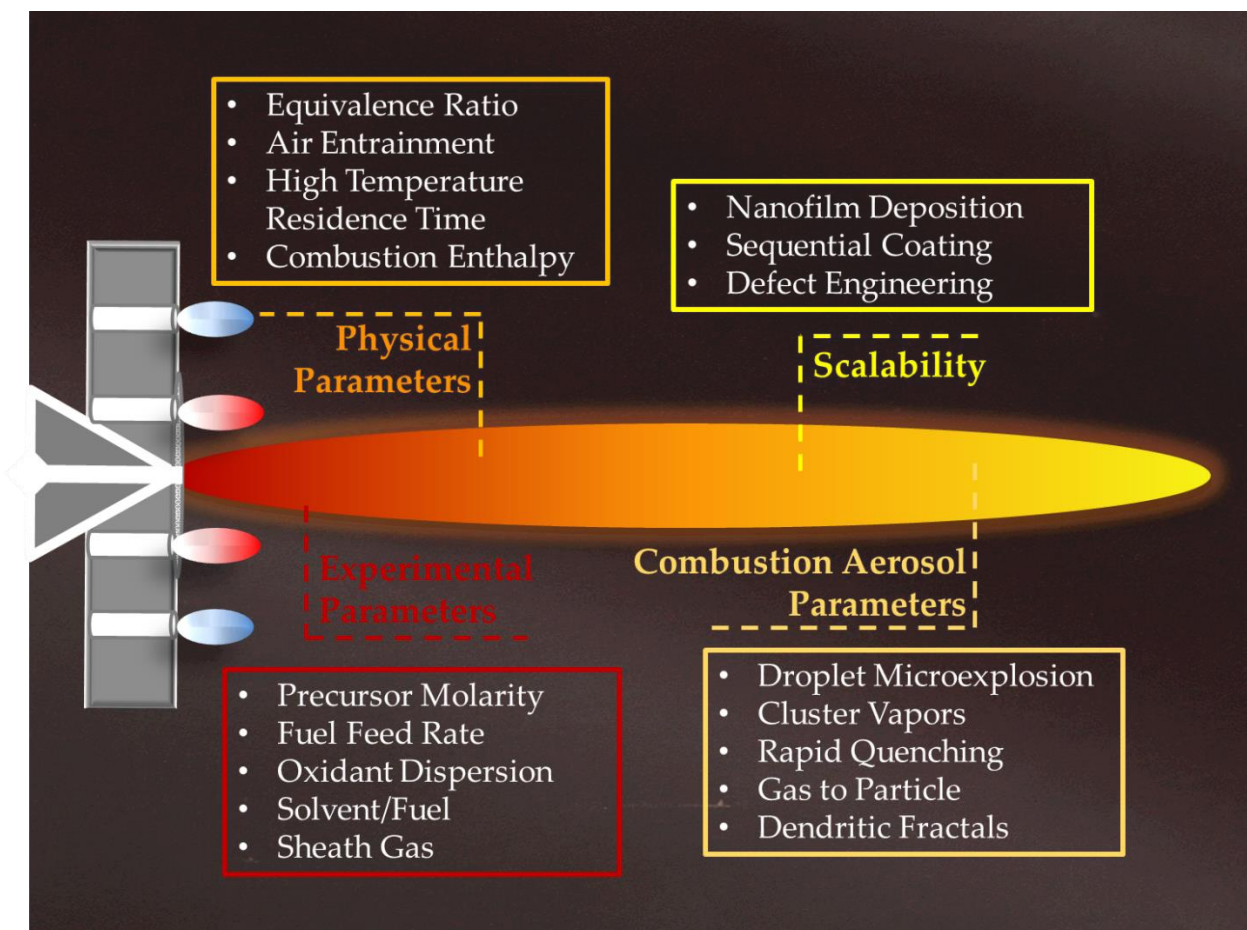


Figure 1.26. A schematic depicting the multi-parameter character of flame spray pyrolysis process.

1.5.2.2 Flame Spray Pyrolysis as a Versatile Nanoparticle Synthesis Technology

The implementation of nanotechnology into every day routine requires versatile particle fabrication technologies and robust and functional multicomponent nanomaterials such as flame aerosol synthesis and flame-made particles respectively. In light of this, FSP provides a single-step procedure that expands the spectrum of possibilities over the periodical table and a desired lab-to-industry link. During the last decade, many studies offer an exhaustive coverage of the theoretical^{242–245} and experimental^{246–252} progress in understanding flame aerosol particle formation, thus a detailed literature review is out of scope in this thesis. However, due to the numerous research fields in which flame-made nanomaterials shine, with notable examples being gas sensing²⁵³, biomedicine²⁵⁴, energy storage²⁵⁵, thermal catalysis²⁵⁶, electrocatalysis^{257,258}, fuel cells²⁵⁹, environment^{260,261} and photocatalysis^{262–266}, the versatility

and scalability provided by FSP, enables the integration of functional nanomaterials in these applications and deserves a brief summary.²⁶⁷

Material-wise, FSP is a well-established synthesis approach regarding the fabrication of oxides, metal/oxides and mixed heterostructures where all elements participate and react in the same flame.^{268,269} In this case, the metal/oxides can vary from metallic particles deposited on oxide substrates to heteroatom doping, as reported in numerous works such as Pt/TiO₂²⁷⁰, Ag/ZnO²⁷¹, PtPd/Al₂O₃²⁷², Si:WO₃²⁷³, Sb: and Pd: SnO₂²⁷⁴ and La:Al₂O₃.^{275,276} Furthermore, when the flame is enclosed, the air entrainment and controlled atmosphere allows the synthesis of pure metallic nanoparticles²⁷⁷⁻²⁷⁹ and even the introduction of a protecting carbon layer encapsulating the particle core²⁸⁰⁻²⁸³, when an additional carbon source is inserted in the oxygen-lean flame (C₂H₂).²⁸⁴ In this context, FSP can be a useful toolbox regarding defect engineering, especially for catalytic and energy applications.²⁸⁵⁻²⁸⁸ In particular, when the reducing conditions in the enclosed flame are amplified in a properly modified reactor, more oxygen vacancies are generated that act as active sites that can be selectively tailored in the oxide lattice, facilitating charge-transfer events.²⁶³

Moreover, FSP-made perovskites have been an elusive project for year as well, since the rapid reactions and the short time scales in flames do not meet the criteria of the “slower” stoichiometric ion diffusion in intra-particle level in high temperatures required for the synthesis of perovskites of high purity.²⁴⁹ However, perovskite synthesis can be achieved in enclosed reactors, where the flames are longer and more homogeneous thermal gradients of high temperature are present. Some recent works reported the successful engineering of FSP perovskites such as BiVO₄²⁸⁹, La(Mn-Fe-Co)O₃^{290,291}, Li₄Ti₅O₁₂^{292,293}, La₂Ti₂O₇²⁹⁴, ITO²⁹⁵, BiFeO₃^{264,296} and NaTaO₃ where the precursor chemistry is of paramount importance for the proper heteroatom mixing.

In terms of multicomponent mixing and deposit/support materials, the solid-phase miscibility induces randomness in the single flame configuration that limits the formation of complex heterostructures with controlled phase composition. To overcome this bottleneck, a twin-flame configuration is employed, as illustrated in Figure 1.26.²⁹⁷ The separate flames allow for the design of mixed heterostructures with tunable mixing and dispersion and the independent tailoring of each synthesis parameters such as particle size.²⁹⁸ Furthermore, the controlled intersection distance defines the mixing point and enables the component's coupling in atomic, primary particle and aggregate scale giving birth to uniquely designed

nanomaterials.^{265,276,299,300} On the same note, the delayed introduction of a secondary metal in the FSP reactor can be achieved by inserting it as vapor outside flame field meeting the formed particles in flight.³⁰¹ This configuration enables the formation of core@shell structures in a single-step process, where the secondary metal forms a layer of controlled thickness encapsulating the flame-made core particles and act as particle protector and aggregation tuner.^{302,303}

Furthermore, the versatile FSP synthesis allows for the in situ particle deposition on a substrate.^{304,305} The flame aerosol deposition is established by placing the chosen substrate in a water-cooled holder in a tunable height above the flame. On the same note with HTRT for the particle formation in flames, the two significant parameters in the flame aerosol deposition are the height above flame (HAF) where the substrate is located and the deposition time. These parameters control sintering times, and thus the film's thickness, porosity and robustness, as reported in numerous works.³⁰⁶⁻³⁰⁸

Lastly, some recent remarkable works push FSP limits and impact even beyond the current state-of-the-art. In terms of synthesis, Riad et al. reported the flame synthesis of quantum dots of TiO₂, ZnO, CuO, SnO₂ embedded in a silica matrix³⁰⁹, while Balakrishnan et al. demonstrated the gas phase engineering of metal sulfides in flame for the first time, expanding FSP potential to the controlled formation of non-oxides.³¹⁰ From theoretical perspective, Li et al. developed a single droplet combustion process and studied the formation of SnO₂ particles.³¹¹ Compared to conventional FSP process, this study fills the gap between precursor decomposition and droplet microexplosions and unravel some long standing unexplained phenomena in particle nucleation in flames.³¹² In terms of applications, Sotiriou group employed sunlight active flame-made nanomaterials both against SARS-Cov-2³¹³ and skin diseases³¹⁴, while Louloudi and co-workers reported an unorthodox phenomenon in oxidation catalysis using plasmonic flame-made nanoaggregates.¹⁶⁴ On the same note, Deligiannakis group reported the single-step synthesis of NaTaO₃ photocatalytic perovskites using a low-enthalpy FSP process. Besides the challenging synthesis of perovskites in flames, the FSP-made NaTaO₃ particles have the smallest size reported so far in literature (12 nm). Furthermore, the same group demonstrated enhanced activity of flame-made cobalt oxide nanoaggregates in oxygen reduction reaction (ORR), by engineering the defects in catalyst's surface (Co²⁺/Co³⁺) and controlling the flame's reducing character ($\Phi > 1$).³¹⁵ All these notable studies strengthen the "roots" of flame aerosol synthesis in industrial market and the development of robust functional nanodevices expanding the FSP landscape even further.

1.5.2.3 Flame-made Plasmonic Nanoaggregates

Regarding the flame synthesis of plasmonic nanomaterials, following the pioneering gas phase production of Ag particles³¹⁶ and the Ag deposition on substrates by flame spray pyrolysis^{271,317}, Sotiriou and co-workers laid the foundations for the tuning of plasmonic properties of nanosilver via controlled morphology employing the scalable flame spray pyrolysis. In particular, using a modified FSP reactor (more details in Chapter 2), where the in situ encapsulation of Ag particles by a thin amorphous SiO₂ layer, provided the risk mitigation of undesirable Ag⁺ leaching.^{318–320} The protective role of SiO₂ coating enables the safe implementation of nanosilver in vivo bio-applications hindering its toxicity.^{321,322} In this context, Merkl et al. developed Ag/SiO₂ composites nanofilms via flame aerosol direct deposition and demonstrated the NIR photothermal³²³ and antibacterial properties³¹³, while Li et al. utilized similar plasmonic nanocomposites and reported pesticide SERS detection on fruits surface by engineering the hot spot intensity.³²⁴ Moreover, Tricoli et al. used flame-made Au/Bi₂O₃ nanoaggregates to amplify CO₂ reduction (CO₂RR) and optical sensing and attributed the enhanced performance to the FSP-induced fractal geometry and plasmonic hot spots.³²⁵

1.6 Motivation and Scope of the Thesis

As thoroughly explained in the sections above, plasmonic catalysis offers a promising landscape to explore, considering the constantly expanding needs for energy and climate neutrality. The complex degrees of freedom in such systems due to the presence of numerous plasmon-driven events requires their proper discrimination. Regarding the charge-transfer events, all the possible electronic pathways should be considered as well, especially in the case of a metal/semiconductor/adsorbate, in which the formation of new electron channels due to overlapped energy states enables the electron migration of variable energy.

On this note, the implementation of these well-established plasmon-induced mechanisms (hot carriers, CID, hot spots, thermal effects) to plasmonic catalysis (reaction rate, selectivity) requires the fabrication of sophisticated nanomaterials and the diligent control of their characteristics (particle size, phase composition, aggregation degree, surface chemistry, metal/semiconductor interface). In this context, FSP provides a versatile, single-step process that expands the spectrum of possibilities over the periodic table and links the lab-scale synthesis plasmonic heterostructures to industrial market.

The present study focuses on the synthesis of plasmonic nanostructures using flame spray pyrolysis (FSP) of controlled characteristics and properties, the study of plasmon-driven

phenomena under solar light and their integration in catalytic reactions. Specifically, the aims of this thesis can be summarized as follow:

- [1]. The one-step synthesis and characterization of plasmonic/semiconducting nanoparticles using FSP, with the notable cases of core@shell (Ag@SiO_2), black Ag/TiO_x and Ag/NaTaO_3 nanostructures.
- [2]. Understanding the effect of interparticle distance, i.e. SiO_2 shell thickness in the photothermal performance of flame-made Ag@SiO_2 nanoaggregates by tuning the plasmonic coupling of neighboring Ag cores.
- [3]. Develop a method for the quantitative detection of the ultrafast hot electrons using electron paramagnetic resonance (EPR) spectroscopy and the effect of aggregation degree (i.e. plasmonic coupling) of flame-made Ag@SiO_2 on the hot-electron generation.
- [4]. The mechanistic insight on the plasmon-enhanced environmental remediation of hexavalent chromium (Cr^{6+}) under sunlight employing flame-made Ag@SiO_2 nanoaggregates.
- [5]. The synergistic effect of the distorted flame-made Ag/TiO_2 interface and the photo-excited trapped electrons in terms of electron storage and “dark” photocatalysis.
- [6]. Understanding the photo-stimulated electron/hole pair dynamics in flame-made NaTaO_3 and Ag/NaTaO_3 nanostructures.

1.7 Thesis Outline

Chapter 1 includes an introduction in the fundamentals of local surface plasmon resonance (LSPR), i.e. the source of all optical/electronic/thermal events in plasmonic nanomaterials and a thorough summary of all involved charge-transfer-phenomena in the interface when a semiconductor and/or an adsorbate is attached on the plasmonic particle. Moreover, the potential of plasmon-assisted chemistry is reviewed, including the current challenges and debates, and the fundamental set of experimental rules identifying the dominant mechanism, is fully described. Lastly, the state-of-the-art in flame aerosol synthesis is summarized, especially the flexibility and potential that flame spray pyrolysis provides in the engineering of hybrid plasmonic/semiconducting heterostructures.

Chapter 2 describes the characterization methods and techniques. In particular, emphasis was given in flame spray pyrolysis (FSP), the single-step process employed in this thesis for the fabrication of the plasmonic-semiconducting nanostructures (Ag@SiO_2 , Black $\text{Ag/TiO}_x/\text{TiO}_2$, Ag/NaTaO_3). Moreover, the fundamental theoretical framework of electron paramagnetic resonance (EPR) spectroscopy is provided, plus the description of the

quantitative EPR (spin standards, calibration curves, EasySpin simulations) and the ROS detection (spin trapping). Lastly, the rest of characterization methods are briefly described: Transmission Electron Microscopy (TEM), X-ray Diffraction (XRD), N₂ Porosimetry, UV/Vis spectroscopy, Raman spectroscopy and X-ray Photoelectron spectroscopy (XPS).

Chapter 3 focuses on the plasmon-induced heat generation utilizing core-shell Ag@SiO₂ nanoaggregates, i.e. silver nanoparticles coated with a nanometric, amorphous SiO₂ layer, has been studied either as liquid suspensions or nanofilms. Non-monodispersed, fractal-like Ag@SiO₂ ensembles were synthesized by flame spray pyrolysis (FSP), varying particle size distribution, and SiO₂-shell thickness, ranging from 1 up to 5 nm. The particles were characterized by TEM, XRD, XPS and UV/Vis spectroscopy, while the thermoplasmonic heat-generation efficiency was monitored *in-situ* by measuring the temperature rise over the nanoaggregate ensemble by a thermal imager, under UV-Vis irradiation or ambient solar light. A systematic investigation of parameters regarding [i] the particle characteristics, [ii] the surrounding medium and [iii] the irradiation characteristics was carried out. For the ultrathin SiO₂ coating tailored herein (~1nm), under focused solar light, Ag@SiO₂ nanofilms were able to produce a significant temperature rise up to T_{max}~400°C. The data are analyzed quantitatively within the theoretical frame of Mie theory as extended by Baffou for multiple plasmonic nano-heaters, where the fractal dimension of the flame-made Ag@SiO₂ nanoaggregates and the occurring collective thermal effects are taken into account. In this context, we interpret the observed phenomena in terms of the neighboring Ag-Ag coupling within each fractal, and the dual role of SiO₂ as the dielectric shell-medium around the metallic core, as well as the plasmonic separator. Accordingly, a consistent theoretical frame is provided, that includes a quantitative hierarchy of the physicochemical parameters and determines the photoinduced heat generation for realistic non-ideal/-monodisperse plasmonic ensembles.

Chapter 4 provides an in-depth look in the understanding of the complex plasmon-mediated electron-transfer mechanisms from plasmonic nanostructures to redox-active species. Electron paramagnetic resonance (EPR) spectroscopy is well established as a state-of-the-art tool to selectively detect the redox evolution of paramagnetic metals, however its use in plasmon-driven-charge-transfer processes has not been explored so far. In this chapter, we present a quantitative study on the mechanism of hot-electron transfer, from plasmonic Ag@SiO₂ nanoaggregates, to drive sequential Cr⁶⁺ reduction towards Cr⁵⁺/Cr³⁺. Employing flame spray pyrolysis (FSP), core-shell Ag@SiO₂ nanoaggregates are engineered with varying

SiO₂-shell thickness, in the range 1-5 nm. Using EPR spectroscopy, the Spin-Hamiltonian parameters for the $S = 1/2$ {oxalate-Cr⁵⁺} and $S = 3/2$ {oxalate-Cr³⁺} systems at the Ag@SiO₂/Cr interface are analyzed and used to quantitatively monitor the sequential electron transfer steps during Cr⁶⁺ reduction. In the absence of the SiO₂ shell, the oxidative path *via* the dark reduction of Cr⁶⁺ due to oxidation of bare Ag is deduced accordingly. Importantly, we show that the SiO₂ shell plays a key role in hot-electron transfer, as the 1 nm shell allows a predominant hot-electron transfer via a light-induced decrease of activation barrier, suppressing the oxidative path and excluding photothermal effects.

Chapter 5 provides an introduction in the study of plasmonic-semiconducting interface and the associated charge-transfer phenomena. In particular, it demonstrates the synthesis of flame-made NaTaO₃ and Ag/NaTaO₃ heterostructures and the study of the photo-induced electron/hole pairs. NaTaO₃ perovskites are highly potent photocatalysts, however the direct detection of photo-generated hole-electron {h⁺/e⁻} pairs in NaTaO₃ nanocrystals remains elusive. In this chapter, we present an electron paramagnetic resonance (EPR) study of photo-generated carriers in NaTaO₃ particles, of controlled composition, crystallinity and particle size (14 & 26 nm), produced by flame spray pyrolysis (FSP) for the first time in the existing literature. Based on the EPR-resolved **g** and **A**[¹⁸¹Ta(I=7/2)] tensors, as well as the {h⁺/e⁻} formation/recombination dynamics, the lattice *vs.* surface nature of the trapped {h⁺/e⁻} centers in the 14nm-NaTaO₃ particles are distinguished. Larger 26nm-NaTaO₃ particles yield significantly lower photo-induced carriers due to rapid recombination phenomena. The interplay of size effect and detection of photo-excited carriers by EPR (i.e. improved carrier migration) is inherently related to high photocatalytic performance of 14nm-NaTaO₃ with a yield of 1.6 mmol H₂ g⁻¹h⁻¹. For the case of Ag/NaTaO₃ nanostructures, measurements by XRD, Raman and UV/Vis spectroscopy do not reveal conclusively the interaction between Ag and NaTaO₃ particles.

Chapter 6, on a similar note to Chapter 5, focuses on the plasmonic/semiconducting interface and, specifically, the case of flame-made black Ag/TiO₂ nanocomposites. The Ag/TiO₂ nanocomposites are produced using flame spray pyrolysis, tuning both Ag content and TiO₂ particle size, with emphasis given to the interfacial contact (loose or tight). In the latter case, crystalline TiO_x suboxide phases (Magneli) are introduced as nano-islands upon Ag-TiO₂ contact, distorting the interface, evidenced by TEM, XRD and XPS. Regarding the electronic structure, the DRS, EPR, PL and electrochemical measurements reveal that photo-excited electrons can be efficiently “trapped” near the surface, thus prolonging the

electron/hole separation and their potential chemical activity. Therefore, the interfacial Magneli phases introduce sub-gap energy states, improving drastically both electron storage and visible-light activity. In terms of dark photocatalysis, the pre-irradiated black Ag/TiO₂ nanocomposites reduce hexavalent Cr⁶⁺ ions, providing electrons even after 2 hours under dark conditions, verifying the role of interfacial Magneli nano-islands to trap surface electrons in active sites under sunlight.

1.8 Bibliography

- (1) Feynman, R. There's Plenty of Room at the Bottom. *Engineering and Science*. 1960, pp 22–36.
- (2) Burda, C.; Chen, X.; Narayanan, R.; El-Sayed, M. A. Chemistry and Properties of Nanocrystals of Different Shapes. *Chem. Rev.* **2005**, *105* (4), 1025–1102. <https://doi.org/10.1021/cr030063a>.
- (3) Roduner, E. Size Matters: Why Nanomaterials Are Different. *Chem. Soc. Rev.* **2006**, *35* (7), 583. <https://doi.org/10.1039/b502142c>.
- (4) Hornyak, G. L.; Tibbals, H. F.; Dutta, J.; Moore, J. J. *Introduction to Nanoscience and Nanotechnology*, 0 ed.; CRC Press, 2008. <https://doi.org/10.1201/9781420047806>.
- (5) Poole, C. P.; Owens, F. J. *Introduction to Nanotechnology*; J. Wiley: Hoboken, NJ, 2003.
- (6) Stockman, M. Nanoplasmonics: Past, Present, and Glimpse into Future. *Optics Express* **2011**, 22029–22106.
- (7) Brongersma, M. L.; Shalaev, V. M. The Case for Plasmonics. *Science* **2010**, *328* (5977), 440–441. <https://doi.org/10.1126/science.1186905>.
- (8) Stefan, E.; Nicolas, B. *Plasmonics: From Basics to Advanced Topics*; Springer, 2012.
- (9) Stockman, M. I. Nanoplasmonics: The Physics behind the Applications. *Physics Today* **2011**, *64* (2), 39–44. <https://doi.org/10.1063/1.3554315>.
- (10) Barbillon, G. *Nanoplasmonics: Fundamentals and Applications*; InTech: Rijeka, Croatia, 2017.
- (11) Murray, W. A.; Barnes, W. L. Plasmonics Materials. *ADVANCED MATERIALS* **2007**, 3771–3782.
- (12) Drude, P. Zur Elektronentheorie Der Metalle. *Annalen der Physik* **1900**.
- (13) Quinten, M. *Optical Properties of Nanoparticle Systems: Mie and Beyond*; Wiley-VCH, 2011.

- (14) Naik, G. V.; Shalaev, V. M.; Boltasseva, A. Alternative Plasmonic Materials: Beyond Gold and Silver. *Adv. Mater.* **2013**. <https://doi.org/10.1002/adma.201205076>.
- (15) West, P. R.; Ishii, S.; Naik, G. V.; Emani, N. K.; Shalaev, V. M.; Boltasseva, A. Searching for Better Plasmonic Materials. *Laser & Photon. Rev.* **2010**, *4* (6), 795–808. <https://doi.org/10.1002/lpor.200900055>.
- (16) Kreibig, U.; Vollmer, M. *Optical Properties of Metal Clusters*; Springer, 1995.
- (17) Faraday, M. Experimental Relation of Gold to Light. *Phil. Trans. R. Soc.* **1857**, *147*, 145–181. <https://doi.org/10.1098/rstl.1857.0011>.
- (18) Mie, G. Beiträge Zur Optik Trüber Medien, Speziell Kolloidaler Metallösungen. *Ann. Phys.* **1908**.
- (19) *The MIE Theory*; Springer: New York, 2012.
- (20) Myroshnychenko, V.; Rodriguez-Fernandez, J.; Pastoriza-Santos, I.; Funston, A.; Novo, C.; Mulvaney, P.; Liz-Marzan, L.; Garcia de Abajo, J. Modelling the Optical Response of Gold Nanoparticles. *Chem. Soc. Rev.* **2008**.
- (21) Jain, P. K.; Lee, K. S.; El-Sayed, I. H.; El-Sayed, M. A. Calculated Absorption and Scattering Properties of Gold Nanoparticles of Different Size, Shape, and Composition: Applications in Biological Imaging and Biomedicine. *The Journal of Physical Chemistry B* **2006**, *110* (14), 7238–7248. <https://doi.org/10.1021/jp057170o>.
- (22) Bastús, N. G.; Piella, J.; Puntès, V. Quantifying the Sensitivity of Multipolar (Dipolar, Quadrupolar, and Octapolar) Surface Plasmon Resonances in Silver Nanoparticles: The Effect of Size, Composition, and Surface Coating. *Langmuir* **2016**, *32* (1), 290–300. <https://doi.org/10.1021/acs.langmuir.5b03859>.
- (23) Mulvaney, P. Surface Plasmon Spectroscopy of Nanosized Metal Particles. *Langmuir* **1996**, *12*, 788–800.
- (24) Link, S.; Mohamed, M. B.; El-Sayed, M. A. Simulation of the Optical Absorption Spectra of Gold Nanorods as a Function of Their Aspect Ratio and the Effect of the Medium Dielectric Constant. *J. Phys. Chem. B* **1999**, *103* (16), 3073–3077. <https://doi.org/10.1021/jp990183f>.
- (25) Li, J.; Guo, H.; Li, Z.-Y. Microscopic and Macroscopic Manipulation of Gold Nanorod and Its Hybrid Nanostructures [Invited]. *Photon. Res.* **2013**, *1* (1), 28. <https://doi.org/10.1364/PRJ.1.000028>.
- (26) Jiang, M.-M.; Chen, H.-Y.; Li, B.-H.; Liu, K.-W.; Shan, C.-X.; Shen, D.-Z. Hybrid Quadrupolar Resonances Stimulated at Short Wavelengths Using Coupled Plasmonic

- Silver Nanoparticle Aggregation. *J. Mater. Chem. C* **2014**, *2* (1), 56–63. <https://doi.org/10.1039/C3TC31910E>.
- (27) El-Sayed, M.; Neretina, S.; Xiaohua, H. Gold Nanorods: From Synthesis and Properties to Biological and Biomedical Applications. *ADVANCED MATERIALS* **2009**, *21*, 4880–4910. <https://doi.org/10.1002/adma.200802789>.
- (28) El-Sayed, M.; El Sayed, I.; Jain, P.; Huang, X. Gold Nanoparticles: Interesting Optical Properties and Recent Applications in Cancer Diagnostics and Therapy. *Nanomedicine* **2007**, 681–693.
- (29) Grésillon, S.; Aigouy, L.; Boccara, A. C.; Rivoal, J. C.; Quelin, X.; Desmarest, C.; Gadenne, P.; Shubin, V. A.; Sarychev, A. K.; Shalaev, V. M. Experimental Observation of Localized Optical Excitations in Random Metal-Dielectric Films. *Phys. Rev. Lett.* **1999**, *82* (22), 4520–4523. <https://doi.org/10.1103/PhysRevLett.82.4520>.
- (30) Linic, S.; Christopher, P.; Ingram, D. B. Plasmonic-Metal Nanostructures for Efficient Conversion of Solar to Chemical Energy. *Nature Materials* **2011**, *10* (12), 911–921. <https://doi.org/10.1038/nmat3151>.
- (31) Brongersma, M. L.; Halas, N. J.; Nordlander, P. Plasmon-Induced Hot Carrier Science and Technology. *Nature Nanotechnology* **2015**, *10* (1), 25–34. <https://doi.org/10.1038/nnano.2014.311>.
- (32) Hartland, G. V.; Besteiro, L. V.; Johns, P.; Govorov, A. O. What's so Hot about Electrons in Metal Nanoparticles? *ACS Energy Letters* **2017**, *2* (7), 1641–1653. <https://doi.org/10.1021/acsenergylett.7b00333>.
- (33) Giesecking, R. L.; Ratner, M. A.; Schatz, G. A. Review of Plasmon-Induced Hot-Electron Dynamics and Related SERS Chemical Effects. In *Frontiers of Plasmon Enhanced Spectroscopy Volume 1*; 2016; Vol. 1245, pp 1–22.
- (34) Govorov, A. O.; Zhang, H.; Gun'ko, Y. K. Theory of Photoinjection of Hot Plasmonic Carriers from Metal Nanostructures into Semiconductors and Surface Molecules. *The Journal of Physical Chemistry C* **2013**, *117* (32), 16616–16631. <https://doi.org/10.1021/jp405430m>.
- (35) Govorov, A. O.; Zhang, H.; Demir, H. V.; Gun'ko, Y. K. Photogeneration of Hot Plasmonic Electrons with Metal Nanocrystals: Quantum Description and Potential Applications. *Nano Today* **2014**, *9* (1), 85–101. <https://doi.org/10.1016/j.nantod.2014.02.006>.

- (36) Stewart, S.; Wei, Q.; Sun, Y. Surface Chemistry of Quantum-Sized Metal Nanoparticles under Light Illumination. *Chem. Sci.* **2021**, *12* (4), 1227–1239. <https://doi.org/10.1039/D0SC04651E>.
- (37) Kreibig, U. Electronic Properties of Small Silver Particles: The Optical Constants and Their Temperature Dependence. *Journal of Physics F: Metal Physics* **1974**, *4* (7), 999–1014. <https://doi.org/10.1088/0305-4608/4/7/007>.
- (38) Li, X.; Xiao, D.; Zhang, Z. Landau Damping of Quantum Plasmons in Metal Nanostructures. *New Journal of Physics* **2013**, *15* (2), 23011. <https://doi.org/10.1088/1367-2630/15/2/023011>.
- (39) Uskov, A. V.; Khurgin, J. B.; Smetanin, I. V.; Protsenko, I. E.; Nikonorov, N. V. Landau Damping in Hybrid Plasmonics. *J. Phys. Chem. Lett.* **2022**, *13* (4), 997–1001. <https://doi.org/10.1021/acs.jpcclett.1c04031>.
- (40) Sundararaman, R.; Narang, P.; Jermyn, A. S.; Goddard III, W. A.; Atwater, H. A. Theoretical Predictions for Hot-Carrier Generation from Surface Plasmon Decay. *Nature Communications* **2014**, *5* (1), 5788. <https://doi.org/10.1038/ncomms6788>.
- (41) Manjavacas, A.; Liu, J. G.; Kulkarni, V.; Nordlander, P. Plasmon-Induced Hot Carriers in Metallic Nanoparticles. *ACS Nano* **2014**, *8* (8), 7630–7638. <https://doi.org/10.1021/nn502445f>.
- (42) Dal Forno, S.; Ranno, L.; Lischner, J. Material, Size, and Environment Dependence of Plasmon-Induced Hot Carriers in Metallic Nanoparticles. *The Journal of Physical Chemistry C* **2018**, *122* (15), 8517–8527. <https://doi.org/10.1021/acs.jpcc.8b00651>.
- (43) Besteiro, L. V.; Yu, P.; Wang, Z.; Holleitner, A. W.; Hartland, G. V.; Wiederrecht, G. P.; Govorov, A. O. The Fast and the Furious: Ultrafast Hot Electrons in Plasmonic Metastructures. Size and Structure Matter. *Nano Today* **2019**, *27*, 120–145. <https://doi.org/10.1016/j.nantod.2019.05.006>.
- (44) Halas, N. J.; Lal, S.; Chang, W.-S.; Link, S.; Nordlander, P. Plasmons in Strongly Coupled Metallic Nanostructures. *Chemical Reviews* **2011**, *111* (6), 3913–3961. <https://doi.org/10.1021/cr200061k>.
- (45) Besteiro, L. V.; Govorov, A. O. Amplified Generation of Hot Electrons and Quantum Surface Effects in Nanoparticle Dimers with Plasmonic Hot Spots. *The Journal of Physical Chemistry C* **2016**, *120* (34), 19329–19339. <https://doi.org/10.1021/acs.jpcc.6b05968>.
- (46) Santiago, E. Y.; Besteiro, L. V.; Kong, X.-T.; Correa-Duarte, M. A.; Wang, Z.; Govorov, A. O. Efficiency of Hot-Electron Generation in Plasmonic Nanocrystals with

- Complex Shapes: Surface-Induced Scattering, Hot Spots, and Interband Transitions. *ACS Photonics* **2020**, *7* (10), 2807–2824. <https://doi.org/10.1021/acsp Photonics.0c01065>.
- (47) Maurice, M. S.; Barros, N.; Kachkachi, H. Orientational Selectivity of Hot Electrons Generated by a Dimer of Plasmonic Nanoparticles. *J. Phys. Chem. C* **2021**, *125* (43), 23991–24000. <https://doi.org/10.1021/acs.jpcc.1c04172>.
- (48) Besteiro, L. V.; Kong, X.-T.; Wang, Z.; Hartland, G.; Govorov, A. O. Understanding Hot-Electron Generation and Plasmon Relaxation in Metal Nanocrystals: Quantum and Classical Mechanisms. *ACS Photonics* **2017**, *4* (11), 2759–2781. <https://doi.org/10.1021/acsp Photonics.7b00751>.
- (49) Hartland, G. V. Optical Studies of Dynamics in Noble Metal Nanostructures. *Chem. Rev.* **2011**, *111*, 3858–3887. <https://doi.org/10.1021/cr1002547>.
- (50) Saavedra, J. R. M.; Asenjo-Garcia, A.; García de Abajo, F. J. Hot-Electron Dynamics and Thermalization in Small Metallic Nanoparticles. *ACS Photonics* **2016**, *3* (9), 1637–1646. <https://doi.org/10.1021/acsp Photonics.6b00217>.
- (51) Narang, P.; Sundararaman, R.; Atwater, H. A. Plasmonic Hot Carrier Dynamics in Solid-State and Chemical Systems for Energy Conversion. *Nanophotonics* **2016**, *5* (1), 96–111. <https://doi.org/10.1515/nanoph-2016-0007>.
- (52) Huang, W.; Qian, W.; El-Sayed, M. Effect of the Lattice Crystallinity on the Electron-Phonon Relaxation Rates in Gold Nanoparticles. *J. Phys. Chem. C* **111**, 10751–10757.
- (53) El-Sayed, M.; Link, S. Spectral Properties and Relaxation Dynamics of Surface Plasmon Electronic Oscillations in Gold and Silver Nanodots and Nanorods. *J. Phys. Chem.* **1999**, *103*, 8410–8426.
- (54) Link, S.; El-Sayed, M. A. Size and Temperature Dependence of the Plasmon Absorption of Colloidal Gold Nanoparticles. *J. Phys. Chem. B* **1999**, *103* (21), 4212–4217. <https://doi.org/10.1021/jp984796o>.
- (55) Baffou, G. Q. Thermo-Plasmonics: Using Metallic Nanostructures as Nano-Sources of Heat. *Laser Photonic Rev.* **2012**, 1–17. <https://doi.org/10.1002/lpor.201200003>.
- (56) Chang, L.; Besteiro, L. V.; Sun, J.; Santiago, E. Y.; Gray, S. K.; Wang, Z.; Govorov, A. O. Electronic Structure of the Plasmons in Metal Nanocrystals: Fundamental Limitations for the Energy Efficiency of Hot Electron Generation. *ACS Energy Lett.* **2019**, *4* (10), 2552–2568. <https://doi.org/10.1021/acsenerylett.9b01617>.
- (57) Liu, J. G.; Zhang, H.; Link, S.; Nordlander, P. Relaxation of Plasmon-Induced Hot Carriers. *ACS Photonics* **2018**, *5* (7), 2584–2595. <https://doi.org/10.1021/acsp Photonics.7b00881>.

- (58) Berdakin, M.; Douglas-Gallardo, O. A.; Sánchez, C. G. Interplay between Intra- and Interband Transitions Associated with the Plasmon-Induced Hot Carrier Generation Process in Silver and Gold Nanoclusters. *J. Phys. Chem. C* **2020**, *124* (2), 1631–1639. <https://doi.org/10.1021/acs.jpcc.9b10871>.
- (59) Zhang, H.; Govorov, A. O. Optical Generation of Hot Plasmonic Carriers in Metal Nanocrystals: The Effects of Shape and Field Enhancement. *The Journal of Physical Chemistry C* **2014**, *118* (14), 7606–7614. <https://doi.org/10.1021/jp500009k>.
- (60) Harutyunyan, H.; Martinson, A. B. F.; Rosenmann, D.; Khorashad, L. K.; Besteiro, L. V.; Govorov, A. O.; Wiederrecht, G. P. Anomalous Ultrafast Dynamics of Hot Plasmonic Electrons in Nanostructures with Hot Spots. *Nature Nanotechnology* **2015**, *10* (9), 770–774. <https://doi.org/10.1038/nnano.2015.165>.
- (61) Kong, X.-T.; Wang, Z.; Govorov, A. O. Plasmonic Nanostars with Hot Spots for Efficient Generation of Hot Electrons under Solar Illumination. *Advanced Optical Materials* **2017**, *5* (15). <https://doi.org/10.1002/adom.201600594>.
- (62) Khurgin, J. B. Fundamental Limits of Hot Carrier Injection from Metal in Nanoplasmonics. *Nanophotonics* **2020**, *9* (2), 453–471. <https://doi.org/10.1515/nanoph-2019-0396>.
- (63) Solís, D. M.; Taboada, J. M.; Obelleiro, F.; Liz-Marzán, L. M.; García de Abajo, F. J. Optimization of Nanoparticle-Based SERS Substrates through Large-Scale Realistic Simulations. *ACS Photonics* **2017**, *4* (2), 329–337. <https://doi.org/10.1021/acsp Photonics.6b00786>.
- (64) Liao, P. F.; Wokaun, A. Lightning Rod Effect in Surface Enhanced Raman Scattering. *The Journal of Chemical Physics* **1982**, *76* (751). <https://doi.org/10.1063/1.442690>.
- (65) Prodan, E.; Radloff, C.; Halas, N. J.; Nordlander, P. A Hybridization Model for the Plasmon Response of Complex Nanostructures. *Science* **2003**, *302* (5644), 419–422. <https://doi.org/10.1126/science.1089171>.
- (66) Van Duyne, R.; Jeanmarie, D. L. Surface Raman Spectroelectrochemistry, Part 1: Heterocyclic, Aromatic, and Aliphatic Amines Adsorbed on the Anodized Silver Electrode. *J. Electroanal. Chem.* **1977**, *84*, 1–20.
- (67) Moskovits, M. Surface Roughness and the Enhanced Intensity of Raman Scattering by Molecules Adsorbed on Metals. *The Journal of Chemical Physics* **1978**, *69* (9), 4159–4161. <https://doi.org/10.1063/1.437095>.
- (68) Schatz, G.; Young, M. A.; Van Duyne, R. Electromagnetic Mechanism of SERS. In *Enhanced Raman Scattering – Physics and Applications*; SPRINGER, 2006; pp 19–46.

- (69) Van Duyne, R.; Shah, N.; Dieringer, J.; Stiles, P. Surface-Enhanced Raman Spectroscopy. *Annu. Rev. Anal. Chem.* **2008**, 601–626. <https://doi.org/10.1146/annurev.anchem.1.031207.112814>.
- (70) Kleinman, S.; Frontiera, R.; Henry, A.; Dieringer, J.; Van Duyne, R. Creating, Characterizing, and Controlling Chemistry with SERS Hot Spots. *Phys. Chem. Chem. Phys.* **2013**. <https://doi.org/10.1039/c2cp42598j>.
- (71) Shanthil, M.; Thomas, R.; Swathi, R. S.; George Thomas, K. Ag@SiO₂ Core–Shell Nanostructures: Distance-Dependent Plasmon Coupling and SERS Investigation. *The Journal of Physical Chemistry Letters* **2012**, 3 (11), 1459–1464. <https://doi.org/10.1021/jz3004014>.
- (72) West, J. L.; Halas, N. J.; Hazle, J. D.; Price, R. E.; Rivera, B.; Sershen, S.; Bankson, J. A.; Stafford, R. J.; Hirsh, L. R. Nanoshell-Mediated near-Infrared Thermal Therapy of Tumors under Magnetic Resonance Guidance. *Proc Natl Acad Sci U S A.* **2003**, 13549–13554. <https://doi.org/10.1073/pnas.2232479100>.
- (73) O’Neal, D. P.; Hirsch, L. R.; Halas, N. J.; Payne, J. D.; West, J. L. Photo-Thermal Tumor Ablation in Mice Using near Infrared-Absorbing Nanoparticles. *Cancer Letters* **2004**, 209 (2), 171–176. <https://doi.org/10.1016/j.canlet.2004.02.004>.
- (74) Link, S.; El-Sayed, M. Shape and Size Dependence of Radiative, Non-Radiative and Photothermal Properties of Gold Nanocrystals. *Int. Rev. Phys. Chem.* **2000**, 19, 409–453.
- (75) Khurgin, J. B.; Boltasseva, A. Reflecting upon the Losses in Plasmonics and Metamaterials. *MRS Bulletin* **2012**, 37 (08), 768–779. <https://doi.org/10.1557/mrs.2012.173>.
- (76) Baffou, G.; Quidant, R.; García de Abajo, F. J. Nanoscale Control of Optical Heating in Complex Plasmonic Systems. *ACS Nano* **2010**, 4 (2), 709–716. <https://doi.org/10.1021/nn901144d>.
- (77) Baffou, G.; Girard, C.; Quidant, R. Mapping Heat Origin in Plasmonic Structures. *Phys. Rev. Lett.* **2010**. <https://doi.org/10.1103/PhysRevLett.104.136805>.
- (78) Govorov, A. O. R. Generating Heat with Metal Nanoparticles. *nanotoday* **2007**, 2, 30–38. [https://doi.org/10.1016/S1748-0132\(07\)70017-8](https://doi.org/10.1016/S1748-0132(07)70017-8).
- (79) Govorov, A. O.; Hernandez, P.; Tandler, P. J.; T, C. M.; Richardson, H. H. Experimental and Theoretical Studies of Light-to-Heat Conversion and Collective Heating Effects in Metal Nanoparticle Solutions. *NANO LETTERS* **2009**, 9, 1139–1146.

- (80) Govorov, A. O. Z. Gold Nanoparticle Ensembles as Heaters and Actuators: Melting and Collective Plasmon Resonances. *Nanoscale Res Lett* **2006**, 84–90. <https://doi.org/10.1007/s11671-006-9015-7>.
- (81) Baffou, G.; Berto, P.; Urena, E. B.; Quidant, R.; Monneret, S.; Polleux, J.; Rigneault, H. Photoinduced Heating of Nanoparticle Arrays. *ACS Nano* **2013**, 7, 6478–6488.
- (82) Baffou, G.; Quidant, R.; Girard, C. Thermoplasmonics Modeling: A Green's Function Approach. *Phys. Rev. B* **2010**, 82. <https://doi.org/10.1103/PhysRevB.82.165424>.
- (83) Baffou, G. *Thermoplasmonics: Heating Metal Nanoparticles Using Light*; Cambridge University Press, 2017.
- (84) Jauffred, L.; Samadi, A.; Klingberg, H.; Bendix, P. M.; Oddershede, L. B. Plasmonic Heating of Nanostructures. *Chem. Rev.* **2019**, 119 (13), 8087–8130. <https://doi.org/10.1021/acs.chemrev.8b00738>.
- (85) Keblinski, P.; Cahill, D. G.; Bodapati, A.; Sullivan, C. R.; Taton, T. A. Limits of Localized Heating by Electromagnetically Excited Nanoparticles. *Journal of Applied Physics* **2006**, 100 (5), 054305. <https://doi.org/10.1063/1.2335783>.
- (86) Ingram, D. B.; Linic, S. Water Splitting on Composite Plasmonic-Metal/Semiconductor Photoelectrodes: Evidence for Selective Plasmon-Induced Formation of Charge Carriers near the Semiconductor Surface. *Journal of the American Chemical Society* **2011**, 133 (14), 5202–5205. <https://doi.org/10.1021/ja200086g>.
- (87) Zhang, Z.; Yates, J. T. Band Bending in Semiconductors: Chemical and Physical Consequences at Surfaces and Interfaces. *Chem. Rev.* **2012**, 112 (10), 5520–5551. <https://doi.org/10.1021/cr3000626>.
- (88) Khan, M. R.; Chuan, T. W.; Yousuf, A.; Chowdhury, M. N. K.; Cheng, C. K. Schottky Barrier and Surface Plasmonic Resonance Phenomena towards the Photocatalytic Reaction: Study of Their Mechanisms to Enhance Photocatalytic Activity. *Catal. Sci. Technol.* **2015**, 5 (5), 2522–2531. <https://doi.org/10.1039/C4CY01545B>.
- (89) Sistani, M.; Bartmann, M. G.; Gsken, N. A.; Oulton, R. F.; Keshmiri, H.; Luong, M. A.; Momtaz, Z. S.; Den Hertog, M. I.; Lugstein, A. Plasmon-Driven Hot Electron Transfer at Atomically Sharp Metal–Semiconductor Nanojunctions. *ACS Photonics* **2020**, 7 (7), 1642–1648. <https://doi.org/10.1021/acsp Photonics.0c00557>.
- (90) Tagliabue, G.; DuChene, J. S.; Habib, A.; Sundararaman, R.; Atwater, H. A. Hot-Hole versus Hot-Electron Transport at Cu/GaN Heterojunction Interfaces. *ACS Nano* **2020**, 14 (5), 5788–5797. <https://doi.org/10.1021/acsnano.0c00713>.

- (91) Jeffries, W. R.; Fagan, A. M.; Schaak, R. E.; Knappenberger, K. L. Influence of Band Alignment on Electronic Relaxation in Plasmonic Metal–Semiconductor Hybrid Nanoparticles. *J. Phys. Chem. C* **2022**, *126* (19), 8384–8392. <https://doi.org/10.1021/acs.jpcc.2c01378>.
- (92) Takahashi, Y.; Tatsuma, T. Solid State Photovoltaic Cells Based on Localized Surface Plasmon-Induced Charge Separation. *Appl. Phys. Lett.* **2011**, *99* (18), 182110. <https://doi.org/10.1063/1.3659476>.
- (93) Furube, A.; Du, L.; Hara, K.; Katoh, R.; Tachiya, M. Ultrafast Plasmon-Induced Electron Transfer from Gold Nanodots into TiO₂ Nanoparticles. *Journal of the American Chemical Society* **2007**, *129* (48), 14852–14853. <https://doi.org/10.1021/ja076134v>.
- (94) Sousa-Castillo, A.; Comesaña-Hermo, M.; Rodríguez-González, B.; Pérez-Lorenzo, M.; Wang, Z.; Kong, X.-T.; Govorov, A. O.; Correa-Duarte, M. A. Boosting Hot Electron-Driven Photocatalysis through Anisotropic Plasmonic Nanoparticles with Hot Spots in Au–TiO₂ Nanoarchitectures. *The Journal of Physical Chemistry C* **2016**, *120* (21), 11690–11699. <https://doi.org/10.1021/acs.jpcc.6b02370>.
- (95) Lee, Y. K.; Jung, C. H.; Park, J.; Seo, H.; Somorjai, G. A.; Park, J. Y. Surface Plasmon-Driven Hot Electron Flow Probed with Metal-Semiconductor Nanodiodes. *Nano Lett.* **2011**, *11* (10), 4251–4255. <https://doi.org/10.1021/nl2022459>.
- (96) Li, Y.; Cheng, J.; Li, J.; Delville, M.-H.; Tréguer-Delapierre, M.; He, T.; Chen, R.; Tang, Z. Ultrafast Dynamics of Photoexcited Hot Carrier Generation and Injection in AgNWs@TiO₂@GNS Nanostructures. *J. Phys. Chem. C* **2018**, *122* (26), 14857–14864. <https://doi.org/10.1021/acs.jpcc.8b05017>.
- (97) Ishida, T.; Tatsuma, T. Effect of Plasmon Coupling on Quantum Efficiencies of Plasmon-Induced Charge Separation. *J. Phys. Chem. C* **2018**, *122* (45), 26153–26159. <https://doi.org/10.1021/acs.jpcc.8b07986>.
- (98) Varapragasam, S. J. P.; Mia, S.; Wieting, C.; Balasanthiran, C.; Hossan, M. Y.; Baride, A.; Rioux, R. M.; Hoefelmeyer, J. D. Ag–TiO₂ Hybrid Nanocrystal Photocatalyst: Hydrogen Evolution under UV Irradiation but Not under Visible-Light Irradiation. *ACS Appl. Energy Mater.* **2019**, *2* (11), 8274–8282. <https://doi.org/10.1021/acsaem.9b01730>.
- (99) Lee, J.; Mubeen, S.; Ji, X.; Stucky, G. D.; Moskovits, M. Plasmonic Photoanodes for Solar Water Splitting with Visible Light. *Nano Letters* **2012**, *12* (9), 5014–5019. <https://doi.org/10.1021/nl302796f>.

- (100) Zhu, H.; Xie, H.; Yang, Y.; Wang, K.; Zhao, F.; Ye, W.; Ni, W. Mapping Hot Electron Response of Individual Gold Nanocrystals on a TiO₂ Photoanode. *Nano Lett.* **2020**, *20* (4), 2423–2431. <https://doi.org/10.1021/acs.nanolett.9b05125>.
- (101) Ratchford, D. C.; Dunkelberger, A. D.; Vurgaftman, I.; Owrutsky, J. C.; Pehrsson, P. E. Quantification of Efficient Plasmonic Hot-Electron Injection in Gold Nanoparticle–TiO₂ Films. *Nano Lett.* **2017**, *17* (10), 6047–6055. <https://doi.org/10.1021/acs.nanolett.7b02366>.
- (102) Negrín-Montecelo, Y.; Comesaña-Hermo, M.; Khorashad, L. K.; Sousa-Castillo, A.; Wang, Z.; Pérez-Lorenzo, M.; Liedl, T.; Govorov, A. O.; Correa-Duarte, M. A. Photophysical Effects behind the Efficiency of Hot Electron Injection in Plasmon-Assisted Catalysis: The Joint Role of Morphology and Composition. *ACS Energy Lett.* **2020**, *5* (2), 395–402. <https://doi.org/10.1021/acsenerylett.9b02478>.
- (103) Kumar, A.; Choudhary, P.; Kumar, A.; Camargo, P. H. C.; Krishnan, V. Recent Advances in Plasmonic Photocatalysis Based on TiO₂ and Noble Metal Nanoparticles for Energy Conversion, Environmental Remediation, and Organic Synthesis. *Small* **2022**, *18* (1), 2101638. <https://doi.org/10.1002/smll.202101638>.
- (104) Manuel, A.; Shankar, K. Hot Electrons in TiO₂–Noble Metal Nano-Heterojunctions: Fundamental Science and Applications in Photocatalysis. *Nanomaterials* **2021**, *11* (5), 1249. <https://doi.org/10.3390/nano11051249>.
- (105) Yuan, L.; Kuriakose, A.; Zhou, J.; Robatjazi, H.; Nordlander, P.; Halas, N. J. Plasmonically Enhanced Hydrogen Evolution with an Al–TiO₂-Based Photoelectrode. *J. Phys. Chem. C* **2022**, *126* (32), 13714–13719. <https://doi.org/10.1021/acs.jpcc.2c03961>.
- (106) Tian, Y.; Tatsuma, T. Mechanisms and Applications of Plasmon-Induced Charge Separation at TiO₂ Films Loaded with Gold Nanoparticles. *J. Am. Chem. Soc.* **2005**, *127* (20), 7632–7637. <https://doi.org/10.1021/ja042192u>.
- (107) DuChene, J. S.; Sweeny, B. C.; Johnston-Peck, A. C.; Su, D.; Stach, E. A.; Wei, W. D. Prolonged Hot Electron Dynamics in Plasmonic-Metal/Semiconductor Heterostructures with Implications for Solar Photocatalysis. *Angew. Chem. Int. Ed.* **2014**, *53* (30), 7887–7891. <https://doi.org/10.1002/anie.201404259>.
- (108) Ma, X.-C.; Dai, Y.; Yu, L.; Huang, B.-B. Energy Transfer in Plasmonic Photocatalytic Composites. *Light: Science & Applications* **2016**, *5* (2), e16017–e16017. <https://doi.org/10.1038/lsa.2016.17>.

- (109) Liu, G.; Lou, Y.; Zhao, Y.; Burda, C. Directional Damping of Plasmons at Metal–Semiconductor Interfaces. *Acc. Chem. Res.* **2022**, *55* (13), 1845–1856. <https://doi.org/10.1021/acs.accounts.2c00001>.
- (110) Wu, K.; Chen, J.; McBride, J. R.; Lian, T. Efficient Hot-Electron Transfer by a Plasmon-Induced Interfacial Charge-Transfer Transition. *Science* **2015**, *349* (6248), 632–635. <https://doi.org/10.1126/science.aac5443>.
- (111) Camargo, F. V. A.; Ben-Shahar, Y.; Nagahara, T.; Panfil, Y. E.; Russo, M.; Banin, U.; Cerullo, G. Visualizing Ultrafast Electron Transfer Processes in Semiconductor–Metal Hybrid Nanoparticles: Toward Excitonic–Plasmonic Light Harvesting. *Nano Lett.* **2021**, *21* (3), 1461–1468. <https://doi.org/10.1021/acs.nanolett.0c04614>.
- (112) Kumar, P. V.; Rossi, T. P.; Marti-Dafcik, D.; Reichmuth, D.; Kuisma, M.; Erhart, P.; Puska, M. J.; Norris, D. J. Plasmon-Induced Direct Hot-Carrier Transfer at Metal–Acceptor Interfaces. *ACS Nano* **2019**, *13* (3), 3188–3195. <https://doi.org/10.1021/acsnano.8b08703>.
- (113) Ma, J.; Gao, S. Plasmon-Induced Electron–Hole Separation at the Ag/TiO₂ Interface. *ACS Nano* **2019**, *13* (12), 13658–13667. <https://doi.org/10.1021/acsnano.9b03555>.
- (114) Chen, Z.; Yin, H.; Wang, R.; Peng, Y.; You, C.; Li, J. Efficient Electron Transfer by Plasmonic Silver in SrTiO₃ for Low-Concentration Photocatalytic NO Oxidation. *Environ. Sci. Technol.* **2022**, *56* (6), 3604–3612. <https://doi.org/10.1021/acs.est.2c00262>.
- (115) Song, J.; Long, J.; Liu, Y.; Xu, Z.; Ge, A.; Piercy, B. D.; Cullen, D. A.; Ivanov, I. N.; McBride, J. R.; Losego, M. D.; Lian, T. Highly Efficient Plasmon Induced Hot-Electron Transfer at Ag/TiO₂ Interface. *ACS Photonics* **2021**, *8* (5), 1497–1504. <https://doi.org/10.1021/acsphotonics.1c00321>.
- (116) Collado, L.; Reynal, A.; Fresno, F.; Barawi, M.; Escudero, C.; Perez-Dieste, V.; Coronado, J. M.; Serrano, D. P.; Durrant, J. R.; de la Peña O’Shea, V. A. Unravelling the Effect of Charge Dynamics at the Plasmonic Metal/Semiconductor Interface for CO₂ Photoreduction. *Nat Commun* **2018**, *9* (1), 4986. <https://doi.org/10.1038/s41467-018-07397-2>.
- (117) Hou, W.; Hung, W. H.; Pavaskar, P.; Goepfert, A.; Aykol, M.; Cronin, S. B. Photocatalytic Conversion of CO₂ to Hydrocarbon Fuels via Plasmon-Enhanced Absorption and Metallic Interband Transitions. *ACS Catalysis* **2011**, *1* (8), 929–936. <https://doi.org/10.1021/cs2001434>.
- (118) Guan, J.; Wu, S.; Li, L.; Wang, X.; Ji, W.; Ozaki, Y. New Insights of Charge Transfer at Metal/Semiconductor Interfaces for Hot-Electron Generation Studied by Surface-

- Enhanced Raman Spectroscopy. *J. Phys. Chem. Lett.* **2022**, *13* (16), 3571–3578. <https://doi.org/10.1021/acs.jpcllett.2c00239>.
- (119) Gellé, A.; Jin, T.; de la Garza, L.; Price, G. D.; Besteiro, L. V.; Moores, A. Applications of Plasmon-Enhanced Nanocatalysis to Organic Transformations. *Chem. Rev.* **2020**, *120* (2), 986–1041. <https://doi.org/10.1021/acs.chemrev.9b00187>.
- (120) Seemala, B.; Therrien, A. J.; Lou, M.; Li, K.; Finzel, J. P.; Qi, J.; Nordlander, P.; Christopher, P. Plasmon-Mediated Catalytic O₂ Dissociation on Ag Nanostructures: Hot Electrons or Near Fields? *ACS Energy Lett.* **2019**, *4* (8), 1803–1809. <https://doi.org/10.1021/acsenergylett.9b00990>.
- (121) Boerigter, C.; Campana, R.; Morabito, M.; Linic, S. Evidence and Implications of Direct Charge Excitation as the Dominant Mechanism in Plasmon-Mediated Photocatalysis. *Nat Commun* **2016**, *7* (1), 10545. <https://doi.org/10.1038/ncomms10545>.
- (122) Quiroz, J.; Barbosa, E. C. M.; Araujo, T. P.; Fiorio, J. L.; Wang, Y.-C.; Zou, Y.-C.; Mou, T.; Alves, T. V.; de Oliveira, D. C.; Wang, B.; Haigh, S. J.; Rossi, L. M.; Camargo, P. H. C. Controlling Reaction Selectivity over Hybrid Plasmonic Nanocatalysts. *Nano Lett.* **2018**, *18* (11), 7289–7297. <https://doi.org/10.1021/acs.nanolett.8b03499>.
- (123) Yin, H.; Lan, J.; Goubert, G.; Wang, Y.; Li, J.; Zenobi, R. Nanoscale Surface Redox Chemistry Triggered by Plasmon-Generated Hot Carriers. *Small* **2019**, *15* (47), 1903674. <https://doi.org/10.1002/sml.201903674>.
- (124) Kim, N. H.; Meinhart, C. D.; Moskovits, M. Plasmon-Mediated Reduction of Aqueous Platinum Ions: The Competing Roles of Field Enhancement and Hot Charge Carriers. *J. Phys. Chem. C* **2016**, *120* (12), 6750–6755. <https://doi.org/10.1021/acs.jpcc.6b00530>.
- (125) Lee, S.; Hwang, H.; Lee, W.; Schebarchov, D.; Wy, Y.; Grand, J.; Auguié, B.; Wi, D. H.; Cortés, E.; Han, S. W. Core–Shell Bimetallic Nanoparticle Trimers for Efficient Light-to-Chemical Energy Conversion. *ACS Energy Lett.* **2020**, *5* (12), 3881–3890. <https://doi.org/10.1021/acsenergylett.0c02110>.
- (126) Cortés, E.; Xie, W.; Cambiasso, J.; Jermyn, A. S.; Sundararaman, R.; Narang, P.; Schlücker, S.; Maier, S. A. Plasmonic Hot Electron Transport Drives Nano-Localized Chemistry. *Nature Communications* **2017**, *8* (1), 14880. <https://doi.org/10.1038/ncomms14880>.
- (127) Tesema, T. E.; Kafle, B.; Tadesse, M. G.; Habteyes, T. G. Plasmon-Enhanced Resonant Excitation and Demethylation of Methylene Blue. *J. Phys. Chem. C* **2017**, *121* (13), 7421–7428. <https://doi.org/10.1021/acs.jpcc.7b00864>.

- (128) Sotiriou, G. A.; Blattmann, C. O.; Deligiannakis, Y. Nanoantioxidant-Driven Plasmon Enhanced Proton-Coupled Electron Transfer. *Nanoscale* **2016**, *8* (2), 796–803. <https://doi.org/10.1039/C5NR04942C>.
- (129) Engelbrekt, C.; Crampton, K. T.; Fishman, D. A.; Law, M.; Apkarian, V. A. Efficient Plasmon-Mediated Energy Funneling to the Surface of Au@Pt Core–Shell Nanocrystals. *ACS Nano* **2020**, *14* (4), 5061–5074. <https://doi.org/10.1021/acsnano.0c01653>.
- (130) Li, K.; Hogan, N. J.; Kale, M. J.; Halas, N. J.; Nordlander, P.; Christopher, P. Balancing Near-Field Enhancement, Absorption, and Scattering for Effective Antenna–Reactor Plasmonic Photocatalysis. *Nano Lett.* **2017**, *17* (6), 3710–3717. <https://doi.org/10.1021/acs.nanolett.7b00992>.
- (131) Herran, M.; Sousa-Castillo, A.; Fan, C.; Lee, S.; Xie, W.; Döblinger, M.; Auguie, B.; Cortés, E. Tailoring Plasmonic Bimetallic Nanocatalysts Toward Sunlight-Driven H₂ Production. *Adv Funct Materials* **2022**, 2203418. <https://doi.org/10.1002/adfm.202203418>.
- (132) Zheng, Z.; Tachikawa, T.; Majima, T. Plasmon-Enhanced Formic Acid Dehydrogenation Using Anisotropic Pd–Au Nanorods Studied at the Single-Particle Level. *J. Am. Chem. Soc.* **2015**, *137* (2), 948–957. <https://doi.org/10.1021/ja511719g>.
- (133) Wu, B.; Lee, J.; Mubeen, S.; Jun, Y.; Stucky, G. D.; Moskovits, M. Plasmon-Mediated Photocatalytic Decomposition of Formic Acid on Palladium Nanostructures. *Advanced Optical Materials* **2016**, *4* (7), 1041–1046. <https://doi.org/10.1002/adom.201600055>.
- (134) Wen, M.; Mori, K.; Kuwahara, Y.; Yamashita, H. Plasmonic Au@Pd Nanoparticles Supported on a Basic Metal–Organic Framework: Synergic Boosting of H₂ Production from Formic Acid. *ACS Energy Lett.* **2017**, *2* (1), 1–7. <https://doi.org/10.1021/acsenerylett.6b00558>.
- (135) Robotjazi, H.; Zhao, H.; Swearer, D. F.; Hogan, N. J.; Zhou, L.; Alabastri, A.; McClain, M. J.; Nordlander, P.; Halas, N. J. Plasmon-Induced Selective Carbon Dioxide Conversion on Earth-Abundant Aluminum-Cuprous Oxide Antenna-Reactor Nanoparticles. *Nature Communications* **2017**, *8* (1). <https://doi.org/10.1038/s41467-017-00055-z>.
- (136) Aslam, U.; Chavez, S.; Linic, S. Controlling Energy Flow in Multimetallic Nanostructures for Plasmonic Catalysis. *Nature Nanotech* **2017**, *12* (10), 1000–1005. <https://doi.org/10.1038/nnano.2017.131>.
- (137) Kale, M. J.; Avanesian, T.; Christopher, P. Direct Photocatalysis by Plasmonic Nanostructures. *ACS Catalysis* **2014**, *4* (1), 116–128. <https://doi.org/10.1021/cs400993w>.

- (138) Cortés, E. Activating Plasmonic Chemistry. *Science* **2018**, *362* (6410), 28–29. <https://doi.org/10.1126/science.aav1133>.
- (139) Pensa, E.; Gargiulo, J.; Lauri, A.; Schlücker, S.; Cortés, E.; Maier, S. A. Spectral Screening of the Energy of Hot Holes over a Particle Plasmon Resonance. *Nano Letters* **2019**, *19* (3), 1867–1874. <https://doi.org/10.1021/acs.nanolett.8b04950>.
- (140) Zhang, Q.; Chen, K.; Wang, H. Hot-Hole-Induced Molecular Scissoring: A Case Study of Plasmon-Driven Decarboxylation of Aromatic Carboxylates. *J. Phys. Chem. C* **2021**, *125* (38), 20958–20971. <https://doi.org/10.1021/acs.jpcc.1c07177>.
- (141) Zhan, C.; Wang, Z.-Y.; Zhang, X.-G.; Chen, X.-J.; Huang, Y.-F.; Hu, S.; Li, J.-F.; Wu, D.-Y.; Moskovits, M.; Tian, Z.-Q. Interfacial Construction of Plasmonic Nanostructures for the Utilization of the Plasmon-Excited Electrons and Holes. *Journal of the American Chemical Society* **2019**, jacs.9b02518. <https://doi.org/10.1021/jacs.9b02518>.
- (142) Peng, T.; Miao, J.; Gao, Z.; Zhang, L.; Gao, Y.; Fan, C.; Li, D. Reactivating Catalytic Surface: Insights into the Role of Hot Holes in Plasmonic Catalysis. *Small* **2018**, *14* (12), 1703510. <https://doi.org/10.1002/sml.201703510>.
- (143) Schlather, A. E.; Manjavacas, A.; Lauchner, A.; Marangoni, V. S.; DeSantis, C. J.; Nordlander, P.; Halas, N. J. Hot Hole Photoelectrochemistry on Au@SiO₂@Au Nanoparticles. *J. Phys. Chem. Lett.* **2017**, *8* (9), 2060–2067. <https://doi.org/10.1021/acs.jpcclett.7b00563>.
- (144) Kontoleta, E.; Tsoukala, A.; Askes, S. H. C.; Zoethout, E.; Oksenberg, E.; Agrawal, H.; Garnett, E. C. Using Hot Electrons and Hot Holes for Simultaneous Cocatalyst Deposition on Plasmonic Nanostructures. *ACS Appl. Mater. Interfaces* **2020**, *12* (32), 35986–35994. <https://doi.org/10.1021/acsami.0c04941>.
- (145) Zhang, Y.; Nelson, T.; Tretiak, S.; Guo, H.; Schatz, G. C. Plasmonic Hot-Carrier-Mediated Tunable Photochemical Reactions. *ACS Nano* **2018**, *12* (8), 8415–8422. <https://doi.org/10.1021/acs.nano.8b03830>.
- (146) Dutta, A.; Naldoni, A.; Malara, F.; Govorov, A. O.; Shalaev, V. M.; Boltasseva, A. Gap-Plasmon Enhanced Water Splitting with Ultrathin Hematite Films: The Role of Plasmonic-Based Light Trapping and Hot Electrons. *Faraday Discuss.* **2019**, *214*, 283–295. <https://doi.org/10.1039/C8FD00148K>.
- (147) Besteiro, L. V.; Cortés, E.; Ishii, S.; Narang, P.; Oulton, R. F. Hot Electron Physics and Applications. *Journal of Applied Physics* **2021**, *129* (15), 150401. <https://doi.org/10.1063/5.0050796>.

- (148) Wu, Y.; Yang, M.; Ueltschi, T. W.; Mosquera, M. A.; Chen, Z.; Schatz, G. C.; Van Duyne, R. P. SERS Study of the Mechanism of Plasmon-Driven Hot Electron Transfer between Gold Nanoparticles and PCBM. *J. Phys. Chem. C* **2019**, *123* (49), 29908–29915. <https://doi.org/10.1021/acs.jpcc.9b10395>.
- (149) Qi, Y.; Brasiliense, V.; Ueltschi, T. W.; Park, J. E.; Wasielewski, M. R.; Schatz, G. C.; Van Duyne, R. P. Plasmon-Driven Chemistry in Ferri-/Ferrocyanide Gold Nanoparticle Oligomers: A SERS Study. *J. Am. Chem. Soc.* **2020**, *142* (30), 13120–13129. <https://doi.org/10.1021/jacs.0c05031>.
- (150) Takeyasu, N.; Yamaguchi, K.; Kagawa, R.; Kaneta, T.; Benz, F.; Fujii, M.; Baumberg, J. J. Blocking Hot Electron Emission by SiO₂ Coating Plasmonic Nanostructures. *J. Phys. Chem. C* **2017**, *121* (34), 18795–18799. <https://doi.org/10.1021/acs.jpcc.7b02345>.
- (151) Warren, S. C.; Thimsen, E. Plasmonic Solar Water Splitting. *Energy Environ. Sci.* **2012**, *5* (1), 5133–5146. <https://doi.org/10.1039/C1EE02875H>.
- (152) Zhou, L.; Martirez, J. M. P.; Finzel, J.; Zhang, C.; Swearer, D. F.; Tian, S.; Robotjazi, H.; Lou, M.; Dong, L.; Henderson, L.; Christopher, P.; Carter, E. A.; Nordlander, P.; Halas, N. J. Light-Driven Methane Dry Reforming with Single Atomic Site Antenna-Reactor Plasmonic Photocatalysts. *Nature Energy* **2020**, *5* (1), 61–70. <https://doi.org/10.1038/s41560-019-0517-9>.
- (153) Meng, X.; Liu, L.; Ouyang, S.; Xu, H.; Wang, D.; Zhao, N.; Ye, J. Nanometals for Solar-to-Chemical Energy Conversion: From Semiconductor-Based Photocatalysis to Plasmon-Mediated Photocatalysis and Photo-Thermocatalysis. *Adv. Mater.* **2016**, *28* (32), 6781–6803. <https://doi.org/10.1002/adma.201600305>.
- (154) Mascaretti, L.; Dutta, A.; Kment, Š.; Shalaev, V. M.; Boltasseva, A.; Zbořil, R.; Naldoni, A. Plasmon-Enhanced Photoelectrochemical Water Splitting for Efficient Renewable Energy Storage. *Adv. Mater.* **2019**, *31* (31), 1805513. <https://doi.org/10.1002/adma.201805513>.
- (155) Yuan, L.; Lou, M.; Clark, B. D.; Lou, M.; Zhou, L.; Tian, S.; Jacobson, C. R.; Nordlander, P.; Halas, N. J. Morphology-Dependent Reactivity of a Plasmonic Photocatalyst. *ACS Nano* **2020**, *14* (9), 12054–12063. <https://doi.org/10.1021/acsnano.0c05383>.
- (156) Robotjazi, H.; Bao, J. L.; Zhang, M.; Zhou, L.; Christopher, P.; Carter, E. A.; Nordlander, P.; Halas, N. J. Plasmon-Driven Carbon–Fluorine (C(Sp³)-F) Bond Activation with Mechanistic Insights into Hot-Carrier-Mediated Pathways. *Nat Catal* **2020**, *3* (7), 564–573. <https://doi.org/10.1038/s41929-020-0466-5>.

- (157) Yu, S.; Wilson, A. J.; Heo, J.; Jain, P. K. Plasmonic Control of Multi-Electron Transfer and C–C Coupling in Visible-Light-Driven CO₂ Reduction on Au Nanoparticles. *Nano Lett.* **2018**, *18* (4), 2189–2194. <https://doi.org/10.1021/acs.nanolett.7b05410>.
- (158) Chen, L.-W.; Hao, Y.-C.; Guo, Y.; Zhang, Q.; Li, J.; Gao, W.-Y.; Ren, L.; Su, X.; Hu, L.; Zhang, N.; Li, S.; Feng, X.; Gu, L.; Zhang, Y.-W.; Yin, A.-X.; Wang, B. Metal–Organic Framework Membranes Encapsulating Gold Nanoparticles for Direct Plasmonic Photocatalytic Nitrogen Fixation. *J. Am. Chem. Soc.* **2021**, *143* (15), 5727–5736. <https://doi.org/10.1021/jacs.0c13342>.
- (159) Devasia, D.; Wilson, A. J.; Heo, J.; Mohan, V.; Jain, P. K. A Rich Catalog of C–C Bonded Species Formed in CO₂ Reduction on a Plasmonic Photocatalyst. *Nat Commun* **2021**, *12* (1), 2612. <https://doi.org/10.1038/s41467-021-22868-9>.
- (160) Mukherjee, S.; Libisch, F.; Large, N.; Neumann, O.; Brown, L. V.; Cheng, J.; Lassiter, J. B.; Carter, E. A.; Nordlander, P.; Halas, N. J. Hot Electrons Do the Impossible: Plasmon-Induced Dissociation of H₂ on Au. *Nano Letters* **2013**, *13* (1), 240–247. <https://doi.org/10.1021/nl303940z>.
- (161) Mukherjee, S.; Zhou, L.; Goodman, A. M.; Large, N.; Ayala-Orozco, C.; Zhang, Y.; Nordlander, P.; Halas, N. J. Hot-Electron-Induced Dissociation of H₂ on Gold Nanoparticles Supported on SiO₂. *J. Am. Chem. Soc.* **2014**, *136* (1), 64–67. <https://doi.org/10.1021/ja411017b>.
- (162) Román Castellanos, L.; Hess, O.; Lischner, J. Dielectric Engineering of Hot-Carrier Generation by Quantized Plasmons in Embedded Silver Nanoparticles. *J. Phys. Chem. C* **2021**, *125* (5), 3081–3087. <https://doi.org/10.1021/acs.jpcc.0c07617>.
- (163) Christopher, P.; Xin, H.; Linic, S. Visible-Light-Enhanced Catalytic Oxidation Reactions on Plasmonic Silver Nanostructures. *Nature Chem* **2011**, *3* (6), 467–472. <https://doi.org/10.1038/nchem.1032>.
- (164) Gemenetzi, A.; Moularas, C.; Belles, L.; Deligiannakis, Y.; Louloudi, M. Reversible Plasmonic Switch in a Molecular Oxidation Catalysis Process. *ACS Catal.* **2022**, *12* (16), 9908–9921. <https://doi.org/10.1021/acscatal.2c02287>.
- (165) Foerster, B.; Joplin, A.; Kaefer, K.; Celiksoy, S.; Link, S.; Sönnichsen, C. Chemical Interface Damping Depends on Electrons Reaching the Surface. *ACS Nano* **2017**, *11* (3), 2886–2893. <https://doi.org/10.1021/acsnano.6b08010>.
- (166) Lee, S. A.; Link, S. Chemical Interface Damping of Surface Plasmon Resonances. *Acc. Chem. Res.* **2021**, *54* (8), 1950–1960. <https://doi.org/10.1021/acs.accounts.0c00872>.

- (167) Foerster, B.; Spata, V. A.; Carter, E. A.; Sönnichsen, C.; Link, S. Plasmon Damping Depends on the Chemical Nature of the Nanoparticle Interface. *Sci. Adv.* **2019**, *5* (3), eaav0704. <https://doi.org/10.1126/sciadv.aav0704>.
- (168) Boerigter, C.; Aslam, U.; Linic, S. Mechanism of Charge Transfer from Plasmonic Nanostructures to Chemically Attached Materials. *ACS Nano* **2016**, *10* (6), 6108–6115. <https://doi.org/10.1021/acsnano.6b01846>.
- (169) Kale, M. J.; Avanesian, T.; Xin, H.; Yan, J.; Christopher, P. Controlling Catalytic Selectivity on Metal Nanoparticles by Direct Photoexcitation of Adsorbate–Metal Bonds. *Nano Lett.* **2014**, *14* (9), 5405–5412. <https://doi.org/10.1021/nl502571b>.
- (170) Baffou, G.; Quidant, R. Nanoplasmonics for Chemistry. *Chem Soc Rev* **2014**, *43*, 3898–3907. <https://doi.org/10.1039/c3cs60364d>.
- (171) Naldoni, A.; Riboni, F.; Guler, U.; Boltasseva, A.; Shalaev, V. M.; Kildishev, A. V. Solar-Powered Plasmon-Enhanced Heterogeneous Catalysis. *Nanophotonics* **2016**, *5* (1), 112–133. <https://doi.org/10.1515/nanoph-2016-0018>.
- (172) Ueno, K.; Misawa, H. Surface Plasmon-Enhanced Photochemical Reactions. *Journal of Photochemistry and Photobiology C: Photochemistry Reviews* **2013**, *15*, 31–52. <https://doi.org/10.1016/j.jphotochemrev.2013.04.001>.
- (173) Cortés, E. Efficiency and Bond Selectivity in Plasmon-Induced Photochemistry. *Advanced Optical Materials* **2017**, *5* (15), 1700191. <https://doi.org/10.1002/adom.201700191>.
- (174) Swearer, D. F.; Zhao, H.; Zhou, L.; Zhang, C.; Robotjazi, H.; Martirez, J. M. P.; Krauter, C. M.; Yazdi, S.; McClain, M. J.; Ringe, E.; Carter, E. A.; Nordlander, P.; Halas, N. J. Heterometallic Antenna–reactor Complexes for Photocatalysis. *Proc. Natl. Acad. Sci. U.S.A.* **2016**, *113* (32), 8916–8920. <https://doi.org/10.1073/pnas.1609769113>.
- (175) Erwin, W. R.; Zarick, H. F.; Talbert, E. M.; Bardhan, R. Light Trapping in Mesoporous Solar Cells with Plasmonic Nanostructures. *Energy Environ. Sci.* **2016**, 1577–1601.
- (176) Wang, D.; Pillai, S. C.; Ho, S.-H.; Zeng, J.; Li, Y.; Dionysiou, D. D. Plasmonic-Based Nanomaterials for Environmental Remediation. *Applied Catalysis B: Environmental* **2018**, *237*, 721–741. <https://doi.org/10.1016/j.apcatb.2018.05.094>.
- (177) Du, L.; Shi, G.; Zhao, Y.; Chen, X.; Sun, H.; Liu, F.; Cheng, F.; Xie, W. Plasmon-Promoted Electrocatalytic Water Splitting on Metal–Semiconductor Nanocomposites: The Interfacial Charge Transfer and the Real Catalytic Sites. *Chem. Sci.* **2019**, *10* (41), 9605–9612. <https://doi.org/10.1039/C9SC03360B>.

- (178) Puértolas, B.; Comesaña-Hermo, M.; Besteiro, L. V.; Vázquez-González, M.; Correa-Duarte, M. A. Challenges and Opportunities for Renewable Ammonia Production via Plasmon-Assisted Photocatalysis. *Advanced Energy Materials* **2022**, *12* (18), 2103909. <https://doi.org/10.1002/aenm.202103909>.
- (179) Smith, J. G.; Faucheaux, J. A.; Jain, P. K. Plasmon Resonances for Solar Energy Harvesting: A Mechanistic Outlook. *Nano Today* **2015**, *10* (1), 67–80. <https://doi.org/10.1016/j.nantod.2014.12.004>.
- (180) *Plasmonic Catalysis: From Fundamentals to Applications*; Camargo, P. H. C., Cortés, E., Eds.; Wiley-VCH: Weinheim, 2021.
- (181) Kazuma, E.; Kim, Y. Mechanistic Studies of Plasmon Chemistry on Metal Catalysts. *Angew. Chem. Int. Ed.* **2019**, *58* (15), 4800–4808. <https://doi.org/10.1002/anie.201811234>.
- (182) da Silva, A. G. M.; Rodrigues, T. S.; Wang, J.; Camargo, P. H. C. Plasmonic Catalysis with Designer Nanoparticles. *Chem. Commun.* **2022**, *58* (13), 2055–2074. <https://doi.org/10.1039/D1CC03779J>.
- (183) Cortés, E.; Besteiro, L. V.; Alabastri, A.; Baldi, A.; Tagliabue, G.; Demetriadou, A.; Narang, P. Challenges in Plasmonic Catalysis. *ACS Nano* **2020**, *14* (12), 16202–16219. <https://doi.org/10.1021/acsnano.0c08773>.
- (184) Zhou, L.; Swearer, D. F.; Zhang, C.; Robatjazi, H.; Zhao, H.; Henderson, L.; Dong, L.; Christopher, P.; Carter, E. A.; Nordlander, P.; Halas, N. J. Quantifying Hot Carrier and Thermal Contributions in Plasmonic Photocatalysis. *Science* **2018**, *362* (6410), 69–72. <https://doi.org/10.1126/science.aat6967>.
- (185) Sivan, Y.; Baraban, J.; Un, I. W.; Dubi, Y. Comment on “Quantifying Hot Carrier and Thermal Contributions in Plasmonic Photocatalysis.” *Science* **2019**, *364* (6439), eaaw9367. <https://doi.org/10.1126/science.aaw9367>.
- (186) Zhou, L.; Swearer, D. F.; Robatjazi, H.; Alabastri, A.; Christopher, P.; Carter, E. A.; Nordlander, P.; Halas, N. J. Response to Comment on “Quantifying Hot Carrier and Thermal Contributions in Plasmonic Photocatalysis.” *Science* **2019**, *364* (6439), eaaw9545. <https://doi.org/10.1126/science.aaw9545>.
- (187) Dubi, Y.; Un, I. W.; Sivan, Y. Thermal Effects – an Alternative Mechanism for Plasmon-Assisted Photocatalysis. *Chem. Sci.* **2020**, *11* (19), 5017–5027. <https://doi.org/10.1039/C9SC06480J>.
- (188) Sivan, Y.; Baraban, J. H.; Dubi, Y. Experimental Practices Required to Isolate Thermal Effects in Plasmonic Photo-Catalysis: Lessons from Recent Experiments. *OSA Continuum* **2020**, *3* (3), 483. <https://doi.org/10.1364/OSAC.376809>.

- (189) Aizpurua, J.; Ashfold, M.; Baletto, F.; Baumberg, J.; Christopher, P.; Cortés, E.; de Nijs, B.; Diaz Fernandez, Y.; Gargiulo, J.; Gawinkowski, S.; Halas, N.; Hamans, R.; Jankiewicz, B.; Khurgin, J.; Kumar, P. V.; Liu, J.; Maier, S.; Maurer, R. J.; Mount, A.; Mueller, N. S.; Oulton, R.; Parente, M.; Park, J. Y.; Polanyi, J.; Quiroz, J.; Rejman, S.; Schlücker, S.; Schultz, Z.; Sivan, Y.; Tagliabue, G.; Thangamuthu, M.; Torrente-Murciano, L.; Xiao, X.; Zayats, A.; Zhan, C. Dynamics of Hot Electron Generation in Metallic Nanostructures: General Discussion. *Faraday Discuss.* **2019**, *214*, 123–146. <https://doi.org/10.1039/C9FD90011J>.
- (190) Aizpurua, J.; Baletto, F.; Baumberg, J.; Christopher, P.; Nijs, B. de; Deshpande, P.; Diaz Fernandez, Y.; Fabris, L.; Freakley, S.; Gawinkowski, S.; Govorov, A.; Halas, N.; Hernandez, R.; Jankiewicz, B.; Khurgin, J.; Kuisma, M.; Kumar, P. V.; Lischner, J.; Liu, J.; Marini, A.; Maurer, R. J.; Mueller, N. S.; Parente, M.; Park, J. Y.; Reich, S.; Sivan, Y.; Tagliabue, G.; Torrente-Murciano, L.; Thangamuthu, M.; Xiao, X.; Zayats, A. Theory of Hot Electrons: General Discussion. *Faraday Discuss.* **2019**, *214*, 245–281. <https://doi.org/10.1039/C9FD90012H>.
- (191) Khurgin, J. B. Hot Carriers Generated by Plasmons: Where Are They Generated and Where Do They Go from There? *Faraday Discuss.* **2019**, *214*, 35–58. <https://doi.org/10.1039/C8FD00200B>.
- (192) Jain, P. K. Comment on “Thermal Effects – an Alternative Mechanism for Plasmon-Assisted Photocatalysis” by Y. Dubi, I. W. Un and Y. Sivan, *Chem. Sci.*, 2020, **11**, 5017. *Chem. Sci.* **2020**, *11* (33), 9022–9023. <https://doi.org/10.1039/D0SC02914A>.
- (193) Baffou, G.; Bordacchini, I.; Baldi, A.; Quidant, R. Simple Experimental Procedures to Distinguish Photothermal from Hot-Carrier Processes in Plasmonics. *Light Sci Appl* **2020**, *9* (1), 108. <https://doi.org/10.1038/s41377-020-00345-0>.
- (194) Jain, P. K. Taking the Heat Off of Plasmonic Chemistry. *J. Phys. Chem. C* **2019**, *123* (40), 24347–24351. <https://doi.org/10.1021/acs.jpcc.9b08143>.
- (195) Mascaretti, L.; Naldoni, A. Hot Electron and Thermal Effects in Plasmonic Photocatalysis. *Journal of Applied Physics* **2020**, *128* (4), 041101. <https://doi.org/10.1063/5.0013945>.
- (196) Zhang, X.; Li, X.; Reish, M. E.; Zhang, D.; Su, N. Q.; Gutiérrez, Y.; Moreno, F.; Yang, W.; Everitt, H. O.; Liu, J. Plasmon-Enhanced Catalysis: Distinguishing Thermal and Nonthermal Effects. *Nano Letters* **2018**, *18* (3), 1714–1723. <https://doi.org/10.1021/acs.nanolett.7b04776>.

- (197) Li, X.; Zhang, X.; Everitt, H. O.; Liu, J. Light-Induced Thermal Gradients in Ruthenium Catalysts Significantly Enhance Ammonia Production. *Nano Lett.* **2019**, *19* (3), 1706–1711. <https://doi.org/10.1021/acs.nanolett.8b04706>.
- (198) Rodio, M.; Graf, M.; Schulz, F.; Mueller, N. S.; Eich, M.; Lange, H. Experimental Evidence for Nonthermal Contributions to Plasmon-Enhanced Electrochemical Oxidation Reactions. *ACS Catal.* **2020**, *10* (3), 2345–2353. <https://doi.org/10.1021/acscatal.9b05401>.
- (199) Yu, Y.; Sundaresan, V.; Willets, K. A. Hot Carriers versus Thermal Effects: Resolving the Enhancement Mechanisms for Plasmon-Mediated Photoelectrochemical Reactions. *The Journal of Physical Chemistry C* **2018**, *122* (9), 5040–5048. <https://doi.org/10.1021/acs.jpcc.7b12080>.
- (200) Zhan, C.; Liu, B.-W.; Huang, Y.-F.; Hu, S.; Ren, B.; Moskovits, M.; Tian, Z.-Q. Disentangling Charge Carrier from Photothermal Effects in Plasmonic Metal Nanostructures. *Nat Commun* **2019**, *10* (1), 2671. <https://doi.org/10.1038/s41467-019-10771-3>.
- (201) Zhang, X.; Li, X.; Zhang, D.; Su, N. Q.; Yang, W.; Everitt, H. O.; Liu, J. Product Selectivity in Plasmonic Photocatalysis for Carbon Dioxide Hydrogenation. *Nat Commun* **2017**, *8* (1), 14542. <https://doi.org/10.1038/ncomms14542>.
- (202) Kim, Y.; Smith, J. G.; Jain, P. K. Harvesting Multiple Electron–Hole Pairs Generated through Plasmonic Excitation of Au Nanoparticles. *Nature Chem* **2018**, *10* (7), 763–769. <https://doi.org/10.1038/s41557-018-0054-3>.
- (203) Li, X.; Everitt, H. O.; Liu, J. Confirming Nonthermal Plasmonic Effects Enhance CO₂ Methanation on Rh/TiO₂ Catalysts. *Nano Res.* **2019**, *12* (8), 1906–1911. <https://doi.org/10.1007/s12274-019-2457-x>.
- (204) Wang, F.; Li, C.; Chen, H.; Jiang, R.; Sun, L.-D.; Li, Q.; Wang, J.; Yu, J. C.; Yan, C.-H. Plasmonic Harvesting of Light Energy for Suzuki Coupling Reactions. *J. Am. Chem. Soc.* **2013**, *135* (15), 5588–5601. <https://doi.org/10.1021/ja310501y>.
- (205) Zhang, Q.; Zhou, Y.; Fu, X.; Villarreal, E.; Sun, L.; Zou, S.; Wang, H. Photothermal Effect, Local Field Dependence, and Charge Carrier Relaying Species in Plasmon-Driven Photocatalysis: A Case Study of Aerobic Nitrothiophenol Coupling Reaction. *J. Phys. Chem. C* **2019**, *123* (43), 26695–26704. <https://doi.org/10.1021/acs.jpcc.9b08181>.
- (206) Zhan, C.; Wang, Q.-X.; Yi, J.; Chen, L.; Wu, D.-Y.; Wang, Y.; Xie, Z.-X.; Moskovits, M.; Tian, Z.-Q. Plasmonic Nanoreactors Regulating Selective Oxidation by Energetic Electrons and Nanoconfined Thermal Fields. *Sci. Adv.* **2021**, *7* (10), eabf0962. <https://doi.org/10.1126/sciadv.abf0962>.

- (207) Li, X.; Everitt, H. O.; Liu, J. Synergy between Thermal and Nonthermal Effects in Plasmonic Photocatalysis. *Nano Res.* **2020**, *13* (5), 1268–1280. <https://doi.org/10.1007/s12274-020-2694-z>.
- (208) Gutiérrez, Y.; Losurdo, M.; González, F.; Everitt, H. O.; Moreno, F. Nanoplasmonic Photothermal Heating and Near-Field Enhancements: A Comparative Survey of 19 Metals. *J. Phys. Chem. C* **2020**, *124* (13), 7386–7395. <https://doi.org/10.1021/acs.jpcc.0c00757>.
- (209) Lalis, A.; Tessier, G.; Plain, J.; Baffou, G. Quantifying the Efficiency of Plasmonic Materials for Near-Field Enhancement and Photothermal Conversion. *J. Phys. Chem. C* **2015**, *119*, 28586–28596. <https://doi.org/10.1021/acs.jpcc.5b09294>.
- (210) Doiron, B.; Mota, M.; Wells, M. P.; Bower, R.; Mihai, A.; Li, Y.; Cohen, L. F.; Alford, N. McN.; Petrov, P. K.; Oulton, R. F.; Maier, S. A. Quantifying Figures of Merit for Localized Surface Plasmon Resonance Applications: A Materials Survey. *ACS Photonics* **2019**, *6* (2), 240–259. <https://doi.org/10.1021/acsp Photonics.8b01369>.
- (211) Kunzmann, A.; Andersson, B.; Thurnherr, T.; Krug, H.; Scheynius, A.; Fadeel, B. Toxicology of Engineered Nanomaterials: Focus on Biocompatibility, Biodistribution and Biodegradation. *Biochimica et Biophysica Acta (BBA) - General Subjects* **2011**, *1810* (3), 361–373. <https://doi.org/10.1016/j.bbagen.2010.04.007>.
- (212) Sotiriou, G. A.; Meyer, A.; Knijnenburg, J. T. N.; Panke, S.; Pratsinis, S. E. Quantifying the Origin of Released Ag⁺ Ions from Nanosilver. *Langmuir* **2012**, *28* (45), 15929–15936. <https://doi.org/10.1021/la303370d>.
- (213) Boltasseva, A.; Atwater, H. A. Low-Loss Plasmonic Metamaterials. *Science* **2011**, *331* (6015), 290–291. <https://doi.org/10.1126/science.1198258>.
- (214) Guler, U.; Boltasseva, A.; Shalae, V. M. Refractory Plasmonics. *Science* **2014**, *344* (6181), 263–264. <https://doi.org/10.1126/science.1252722>.
- (215) Naik, G. V.; Schroeder, J. L.; Ni, X.; Kildishev, A. V.; Sands, T. D.; Boltasseva, A. Titanium Nitride as a Plasmonic Material for Visible and Near-Infrared Wavelengths. *Opt. Mater. Express* **2012**, *2* (4), 478. <https://doi.org/10.1364/OME.2.000478>.
- (216) Rycenga, M.; Cobley, C. M.; Zeng, J.; Li, W.; Moran, C. H.; Zhang, Q.; Qin, D.; Xia, Y. Controlling the Synthesis and Assembly of Silver Nanostructures for Plasmonic Applications. *Chemical Reviews* **2011**, *111* (6), 3669–3712. <https://doi.org/10.1021/cr100275d>.
- (217) Haynes, C. L.; Van Duyne, R. P. Nanosphere Lithography: A Versatile Nanofabrication Tool for Studies of Size-Dependent Nanoparticle Optics. *J. Phys. Chem. B* **2001**, *105* (24), 5599–5611. <https://doi.org/10.1021/jp010657m>.

- (218) Jensen, T.; Malinsky, M.; Haynes, C.; Van Duyne, R. Nanosphere Lithography: Tunable Localized Surface Plasmon Resonance Spectra of Silver Nanoparticles. *J. Phys. Chem.* **2000**, 10549–10556. <https://doi.org/10.1021/jp002435e>.
- (219) Priebe, J. B.; Karnahl, M.; Junge, H.; Beller, M.; Hollmann, D.; Brückner, A. Water Reduction with Visible Light: Synergy between Optical Transitions and Electron Transfer in Au-TiO₂ Catalysts Visualized by In Situ EPR Spectroscopy. *Angew. Chem. Int. Ed.* **2013**, 52 (43), 11420–11424. <https://doi.org/10.1002/anie.201306504>.
- (220) Li, R.; Han, C.; Chen, Q.-W. A Facile Synthesis of Multifunctional ZnO/Ag Sea Urchin-like Hybrids as Highly Sensitive Substrates for Surface-Enhanced Raman Detection. *RSC Adv.* **2013**, 3 (29), 11715. <https://doi.org/10.1039/c3ra41203b>.
- (221) Huang, Q.; Liu, S.; Wei, W.; Yan, Q.; Wu, C. Selective Synthesis of Different ZnO/Ag Nanocomposites as Surface Enhanced Raman Scattering Substrates and Highly Efficient Photocatalytic Catalysts. *RSC Adv.* **2015**, 5 (34), 27075–27081. <https://doi.org/10.1039/C5RA01068C>.
- (222) Ulrich, G. D. Flame Synthesis of Fine Particles. *Chemical & Engineering News Archive* **1984**. <https://doi.org/10.1021/cen-v062n032.p022>.
- (223) Cabot, T. D. *Beggar on Horseback: The Autobiography of Thomas D. Cabot*; D. R. Godine: Boston, 1979.
- (224) Pratsinis, S.; Wegner, K. Scale-up of Nanoparticle Synthesis in Diffusion Flame Reactors. *Chemical Engineering Science* **2003**, 58, 4581–4589. <https://doi.org/10.1016/j.ces.2003.07.010>.
- (225) Ulrich, G. D. Theory of Particle Formation and Growth in Oxide Synthesis Flames. *Combustion Science and Technology* **1971**, 4 (1), 47–57. <https://doi.org/10.1080/00102207108952471>.
- (226) Marshall, B. S.; Telford, I.; Wood, R. A Field Method for the Determination of Zinc Oxide Fume in Air. *Analyst* **1971**, 96 (1145), 569. <https://doi.org/10.1039/an9719600569>.
- (227) Sokolowski, M.; Sokolowska, A.; Michalski, A.; Gokieli, B. The “in-Flame-Reaction” Method for Al₂O₃ Aerosol Formation. *Journal of Aerosol Science* **1977**, 8 (4), 219–230. [https://doi.org/10.1016/0021-8502\(77\)90041-6](https://doi.org/10.1016/0021-8502(77)90041-6).
- (228) Pratsinis, S.; Mueller, R.; Kammler, H. K.; Madler, L. Controlled Synthesis of Nanostructured Particles by Flame Spray Pyrolysis. *Aerosol Science* **2002**, 33, 369–389.
- (229) Pratsinis, S.; Madler, L.; Mueller, R. Nanoparticle Synthesis at High Production Rates by Flame Spray Pyrolysis. *Chemical Engineering Science* **2002**, 58, 1969–1976.

- (230) Pratsinis, S. E. *Flame Aerosol Synthesis of Ceramic Powders*; 1998. [https://doi.org/10.1016/S0360-1285\(97\)00028-2](https://doi.org/10.1016/S0360-1285(97)00028-2).
- (231) Kraft, M. Modelling of Particulate Processes. *KONA* **2005**, *23* (0), 18–35. <https://doi.org/10.14356/kona.2005007>.
- (232) Dreier, T.; Schulz, C. Laser-Based Diagnostics in the Gas-Phase Synthesis of Inorganic Nanoparticles. *Powder Technology* **2016**, *287*, 226–238. <https://doi.org/10.1016/j.powtec.2015.10.015>.
- (233) Jossen, R.; Pratsinis, S. E.; Stark, W. J.; Madler, L. Criteria for Flame-Spray Synthesis of Hollow, Shell-Like, or Inhomogeneous Oxides. *J American Ceramic Society* **2005**, *88* (6), 1388–1393. <https://doi.org/10.1111/j.1551-2916.2005.00249.x>.
- (234) Rosebrock, C. D.; Wriedt, T.; Mädler, L.; Wegner, K. The Role of Microexplosions in Flame Spray Synthesis for Homogeneous Nanopowders from Low-Cost Metal Precursors. *AIChE J.* **2016**, *62* (2), 381–391. <https://doi.org/10.1002/aic.15056>.
- (235) Rosebrock, C. D.; Riefler, N.; Wriedt, T.; Mädler, L.; Tse, S. D. Disruptive Burning of Precursor/Solvent Droplets in Flame-Spray Synthesis of Nanoparticles. *AIChE J.* **2013**, *59* (12), 4553–4566. <https://doi.org/10.1002/aic.14234>.
- (236) Strobel, R.; Pratsinis, S. E. Effect of Solvent Composition on Oxide Morphology during Flame Spray Pyrolysis of Metal Nitrates. *Phys. Chem. Chem. Phys.* **2011**, *13* (20), 9246. <https://doi.org/10.1039/c0cp01416h>.
- (237) Gröhn, A. J.; Pratsinis, S. E.; Sánchez-Ferrer, A.; Mezzenga, R.; Wegner, K. Scale-up of Nanoparticle Synthesis by Flame Spray Pyrolysis: The High-Temperature Particle Residence Time. *Ind. Eng. Chem. Res.* **2014**, *53* (26), 10734–10742. <https://doi.org/10.1021/ie501709s>.
- (238) Mädler, L.; Pratsinis, S. E. Bismuth Oxide Nanoparticles by Flame Spray Pyrolysis. *Journal of the American Ceramic Society* **2004**, *85* (7), 1713–1718. <https://doi.org/10.1111/j.1151-2916.2002.tb00340.x>.
- (239) Mädler, L.; Stark, W. J.; Pratsinis, S. E. Flame-Made Ceria Nanoparticles. *J. Mater. Res.* **2002**, *17* (6), 1356–1362. <https://doi.org/10.1557/JMR.2002.0202>.
- (240) Baker, C.; Kim, W.; Sanghera, J.; Goswami, R.; Villalobos, G.; Sadowski, B.; Aggarwal, I. Flame Spray Synthesis of Lu₂O₃ Nanoparticles. *Materials Letters* **2012**, *66* (1), 132–134. <https://doi.org/10.1016/j.matlet.2011.08.058>.
- (241) Mueller, R.; Kammler, H. K.; Pratsinis, S. E.; Vital, A.; Beaucage, G.; Burtscher, P. Non-Agglomerated Dry Silica Nanoparticles. *Powder Technology* **2004**, *140* (1–2), 40–48. <https://doi.org/10.1016/j.powtec.2004.01.004>.

- (242) Meierhofer, F.; Mädler, L.; Fritsching, U. Nanoparticle Evolution in Flame Spray Pyrolysis—Process Design via Experimental and Computational Analysis. *AIChE Journal* **2020**, *66* (2). <https://doi.org/10.1002/aic.16885>.
- (243) Buesser, B.; Gröhn, A. J. Multiscale Aspects of Modeling Gas-Phase Nanoparticle Synthesis. *Chem. Eng. Technol.* **2012**, *35* (7), 1133–1143. <https://doi.org/10.1002/ceat.201100723>.
- (244) Kelesidis, G. A.; Goudeli, E.; Pratsinis, S. E. Flame Synthesis of Functional Nanostructured Materials and Devices: Surface Growth and Aggregation. *Proceedings of the Combustion Institute* **2017**, *36* (1), 29–50. <https://doi.org/10.1016/j.proci.2016.08.078>.
- (245) Goudeli, E.; Eggersdorfer, M. L.; Pratsinis, S. E. Aggregate Characteristics Accounting for the Evolving Fractal-like Structure during Coagulation and Sintering. *Journal of Aerosol Science* **2015**, *89*, 58–68. <https://doi.org/10.1016/j.jaerosci.2015.06.008>.
- (246) Madler, L.; Amal, R.; Teoh, W. Y. Flame Spray Pyrolysis: An Enabling Technology for Nanoparticles Design and Fabrication. *Nanoscale* **2010**, *2*, 1324–1347. <https://doi.org/10.1039/c0nr00017e>.
- (247) Strobel, R.; Pratsinis, S. E. Flame Aerosol Synthesis of Smart Nanostructured Materials. *Journal of Materials Chemistry* **2007**. <https://doi.org/10.1039/b711652g>.
- (248) Buesser, B.; Pratsinis, S. E. Design of Nanomaterial Synthesis by Aerosol Processes. *Annual Review of Chemical and Biomolecular Engineering* **2012**, *3* (1), 103–127. <https://doi.org/10.1146/annurev-chembioeng-062011-080930>.
- (249) Schulz, C.; Dreier, T.; Fikri, M.; Wiggers, H. Gas-Phase Synthesis of Functional Nanomaterials: Challenges to Kinetics, Diagnostics, and Process Development. *Proceedings of the Combustion Institute* **2019**, *37* (1), 83–108. <https://doi.org/10.1016/j.proci.2018.06.231>.
- (250) Pratsinis, S. E. Aerosol-Based Technologies in Nanoscale Manufacturing: From Functional Materials to Devices through Core Chemical Engineering. *AIChE J.* **2010**, *56* (12), 3028–3035. <https://doi.org/10.1002/aic.12478>.
- (251) Li, S.; Ren, Y.; Biswas, P.; Tse, S. D. Flame Aerosol Synthesis of Nanostructured Materials and Functional Devices: Processing, Modeling, and Diagnostics. *Progress in Energy and Combustion Science* **2016**, *55*, 1–59. <https://doi.org/10.1016/j.pecs.2016.04.002>.
- (252) Wegner, K.; Schimmöller, B.; Thiebaut, B.; Fernandez, C.; Rao, T. N. Pilot Plants for Industrial Nanoparticle Production by Flame Spray Pyrolysis. *KONA* **2011**, *29* (0), 251–265. <https://doi.org/10.14356/kona.2011025>.

- (253) Güntner, A. T.; Pineau, N. J.; Pratsinis, S. E. Flame-Made Chemoresistive Gas Sensors and Devices. *Progress in Energy and Combustion Science* **2022**, *90*, 100992. <https://doi.org/10.1016/j.pecs.2022.100992>.
- (254) Starsich, F. H. L.; Herrmann, I. K.; Pratsinis, S. E. Nanoparticles for Biomedicine: Coagulation During Synthesis and Applications. *Annu. Rev. Chem. Biomol. Eng.* **2019**, *10* (1), 155–174. <https://doi.org/10.1146/annurev-chembioeng-060718-030203>.
- (255) Pokhrel, S.; Mädler, L. Flame-Made Particles for Sensors, Catalysis, and Energy Storage Applications. *Energy Fuels* **2020**, *34* (11), 13209–13224. <https://doi.org/10.1021/acs.energyfuels.0c02220>.
- (256) Sheng, Y.; Kraft, M.; Xu, R. Emerging Applications of Nanocatalysts Synthesized by Flame Aerosol Processes. *Current Opinion in Chemical Engineering* **2018**, *20*, 39–49. <https://doi.org/10.1016/j.coche.2018.01.009>.
- (257) Tran-Phu, T.; Daiyan, R.; Ta, X. M. C.; Amal, R.; Tricoli, A. From Stochastic Self-Assembly of Nanoparticles to Nanostructured (Photo)Electrocatalysts for Renewable Power-to-X Applications via Scalable Flame Synthesis. *Adv Funct Materials* **2022**, *32* (13), 2110020. <https://doi.org/10.1002/adfm.202110020>.
- (258) Chen, H.; Mulmudi, H. K.; Tricoli, A. Flame Spray Pyrolysis for the One-Step Fabrication of Transition Metal Oxide Films: Recent Progress in Electrochemical and Photoelectrochemical Water Splitting. *Chinese Chemical Letters* **2020**, *31* (3), 601–604. <https://doi.org/10.1016/j.ccllet.2019.05.016>.
- (259) Venkatesan, S.; Mitzel, J.; Wegner, K.; Costa, R.; Gazdzicki, P.; Friedrich, K. A. Nanomaterials and Films for Polymer Electrolyte Membrane Fuel Cells and Solid Oxide Cells by Flame Spray Pyrolysis. *Renewable and Sustainable Energy Reviews* **2022**, *158*, 112080. <https://doi.org/10.1016/j.rser.2022.112080>.
- (260) Kelesidis, G. A.; Neubauer, D.; Fan, L.-S.; Lohmann, U.; Pratsinis, S. E. Enhanced Light Absorption and Radiative Forcing by Black Carbon Agglomerates. *Environ. Sci. Technol.* **2022**, *56* (12), 8610–8618. <https://doi.org/10.1021/acs.est.2c00428>.
- (261) Trivanovic, U.; Kelesidis, G. A.; Pratsinis, S. E. High-Throughput Generation of Aircraft-like Soot. *Aerosol Science and Technology* **2022**, *56* (8), 732–743. <https://doi.org/10.1080/02786826.2022.2070055>.
- (262) Fujiwara, K.; Müller, U.; Pratsinis, S. E. Pd Subnano-Clusters on TiO₂ for Solar-Light Removal of NO. *ACS Catal.* **2016**, *6* (3), 1887–1893. <https://doi.org/10.1021/acscatal.5b02685>.

- (263) Deligiannakis, Y.; Mantzanis, A.; Zindrou, A.; Smykala, S.; Solakidou, M. Control of Monomeric Vo's versus Vo Clusters in ZrO_{2-x} for Solar-Light H₂ Production from H₂O at High-Yield (Millimoles Gr⁻¹ H⁻¹). *Sci Rep* **2022**, *12* (1), 15132. <https://doi.org/10.1038/s41598-022-19382-3>.
- (264) Psathas, P.; Solakidou, M.; Mantzanis, A.; Deligiannakis, Y. Flame Spray Pyrolysis Engineering of Nanosized Mullite-Bi₂Fe₄O₉ and Perovskite-BiFeO₃ as Highly Efficient Photocatalysts for O₂ Production from H₂O Splitting. *Energies* **2021**, *14* (17), 5235. <https://doi.org/10.3390/en14175235>.
- (265) Solakidou, M.; Georgiou, Y.; Deligiannakis, Y. Double-Nozzle Flame Spray Pyrolysis as a Potent Technology to Engineer Noble Metal-TiO₂ Nanophotocatalysts for Efficient H₂ Production. *Energies* **2021**, *14* (4), 817. <https://doi.org/10.3390/en14040817>.
- (266) Moularas, C.; Psathas, P.; Deligiannakis, Y. Electron Paramagnetic Resonance Study of Photo-Induced Hole/Electron Pairs in NaTaO₃ Nanoparticles. *Chemical Physics Letters* **2021**, 782, 139031. <https://doi.org/10.1016/j.cplett.2021.139031>.
- (267) John, A. T.; Tricoli, A. Flame Assisted Synthesis of Nanostructures for Device Applications. *Advances in Physics: X* **2022**, *7* (1), 1997153. <https://doi.org/10.1080/23746149.2021.1997153>.
- (268) Stark, W. J.; Mädler, L.; Maciejewski, M.; Pratsinis, S. E.; Baiker, A. Flame Synthesis of Nanocrystalline Ceria–Zirconia: Effect of Carrier Liquid. *Chem. Commun.* **2003**, No. 5, 588–589. <https://doi.org/10.1039/b211831a>.
- (269) Lovell, E. C.; Horlyck, J.; Scott, J.; Amal, R. Flame Spray Pyrolysis-Designed Silica/Ceria-Zirconia Supports for the Carbon Dioxide Reforming of Methane. *Applied Catalysis A: General* **2017**, *546*, 47–57. <https://doi.org/10.1016/j.apcata.2017.08.002>.
- (270) Johannessen, T.; Koutsopoulos, S. One-Step Flame Synthesis of an Active Pt/TiO₂ Catalyst for SO₂ Oxidation—A Possible Alternative to Traditional Methods for Parallel Screening. *Journal of Catalysis* **2002**, *205* (2), 404–408. <https://doi.org/10.1006/jcat.2001.3447>.
- (271) Height, M. J.; Pratsinis, S. E.; Mekasuwandumrong, O.; Praserttham, P. Ag-ZnO Catalysts for UV-Photodegradation of Methylene Blue. *Applied Catalysis B: Environmental* **2006**, *63* (3–4), 305–312. <https://doi.org/10.1016/j.apcatb.2005.10.018>.
- (272) Strobel, R.; Grunwaldt, J.-D.; Camenzind, A.; Pratsinis, S. E.; Baiker, A. Flame-Made Alumina Supported Pd–Pt Nanoparticles: Structural Properties and Catalytic Behavior in Methane Combustion. *Catal Lett* **2005**, *104* (1–2), 9–16. <https://doi.org/10.1007/s10562-005-7429-y>.

- (273) Righettoni, M.; Tricoli, A.; Pratsinis, S. E. Si:WO₃ Sensors for Highly Selective Detection of Acetone for Easy Diagnosis of Diabetes by Breath Analysis. *Anal. Chem.* **2010**, *82* (9), 3581–3587. <https://doi.org/10.1021/ac902695n>.
- (274) Großmann, K.; Kovács, K. E.; Pham, D. K.; Mädler, L.; Barsan, N.; Weimar, U. Enhancing Performance of FSP SnO₂-Based Gas Sensors through Sb-Doping and Pd-Functionalization. *Sensors and Actuators B: Chemical* **2011**, *158* (1), 388–392. <https://doi.org/10.1016/j.snb.2011.06.044>.
- (275) Horlyck, J.; Lewis, S.; Amal, R.; Scott, J. The Impact of La Doping on Dry Reforming Ni-Based Catalysts Loaded on FSP-Alumina. *Top Catal* **2018**, *61* (18–19), 1842–1855. <https://doi.org/10.1007/s11244-018-1015-1>.
- (276) Horlyck, J.; Pokhrel, S.; Lovell, E.; Bedford, N. M.; Mädler, L.; Amal, R.; Scott, J. Unifying Double Flame Spray Pyrolysis with Lanthanum Doping to Restrict Cobalt–Aluminate Formation in Co/Al₂O₃ Catalysts for the Dry Reforming of Methane. *Catal. Sci. Technol.* **2019**, *9* (18), 4970–4980. <https://doi.org/10.1039/C9CY01293A>.
- (277) Grass, R. N.; Stark, W. J. Gas Phase Synthesis of Fcc-Cobalt Nanoparticles. *Journal of Materials Chemistry* **2006**, *16* (19), 1825. <https://doi.org/10.1039/b601013j>.
- (278) Grass, R. N.; Albrecht, T. F.; Krumeich, F.; Stark, W. J. Large-Scale Preparation of Ceria/Bismuth Metal-Matrix Nano-Composites with a Hardness Comparable to Steel. *J. Mater. Chem.* **2007**, *17* (15), 1485. <https://doi.org/10.1039/b614317b>.
- (279) Grass, R. N.; Stark, W. J. Flame Spray Synthesis under a Non-Oxidizing Atmosphere: Preparation of Metallic Bismuth Nanoparticles and Nanocrystalline Bulk Bismuth Metal. *J Nanopart Res* **2006**, *8* (5), 729–736. <https://doi.org/10.1007/s11051-006-9097-2>.
- (280) Athanassiou, E. K.; Grass, R. N.; Stark, W. J. Large-Scale Production of Carbon-Coated Copper Nanoparticles for Sensor Applications. *Nanotechnology* **2006**, *17* (6), 1668–1673. <https://doi.org/10.1088/0957-4484/17/6/022>.
- (281) Athanassiou, E. K.; Mensing, C.; Stark, W. J. Insulator Coated Metal Nanoparticles with a Core/Shell Geometry Exhibit a Temperature Sensitivity Similar to Advanced Spinel. *Sensors and Actuators A: Physical* **2007**, *138* (1), 120–129. <https://doi.org/10.1016/j.sna.2007.04.005>.
- (282) Luechinger, N. A.; Athanassiou, E. K.; Stark, W. J. Graphene-Stabilized Copper Nanoparticles as an Air-Stable Substitute for Silver and Gold in Low-Cost Ink-Jet Printable Electronics. *Nanotechnology* **2008**, *19* (44), 445201. <https://doi.org/10.1088/0957-4484/19/44/445201>.

- (283) Waser, O.; Büchel, R.; Hintennach, A.; Novák, P.; Pratsinis, S. E. Continuous Flame Aerosol Synthesis of Carbon-Coated Nano-LiFePO₄ for Li-Ion Batteries. *Journal of Aerosol Science* **2011**, *42* (10), 657–667. <https://doi.org/10.1016/j.jaerosci.2011.06.003>.
- (284) Athanassiou, E. K.; Grass, R. N.; Stark, W. J. Chemical Aerosol Engineering as a Novel Tool for Material Science: From Oxides to Salt and Metal Nanoparticles. *Aerosol Science and Technology* **2010**. <https://doi.org/10.1080/02786820903449665>.
- (285) Daiyan, R.; Lovell, E. C.; Bedford, N. M.; Saputera, W. H.; Wu, K. H.; Lim, S.; Horlyck, J.; Ng, Y. H.; Lu, X.; Amal, R. Modulating Activity through Defect Engineering of Tin Oxides for Electrochemical CO₂ Reduction. *Advanced Science* **2019**. <https://doi.org/10.1002/advs.201900678>.
- (286) Daiyan, R.; Lovell, E. C.; Huang, B.; Zubair, M.; Leverett, J.; Zhang, Q.; Lim, S.; Horlyck, J.; Tang, J.; Lu, X.; Kalantar-Zadeh, K.; Hart, J. N.; Bedford, N. M.; Amal, R. Uncovering Atomic-Scale Stability and Reactivity in Engineered Zinc Oxide Electrocatalysts for Controllable Syngas Production. *Adv. Energy Mater.* **2020**, *10* (28), 2001381. <https://doi.org/10.1002/aenm.202001381>.
- (287) Gunawan, C.; Lord, M. S.; Lovell, E.; Wong, R. J.; Jung, M. S.; Oscar, D.; Mann, R.; Amal, R. Oxygen-Vacancy Engineering of Cerium-Oxide Nanoparticles for Antioxidant Activity. *ACS Omega* **2019**, *4* (5), 9473–9479. <https://doi.org/10.1021/acsomega.9b00521>.
- (288) Saputera, W. H.; Tahini, H. A.; Sabsabi, M.; Tan, T. H.; Bedford, N. M.; Lovell, E.; Cui, Y.; Hart, J. N.; Friedmann, D.; Smith, S. C.; Amal, R.; Scott, J. Light-Induced Synergistic Multidefect Sites on TiO₂/SiO₂ Composites for Catalytic Dehydrogenation. *ACS Catal.* **2019**, *9* (3), 2674–2684. <https://doi.org/10.1021/acscatal.8b04891>.
- (289) Kho, Y. K.; Teoh, W. Y.; Iwase, A.; Mädler, L.; Kudo, A.; Amal, R. Flame Preparation of Visible-Light-Responsive BiVO₄ Oxygen Evolution Photocatalysts with Subsequent Activation via Aqueous Route. *ACS Appl. Mater. Interfaces* **2011**, *3* (6), 1997–2004. <https://doi.org/10.1021/am200247y>.
- (290) Angel, S.; Schneider, F.; Apazeller, S.; Kaziur-Cegla, W.; Schmidt, T. C.; Schulz, C.; Wiggers, H. Spray-Flame Synthesis of LaMO₃ (M = Mn, Fe, Co) Perovskite Nanomaterials: Effect of Spray Droplet Size and Esterification on Particle Size Distribution. *Proceedings of the Combustion Institute* **2021**, *38* (1), 1279–1287. <https://doi.org/10.1016/j.proci.2020.07.116>.
- (291) Alkan, B.; Medina, D.; Landers, J.; Heidelmann, M.; Hagemann, U.; Salamon, S.; Andronescu, C.; Wende, H.; Schulz, C.; Schuhmann, W.; Wiggers, H. Spray-Flame-Prepared LaCo_{1-x}Fe_xO₃ Perovskite Nanoparticles as Active OER Catalysts: Influence

- of Fe Content and Low-Temperature Heating. *ChemElectroChem* **2020**, *7* (12), 2564–2574. <https://doi.org/10.1002/celec.201902051>.
- (292) Gockeln, M.; Ruiter, T.; Palacios Saura, A.; Baric, V.; Glenneberg, J.; Busse, M.; Pokhrel, S.; Kun, R.; Mädler, L. Enhancing the Utilization of Porous $\text{Li}_4\text{Ti}_5\text{O}_{12}$ Layers for Thin-Film Lithium-Ion Batteries. *ACS Appl. Energy Mater.* **2020**, *3* (10), 9667–9675. <https://doi.org/10.1021/acsaem.0c01231>.
- (293) Meierhofer, F.; Li, H.; Gockeln, M.; Kun, R.; Grieb, T.; Rosenauer, A.; Fritsching, U.; Kiefer, J.; Birkenstock, J.; Mädler, L.; Pokhrel, S. Screening Precursor–Solvent Combinations for $\text{Li}_4\text{Ti}_5\text{O}_{12}$ Energy Storage Material Using Flame Spray Pyrolysis. *ACS Appl. Mater. Interfaces* **2017**, *9* (43), 37760–37777. <https://doi.org/10.1021/acsami.7b11435>.
- (294) Abe, Y.; Laine, R. M. Photocatalytic Plate-like $\text{La}_2\text{Ti}_2\text{O}_7$ Nanoparticles Synthesized via Liquid-feed Flame Spray Pyrolysis (LF-FSP) of Metallo-organic Precursors. *J Am Ceram Soc* **2020**, *103* (9), 4832–4839. <https://doi.org/10.1111/jace.17196>.
- (295) Kemmler, J. A.; Pokhrel, S.; Birkenstock, J.; Schowalter, M.; Rosenauer, A.; Bârsan, N.; Weimar, U.; Mädler, L. Quenched, Nanocrystalline $\text{In}_4\text{Sn}_3\text{O}_{12}$ High Temperature Phase for Gas Sensing Applications. *Sensors and Actuators B: Chemical* **2012**, *161* (1), 740–747. <https://doi.org/10.1016/j.snb.2011.11.026>.
- (296) Psathas, P.; Georgiou, Y.; Moularas, C.; Armatas, G. S.; Deligiannakis, Y. Controlled-Phase Synthesis of $\text{Bi}_2\text{Fe}_4\text{O}_9$ & BiFeO_3 by Flame Spray Pyrolysis and Their Evaluation as Non-Noble Metal Catalysts for Efficient Reduction of 4-Nitrophenol. *Powder Technology* **2020**. <https://doi.org/10.1016/j.powtec.2020.04.059>.
- (297) Strobel, R.; Mädler, L.; Piacentini, M.; Maciejewski, M.; Baiker, A.; Pratsinis, S. E. Two-Nozzle Flame Synthesis of $\text{Pt/Ba/Al}_2\text{O}_3$ for NO_x Storage. *Chemistry of Materials* **2006**, *18* (10), 2532–2537. <https://doi.org/10.1021/cm0600529>.
- (298) Grossmann, H. K.; Grieb, T.; Meierhofer, F.; Hodapp, M. J.; Noriler, D.; Gröhn, A.; Meier, H. F.; Fritsching, U.; Wegner, K.; Mädler, L. Nanoscale Mixing during Double-Flame Spray Synthesis of Heterostructured Nanoparticles. *J Nanopart Res* **2015**, *17* (4), 174. <https://doi.org/10.1007/s11051-015-2975-8>.
- (299) Lovell, E. C.; Großman, H.; Horlyck, J.; Scott, J.; Mädler, L.; Amal, R. Asymmetrical Double Flame Spray Pyrolysis-Designed $\text{SiO}_2/\text{Ce}_0.7\text{Zr}_0.3\text{O}_2$ for the Dry Reforming of Methane. *ACS Applied Materials and Interfaces* **2019**, *11* (29). <https://doi.org/10.1021/acsami.9b02572>.

- (300) Henning, D. F.; Merkl, P.; Yun, C.; Iovino, F.; Xie, L.; Mouzourakis, E.; Moularas, C.; Deligiannakis, Y.; Henriques-Normark, B.; Leifer, K.; Sotiriou, G. A. Luminescent CeO₂:Eu³⁺ Nanocrystals for Robust in Situ H₂O₂ Real-Time Detection in Bacterial Cell Cultures. *Biosensors and Bioelectronics* **2019**, *132*, 286–293. <https://doi.org/10.1016/j.bios.2019.03.012>.
- (301) Teleki, A.; Heine, M.; Krumeich, F.; Akhtar, K.; Pratsinis, S. In Situ Coating of Flame-Made TiO₂ Particles with Nanothin SiO₂ Films. *Langmuir* **2008**, 12553–12558. <https://doi.org/10.1021/la801630z>.
- (302) Teleki, A.; Akhtar, M. K.; Pratsinis, S. E. The Quality of SiO₂-Coatings on Flame-Made TiO₂-Based Nanoparticles. *Journal of Materials Chemistry* **2008**, *18* (30), 3547. <https://doi.org/10.1039/b803039a>.
- (303) Teleki, A.; Buesser, B.; Heine, M. C.; Krumeich, F.; Akhtar, M. K.; Pratsinis, S. E. Role of Gas–Aerosol Mixing during in Situ Coating of Flame-Made Titania Particles. *Ind. Eng. Chem. Res.* **2009**, *48* (1), 85–92. <https://doi.org/10.1021/ie800226d>.
- (304) Tricoli, A.; Graf, M.; Mayer, F.; Kuühne, S.; Hierlemann, A.; Pratsinis, S. E. Micropatterning Layers by Flame Aerosol Deposition-Annealing. *Adv. Mater.* **2008**, *20* (16), 3005–3010. <https://doi.org/10.1002/adma.200701844>.
- (305) Tricoli, A.; Elmøe, T. D. Flame Spray Pyrolysis Synthesis and Aerosol Deposition of Nanoparticle Films. *AIChE J.* **2012**, *58* (11), 3578–3588. <https://doi.org/10.1002/aic.13739>.
- (306) Tricoli, A.; Nasiri, N.; Chen, H.; Wallerand, A. S.; Righettoni, M. Ultra-Rapid Synthesis of Highly Porous and Robust Hierarchical ZnO Films for Dye Sensitized Solar Cells. *Solar Energy* **2016**, *136*, 553–559. <https://doi.org/10.1016/j.solener.2016.07.024>.
- (307) Chen, H.; Bo, R.; Tran-Phu, T.; Liu, G.; Tricoli, A. One-Step Rapid and Scalable Flame Synthesis of Efficient WO₃ Photoanodes for Water Splitting. *ChemPlusChem* **2018**, *83* (7), 569–576. <https://doi.org/10.1002/cplu.201800061>.
- (308) Tran-Phu, T.; Chen, H.; Bo, R.; Di Bernardo, I.; Fusco, Z.; Simonov, A. N.; Tricoli, A. High-Temperature One-Step Synthesis of Efficient Nanostructured Bismuth Vanadate Photoanodes for Water Oxidation. *Energy Technol.* **2019**, 1801052. <https://doi.org/10.1002/ente.201801052>.
- (309) Riad, K. B.; Hoa, S. V.; Wood-Adams, P. M. Metal Oxide Quantum Dots Embedded in Silica Matrices Made by Flame Spray Pyrolysis. *ACS Omega* **2021**, *6* (17), 11411–11417. <https://doi.org/10.1021/acsomega.0c06227>.

- (310) Balakrishnan, A.; Groeneveld, J. D.; Pokhrel, S.; Mädler, L. Metal Sulfide Nanoparticles: Precursor Chemistry. *Chem. Eur. J.* **2021**, *27* (21), 6390–6406. <https://doi.org/10.1002/chem.202004952>.
- (311) Li, H.; Pokhrel, S.; Schowalter, M.; Rosenauer, A.; Kiefer, J.; Mädler, L. The Gas-Phase Formation of Tin Dioxide Nanoparticles in Single Droplet Combustion and Flame Spray Pyrolysis. *Combustion and Flame* **2020**, *215*, 389–400. <https://doi.org/10.1016/j.combustflame.2020.02.004>.
- (312) Li, H.; Rosebrock, C. D.; Wu, Y.; Wriedt, T.; Mädler, L. Single Droplet Combustion of Precursor/Solvent Solutions for Nanoparticle Production: Optical Diagnostics on Single Isolated Burning Droplets with Micro-Explosions. *Proceedings of the Combustion Institute* **2019**, *37* (1), 1203–1211. <https://doi.org/10.1016/j.proci.2018.06.133>.
- (313) Merkl, P.; Long, S.; McInerney, G. M.; Sotiriou, G. A. Antiviral Activity of Silver, Copper Oxide and Zinc Oxide Nanoparticle Coatings against SARS-CoV-2. *Nanomaterials* **2021**, *11* (5), 1312. <https://doi.org/10.3390/nano11051312>.
- (314) Ziesmer, J.; Sondén, I.; Thersleff, T.; Sotiriou, G. A. Highly Efficient Near-IR Photothermal Microneedles with Flame-Made Plasmonic Nanoaggregates for Reduced Intradermal Nanoparticle Deposition. *Adv Materials Inter* **2022**, 2201540. <https://doi.org/10.1002/admi.202201540>.
- (315) Belles, L.; Moularas, C.; Smykała, S.; Deligiannakis, Y. Flame Spray Pyrolysis Co₃O₄/CoO as Highly-Efficient Nanocatalyst for Oxygen Reduction Reaction. *Nanomaterials* **2021**, *11* (4), 925. <https://doi.org/10.3390/nano11040925>.
- (316) Scheibel, H. G.; Porstendorfer, J. Generation of Monodisperse Ag- and NaCl-Aerosols with Particle Diameters between 2 and 300 Nm. *Journal of Aerosol Science* **1983**, *14* (2), 113–126. [https://doi.org/10.1016/0021-8502\(83\)90035-6](https://doi.org/10.1016/0021-8502(83)90035-6).
- (317) Hannemann, S.; Grunwaldt, J.-D.; Krumeich, F.; Kappen, P.; Baiker, A. Electron Microscopy and EXAFS Studies on Oxide-Supported Gold–Silver Nanoparticles Prepared by Flame Spray Pyrolysis. *Applied Surface Science* **2006**, *252* (22), 7862–7873. <https://doi.org/10.1016/j.apsusc.2005.09.065>.
- (318) Sotiriou, G.; Blattmann, C. O.; Pratsinis, S. Composite Nanosilver Structures Suitable for Plasmonic Biosensors. *Materials Research Society* **2012**, 1416.
- (319) Sotiriou, G.; Pratsinis, S. Engineering Nanosilver as an Antibacterial, Biosensor and Bioimaging Material. *Elsevier* **2011**, *1*, 3–10.
- (320) Sotiriou, G.; Gass, S.; Pratsinis, S. Hermetically Coated Nanosilver: No Ag⁺ Ion Leaching. *Materials Research Society* **2012**, 1386.

- (321) Sotiriou, G.; Sannomiya, T.; Teleki, A.; Krumeich, F.; Pratsinis, S. Non-Toxic Dry-Coated Nanosilver for Plasmonic Biosensors. *ADVANCED MATERIALS* **2010**.
- (322) Sotiriou, G. A.; Starsich, F.; Dasargyri, A.; Wurnig, M. C.; Krumeich, F.; Boss, A.; Leroux, J.-C.; Pratsinis, S. E. Photothermal Killing of Cancer Cells by the Controlled Plasmonic Coupling of Silica-Coated Au/Fe₂O₃ Nanoaggregates. *Advanced Functional Materials* **2014**, *24* (19), 2818–2827. <https://doi.org/10.1002/adfm.201303416>.
- (323) Merkl, P.; Zhou, S.; Zaganiaris, A.; Shahata, M.; Eleftheraki, A.; Thersleff, T.; Sotiriou, G. A. Plasmonic Coupling in Silver Nanoparticle Aggregates and Their Polymer Composite Films for Near - Infrared Photothermal Biofilm Eradication. *ACS Appl. Nano Mater.* **2021**, *4* (5), 5330–5339. <https://doi.org/10.1021/acsnm.1c00668>.
- (324) Li, H.; Merkl, P.; Sommertune, J.; Thersleff, T.; Sotiriou, G. A. SERS Hotspot Engineering by Aerosol Self-Assembly of Plasmonic Ag Nanoaggregates with Tunable Interparticle Distance. *Advanced Science* **2022**, *9* (22), 2201133. <https://doi.org/10.1002/advs.202201133>.
- (325) Tran-Phu, T.; Daiyan, R.; Fusco, Z.; Ma, Z.; Rahim, L. R. A.; Kiy, A.; Kluth, P.; Guo, X.; Zhu, Y.; Chen, H.; Amal, R.; Tricoli, A. Multifunctional Nanostructures of Au–Bi₂O₃ Fractals for CO₂ Reduction and Optical Sensing. *J. Mater. Chem. A* **2020**, *8* (22), 11233–11245. <https://doi.org/10.1039/D0TA01723J>.

Chapter 2

Experimental Methods

2.1 Flame Spray Pyrolysis (FSP) Apparatus

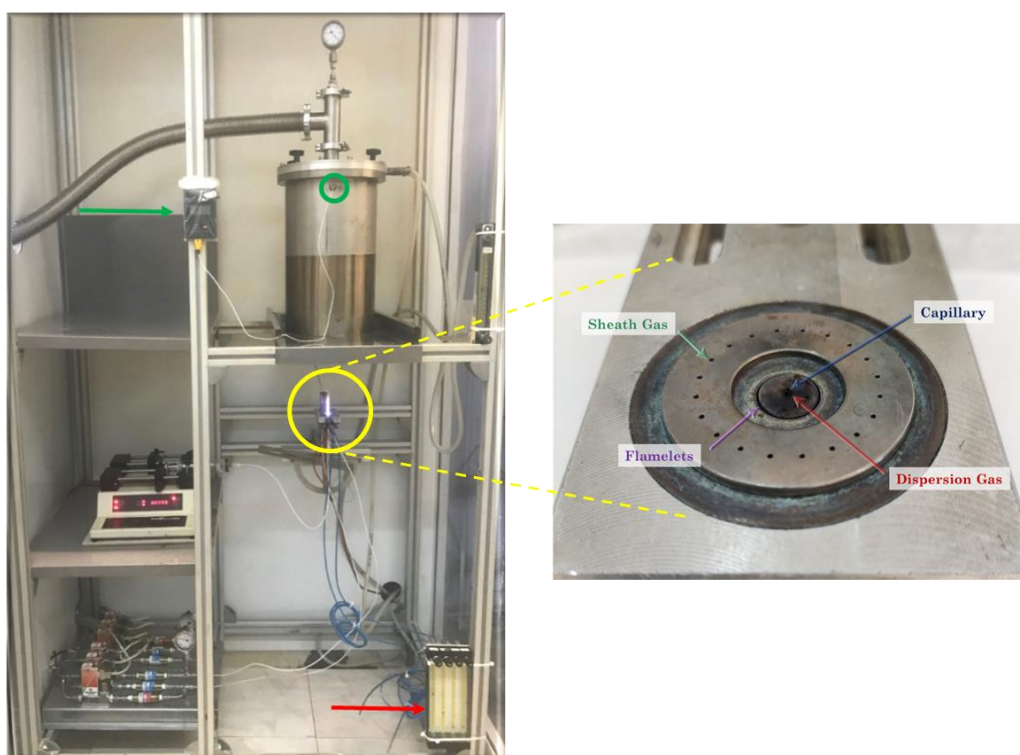


Figure 2.27. (left) The FSP apparatus in Lab of Physical Chemistry and Environment, consisting of a water-cooled, pressure-assisted burner, a collection system, a syringe pump and the flow rate regulators. (right) A magnified image of the pressure-assisted nozzle.

The FSP apparatus used in the present study is installed in the Nanomaterials' Lab (Physics Department, University of Ioannina), presented in Figure 2.1. Specifically, an enlarged image of the FSP burner configuration is also shown in Figure 2.1. The aerosol

formation is accomplished using a gas-assisted atomizer. The precursor fuel is channeled into the flame through a capillary tube (ID 0.5 mm, OD 0.6 mm), in the middle of the atomizer, thus creating an annular gap, in which oxygen gas acts as the dispersion gas. Dispersion gas promotes the precursor fuel's atomization, thus the aerosol formation. The initial ignition is accomplished by a pre-mixed O_2/CH_4 gas flowing through the annuli surrounding the atomizer, as depicted in Figure 2.1. Additional O_2 supply through the holes, acts as the sheath gas, controlling and stabilizing the combustion process and the particle flight. The gas pressure drop across the nozzle tip at the burner was kept constant at 1.5 bar by modifying the nozzle-gap. The particles are collected as product powder in a glass-fiber filter (Albet) with the aid of a vacuum pump (Busch).

2.2 Synthesis of Flame-made Plasmonic Nanomaterials

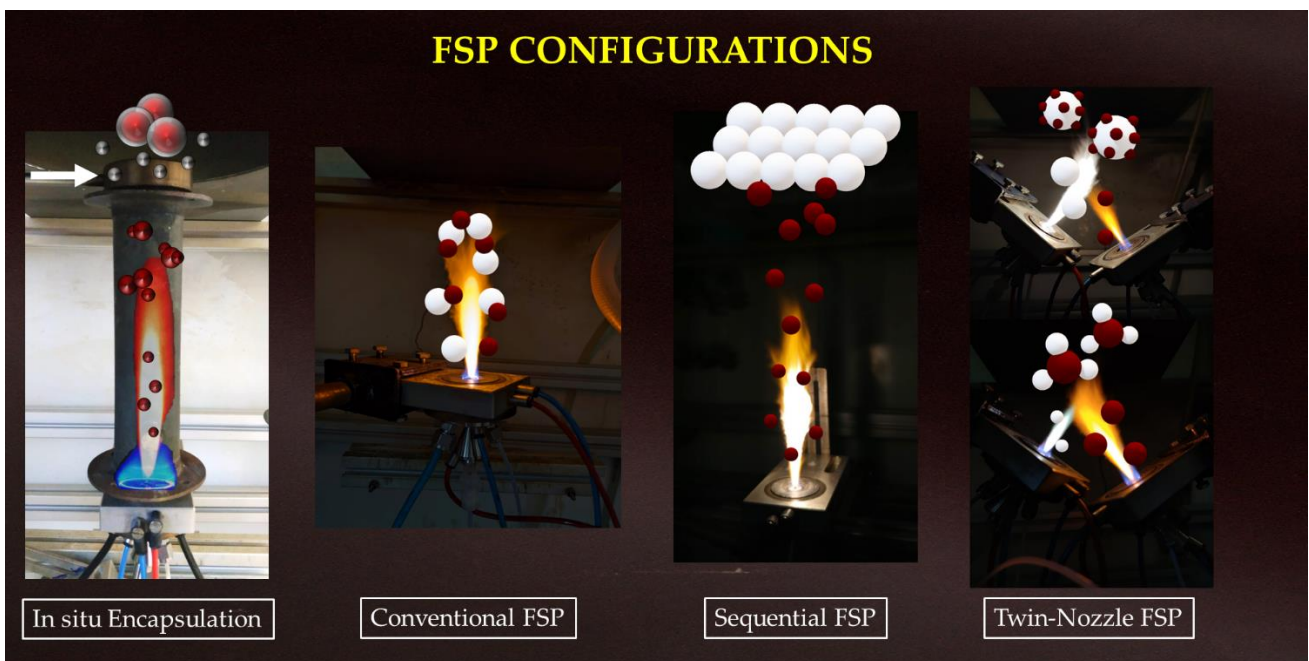


Figure 2.28. The FSP Configurations employed in this thesis. The single-step formation of core@shell nanostructures, the single- and double-nozzle set-up and the sequential deposition of particles on already formed and collected nano-oxides.

In the present thesis, the plasmonic metal of choice, Ag, was integrated in various configurations of heterostructures. Specially, employing FSP, these particle morphologies are manufactured: (i) core@shell $Ag@SiO_2$ nanoaggregates of adjustable SiO_2 shell thickness and Ag particle size, (ii) black $Ag/TiO_x/TiO_2$ nanocomposites and (iii) $Ag/NaTaO_3$ heterostructures.

2.2.1 Single-step Synthesis of Core@Shell Ag@SiO₂ Nanoaggregates

Synthesis of Ag core particles: The precursor solution was prepared by dissolving silver acetate (Sigma-Aldrich, purity > 99%) in 2-ethylhexanoic acid (EHA) and acetonitrile (ACN) (both Sigma-Aldrich, purity > 97%), at volume ratio 1:1, varying concentrations 0.4–0.5 M. Then, the solution was fed through a capillary at precursor feed rate of 5–7 mL min⁻¹ into the flame and atomized into fine droplets by 5 L min⁻¹ dispersed O₂ gas (Linde, purity > 99%). Pressure drop across the nozzle tip was maintained at 1.5 bar. A supporting O₂/CH₄ (5 L min⁻¹, 2.5 L min⁻¹) pilot flame ignites the droplets, initiates combustion, and supports the spray flame. The high temperature inside the flame field triggers the metal vapor to form nuclei through the gas-to-particle formation.^{1,2} Particle coalescence, sintering and agglomeration result in the final powder collected using a vacuum pump (Busch V40) on glass microfiber filters (Albet). Nanoparticles were collected by scraping of the powder from the filter.

Synthesis of core@shell Ag@SiO₂: The *in situ* SiO₂ encapsulation of Ag NPs was engineered in an enclosed FSP reactor, originally described by

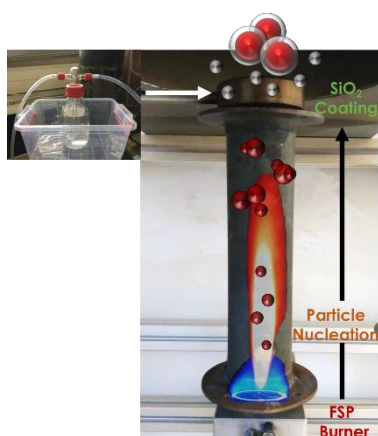


Figure 2.30. Enclosed FSP Reactor consisted of a metallic tube and a coating ring placed above the tube.

Sotiriou *et al.*^{3,4}, as depicted in Figure 2.3. In our study, the desired SiO₂ shell thickness was adjusted in the range of 1 to 5

nm. Specifically, the flame was enclosed by a metallic tube (9 cm diameter, 20 cm height), to prolong the high temperature residence time and thus control the particle size and crystallinity. A toroidal ring, equipped with 16 equidistant holes, 500 μm diameter, was placed above the metallic tube, and used to radially spray the SiO₂ precursor vapor on the Ag

particles. 0.5–3 L min⁻¹ N₂ was used as carrier gas (Linde, purity > 99%) bubbled through hexamethyldisiloxane (HMDSO, Aldrich, purity 98%), fixed at 10 °C, as shown in Figure 2.3. The N₂-HMDSO stream was injected into the particle in-flight trajectory, along with an additional N₂ stream used to enforce the radial convection of the HMDSO vapor, according to the methodology developed by Teleki *et al.*^{5,6} As a reference, co-agglomerated Ag/SiO₂ materials were prepared in a single-nozzle FSP reactor by spraying a mixture of silver acetate/HMDSO. The FSP parameters and characteristics of the Ag@SiO₂ materials are listed in Table 2.1.



Figure 2.29. Ag@SiO₂ core@shell nanoaggregates varying shell thickness.

Table 1. Characteristics of Ag⁰@SiO₂ NPs.

Material*	wt% SiO₂	SiO₂-Shell Thickness (nm)	SSA (m²/g)	d_{XRD} (nm)	Particle diameter** d_{TEM} (nm)
1-15	10	1±0.5	29±3	14±0.5	15±3.5
3-15	20	3±1.0	62±5	15±0.5	15±3.5
5-15	25	5±1.0	61±5	15±0.5	14±4.0
1-25	8	1±0.5	25±3	25±1.0	25±3.5
3-25	20	3±1.0	51±5	24±1.0	25±3.0
5-25	27	5±1.0	56±5	24±1.0	24±5.0

*The naming of each material is as follows: [SiO₂-Thickness]-[Ag-Size], i.e. the first number indicates the SiO₂ thickness, while the second number refers to the Ag⁰ core particle diameter in nm.

**The size distribution and the shell thickness are estimated by TEM images using ImageJ.

2.2.2. Synthesis of Flame-made Visible-light Active Black Ag/TiO₂

Ag/TiO₂@TiO_x heterostructures have been prepared by flame spray pyrolysis using either a single or a dual nozzle configuration shown in Figure 2.2. Precursor molarity, precursor fuel feed rate to dispersion gas rate (P/D ratio) and the internozzle distance was adjusted accordingly so that the desired properties of each element can be controlled independently. The detailed parameters are demonstrated in Table 2.2. Specifically, titanium iso-propoxide (TTIP, Sigma Aldrich) and silver acetate (sigma aldrich, >99%) were dissolved in ethylhexanoic acid/acetonitrile (1:1) for the case of the single flame or dissolved in mixtures of xylene/acetonitrile (2.2:1) and ethylhexanoic acid/acetonitrile (1:1) respectively for the case of the dual flames. A O₂/CH₄ premixed gas (3.2/1.5 L min⁻¹, Linde >99.9%) provided the supporting flame and the initial ignition. The powder product was collected, using a vacuum pump (Busch V40), on a glass microfiber filter (Albet) placed 66 cm above the flame mixing point. In sequential FSP, the Ag precursor was fed to the flame after the already formed TiO₂ particles have been collected and the Ag particles deposition takes place in cooler temperature gradients outside the hotter flame zone.

Table 2.2. FSP parameters and particle characteristics of Ag/TiO₂ heterostructures.

¹ XAg/YTiO ₂	Molarity (M)	P/D ratio	d _{XRD} Ag (nm)	d _{XRD} TiO ₂ (nm) ²	TiO _x Mass Fraction (%)	SSA (m ² /g) ³	Ti ₃₊ /Ti ₄₊ ⁴
18TiO ₂	0.6	5/5	-	18	0	100	0
SN-20Ag/18TiO ₂	0.6	7/5	6	5	18	83	0.33
SN-50Ag/18TiO ₂	0.6	7/5	5	5	20	62	0.42
SEQ-50Ag/18TiO ₂	0.6	7/5	28	18	0	85	0.11
SN-50Ag/11TiO ₂	0.16	7/5	4	18	20	127	0.4

¹ XAg/YTiO₂: X denotes for Ag content and Y for TiO₂ particle size respectively. ² derived by Scherrer equation for the Anatase peak. ³ calculated by BET analysis. ⁴ derived by XPS measurements.

2.2.2 Synthesis of NaTaO₃ and Ag/NaTaO₃

Synthesis of NaTaO₃ by Flame Spray Pyrolysis: The nanoparticles were produced in a single-nozzle enclosed FSP reactor, as described previously.⁷ The precursor solution contained Tantalum(V) chloride (anhydrous 99.9%, STREM) and sodium 2-ethylhexanoate (98%, TCI) of molar ratio 1:1, dissolved in ethanol. The FSP parameters comprised of a dispersion oxygen flow rate of 5 L/min (Linde 99%) and a precursor flow rate of 5 mL/min. To control the particle size, the low molarity of 60mM for 14 nm particles was used and a high concentration of 240mM for the 26nm particles. The flame was enclosed by a quartz tube of 20 cm height. The produced particles were deposited on a glass microfibre filter with a binder (Albet Labsience), assisted by a vacuum pump (BUSCH) and collected by scraping of the powder. The nanomaterials were stored in glass vials under an inert Argon atmosphere, until use.

Synthesis of Ag/NaTaO₃ by Flame Spray Pyrolysis: Ag/NaTaO₃ heterostructures have been

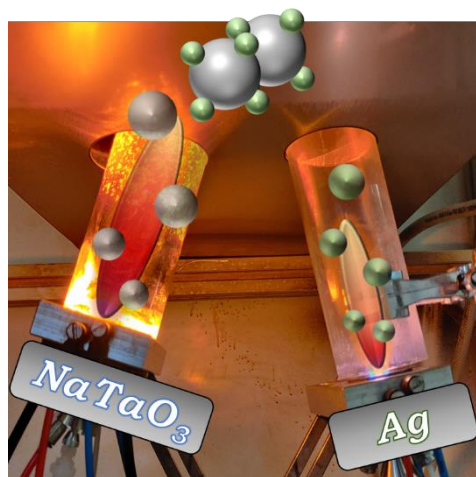


Figure 2.31. Double-nozzle FSP configuration for the synthesis of Ag/NaTaO₃.

prepared by flame spray pyrolysis using a dual nozzle configuration shown in Figure 2.2 and described in previous work. Precursor molarity, fuel feed rate to dispersion gas rate (P/D ratio) and the internozzle distance was adjusted accordingly so that the desired particle size of each element can be controlled independently. For the NaTaO₃ case, the setup parameters are described above, while for Ag, silver acetate (sigma aldrich, >99%) was dissolved in acid/acetonitrile (1:1). The detailed parameters are demonstrated in Table 2.3. The powder product was collected 66 cm above the flame mixing point.

Table 2.3. FSP parameters of Ag/NaTaO₃ heterostructures.

#	FSP Parameters				NaTaO ₃ d _{XRD} (nm)	Energy Gap E _g (eV)
	Na+Ta Molarity	%wt Ag	Flame #1 P/D	Flame #2 P/D		
13NTO	0.2	0	5/5	-	13	3.95
2Ag/13NTO	0.2	2	5/5	5/5	12	3.95
20Ag/13NTO	0.2	20	5/5	3/5	12	4.1
20NTO	0.6	0	7/5	-	18	4
2Ag/20NTO	0.6	2	7/5	5/5	20	4.05
20Ag/20NTO	0.6	20	7/5	3/5	20	3.96

2.3 Electron Paramagnetic Resonance (EPR) Spectroscopy

2.3.1 Fundamentals Principles

The electron possesses an intrinsic angular momentum, the spin. Electron is a spin $S=1/2$ particle and in the quantum mechanical description the electron spin can be in two states $m_s = +1/2$ and $m_s = -1/2$. These two states, which are the projection of the electron spin, differ only in the orientation of the angular momentum in space and not in the magnitude. Postulate of quantum mechanics states that definite components of the spin can be determined only in a specific axis. This means that the two spin states can be in only one axis usually around z-axis. At the absence of interactions between the electron spin with its environment, any choice for the direction in space of the z-axis is allowed. The electrons spin randomly, and the two states have the same energy; they are degenerate.

The electron spin angular momentum is associated with the magnetic moment by the formula:

$$\boldsymbol{\mu}_e = g\mu_B\mathbf{S} \quad (2.1)$$

where μ_B is Bohr's magneton and g is the Lande factor or simply the g-factor. The energy of a magnetic moment when a constant magnetic field is applied is given by the scalar product between the magnetic moment $\boldsymbol{\mu}_e$ and the magnetic field \mathbf{B} . Spin comes along the z-axis as discussed earlier and therefore the scalar product reduces to a single term if the magnetic field is applied into z-direction. This reads as:

$$E = -\boldsymbol{\mu}_e \cdot \mathbf{B} = g|\mu_B|\mathbf{S} \cdot \mathbf{B} = g|\mu_B|B_0S_z \quad (2.2)$$

Since spin (S_z) has two states $m_s = +1/2$ and $m_s = -1/2$ by substituting in eq. 2.2 we take the following expression:

$$E_{\pm} = \pm \left(\frac{1}{2}\right) g|\mu_B|B_0 \quad (2.3)$$

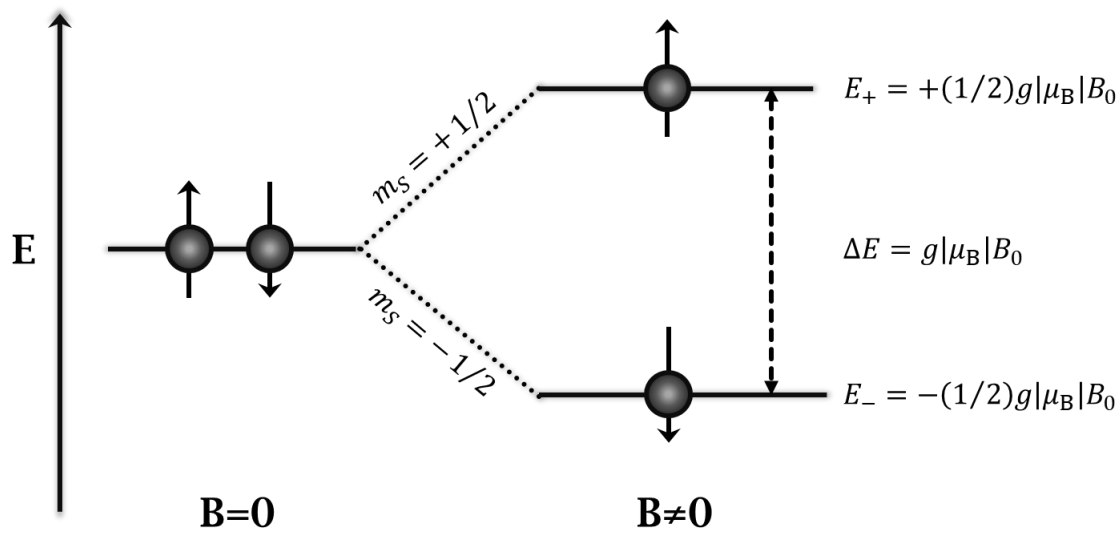


Figure 2.32. The Zeeman effect. At zero field ($B=0$) the spin states have the same energy. Application of static magnetic field ($B \neq 0$) leads to separation of the two states one with high energy when the magnetic moment is aligned with the magnetic field and one with low energy when the magnetic moment is aligned against the magnetic field.

The splitting of the electron spin energy levels into two levels in the presence of magnetic field is called the Zeeman effect⁸. The energy difference between the two states is⁹:

$$\Delta E = h\nu = g|\mu_B|B_0\Delta m_S = g|\mu_B|B_0 \quad (2.4)$$

It is apparent from eq. 2.4 that without a magnetic field there is no energy difference to measure. Another thing to mention is that the energy difference depends linearly on the magnetic field.

There are two different ways to obtain an EPR spectrum. We could either keep the frequency of the electromagnetic radiation constant and scan the magnetic field or we can keep the value of the magnetic field fixed and scan the frequency. Most EPR spectrometers operate at a constant frequency in the range of microwaves and scan the magnetic field. Absorption of energy occurs when the magnetic field “tunes” the spin states so that the energy difference matches the energy of the applied radiation. The spectrum is plotted as the first derivative of the absorption versus the magnetic field.

The parameter used as a fingerprint for each molecule would be the g-factor since it's the only factor that can remain constant at different frequencies and magnetic fields. It helps distinguish and identify types of samples. A useful expression is the following:

$$g = \frac{h\nu}{\mu_B B_0} = 714.5 \frac{\nu(\text{Ghz})}{B_0(\text{Gauss})} \quad (2.5)$$

Zero field splitting (ZFS) describes various interactions of the energy levels of a molecule or ion resulting from the presence of more than one unpaired electron. In quantum mechanics, an energy level is called degenerate if it corresponds to two or more different measurable states of a quantum system. In the presence of a magnetic field, the Zeeman effect is well known to split degenerate states. In quantum mechanics terminology, the degeneracy is said to be lifted by the presence of the magnetic field. In the presence of more than one unpaired electron, the electrons mutually interact to give rise to two or more energy states. Zero field splitting refers to this lifting of degeneracy even in the absence of a magnetic field. ZFS is responsible for many effects related to the magnetic properties of materials, as manifested in their electron spin resonance spectra and magnetism.

The classic case for ZFS is the spin triplet, i.e., the $S = 1$ spin system. In the presence of a magnetic field, the levels with different values of magnetic spin quantum number ($M_S = 0, \pm 1$) are separated and the Zeeman splitting dictates their separation. In the absence of magnetic field, the 3 levels of the triplet are isoenergetic to the first order. However, when the effects of

inter-electron repulsions are considered, the energy of the three sublevels of the triplet can be seen as being separated. This effect is thus an example of ZFS. The degree of separation depends on the symmetry of the system. The corresponding Hamiltonian can be written as

$$\hat{H} = D \left(S_z^2 - \frac{1}{3} S(S+1) \right) + E (S_x^2 - S_y^2), \quad (2.6)$$

where S is the total spin quantum number, $S_{x,y,z}$ and are the spin matrices. The value of the ZFS parameter is usually defined via D and E second-order parameters. D describes the axial component of the magnetic dipole–dipole interaction, and E the transversal component. In the next subsection, utilizing EasySpin, a MATLAB toolbox, our goal is to simulate EPR spectra controlling these E and D parameters in order to obtain the spins of a quantifiable EPR signal.

2.3.2 Quantitative EPR

It is possible to determine the number of spins in a sample without the concurrent measurement of a reference sample. In this case, the double integrated intensity of the experimental spectrum and a software calculation are used to measure the number of spins. The area under the *absorption spectrum* of an EPR signal is, just as in optical spectroscopy, a direct measure for the concentration of unpaired electrons. Unlike electronic absorption spectroscopy, however, there is no extinction coefficient in EPR spectrometry. To correlate the intensity of the EPR signal with a concentration, a standard is needed. Different standards can be used. For an example, if an EPR signal presents a radical at $g = 2$ and $B_0 = 3390$ G, we need a 1/2–spin system standard (e.g. copper nitrate) in order to quantify this signal. By comparing the spin concentration of the copper standard with the spin concentration of the signal of interest the concentration of that signal can be determined. To be able to make a comparison between the EPR signal of interest and a standard it is important that the spectra to be compared are obtained under the same conditions.

The recorded EPR spectra are *first derivatives* of the normal absorption spectra. Since an EPR spectrum is a first derivative, we have to integrate twice to obtain the intensity, i.e. the area under the absorption spectrum. The equation describing the double integral of an experimental EPR spectrum and how it relates to the number of spins in the sample is given by⁹

$$DI = c [G_R C_t n] \left(\frac{\sqrt{P} B_m Q^{n_B} S(S+1) n_S}{f(B_1, B_m)} \right) \propto S(S+1), \quad (2.7)$$

where c is a constant input to the software from a sample with known number of spins, G_R the receiver gain, C_t the conversion time, n is the number of scans, P the microwave power in W, B_m the modulation amplitude in Gauss, Q is the quality factor of resonator, n_B the Boltzmann factor for temperature dependence, S with n_S are the total electron spin and the number of spins, respectively, and $f(B_1, B_m)$ is the spatial distribution of the microwave field and the modulation field experienced by the sample. Once these values are input to the software's spin quantitation parameter file, the double integration of the experimental EPR spectrum is all that is needed to directly calculate the number of spins in a sample. Equation 3.22 shows the various parameters that will affect the double integrated amplitude of an experimental EPR spectrum. The most essential aspect of eq. 2.7 is that double integrated area of an EPR spectrum is proportional to its spin system as, $DI \propto S(S + 1)$, which as the ratio of two different spin systems will later be applied to this thesis as a corrective spin coefficient.

Some spectra are inherently difficult to integrate, because they do not meet the ideal case of isolated peaks with well-defined flat baselines on either side of the EPR spectrum. If the signal-to-noise is very low, if there is an overlapping spectrum from other species, or the background is large and unavoidable, it may be the best to integrate a computer simulated spectrum by fitting the experimental data. It is important to use a blank tube, since the quartz walls of the EPR tubes concentrate the field lines in the sample and a slightly different spectrum will be obtained when just the cavity without a sample inside is measured. Therefore, the final EPR spectrum is the subtraction of the obtained EPR spectrum from its blank tube spectrum.

In Figure 2.7, an example of Cr(V) EPR simulated spectrum with its double integrated area are presented. The simulation was carried out by EasySpin, a MATLAB toolbox, which will be described thoroughly in the next subsection. The double integration of the simulated EPR spectrum was done with the help of OriginPro software. Once the area is obtained by the double integration of the spectrum, the area value can be substituted to a calibration equation which governs the given spin system, in order to calculate the unknown concentration of Cr(V). For this case, EPR Cr(V) species is described by a spin system of 1/2, therefore a calibration of 1/2 spin standard is required, like copper nitrate, $\text{Cu}(\text{NO}_3)_2$. The above methodology concerning the Cr species will be discussed in detail in the chapter 5.

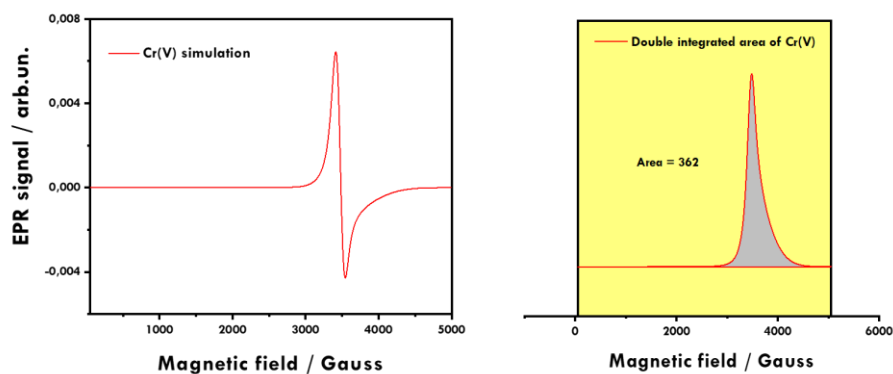


Figure 2.33. Cr(V) EPR spectrum simulated by EasySpin and the double integrated area.

2.3.3 Method Development of Detection of Hot Electrons in Plasmon-enhanced Cr⁶⁺ Reduction

Before testing the behavior of NPs and the efficiency of hot carriers with EPR spectroscopy, a prerequisite calibration of known spin standards compounds for various concentrations should be done. Cu(II) nitrate hexahydrate of spin system $S=1/2$ and Fe-EDTA of $S=5/2$ are chosen, and the EPR spectra for certain concentrations are obtained in Figure 2.8a-b. The EPR signals are double integrated and for each spin system, the corresponding double integrated area vs. concentration graph is plotted (Fig. 2.8c-d), resulting to a linear fitted calibration curve as

$$C = 0.503DI - 4.499, \text{ for spin system standard of } S = 1/2, \quad (2.8)$$

$$C = 0.892DI + 4.886, \text{ for spin system standard of } S = 5/2, \quad (2.9)$$

where C is the concentration in $\mu\text{mol L}^{-1}$ and DI is the double integrated area in arbitrary units.

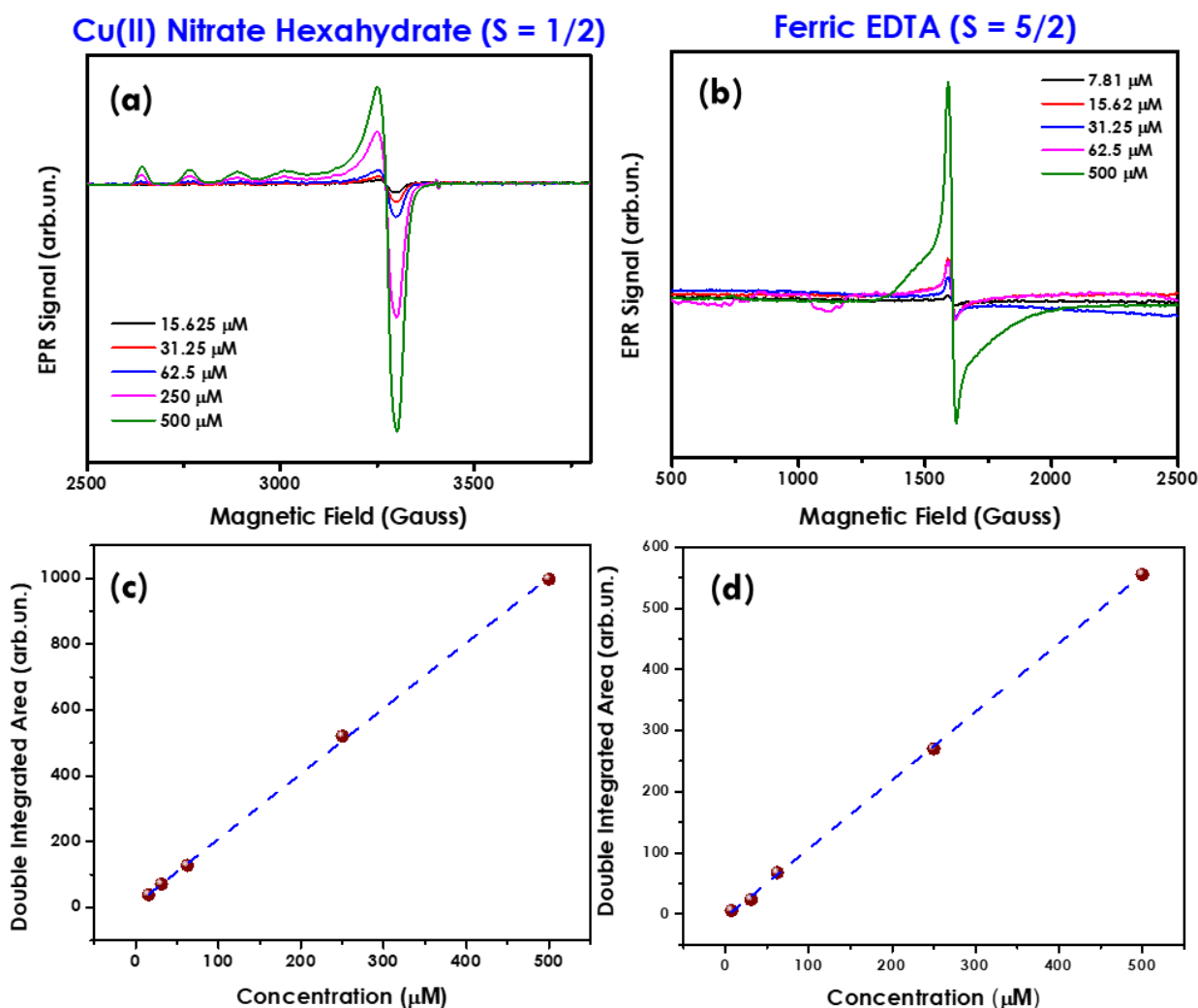


Figure 2.34. Calibration curves of (c) Cu(II) nitrate hexahydrate ($S = 1/2$) and (d) Ferric EDTA ($S = 5/2$) as spin standards and the corresponding (a), (b) EPR signals.

The quantitative assessment of the electron transfer to $\text{Cr}^{(\text{VI})}$, is based on the strict control of the mass-balance of all Cr species, i.e. Cr^{6+} , Cr^{5+} and Cr^{3+} , as described in the mass-balance relation

$$[\text{Cr}]_{\text{TOTAL}} = [\text{Cr}^{6+}] + [\text{Cr}^{5+}] + [\text{Cr}^{3+}]$$

The knowledge of Cr^{5+} , Cr^{3+} at a given time of irradiation, provides stoichiometric accountability of 1-electron and 3-electron transfer events occurred. Accordingly, we have used two independent spectroscopic methods to quantify Cr^{6+} , Cr^{5+} and Cr^{3+} :

[i] Cr^{6+} was quantified by UV-Vis spectroscopy using a well-known standard method based on the complexation of the Cr^{6+} ions by 1,5-diphenylcarbazide (DPC).¹⁰

[ii] Cr^{5+} and Cr^{3+} were identified and quantified using EPR spectroscopy as follows; in aqueous solutions Cr^{5+} is a low-spin $S = 1/2$ system¹¹, detected via a characteristic sharp derivative-like EPR signal, at g value ~ 1.9 , see example in Figure 2, and theoretical spectrum (blue line). Cr^{3+} is a high-spin $S = 3/2$ system, detected via a characteristic axial signal, at g values ~ 4 , see example in Figure 2e, and theoretical spectrum (red line). In our case, EPR spectra of Cr^{5+} and Cr^{3+} were analyzed by numerical simulation. Specifically, for Cr(V) ($S = 1/2$) spin system, a spin-Hamiltonian

$$H = \beta B \cdot \tilde{g} \cdot S. \quad (2.10)$$

For the Cr(III) $S = 3/2$ spin system, a spin-Hamiltonian was used

$$H = \beta B \cdot \tilde{g} \cdot S + S \cdot \tilde{D} \cdot S. \quad (2.11)$$

In both Hamiltonians, \tilde{g} is the electron g -tensor. \tilde{D} is the zero-field splitting tensor describing the spin-spin interaction between the three unpaired electrons of Cr^{3+} . Regarding quantification, the double integral of the EPR spectrum is analogous to the number of spins in the sample. The EPR signals were deconvoluted using theoretical simulations and the double integral of each spectrum was calculated by numerical integration. The proper calibration was done by measuring EPR active spin standards with known spin concentration, demonstrating cognates spin relaxations compared to the measured samples. Therefore, Cu(II) nitrate ($S=1/2$) and Fe(III) EDTA ($S=5/2$) were utilized as calibration tools. The spin deviation and, hence, the induced offset between Fe and Cr^{3+} species can be compensated due to similar carrier relaxations and corrected using eq 2.12⁹

$$\frac{DI(S_1 = 3/2)}{DI(S_2 = 5/2)} \sim \frac{S_1 (S_1 + 1)}{S_2 (S_2 + 1)} = \frac{3}{7} \quad (2.12)$$

where DI is the double integrated area of an EPR signal, thus the spin concentration. Those spin systems can be described by eq 2.9, since both display $S > 1/2$ and hence related dipolar spin-spin interactions. Eventually, Cr^{3+} species are multiplied by the factor of 3, because the $\text{Cr}^{6+} \rightarrow \text{Cr}^{3+}$ reduction is a 3-electron event, thus the correction coefficient of Cr^{3+} population is 9/7.

EPR experimental & simulated spectra of Ag@1SiO_2 NPs

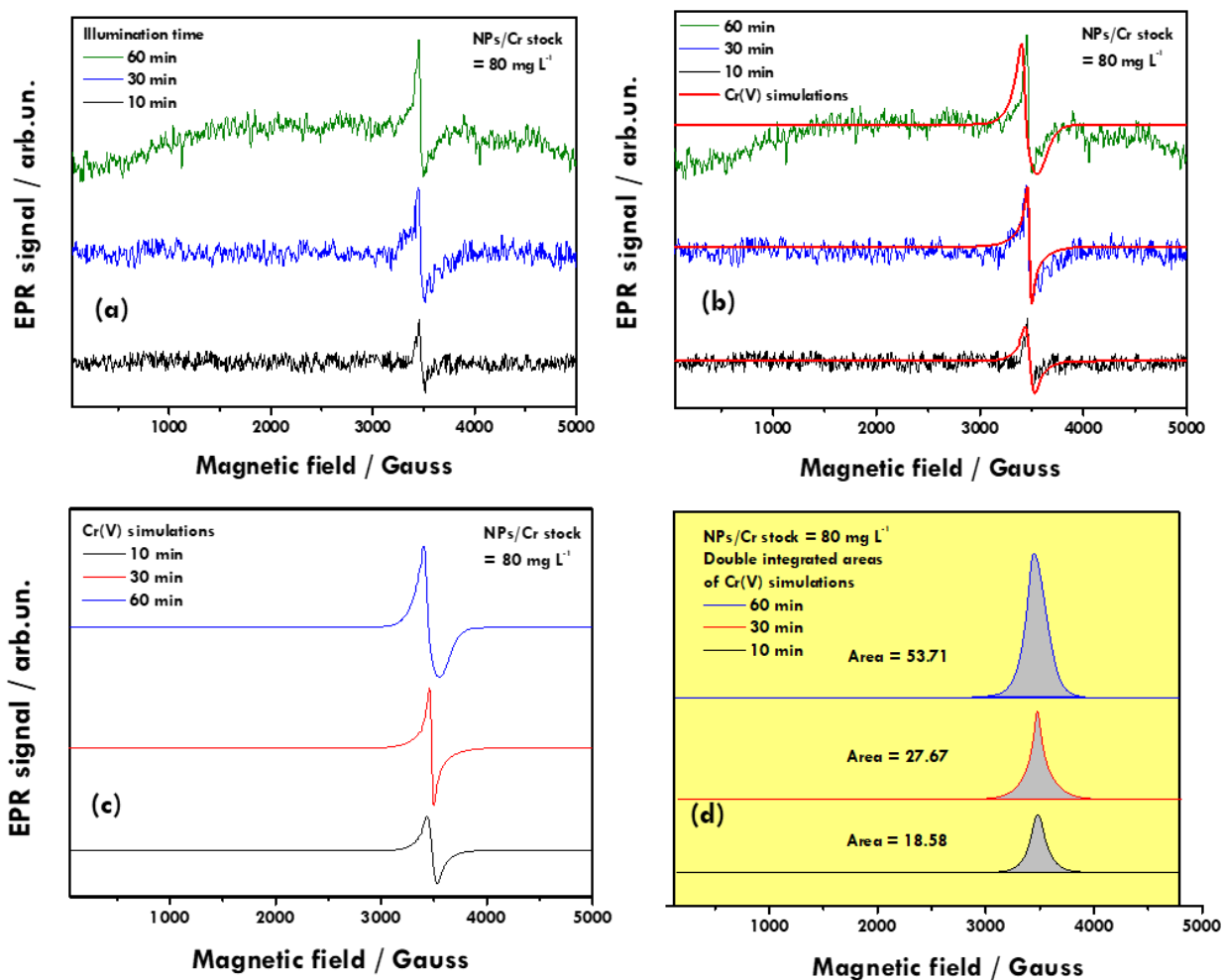


Figure 2.35. SF Ag@1SiO₂ NPs with Cr solution (30 $\mu\text{mol L}^{-1}$ Cr, 60 $\mu\text{mol L}^{-1}$ C₂H₂O₄) under three different illumination times (10, 30 and 60 min), at pH = 3. The particle concentration is 80 mg L⁻¹. (a) EPR spectra of Ag@1SiO₂ NPs. Cr(V) is the only observable EPR signal with the absence of Cr³⁺, because it is a first-order reaction type. (b) Both experimental and simulated EPR spectra of Ag@1SiO₂ NPs. The simulations carried out with the help of MATLAB package EasySpin. (c) The Cr⁵⁺ simulations for each illumination time. (d) Double integrated areas derived from Cr⁵⁺ simulations.

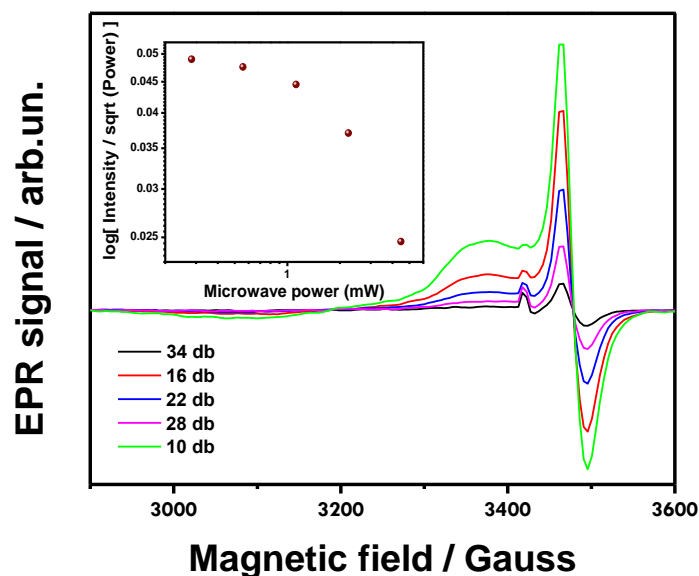


Figure 2.36. Microwave saturation study of the EPR signals corresponding to Cr^{5+} complexes. Inset: $P_{1/2}$ plot revealing that the detected spin interacts with a metallic lattice.

Figure 2.10 shows the microwave saturation study of the EPR signals corresponding to Cr^{5+} complexes. Concerning the inset, $P_{1/2}$ is the power required for the half non-saturated amplitude to be obtained and offers extra insight about the spin-lattice dynamics. The linear increase of EPR signal in proportion to increased microwave power and the $P_{1/2}$ value indicate that the detected spin interacts with a metallic lattice.

Dark modulation

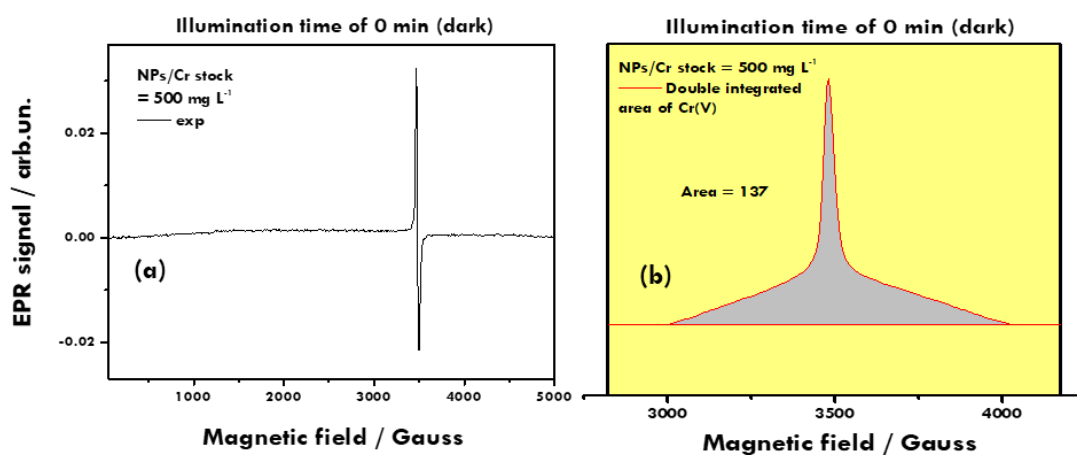


Figure 2.37. EPR spectra of $\text{Ag}@1\text{SiO}_2$ NPs with Cr solution ($2000 \mu\text{mol L}^{-1}$ Cr, $4000 \mu\text{mol L}^{-1}$ $\text{C}_2\text{H}_2\text{O}_4$), before the illumination (dark mode) at $\text{pH} = 3$. The particle concentration is 500

mg L⁻¹. (a) The experimental EPR spectrum is shown. The Cr⁵⁺ is only the observable EPR signal with the absence of Cr³⁺, because it has not reduced to Cr³⁺ yet. (b) Double integrated area derived from Cr⁵⁺ simulation.

Illumination time of 3 minutes

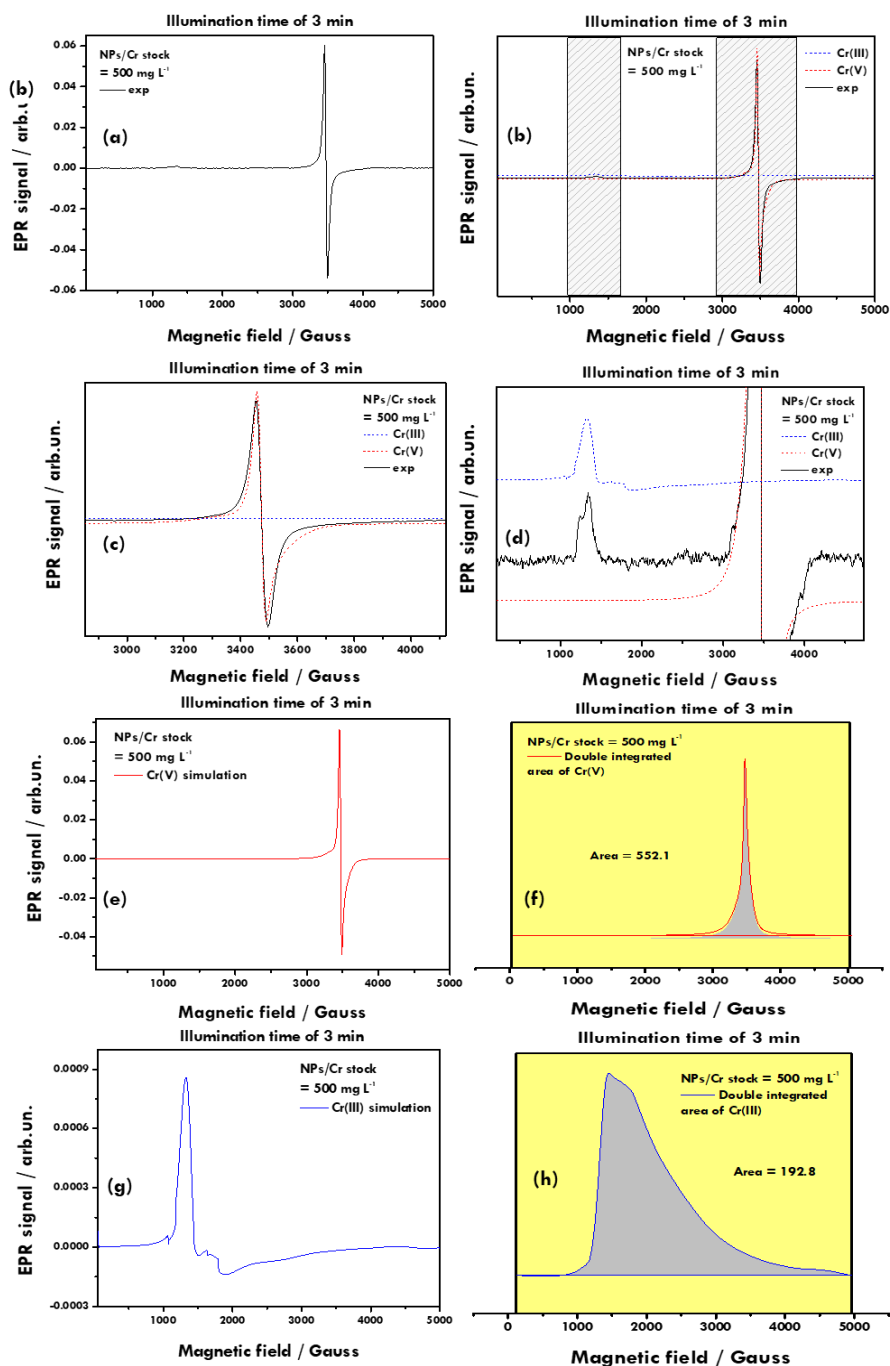


Figure 2.38. EPR spectra of Ag@1SiO₂ NPs with Cr solution (2000 μmol L⁻¹ Cr, 4000 μmol L⁻¹ C₂H₂O₄), at the illumination time of 3 minutes, at pH = 3. The particle concentration is 500 mg L⁻¹. (a) The experimental EPR spectrum is shown. Both Cr(V) and Cr³⁺ are visible. (b) The

experimental EPR spectrum with the addition of Cr(V) and Cr(III) simulations carried out by EasySpin. (c)(d) Enlargement of (b), emphasizing the Cr(V) and Cr³⁺ EPR signals respectively. (e) Cr(V) simulated EPR spectrum. (f) Double integrated area of Cr(V) simulation. (g) Cr³⁺ simulated EPR spectrum. (h) Double integrated area of Cr³⁺ simulation.

Illumination time of 10 minutes

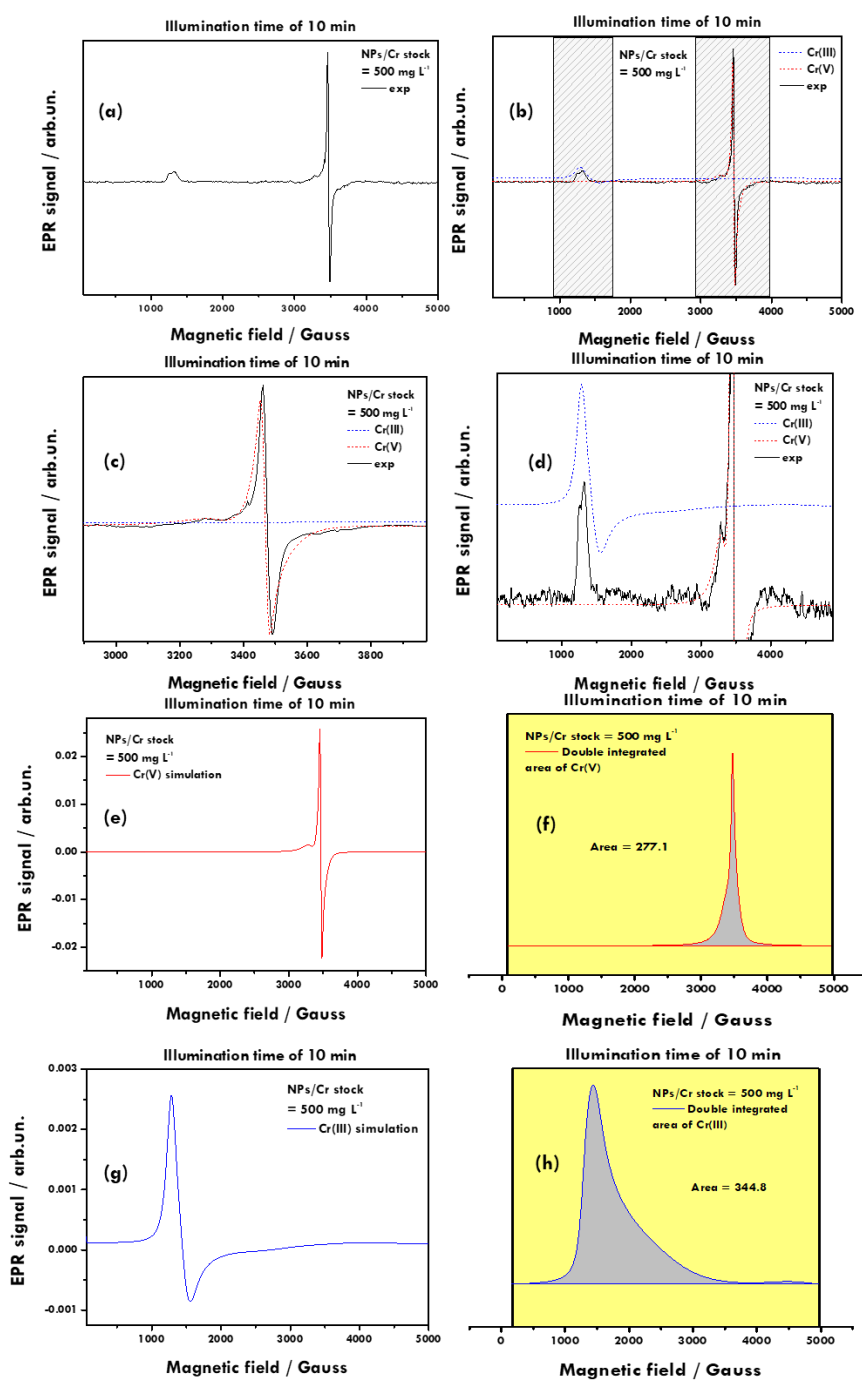


Figure 2.39. SF EPR spectra of Ag@1SiO₂ NPs with Cr solution (2000 μmol L⁻¹ Cr, 4000 μmol L⁻¹ C₂H₂O₄), at the illumination time of 10 minutes, at pH = 3. The particle concentration

is 500 mg L^{-1} . (a) The experimental EPR spectrum is shown. Both Cr(V) and Cr³⁺ are visible. (b) The experimental EPR spectrum with the addition of Cr(V) and Cr³⁺ simulations carried out by EasySpin. (c) Enlargement of Fig. S23b emphasizing the Cr(V) EPR signal with its simulated. (d) Enlargement of Fig. S23b emphasizing the Cr³⁺ EPR signal with its simulated. (e) Cr(V) simulated EPR spectrum. (f) Double integrated area of Cr(V) simulation. (g) Cr³⁺ simulated EPR spectrum. (h) Double integrated area of Cr³⁺ simulation.

Illumination time of 30 minutes

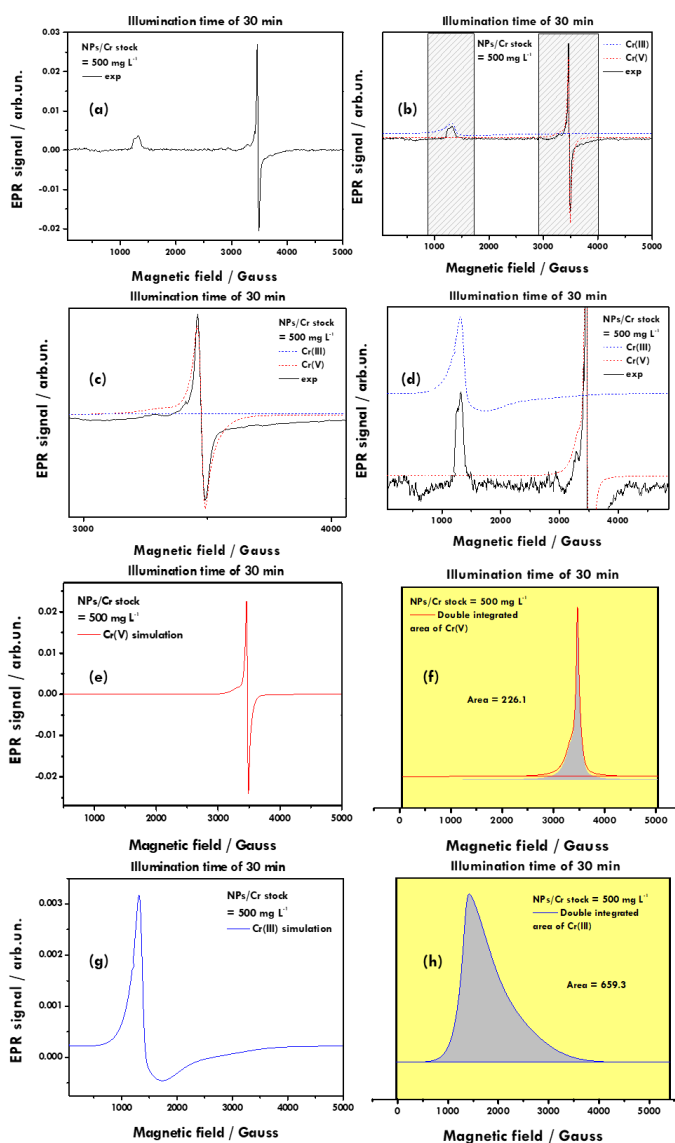


Figure 2.40. SF EPR spectra of Ag@1SiO₂ NPs with Cr solution ($2000 \mu\text{mol L}^{-1}$ Cr, $4000 \mu\text{mol L}^{-1}$ C₂H₂O₄), at the illumination time of 30 minutes, at pH = 3. The particle concentration is 500 mg L^{-1} . (a) The experimental EPR spectrum is shown. Both Cr(V) and Cr³⁺ are visible. (b) The experimental EPR spectrum with the addition of Cr(V) and Cr³⁺ simulations carried

out by EasySpin. (c)(d) Enlargement of (b) emphasizing the Cr(V) and Cr³⁺ EPR signals respectively. (e) Cr(V) simulated EPR spectrum. (f) Double integrated area of Cr(V) simulation. (g) Cr³⁺ simulated EPR spectrum. (h) Double integrated area of Cr³⁺ simulation.

Illumination time of 60 minutes

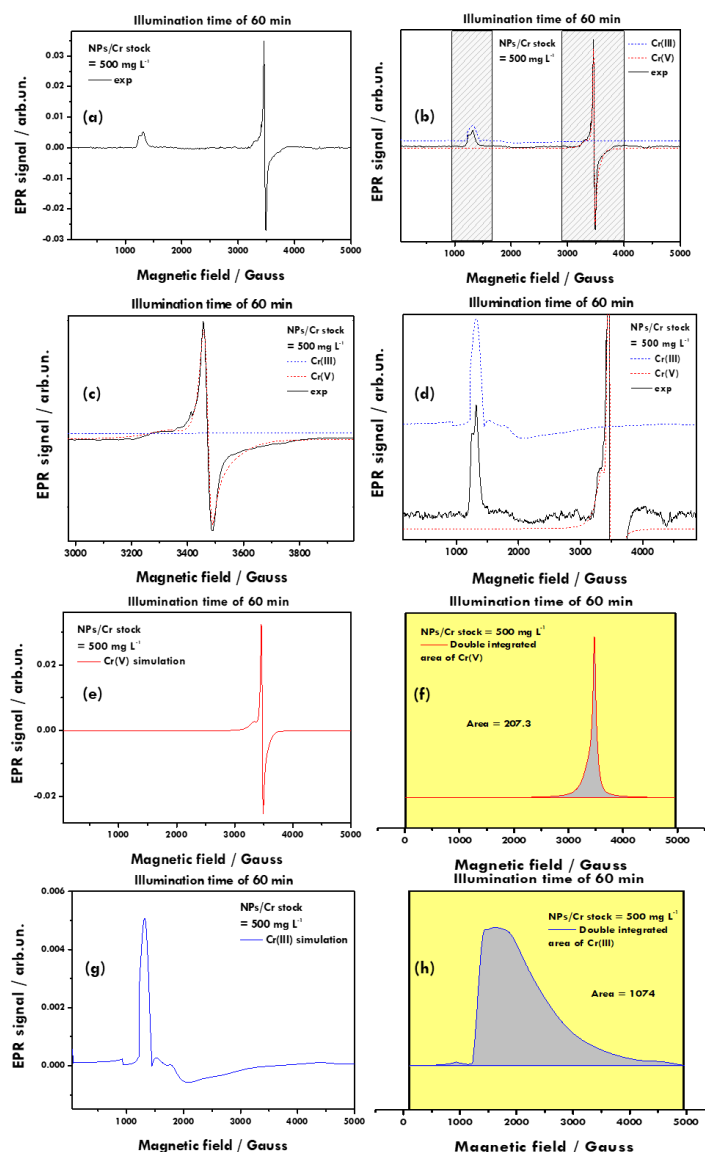


Figure 2.41. SF EPR spectra of Ag@1SiO₂ NPs with Cr solution (2000 μmol L⁻¹ Cr, 4000 μmol L⁻¹ C₂H₂O₄), at the illumination time of 60 minutes, at pH = 3. The particle concentration is 500 mg L⁻¹. (a) The experimental EPR spectrum is shown. Both Cr(V) and Cr³⁺ are visible. (b) The experimental EPR spectrum with the addition of Cr(V) and Cr³⁺ simulations carried out by EasySpin. (c)(d) Enlargement of (b), emphasizing the Cr(V) and Cr³⁺ EPR signals respectively. (e) Cr(V) simulated EPR spectrum. (f) Double integrated area of Cr(V) simulation. (g) Cr³⁺ simulated EPR spectrum. (h) Double integrated area of Cr³⁺ simulation.

FSP-493 NPs of 500 mg L ⁻¹	Double integrated areas (arb.un.)	
	Cr(V)	Cr3+
Dark modulation	137	–
Illumination time of 3 min	552	193
Illumination time of 10 min	277	345
Illumination time of 30 min	226	659
Illumination time of 60 min	207	1074

2.3.4 Spin Trapping

EPR is the technique of choice when it comes to the study of free radicals. The direct detection of free radicals is usually not possible due to their high reactivity and their transient nature. In this case, spin trapping is used. Spin trapping involves the addition to the system under consideration of a small amount of diamagnetic molecule, usually a nitron or nitroso compound, which reacts with a free radical to produce a more stable paramagnetic radical species that can reach EPR detectable levels. The observable radical species is called spin adduct and the molecule undergoing radical addition is a spin trap.

The most used spin trap is the 5,5-dimethyl-1-pyrroline N-oxide (DMPO) and the α -phenyl-N-t-butyl nitron (PBN). A typical spin trapping EPR spectrum is shown in Fig. 2.16.

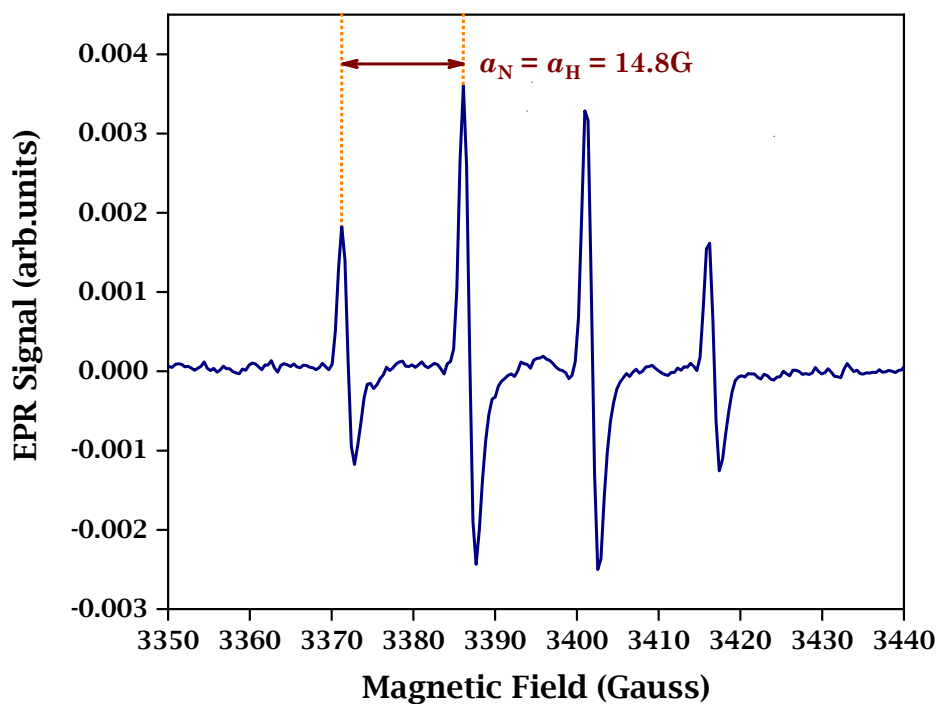


Figure 2.42. Typical EPR spectrum of DMPO-OH spin adduct on TiO₂ nanoparticles. The hyperfine coupling constants are used to determine the spin adduct.

By determination of the parameters such as hyperfine coupling constant and split between peaks we are able to determine the type of radical trapped. The hyperfine coupling constants for the DMPO-OH adduct are¹² $\alpha_N = \alpha_H = 14.8$ Gauss

1

2 2.4 Characterization Techniques

3 *Powder X-Ray Diffraction:* XRD Diffraction
4 Patterns of the nanoparticles were obtained with a
5 D8 Advance Bruker Diffractometer (Fig. 2.4)
6 using (40kV, 40mA) $\lambda = 0.154 \text{ nm}$ Cu K_{α}
7 radiation with a Lynxeye detector. The sample is
8 placed in a silicon holder. All the parameters,
9 including angles wide, angle step, residence time,
10 rotation of sample holder, are defined by a Bruker software.



Figure 2.43. D8 Advance Bruker Diffractometer.

11 *N₂ Porosimetry:* Prior to any measurement, the sample
12 must be preconditioned to remove physically bonded
13 impurities from the surface of the powder in a process
14 called degassing. Samples are usually degassed either
15 at vacuum conditions or with continuously flowing
16 inert gas like N₂ at elevated temperatures. The
17 temperature of the degassing process as well as the
18 duration are carefully chosen to avoid structural
19 changes on the sample. Specific surface area (SSA)
20 and the pore size distribution of the samples were
21 determined from the adsorption and desorption isotherms of nitrogen at 196 °C using a
22 TriStar 3000 Micromeritics instrument. Prior to the measurements, the samples were
23 outgassed at 150⁰ for 10h, under N₂ flow.



Figure 2.44. TriStar 3000 Micromeritics instrument.

24 *Raman Spectroscopy:* Raman spectroscopy
25 measurements were taken using a Horiba
26 XploRA Plus Raman microscope coupled to
27 an Olympus BX41 microscope and using a
28 785 nm laser as an excitation source. The
29 microscope is coupled to a CCD which helped
30 using low laser intensities of 1% or 10% in
31 samples that were experiencing phase changes
32 due to heating. Spectrum were recorded and processed with Lab Spec software.

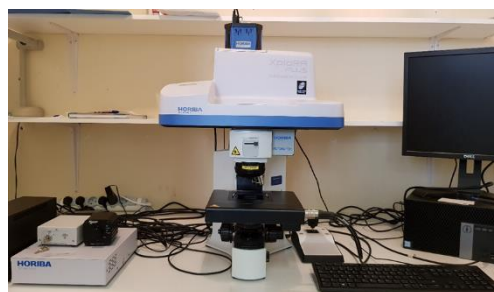


Figure 2.45. Horiba XploRA PLUS Raman microscope.

1 *X-ray Photoelectron Spectroscopy:*

2 The measurements were acquired in a
3 surface analysis ultrahigh vacuum
4 system (SPECS GmbH) equipped
5 with a twin Al-Mg anode X-ray source
6 and a multichannel hemispherical
7 sector electron analyzer (HSA-
8 Phoibos 100). The base pressure was
9 $2-5 \times 10^{-9}$ mbar. A monochromatized
10 Mg K α line at 1253.6 eV and analyzer

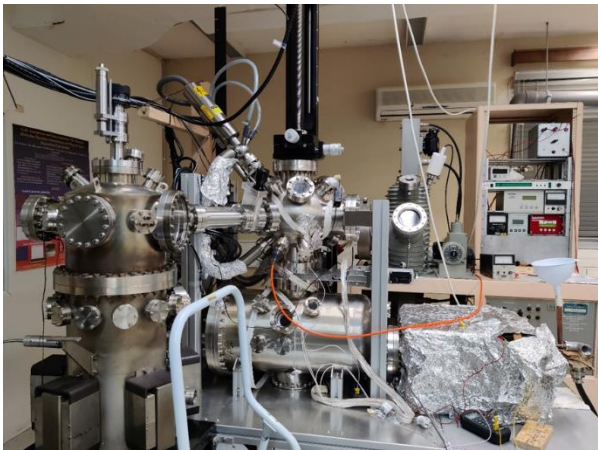
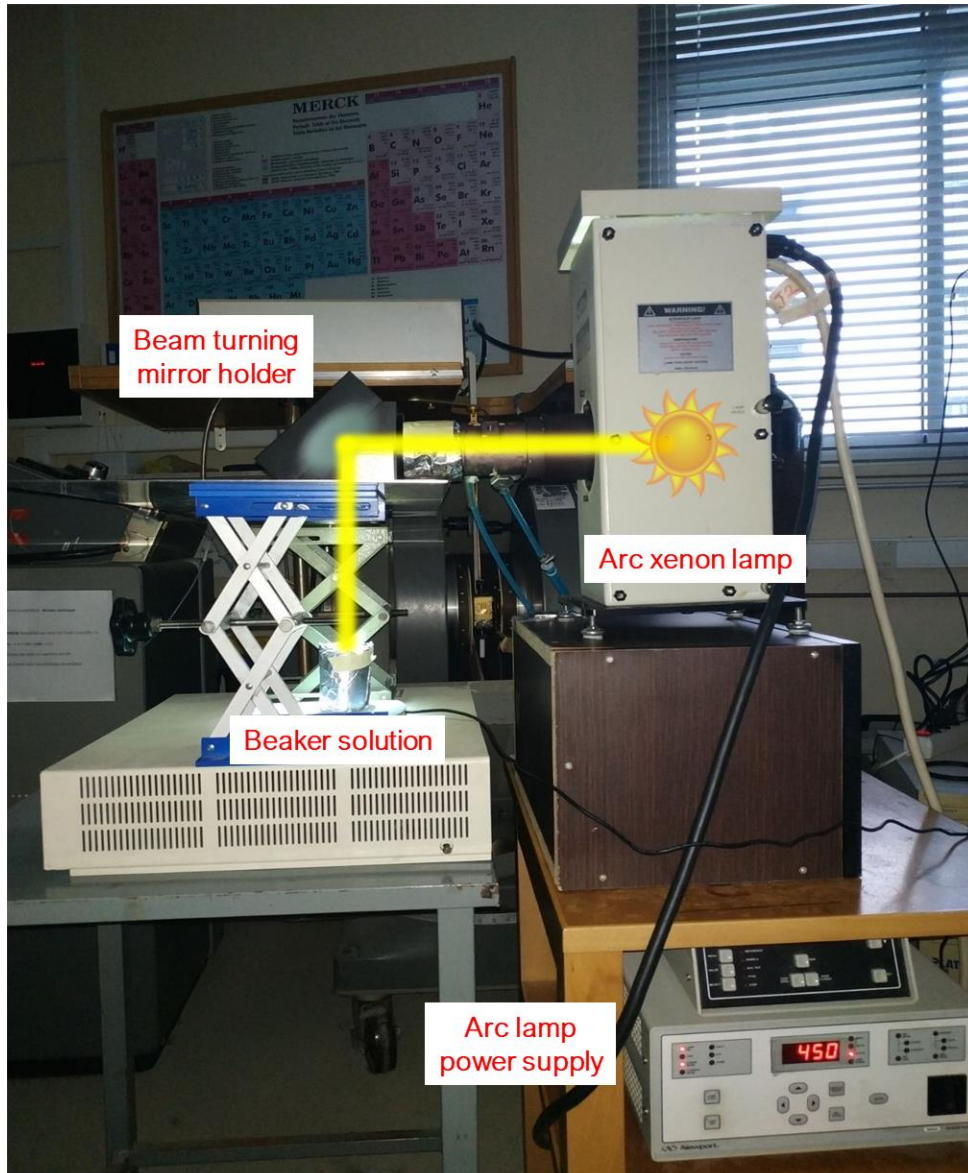


Figure 2.46. XPS experimental setup.

11 pass energy of 20 eV were used in all XPS measurements. The binding energies were
12 calculated with reference to the energy of C 1s peak of contaminant carbon at 284.5 eV.
13 The peak deconvolution was calculated using a Shirley background.

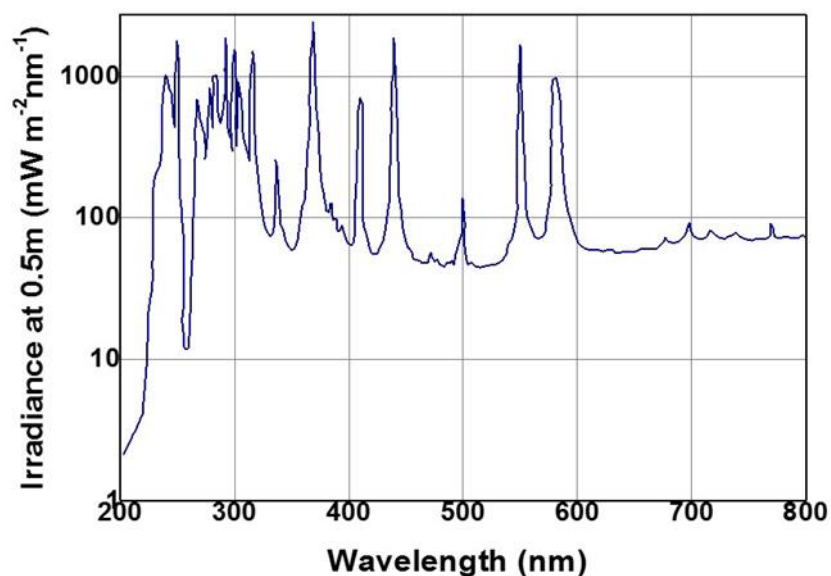
14 **2.5 Light Irradiation Set-up**

15 The custom-made illumination set-up, employed in the measurements of Cr⁶⁺
16 photo-reduction in the presence of Ag@SiO₂ nanoaggregates, is demonstrated in
17 Figure 2.21. In particular, the experimental illumination set-up (EIS) consists of an Arc
18 Xenon Lamp (model: Oriel 6293, 1000 W) that radiates through a pipe, and a 62245-
19 beam turning mirror holder, which bends the beam by 90°, absorbing most of the
20 radiation. The input power of the arc xenon lamp will be set to 450 W for our
21 experiments. Its male flange end fits to the output of an Oriel Lamp Housing condenser.
22 Most of the IR is transmitted through the dichroic mirror and absorbed by the mirror
23 housing where a heat sink dissipates the heat. The optimal surface-lens distance is close
24 to 0.5 m. Figure 2.22 exhibits the lamp spectral irradiance with the wavelength λ as
25 spectral variable. Integrating the area from 390 to 700 nm, the total irradiance in visible
26 spectrum can be obtained in W/m². Moreover, a magnetic stirrer (VWR, part of
27 Avantor) is placed under the reflector and on top of which, a beaker with the solution
28 is set and agitated, so the light can interact with all the particles homogeneously. The
29 beaker is covered with aluminum foil, so that the entire light percentage is kept in the
30 glass and falls onto the solution.



1

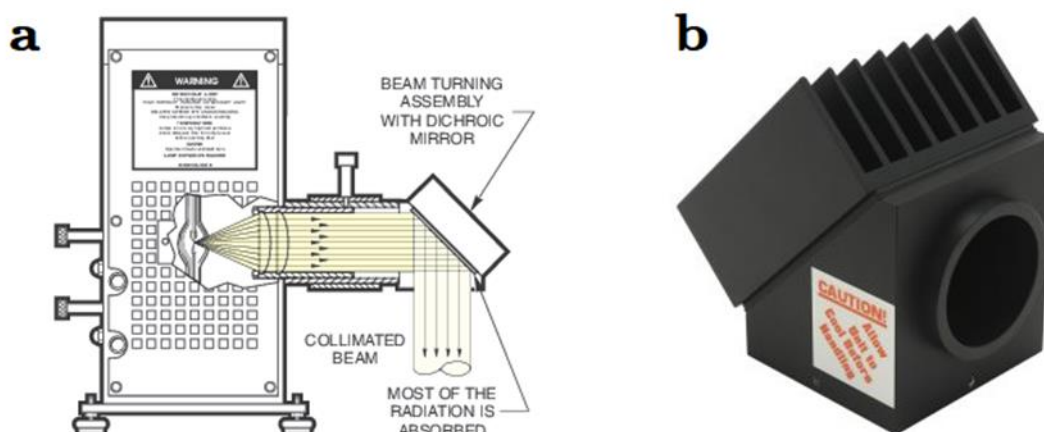
2 **Figure 2.47.** Experimental illumination set-up (EIS), consisting of the arc xenon lamp
3 and the beam turning mirror holder. All the experiments were performed with a standard
4 lamp power of 450 W.



1

2

Figure 2.48. Oriel Lamp (model: 6293) irradiance spectrum



3

4 **Figure 2.49.**(a) Schematic figure of beam turner attached to the lamp housing
 5 condenser. (b) Beam turning mirror holder (Model 62245) with dichroic mirror,
 6 changing the direction of the beam by 90 degrees.

7

8 2.6 References

- 9 (1) Pratsinis, S.; Mueller, R.; Kammler, H. K.; Madler, L. Controlled Synthesis of
 10 Nanostructured Particles by Flame Spray Pyrolysis. *Aerosol Science* **2002**, *33*, 369–
 11 389.

- 1 (2) Madler, L.; Amal, R.; Teoh, W. Y. Flame Spray Pyrolysis: An Enabling
2 Technology for Nanoparticles Design and Fabrication. *Nanoscale* **2010**, *2*, 1324–
3 1347. <https://doi.org/10.1039/c0nr00017e>.
- 4 (3) Sotiriou, G. A.; Blattmann, C. O.; Deligiannakis, Y. Nanoantioxidant-Driven
5 Plasmon Enhanced Proton-Coupled Electron Transfer. *Nanoscale* **2016**, *8* (2), 796–
6 803. <https://doi.org/10.1039/C5NR04942C>.
- 7 (4) Sotiriou, G.; Sannomiya, T.; Teleki, A.; Krumeich, F.; Pratsinis, S. Non-Toxic Dry-
8 Coated Nanosilver for Plasmonic Biosensors. *ADVANCED MATERIALS* **2010**.
- 9 (5) Teleki, A.; Heine, M.; Krumeich, F.; Akhtar, K.; Pratsinis, S. In Situ Coating of
10 Flame-Made TiO₂ Particles with Nanothin SiO₂ Films. *Langmuir* **2008**, 12553–
11 12558. <https://doi.org/10.1021/la801630z>.
- 12 (6) Teleki, A.; Akhtar, M. K.; Pratsinis, S. E. The Quality of SiO₂-Coatings on Flame-
13 Made TiO₂-Based Nanoparticles. *Journal of Materials Chemistry* **2008**, *18* (30),
14 3547. <https://doi.org/10.1039/b803039a>.
- 15 (7) Psathas, P.; Georgiou, Y.; Moularas, C.; Armatas, G. S.; Deligiannakis, Y.
16 Controlled-Phase Synthesis of Bi₂Fe₄O₉ & BiFeO₃ by Flame Spray Pyrolysis and
17 Their Evaluation as Non-Noble Metal Catalysts for Efficient Reduction of 4-
18 Nitrophenol. *Powder Technology* **2020**, *368*, 268–277.
19 <https://doi.org/10.1016/j.powtec.2020.04.059>.
- 20 (8) Zeeman, P. The Effect of Magnetisation on the Nature of Light Emitted by a
21 Substance. *Nature*. 1897, p 347. <https://doi.org/10.1038/055347a0>.
- 22 (9) Eaton, G. R.; Eaton, S. S.; Barr, D. P.; Weber, R. T.; Springer-Verlag (Wieden).
23 *Quantitative EPR*; Springer: Wien; New York, 2014.
- 24 (10) Stover, N. M. DIPHENYLCARBAZIDE AS A TEST FOR CHROMIUM. *J.*
25 *Am. Chem. Soc.* **1928**, *50* (9), 2363–2366. <https://doi.org/10.1021/ja01396a007>.
- 26 (11) Pilbrow, J. R. *Transition Ion Electron Paramagnetic Resonance*; Clarendon
27 Press ; Oxford University Press: Oxford : New York, 1990.
- 28 (12) Rowlands, C. C.; Murphy, D. M. Chemical Reactions of EPR. In *Encyclopedia*
29 *of Spectroscopy and Spectrometry*; 2016; Vol. 1, pp 221–223.

30

31

32

Chapter 3

Photothermal Effects by Flame-made Core@Shell Plasmonic Nanoaggregates

3.1 Introduction

Metallic nanoparticles (mNPs) are well-known for their optical properties. The interaction between an electromagnetic stimulation and the metal's conduction electrons, confined in the nanoscale, drives the phenomenon of Local Surface Plasmon Resonance (LSPR)^{1,2}, i.e. the photoinduced collective oscillation of the free electron cloud. In general, LSPR can be analyzed in a radiative and a non-radiative process; **[i]** the *radiative* plasmon decay describes the scattering of light by the particle surface, i.e. resulting to the famous vivid colors of noble metals (far-field), and the generation of locally amplified electric fields due to confinement of surface plasmons and incoming photons in the particle vicinity (near-field).³ Thus, as outlined by Mie theory⁴, controlling particle parameters, such as size/morphology/dielectric medium, allows the adjustment of the plasmonic response over the EM spectrum^{5,6}, giving birth a plethora of applications⁷⁻¹¹. **[ii]** the *non-radiative* plasmon decay -and the subsequent heat generation- can be interpreted as a dissipation of electronic energy into heat. This

¹ Part of this chapter is published in *J. Phys. Chem. C* 2019, 123, 36, 22499–22510.

1 phenomenon, gave birth to a new sub-field i.e. Thermoplasmonics¹², which exploits the
2 photothermal properties of such mNPs. It is now anticipated that the absorbed photon
3 energy and the subsequent non-radiative dissipation as heat, can cause a significant
4 temperature rise on the particle's vicinity, i.e. local heating in nanoscale¹³⁻¹⁵, or as
5 homogenized temperature rise in macroscopic particle ensembles¹⁶⁻¹⁸, expanding the
6 field to novel applications¹⁹⁻²⁷.

7 Recently, Baffou *et al.*^{28,29} have further elaborated the theoretical frame
8 describing the phenomenon of heat generation by particle 2D arrays with a
9 *homogeneous* interparticle distance, notable described in subsection 1.2.3.3. In more
10 realistic configurations, however, typically we encounter two main types of deviation
11 from the ideal theoretical approach: [a] a distribution of particle size typically occur,
12 rather than a single-size assembly and the particle-particle distance may be determined
13 by a shell, such as SiO₂, which surrounds the plasmonic particle, thus the coating
14 defines the dielectric medium, and [b] a fractal-like ensemble of interacting mNPs
15 typically occur in many chemically-prepared particles. Noble metals, such as gold^{30,31}
16 and silver³² are among the most efficient plasmonic candidates. De Luca *et al.*^{18,33,34}
17 have studied in-depth the photothermal efficiency for macroscopic ensembles of Au
18 NPs either in colloids or deposited on organic substrates, controlling the interparticle
19 distance by mechanical means. In the present work, Ag is the chosen material,
20 displaying the superior optical and photothermal performance under visible excitation,
21 in terms of near-field enhancement and heat generation, according to Baffou *et al.*³²
22 Encapsulation of Ag core with a nanometric amorphous SiO₂ layer is a common
23 strategy adopted by many works³⁵⁻³⁷, since it serves a 3-fold purpose: [i] it protects the
24 Ag⁰ particles from oxidation. [ii] it prevents the release of toxic Ag⁺ ions³⁸, allowing
25 the utilization of nanosilver in bio-applications. [iii] the SiO₂ surface is suitable to
26 functionalization with well-established chemical methods^{35,39-41}. However, to our
27 knowledge, a systematic study on the effect of SiO₂ coating to the Thermoplasmonic
28 Heat Generation Efficiency [THGE] for non-monodisperse ensembles of SiO₂-coated
29 Ag⁰ is lacking. Our hypothesis is that the hermetic SiO₂ shell will prevent direct Ag⁰-
30 Ag⁰ contact and, based on the shell thickness, will control the photothermal conversion
31 mechanism. In the case of a liquid suspension of Ag⁰@SiO₂ NPs, the THGE should
32 consider the role of the solvent's thermal properties.

1 In this context, we have studied the THGE for fractal-like ensembles of
2 $\text{Ag}^0\text{@SiO}_2$ nanoaggregates with an amorphous SiO_2 coating of controlled thickness
3 varying in the range of 1-5 nm. Sub-nanometric SiO_2 shell was explored in depth as a
4 limiting scenario for non-hermetically coated Ag^0 NPs with maximum $\text{Ag}^0\text{-Ag}^0$
5 proximity. As we demonstrate, these “patchy” $\text{Ag}^0\text{@SiO}_2$ are the ideal
6 thermoplasmonic nano-ensembles, since they trigger collective thermal effects that
7 greatly contribute to plasmon-driven temperature rise. The core@shell synthesis was
8 performed in a single-step process by flame spray pyrolysis (FSP). Flame synthesis^{42,43}
9 allows production of mNPs of high purity and crystallinity and regulation of the desired
10 properties.^{44,45} Typically, FSP-made nanostructures, including $\text{Ag}^0\text{@SiO}_2$, are non-
11 monodisperse due to high-temperature particle sintering and aggregation^{35,46} during
12 particle formation. These ensembles can be described as fractal-like structures with a
13 fractal dimension of 1.8.⁴⁷ Herein, we used a single-nozzle FSP reactor to produce Ag
14 nanoparticles of size distribution in the range 15-25 nm, hermetically coated with a SiO_2
15 layer up to 5 nm thickness. In a previous study, Sotiriou et al. have shown that in such
16 non-monodisperse SiO_2 -coated Ag^0 ensembles, engineering the SiO_2 -thickness well
17 below 10nm, allows light-induced plasmonic excitation of the Ag^0 core to be sensed by
18 surface-grafted antioxidant organics³⁵. In this way, we have shown that SiO_2 of few
19 nanometers is appropriate to efficiently encapsulate the Ag^0 core, thus allowing
20 collective plasmon phenomena to be detectable in antioxidant Hydrogen-Atom-
21 Transfer in suspensions of the particles. Herein, we use this knowledge as guidance for
22 the desired SiO_2 -thickness range, to study the photothermal efficiency of FSP-made
23 $\text{Ag}^0\text{@SiO}_2$ ensembles.

24 Thus, the specific aims of the present research were: [i] to produce and fully
25 characterize hermetically- and patchy-coated $\text{Ag}^0\text{@SiO}_2$ nanoaggregates using FSP, [ii]
26 to study the Thermoplasmonic Heat Generation Efficiency for the $\text{Ag}^0\text{@SiO}_2$ NPs in
27 suspension and deposited on films, and [iii] to discuss the theoretical frame for the
28 description of the THGE for fractal-like ensembles, taking into account the dual role of
29 SiO_2 as a dielectric shell-medium and as Ag-Ag spacer.

30 **3.2 Materials & Methods**

31 The precursor solution was prepared by dissolving Ag Acetate (Sigma Aldrich,
32 purity >99%) in 2-ethylhexanoic acid (EHA) and acetonitrile (ACN) (both Sigma

1 Aldrich, >97%), at volume ratio 1:1 varying concentration 0.3-0.5M. Then, the solution
2 was fed through a capillary at 5-7 ml/L and dispersed by 5 L/min O₂ (Linde, purity
3 >99%) to a stoichiometric, self-sustained oxygen-methane (5 L/min, 2.5 L/min) pilot
4 flame to initiate combustion, resulted to formation of Ag nanoparticles. Pressure drop
5 at the nozzle tip was fixed at 2 bar and additional 5-20 L/min sheath O₂ was used. The
6 product powder was collected, using a vacuum pump (Busch V40), on a glass
7 microfiber filter (Albet). The *in-situ* SiO₂ coating of Ag⁰ NPs was engineered in a
8 modified enclosed FSP reactor, originally described by Sotiriou *et al.*^{35,38,48,49} The flame
9 was enclosed by a 22cm metallic tube, schematically shown in Figure 2a, with a metal
10 ring at the top. The ring (diameter = 4.3 cm), has 12 equidistant holes of diameter 0.5
11 cm, each directed away from the center line of the ring and pointing downstream to
12 avoid stagnation flow. Through these openings, 0.3-3 L/min of N₂ (Linde, purity >99%)
13 gas carrying hexamethyldisiloxane (HMDSO, Aldrich, purity 98%) vapor are injected
14 along with an additional mixing flow rate fixed at 15 L/min N₂ at room temperature,
15 adding the required swirl for increased coating efficiency. The HMDSO vapor was
16 supplied by bubbling N₂ through 300 cm³ of HMDSO in a glass flask, fixed at 10°C.
17 According to the pioneering study of SiO₂ coating by Teleki *et al.*^{50,51}, under saturation
18 conditions, this set-up corresponds to a theoretical 5.9 g/h of SiO₂, i.e. 20 wt% SiO₂ in
19 the product powder.

20 The experimentally obtained SiO₂ coating thickness was estimated by TEM. The
21 nominal SiO₂-content (HMDSO) in the FSP precursor, listed in Table 1, shows that by
22 increasing the HMDSO content, we increase the SiO₂ thickness up to a limit of 5nm,
23 thus yielding 27 wt% SiO₂@Ag⁰. Further increase of HMDSO resulted in formation of
24 separate SiO₂ agglomerates, in accordance with previous literature reports.⁵⁰ The
25 morphology of the samples was analyzed by high-resolution transmission electron
26 microscopy (*HRTEM*) using a Philips CM 20 microscope operated at 200 kV and
27 provided 0.25 nm resolution. Before the measurements, the samples were ground in a
28 mortar and dry loaded onto a support film (Lacey Carbon, 300 mesh, (Cu)). Recorded
29 pictures were analysed by Gatan Digital Micrograph software. Particles size and
30 thickness of the SiO₂ layer were calculated using the ImageJ software. *Powder X-ray*
31 *diffraction (pXRD)* data was collected at room temperature using a Bruker D8 Advance
32 2theta diffractometer with copper radiation (Cu K α , $\lambda = 1.5406 \text{ \AA}$) and a secondary
33 monochromator operating (40 kV, 40 mA), whereby samples were measured between

1 10° and 80°. Crystal size is calculated by Scherrer formula. *Specific surface area (SSA)*
2 and the pore size distribution of the samples were determined from the adsorption and
3 desorption isotherms of nitrogen at 196 °C using a TriStar 3000 Micromeritics
4 instrument. Prior to the measurements, the samples were outgassed at 150° for 10h,
5 under N₂ flow. *Fourier transform infrared* (Thermo Scientific, iS5 Nicolet) data were
6 obtained by placing the product powder in KBr glasses. *UV/Vis* spectra were collected
7 by a Perkin Elmer Lambda 35 Spectrometer, by dispersing particles in aqueous solvents
8 and placing them in quartz cuvettes. *Dynamic Light Scattering (DLS)* Size distributions
9 of particles and aggregates in ethanol solutions were obtained by dynamic light
10 scattering (DLS, Zetasizer, Malvern Instruments). *X-ray photoelectron spectroscopy*
11 (*XPS*) were acquired in a surface analysis ultrahigh vacuum system (SPECS GmbH)
12 equipped with a twin Al-Mg anode X-ray source and a multichannel hemispherical
13 sector electron analyzer (HSA-Phoibos 100). The base pressure was $2\text{-}5 \times 10^{-9}$ mbar.
14 A monochromatized Mg K α line at 1253.6 eV and analyzer pass energy of 20 eV were
15 used in all XPS measurements. The binding energies were calculated with reference to
16 the energy of C 1s peak of contaminant carbon at 284.5 eV. The peak deconvolution
17 was calculated using a Shirley background.

18 *Particle suspensions:* The Ag⁰@SiO₂ powder was dispersed at ethanol, at
19 concentration between 0.01 g/L up to 0.5 g/L. Then, the suspension was sonicated in a
20 Sonic-V500 sonicator. The sonication was carried out in cup-horn holder using a total
21 power of 100W, for 50 sec. This cup-horn holder allows fine dispersion of the particles
22 without contact with the metal tip. In each experiment, freshly prepared particle
23 suspensions were used for the experiments within 30 minutes.

24 *Particle films:* SiO₂@Ag⁰ films were prepared by dropcasting of ethanol-
25 dispersed NPs on a microscope glass-slide. The average film thickness δ of the NP
26 layers was controlled in the range 0.1 to 0.5 μm , estimated by the number of dropcasted
27 particles on the film surface (1x4cm).

28 *Particle Irradiation*

29 *[a] Arc Xenon Lamp Irradiation:* The radiative source was an Arc Xenon Lamp
30 (Oriel 6293). The particle suspensions were irradiated inside a light-isolated box. The
31 samples were put in quartz cuvette (1x1x3mm), fixed inside the box at the focal point
32 of the beam which enters the irradiation compartment by an appropriate narrow

1 opening. The focused beam had a round geometry of 5mm radius. The incident
2 irradiation power was calibrated at the sample position, using a power meter (Newport).
3 Irradiation at different wavelengths was carried out using cut-off filters (Edmonds
4 Optics), allowing selection of spectral ranges $\lambda > 300\text{nm}$, $> 320\text{nm}$, $> 340\text{nm}$, $> 400\text{nm}$
5 and $> 455\text{nm}$.

6 **[b] Focused Sunlight Irradiation:** ambient sunlight irradiation was used in
7 outdoor experiments by exposing particle films to focused and non-focused daylight.
8 The concentrated sunlight was obtained by a Fresnel lens (28x28cm), by Edmonds
9 Optics. The focal point of this Fresnel lens was at 35 cm. The incident light power was
10 monitored by a power meter (Newport). Typically, the daylight in our location was in
11 the range of 60-80 mW/cm² (<http://penteli.meteo.gr/stations/ioannina/>). The irradiation
12 experiments have been repeated 3 times, verifying the precision of our collected data.

13 **Monitoring ΔT Variations:** The temperature was recorded by an infrared thermal
14 imager (Fluke, TiS40). Emissivity was set at 0.7 considering the SiO₂ presence and the
15 background temperature at room temperature, 22⁰C. The image analysis is
16 accomplished by the SmartView software. As a control, in particle-free films, the
17 temperature rise was $\Delta T_{\text{max}} = 5 \pm 1$ °C, while in the quartz cuvette with ethanol,
18 $\Delta T_{\text{max}} = 6 \pm 1$ °C. The standard error values shown at temperature curves in Figures 6-9,
19 are obtained for thermal camera's range (± 1 °C).

20 We assume that the next-neighbor interaction between plasmonic Ag⁰ NPs is
21 determined by the SiO₂-shell thickness, acting as the particle separator. Thus, for the
22 case of an ensemble of Ag⁰@SiO₂ nanaoaggregates, we consider the interparticle
23 distance is determined by the thickness of the SiO₂-shell encapsulating the Ag core.

24 **Particles on a 2D film:** In the case of film geometry ($m=2$), the confined
25 parameter ζ has been estimated in the order of 10^{-7} , indicating that collective
26 phenomena are dominant. Thus, according to Baffou, this enables us to consider the
27 heat density as a continuous function, despite the discrete nature of the heat-generating
28 nano-sources.

29 **Particles in a Liquid Suspension:** For particles suspended in a liquid solvent, we
30 consider that only the next-neighboring particles *within each aggregate*, see TEM
31 images in Figure 1, play the dominant role in thermoplasmonic heat generation. Thus,

1 an estimation of the dominating regime has to be made, considering the fractal-like
 2 geometry of the FSP-made NPs.^{52,53} Assuming that the incoming light illuminates at
 3 least one fractal agglomerate, for our FSP-made ensembles, ζ can be estimated by
 4 equalizing the dimensionality with the mass fractal dimension D_f . Goudeh *et al.*⁴⁷
 5 calculated the D_f evolution as a function of the number of the primary particles n_p ,
 6 consisting the fractal agglomerate:

$$7 \quad D_f = \frac{1.9 \ln^2 \bar{n}_p - 2.6 \ln \bar{n}_p + 3}{\ln^2 \bar{n}_p - \ln \bar{n}_p + 1},$$

$$8 \quad 2 < \bar{n}_p < 400 \quad (3.1)$$

9 Using eq. 3.1, we have estimated the average number of the primary particles \bar{n}_p
 10 per agglomerate from Dynamic Light Scattering (DLS) data as analyzed previously.³⁵
 11 More particularly, we studied the agglomerate size in solution for various sonication
 12 protocols. The DLS data show that the agglomerate size in ethanol was 150 ± 12 nm for
 13 the 5-25 NPs and 160 ± 8 nm for the 1-25 NPs. Based on the DLS and TEM data, we
 14 used an average particle number $\bar{n}_p = 8$. Our theoretical simulations show that using
 15 \bar{n}_p in the range of 6-10, the experimentally observed ΔT trends can be credibly
 16 reproduced.

17 For experiments of particle suspensions in a cuvette, it has been shown⁵⁴⁻⁵⁶ that
 18 the photothermal efficiency of particles to convert the absorbed photons into heat is
 19 given by the expression:

$$20 \quad \eta = \frac{hA(T_{max} - T_{amb}) - Q_0}{P(1 - 10^{-A_\lambda})} \quad (3.2)$$

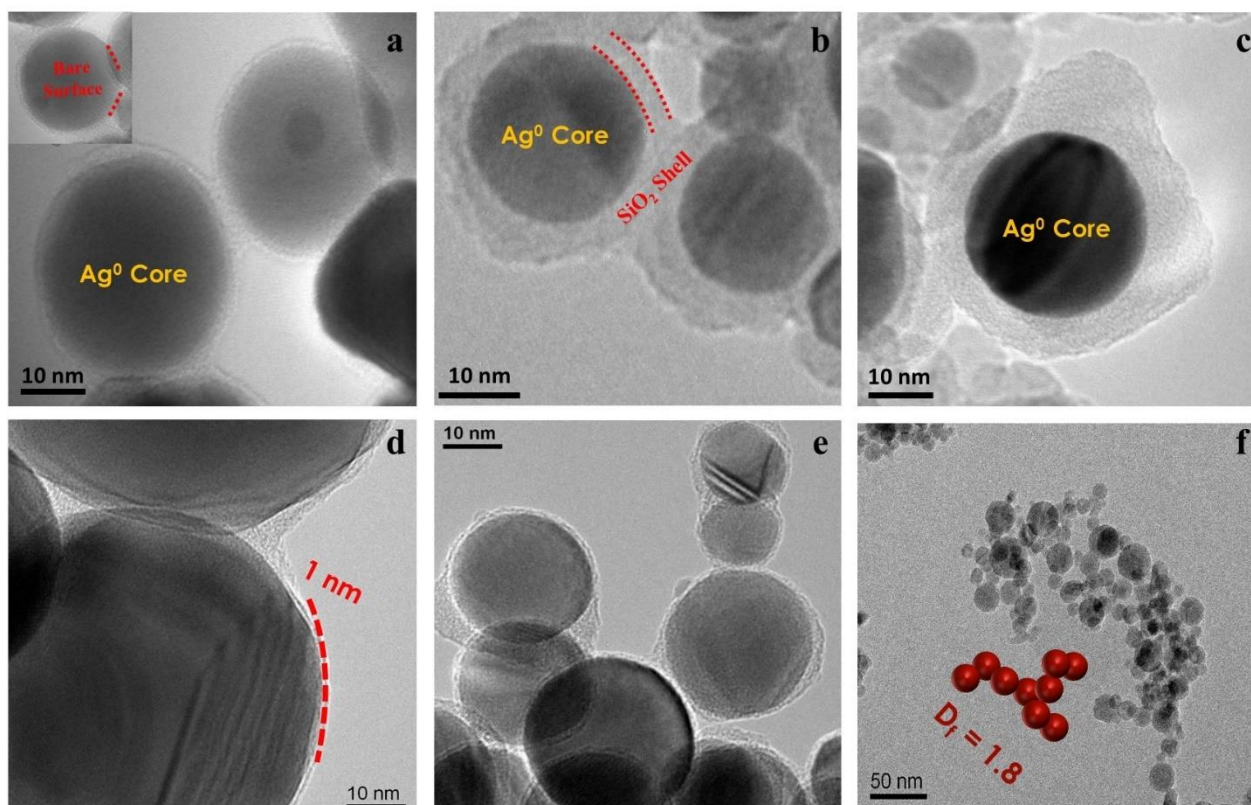
21 where A is the surface area of the cuvette, h the heat transfer coefficient, T_{amb} is
 22 the ambient temperature, fixed at 23°C , T_{max} the equilibrium temperature, Q_0 the energy
 23 input by the cuvette and solvent, P the incident's light power and A_λ is the optical
 24 density of the solution.

25 Overall, in the present work we studied the role of the parameters in eq. 1.33 &
 26 1.37 as follows: the effect of Ag core size, was studied for diameters of 15 nm and 25 nm.
 27 The effect of the interparticle distance ρ in eq. 1.33, was studied using particles with
 28 shell of variable thickness, corresponding to values in the range of 1 up to 5 nm. The
 29 parameters P , I of the irradiance beam were studied by controlling either the lamp

1 irradiation power or the focus of the sunlight. The effect of the surrounding medium
 2 was studied *via* the maximum T_{max} as parametrized by κ 1.33, or *via* the ΔT kinetics as
 3 parametrized by D_s in eq. 1.37.

4 3.3 Results/Discussion

5 3.3.1 Core-shell Quality and Control of Interparticle Distance



6 **Figure 3.1.** TEM images of (a) 1-25 SiO₂@Ag⁰ NPs (SiO₂ thickness=1 nm), (b) 3-25
 7 SiO₂@Ag⁰ NPs (SiO₂ thickness=3 nm) and (c) 5-25 SiO₂@Ag⁰ NPs (SiO₂ thickness=5
 8 nm), (d) the ultrathin SiO₂ layer, (e)-(f) the fractal geometry of 1-25 SiO₂@Ag⁰ NPs.

9 Figure 3.1 shows TEM images of the core-shell Ag⁰@SiO₂ NPs, with
 10 $d_{XRD}=25\text{nm}$. At 8% SiO₂ content, Figure 3.1a & d show the Ag⁰ particle coated by an
 11 ultrathin (1nm), amorphous SiO₂ layer. The SiO₂ layer appears as homogeneous patches
 12 as well, leaving partially uncoated Ag⁰ surface, see inset in Figure 3.1a. By increasing
 13 the SiO₂ layer thickness (Figures 3.1b-c), a hermetic encapsulation of the metallic Ag⁰
 14 core is achieved, and the SiO₂-shell thickness determines the interparticle distance. The
 15 data in Table 3.1, show that an upper limit of the SiO₂-coating thickness of 5nm can be
 16 achieved by our FSP set-up using 27% *wt* SiO₂ in the injected precursor through the
 17 ring.

Table 3.1. Characteristics of Ag⁰@SiO₂ NPs.

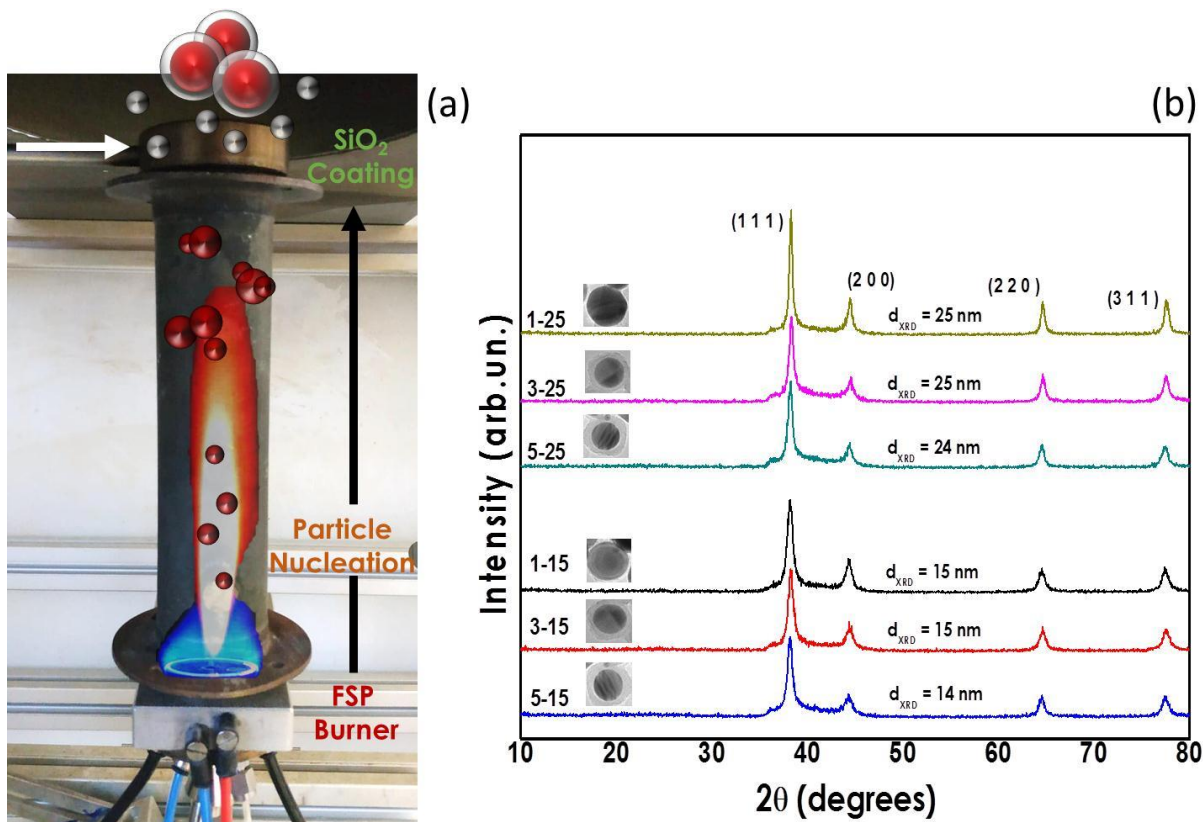
Material*	wt% SiO₂	SiO₂-Shell Thickness (nm)	SSA (m²/g)	d_{XRD} (nm)	Particle diameter** d_{TEM} (nm)
1-15	10	1±0.5	29±3	14±0.5	15±3.5
3-15	20	3±1.0	62±5	15±0.5	15±3.5
5-15	25	5±1.0	61±5	15±0.5	14±4.0
1-25	8	1±0.5	25±3	25±1.0	25±3.5
3-25	20	3±1.0	51±5	24±1.0	25±3.0
5-25	27	5±1.0	56±5	24±1.0	24±5.0

*The naming of each material is as follows: [SiO₂-Thickness]-[Ag⁰-Size], i.e. the first number indicates the SiO₂ thickness, while the second number refers to the Ag⁰ core particle diameter in nm.

**The size distribution and the shell thickness is estimated by TEM images using ImageJ.

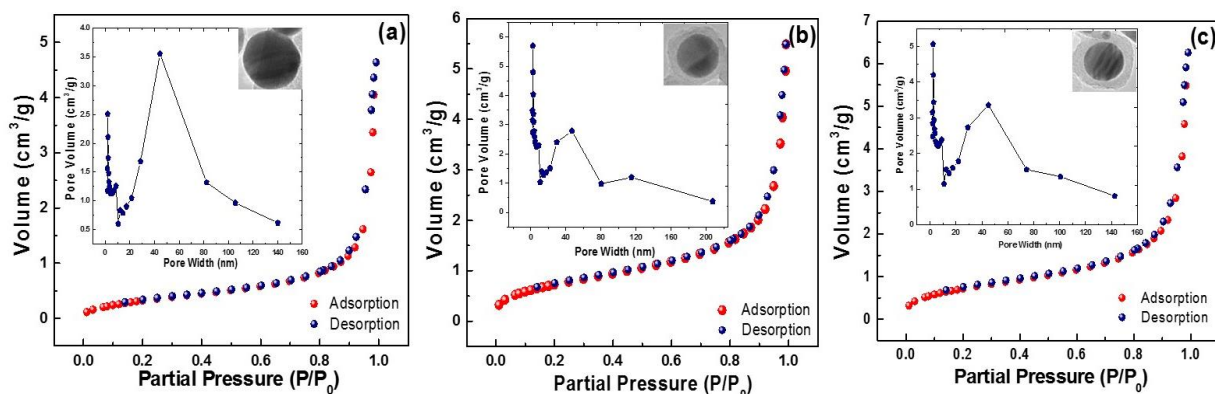
1

2 Figure 3.2 shows the pXRD patterns of the as-prepared Ag⁰ NPs for varying SiO₂
3 layer thickness. The diffraction peaks correspond to (111), (200), (220), (311) crystal
4 planes of Ag, with crystal size fixed at 15 and 25 nm, as listed in Table 3.1. As expected,
5 higher Ag molarity and precursor feed rates yield larger Ag core particles, as the
6 concentration inside the sprayed droplets and, subsequently, the high-temperature-
7 residence-time regime are increased, resulting to improved crystallinity as well.



1 **Figure 3.2.** (a) Schematic of the enclosed FSP reactor and the one-step SiO₂ coating of
 2 the, in-flight, Ag particles. (b) XRD pattern of SiO₂@Ag⁰ NPs varying size and shell
 3 thickness as listed in Table 3.1.

4

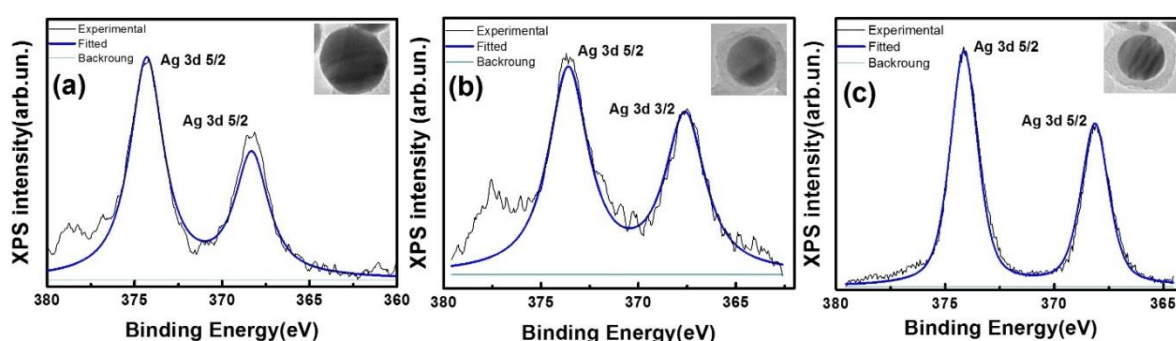


5 **Figure 3.3.** BET isotherms for the (a) 1-25 SiO₂@Ag⁰ NPs (b) 3-25 SiO₂@Ag⁰ NPs
 6 (c) 5-25 SiO₂@Ag⁰ NPs. *Insets:* BJH pore distribution plot.

7

1 Figure 3.3 shows BET isotherms and the specific surface area (SSA)
 2 measurements for the materials 1-25, 3-25, 5-25. The SSA values, listed in Table 3.1,
 3 show that by increasing the SiO₂ shell thickness, higher surface area was achieved, in
 4 agreement with previous study.⁴⁸ The data in Table 3.1 show that when shell thickness
 5 is over 3 nm, then the SiO₂ determines the surface area, while larger Ag core results in
 6 smaller surface area, according to the well-known trend for gas-phase particle
 7 formation.⁴⁵

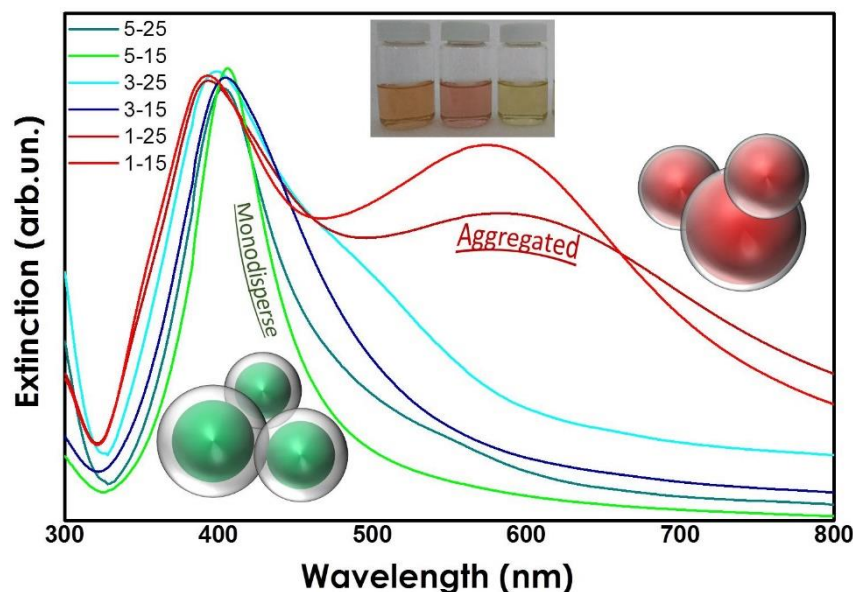
8 **Figure 3.4.** XPS Spectra (a) 1-25 SiO₂@Ag⁰ NPs (b) 3-25 SiO₂@Ag⁰ NPs (c) 5-25



9 SiO₂@Ag⁰ NPs for the core level of Ag 3d 5/2 and Ag 3d 3/2 peaks.

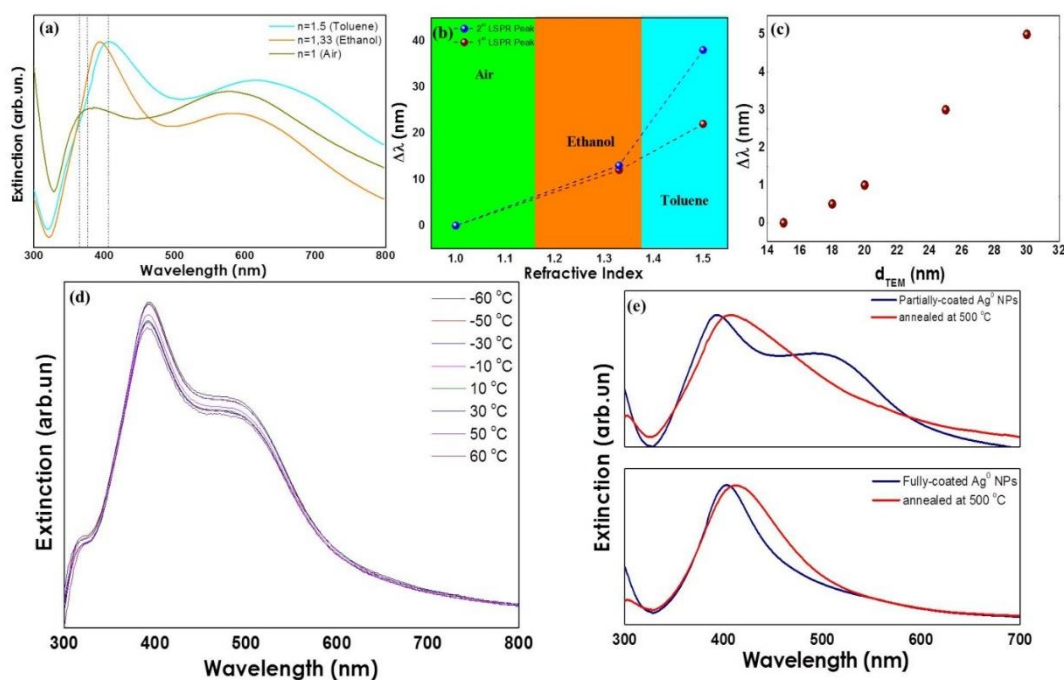
10 Figure 3.4 shows high-resolution core level spectra for the Ag3d of 1-25, 3-25
 11 and 5-25 materials, composed of doublet 3d_{5/2} and 3d_{3/2} peaks. They were found to have
 12 binding energy of 368.25 eV and 374.25 eV/368.15 eV and 374.15 eV/367.5 eV and
 13 373.5 eV, respectively, which shows that the splitting of the 3d doublet of Ag is 6.0
 14 eV⁵⁷. This splitting difference indicates the formation of metallic silver nanoparticles
 15 (Ag⁰) and confirms the protection of the SiO₂ layer against the formation of oxidized
 16 Ag species, even in the case of the ultrathin encapsulation (Figure 3.4a). This suggests
 17 that the SiO₂ coating can inhibit the oxidation of nanosilver core.

1 3.3.2 Regulation of Local Surface Plasmon Resonance



2 **Figure 3.5.** UV/Vis spectra for suspensions of 1-15,25 (red), 3-15,25 (blue) and 5-15,25
3 (green) Ag@SiO₂ NPs of same particle size. *Inset:* Photos of the particle suspensions.
4 The particle schematics indicate the effect of shell thickness.

5 Figure 3.5 depicts the UV-Vis spectra for suspensions of 1-25, 3-25 and 5-25
6 Ag⁰@SiO₂ NPs in ethanol suspensions. Although the plasmonic resonance for isolated
7 Ag⁰ NPs should occur typically at 390 nm⁵⁸, the resonance peak for the SiO₂-coated 3-
8 25 and 5-25 NPs is red-shifted towards 410nm, due to the increased dielectric presence
9 of the SiO₂ shell. The patchy-coated 1-25 material displays an additional strongly red-
10 shifted LSPR peak due to plasmonic coupling, where multipolar mode arise. In non-
11 monodisperse ensembles, the multiple LSPR peaks and band broadenings reflect the
12 extent of particle aggregation^{3,59}. This is clearly demonstrated for the 1-25 Ag⁰@SiO₂
13 where a strong plasmonic coupling is detected, allowed by the ultrathin SiO₂-shell
14 thickness. On the contrary, 5-25 exhibits a single plasmon resonance, approaching the
15 case of isolated Ag particles, as predicted by Mie.



1

2 **Figure 3.6.** (a) UV-Visible spectra of 1-25 material varying dielectric mediums.
 3 Wavelength-shift of 1-25 versus (b) refractive index of the dielectric medium and (c)
 4 the Ag particle size d_{TEM} . (d) UV-Visible spectra of 1-15 for various ambient
 5 temperatures. (e) UV-Visible spectra of patchy coated 1-25 and fully coated 5-25 NPs.
 6 The red lines correspond to post-calcined particles, annealed at 500°C for 1 hour.

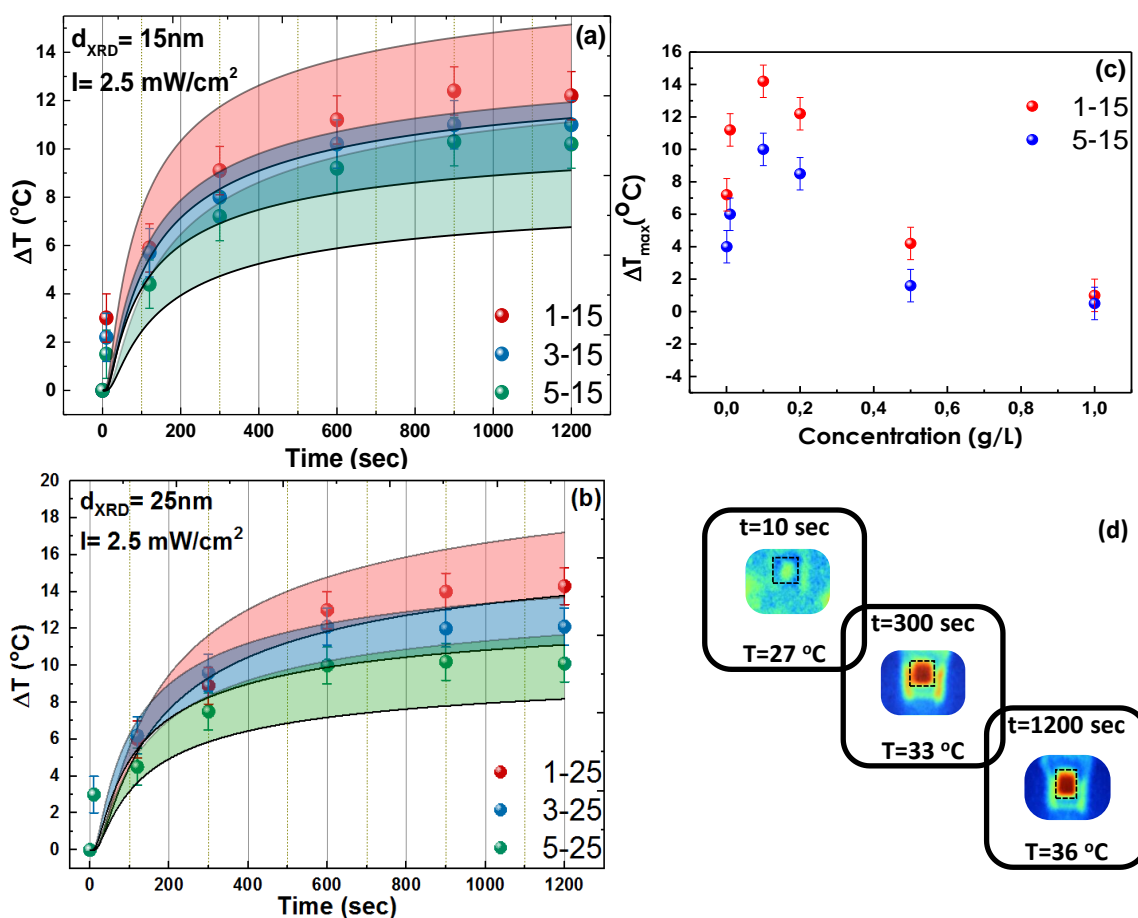
7 Moreover, the plasmon resonance was further regulated, by engineering the
 8 surrounding environment and particle size, where for both cases a red-shift of plasmon
 9 frequency is expected, as seen in Figure 3.6a-c. Increased particle size, in particular,
 10 causes retardation effects, and the incident electric field is not uniform over the whole
 11 particle. The coating efficiency was further proved by annealing the as prepared 1-25
 12 and 5-25 NPs. In both cases, the increased particle size is evident due to plasmon band
 13 broadening, indicating that SiO₂ layer occasionally may encapsulate more than one Ag
 14 core. The broadening is less pronounced in thick shells due to the already well-separated
 15 Ag particles.

16 3.3.3 Thermoplasmonic Performance

17 3.3.3.1 Particles in liquid suspension irradiated by Simulated Solar Light

18 Under simulated solar-light irradiance, 1 mg SiO₂@Ag⁰ NPs dispersed in 10 ml
 19 ethanol achieved temperature rise of several °C, as shown in Figure 3.7a & b for 15nm
 20 and 25nm Ag⁰ NPs respectively. Specifically, the fully coated 3-15 and 5-15 materials

1 achieved a heat generation that resulted in the suspension's temperature rise from 24 °C
 2 up to $T_{\max}=35\pm 1$ °C. 1-15 material was a slightly better heat source, increasing the
 3 temperature by $\Delta T_{\max}=12\pm 1$ °C, i.e. from 24 to 36 °C. As a background measurement, a
 4 SiO₂ NPs/ethanol suspension yielded a $\Delta T_{\max}= 6\pm 1$ °C. Figure 3.7b shows that upon
 5 increasing the Ag particle size to 25 nm, the photothermal conversion is improved, with
 6 a $T_{\max}= 38\pm 1$ °C ($\Delta T_{\max}=14\pm 1$ °C) for the 1-25, making it the most efficient heater
 7 compared to the fully encapsulated 3-25 and 5-25 materials and the smaller Ag
 8 particles, 1, 3 & 5-15, as well.



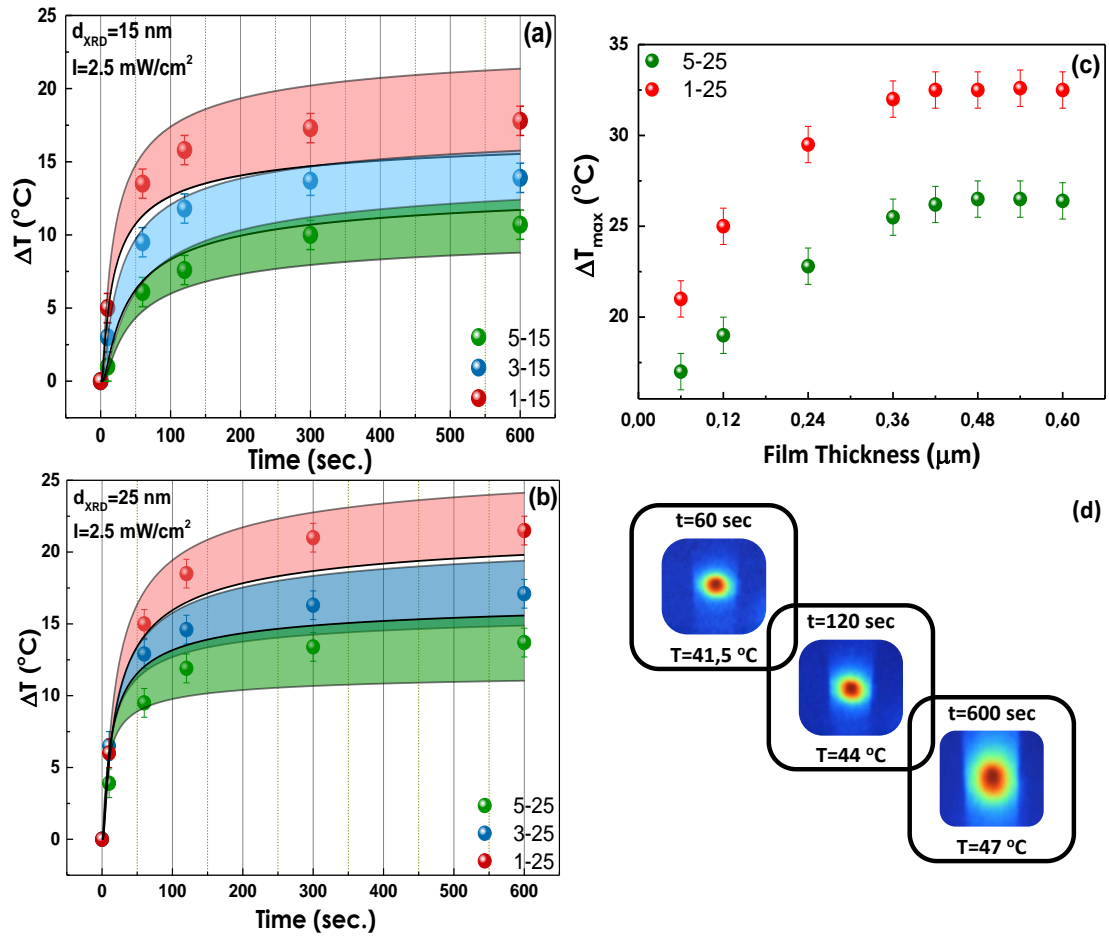
9

10 **Figure 3.7.** Time-temperature profile of 1 mg SiO₂@Ag⁰ NPs dispersed in 10 ml
 11 ethanol for (a) $d_{XRD} = 15$ nm and (b) $d_{XRD} = 25$ nm, for 20 minutes. The colored
 12 bands are attributed to ΔT theoretical calculations, calculated by eq. 6. (c) Temperature
 13 variations of particle suspension versus the concentration. (d) Infrared images of the
 14 temperature distribution for a 0.1g/Lt dispersion of 1-15 samples, as recorded from
 15 above the cuvette by the thermal imager, at 10, 300 and 1200sec irradiation. The dotted
 16 regions display the cuvette bounds.

1 *Effect of Particle concentration:* Figure 3.7c shows the thermoplasmonic
2 efficiency of 1-25 and 5-25 NPs at varying concentration of particles in the suspension.
3 A bell-shaped trend is observed with a maximum ΔT observed for the $C=0.1\text{g/Lt}$
4 suspension. According to Figure 3.7c, for dilute suspensions ($C<0.1\text{ g/Lt}$), ΔT is
5 increasing in proportion to particle concentration. At higher particle concentrations,
6 optical opaqueness causes the quenching of photoexcitation and photothermal
7 efficiency of the NPs. Importantly, the infrared-camera photos shown in Figure 3.7d for
8 a 0.1g/Lt dispersion of 1-15 NPs show that the heat is diffused in the whole suspension's
9 volume, indicating the measured T_{max} is the homogenized equilibrium bulk
10 temperature, in accordance with theory for collective heating.²⁹

11 3.3.3.2 *Particles on a Glass Film*

12 *Simulated Solar Light:* For a film ($1\times 4\text{ cm}$) of thickness $\delta=0.06\text{ }\mu\text{m}$ of $\text{Ag}^0\text{@SiO}_2$
13 NPs deposited on a glass slide, the time-temperature evolution profile is shown in
14 Figures 3.8a and b for the 15nm and 25nm Ag^0 particles respectively. A comparison
15 between the ΔT kinetics for films (Figures 3.8a, b) vs. suspensions (Figures 3.7a, b)
16 reveals that temperature rise was faster in film geometry. The SiO_2 -shell thickness
17 exerts a strong effect on ΔT . Specifically, the patchy-coated 1-15 film yield $\Delta T_{\text{max}}=18\pm 1$
18 $^\circ\text{C}$ that is 8°C higher than the $\Delta T_{\text{max}}=10\pm 1\text{ }^\circ\text{C}$ achieved by the fully-coated 5-15 NPs.



1 **Figure 3.8.** Time-temperature profile of $\delta=0.06 \mu\text{m}$ (0.25mg) $\text{SiO}_2@\text{Ag}^0$ NPs
2 deposited in film via dropcasting for (a) $d_{XRD} = 15 \text{ nm}$ and (b) $d_{XRD} = 25 \text{ nm}$, for the
3 first 10 minutes. (c) Maximum ΔT profile for various film thickness for 1-25 and 5-25
4 NPs. (d) infrared images of the samples, as recorded by the thermal camera at 60, 120
5 and 600 sec illumination. The colored bands are attributed to ΔT theoretical
6 calculations, calculated by eq. 6.

7 In Figure 8b, the ΔT kinetics for the 25 nm Ag^0 particles shows that the patchy-
8 coated 1-25 material is the most efficient heat source in film geometry, yielding $\Delta T_{max} =$
9 $22 \pm 1 \text{ }^\circ\text{C}$. We notice the 1-25 material achieved the highest ΔT_{max} in the liquid
10 suspension (14°C) as well. The effect of film-thickness δ on the thermoplasmonic
11 performance is presented in Figure 3.8c for the 1-25 & 5-25 materials, i.e. patchy vs.
12 fully coated Ag NPs. Based on the data of Figure 3.8c, we observe that for both types
13 of particles, there is a continuous dependence ΔT_{max} on δ for up to $\delta \sim 0.4 \mu\text{m}$, while ΔT
14 $_{max}$ reaches seemingly a plateau for $\delta > 0.4 \mu\text{m}$. A limiting $\Delta T_{max} = 25 \pm 1 \text{ }^\circ\text{C}$ is achieved by
15 5-25 NPs, while the patchy-coated 1-25 NPs yield a higher $\Delta T_{max} = 33 \pm 1 \text{ }^\circ\text{C}$. Thus, the

1 enhanced proximity of Ag⁰ NPs in the 1-25 material promotes an improved
2 photothermal conversion. We notice the limiting $\delta=0.4\ \mu\text{m}$ is the same for the two types
3 of particles, indicating that this is not correlated with the shell thickness, but rather with
4 the optical opaqueness imposed by the thick films.

5 *Theoretical Analysis:* Using the theoretical equations 4 & 6 and the medium's
6 thermal properties, as listed in Table S1 of the Supporting Information, theoretical
7 values of ΔT vs. time of irradiation were calculated. The calculated ΔT vs. time for the
8 1-15 & 1-25 particles are presented by the red-colored belt in Figure 3.7a,b & 3.8a,b.
9 The width of the theoretical-belt stems from the use of the particle size distribution,
10 instead of a single particle diameter. In our calculations, the interparticle distance ρ and
11 the absorption cross section σ_{abs} (eq 3c) were calculated over the particle size
12 distribution estimated from a TEM image (Figure S1), as suggested by Baffou *et al.*²⁸
13 and shown in Table S3. In a similar manner the theoretical values for the 3-15, 3-25, 5-
14 15 & 5-25 materials are depicted as blue and green belts in Figure 3.8a,b respectively.
15 This analysis shows that the particle size distribution by $\pm 5\text{nm}$ causes a variation on the
16 ΔT_{max} by ± 3 degrees in all cases, studied herein. This analysis provides a key-
17 conclusion, which assuming the particle separation is equal to the SiO₂-shell thickness,
18 predicts satisfactory theoretical ΔT evolution with time for all materials studied.
19 Therefore, given the non-monodisperse character of the SiO₂@Ag⁰ NPs, this study
20 provides evidence that the shell thickness can, to a good approximation, be considered
21 as the determining separator of the Ag⁰-Ag⁰ coupling, and, *via* this spacing effect, the
22 tuner of the collective thermal effects in conjunction with the LSPR profile in Figure
23 3.5. We underline that despite the polydispersity of the flame-made Ag⁰ NPs, we can
24 use Baffou's expression²⁸ to simulate the experimental trends to a satisfactory degree
25 assuming a fractal dimensionality for the non-monodispersed Ag@SiO₂
26 nanoaggregates dispersed in solvent.

27 Overall, the present data can be summarised as follows:

28 [i] Comparing the kinetic data between liquid suspension and films in Figure
29 3.7a-b & 3.8a-b, we observe that T_{max} is attained at earlier times in films, i.e. within
30 $t\sim 10\text{min}$ vs. $\sim 15\text{min}$ in liquid suspensions. This trend was consistently observed for all
31 the tested Ag⁰- particle sizes and SiO₂-shell thicknesses.

1 [ii] ΔT_{\max} (liquid suspensions) $<$ ΔT_{\max} (films), making film the superior
2 geometry. The optimal concentration of the particle suspension was 0.1 g/Lt, while in
3 the case of film, the most efficient thickness δ was at 0.5 μ m.

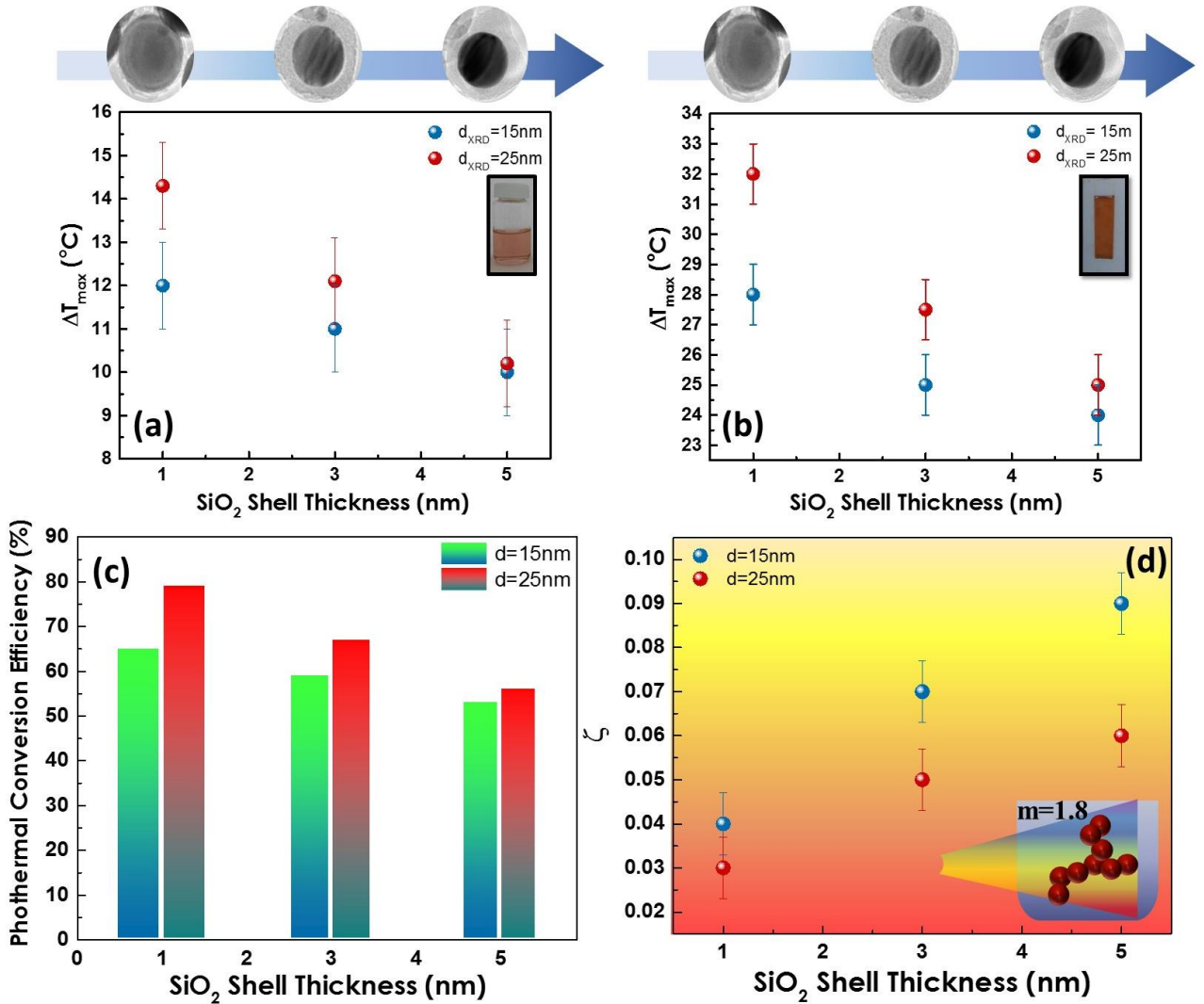
4 [iii] the ΔT_{\max} values, summarized in Figure 3.9a & b, demonstrate the superiority
5 of the film geometry and single out the 1-25 material as the most efficient heat nano-
6 source in this work.

7 The ΔT kinetics and ΔT_{\max} , in the case of film, are attributed to lower specific
8 heat capacity and higher thermal conductivity of the glass-support than ethanol, as well
9 as, to the tighter interaction among the deposited plasmonic NPs. According to Figure
10 3.8a & b, for the thin SiO₂ shells, the larger Ag⁰ NPs (25nm) show higher ΔT_{\max} , and
11 this can be attributed to absorption domination over scattering ($\sigma_{\text{abs}} > \sigma_{\text{sca}}$), as predicted
12 by Mie¹. However, the SiO₂-shell exerts a significant damping effect on the values of
13 the equilibrium ΔT_{\max} increase. When the coating is hermetic (~5nm), the size of the
14 Ag⁰ NPs makes no difference. These trends hold true for any geometry, both for
15 particles on film and liquid suspension.

16 According to Baffou²⁹, the plasmonic heating of a NP ensemble can be attributed
17 to [1] a thermal contribution of the NP itself plus [2] the collective effects of
18 neighboring NPs. Upon decreasing the interparticle distance, i.e. ultrathin SiO₂ shell,
19 the contribution of collective thermal effects is enhanced, i.e. as evidenced by the higher
20 ΔT_{\max} of patchy coated 1-25 Ag⁰@SiO₂, shown in Figure 3.9b.

21 Using eq. 3.2, the photothermal efficiency (η) was calculated for the particle
22 suspension, as shown in Figure 3.9c. The baseline energy Q_0 was calculated by
23 irradiating [ethanol + the quartz cuvette], while the [hA] parameter was calibrated by
24 an ethanol solution. As predicted, the 1-25 material converts the absorbed photon
25 energy into heat more efficiently than the rest of the samples, yielding ~80% efficiency.
26 Figure 3.9d shows the ζ parameter for a fractal agglomerate irradiated in a suspension,
27 where the value of the dimensionality parameter (m) is equal to the fractal dimension
28 $D_f = 1.8$ of the FSP-made nanoaggregates. The number of primary particles in each
29 fractal was 6-8, estimated by DLS measurements. For all the used materials, the
30 resulting value is $\zeta \ll 1$, verifying that the homogeneous collective heating and the
31 observed bulk heating as the dominant photothermal regime in these dispersed NP
32 ensembles.

1

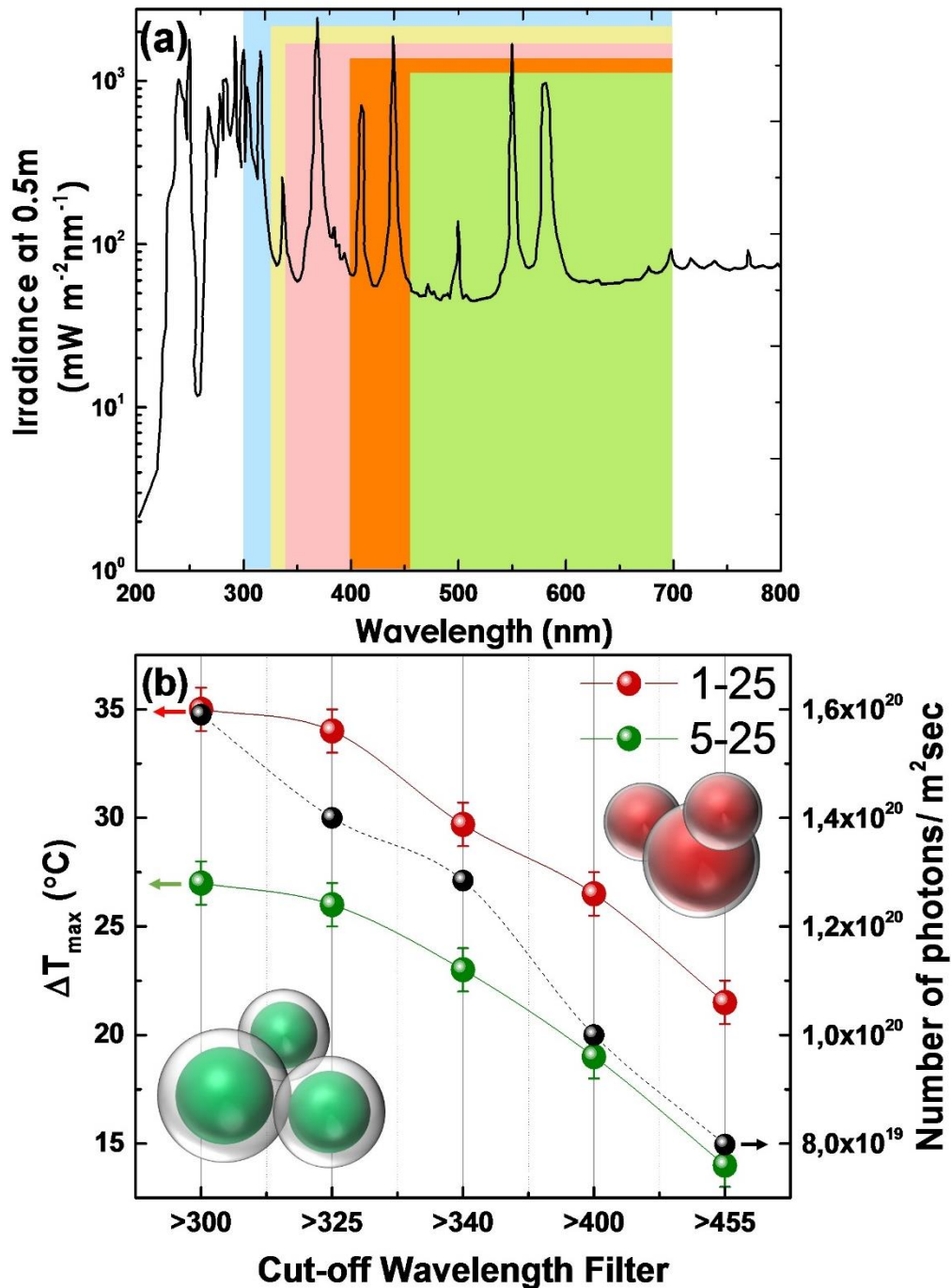


2 **Figure 3.9.** Equilibrium ΔT_{\max} for Ag⁰@SiO₂ NPs (a) in suspension and (b)
 3 deposited on film for particle size of 15 nm (blue) and 25 nm (red) versus the SiO₂-
 4 shell thickness. (c) Photothermal efficiency, estimated by eq 8, and (d) the
 5 dimensionless parameter ζ , calculated by eq. 5, versus the SiO₂-shell thickness and
 6 average particle size. The dimensionality (fractal dimension) was calculated by eq. 7.

7

8 *Effect of wavelength filtering:* In an effort to understand the effect of the
 9 irradiation's wavelength, we have studied our best-performing material, 1-25 on film
 10 in comparison vs. the 5-25 on film, under selective filtering of specific wavelength
 11 ranges of our Xenon lamp, as shown in Figure 3.10a. The resulting ΔT_{\max} vs. λ -range
 12 are displayed in Figure 3.10b. To facilitate a quantitative understanding, the black
 13 symbols in Figure 3.10b show the photon density, i.e. [the number of photons] [per m²]

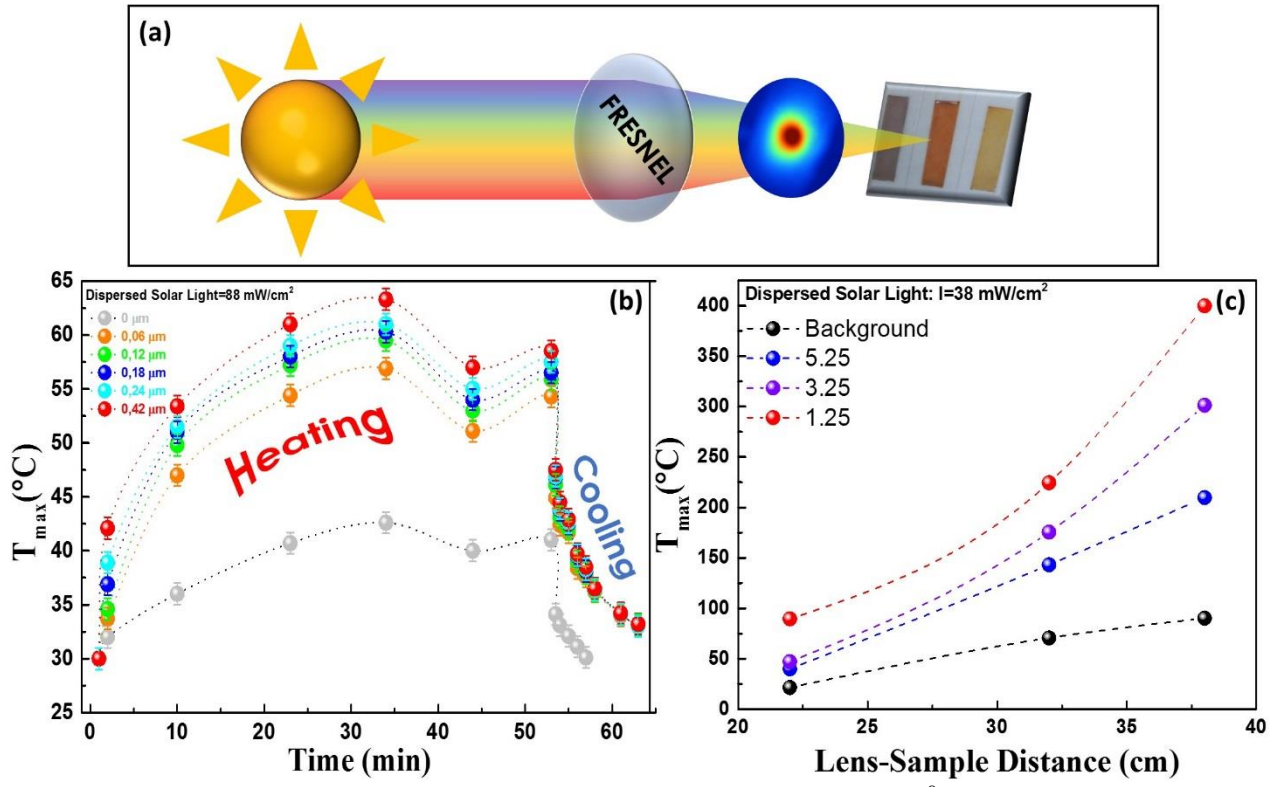
1 [per sec]. There is a decrease of ΔT_{\max} that parallels the photon density, i.e. compare λ
 2 > 300 nm vs. $\lambda > 325$ nm photons, having photon density $1,6 \times 10^{20}$ and $1,4 \times 10^{20}$
 3 respectively. By allowing only the $\lambda > 455$ photons, ΔT_{\max} is further decreased, but not
 4 to 0°C .



5 **Figure 3.10:** (a) Spectral irradiance of Arc Xenon Lamp (Model 6293; 1000W). (b)
 6 Maximum temperature rise of 1-25 and 5-25 material on film ($\delta=0.5 \mu\text{m}$), by filtering
 7 the wavelength range.

1 This observation, considering that cutting of wavelengths $>455\text{nm}$, the nominal
 2 LSPR peak at 410nm is not excited, depicted in Figure 3.5, indicates that the photons
 3 at $>455\text{nm}$ are able to induce thermoplasmonic effects for the 1-25 material, as scaled
 4 by the photon density. Surprisingly, even in the case of fully coated 5-25, where only
 5 the main LSPR excitation at 410nm is evidenced as dominant, a non-negligible
 6 $\Delta T_{\text{max}}=13^\circ\text{C}$ was achieved, even though the LSPR was filtered by $\lambda > 455$ photons,
 7 indicating the effect of particle polydispersity in the plasmon band broadening.

8 *Non-Focused Solar Light:* The photothermal performance of the best-performing
 9 1-25 film, was investigated under natural sunlight as well. Films of varying thickness δ
 10 were placed horizontally at non-focused, ambient sunlight, corresponding to irradiance
 11 $I=88\text{ mW/cm}^2$.



12 **Figure 3.11:** (a) Schematic of solar illumination of $\text{SiO}_2@\text{Ag}^0$ NPs on film under
 13 concentrating light using a Fresnel lens. (b) ΔT kinetics of 1-25 NPs on films, varying
 14 film thickness under dispersed solar light. (c) Equilibrium T_{max} of 1-25, 3-25 and 5-25
 15 NPs under concentrated light varying lens-sample distance.

16 The glass substrate produced a baseline-temperature $T_{\text{amb}}=40^\circ\text{C}$. Figure 3.11b
 17 shows the ΔT kinetics for various film thickness, $\delta=0.06$ up to $0.42\ \mu\text{m}$. The achieved
 18 temperature variation was significant, exceeding 60°C for the $0.42\ \mu\text{m}$ film, i.e. 1.5 mg

1 NPs. Taking into account the glass-substrate heating by the sun, the equilibrium ΔT_{\max}
2 for the $0.42\mu\text{m}$ film was 24°C under this non-focused solar light.

3 *Focused Solar Light:* The 1-25, 3-25 and 5-25 NPs were illuminated under
4 focused solar light, using a Fresnel lens ($28\times 28\text{cm}$) of 35 cm focal length, as shown in
5 Figure 3.11a. This corresponded to significantly amplified irradiance density ($I=53$
6 W/cm^2). Figure 3.11c shows an extremely rapid (~ 1 sec) plasmon-induced temperature
7 rise for the optimal $\delta=0.5\mu\text{m}$ films. The background temperature of the glass was
8 $T_{\max}=90^\circ\text{C}$. In Figure 3.11c, we observe that the positioning of the film vs. the focal
9 point of the lens, exerted a strong effect. This is attributed to maximization of the
10 irradiance density at the focal point, i.e. 38cm from the lens. As expected, the most
11 efficient heat nano-source was the 1-25 material, yielding a remarkable $T_{\max}\sim 400^\circ\text{C}$
12 when positioned at the focal point. Importantly, under concentrated solar light, the
13 effect of the shell thickness in photothermal conversion becomes prominent: the 5-25
14 film achieved $\Delta T_{\max} = 120^\circ\text{C}$, while the yield of the patchy-coated 1-25 film was ΔT_{\max}
15 $= 310^\circ\text{C}$.

16 **3.4 Conclusions**

17 The present data reveal that optimization of the Ag^0 particle size & SiO_2 -shell
18 thickness by FSP, allows engineering of core/shell $\text{Ag}^0@ \text{SiO}_2$ nanomaterials with
19 controllable thermoplasmonic properties. When the photothermal conversion
20 technology is pursued, the patchy-coated ($< 1\text{nm}$ shell) $\text{Ag}^0@ \text{SiO}_2$ nanomaterials are the
21 most promising. The particles were either dispersed in ethanol or deposited on glass
22 film and the temperature variation was monitored, under the tailoring of particle size
23 distribution and SiO_2 shell thickness. The most efficient heat source was proved to be
24 the larger Ag core (25nm) encapsulated by ultrathin SiO_2 layer ($\sim 1\text{nm}$). This
25 observation is in agreement with Mie theory and Baffou's work about the collective
26 thermal effects and enable us to control the thermoplasmonic performance, by adjusting
27 the neighbouring Ag-Ag coupling, i.e. tuning the SiO_2 shell. In liquid suspension, the
28 yield was $\Delta T_{\max} = 14^\circ\text{C}$, while on films was $\Delta T_{\max} = 32^\circ\text{C}$, showing the effect of
29 surrounding medium's thermal properties and film's superior geometry. Selective
30 filtering of the irradiation wavelength revealed that ΔT_{\max} parallels the photons density,
31 even for wavelengths $\lambda > 455\text{ nm}$, which are away from the main LSPR peak at $\sim 410\text{nm}$.
32 This is attributed to the particle size distribution of the flame-synthesized materials, as

1 well as the plasmonic coupling for the case of thin SiO₂ encapsulation. Under focused
2 ambient solar light, the 1-25 SiO₂@Ag⁰ nanomaterials, yield remarkable $\Delta T_{\max} \sim 310$
3 °C. These findings add new insights about the multiple role of the SiO₂ shell, as the
4 surrounding medium, agglomeration limiter and plasmonic separator and a new way to
5 control and monitor the photothermal response of Ag⁰ NPs for the promising
6 applications in Thermoplasmonics.

7

8 **References**

- 9 (1) Kreibig, U.; Vollmer, M. *Optical Properties of Metal Clusters*; Springer, 1995.
- 10 (2) Bohren, C. F.; Huffmann, D. R. *Absorption and Scattering of Light by Small*
11 *Particles*; Wiley-Interscience: New York, 2010.
- 12 (3) Halas, N. J.; Lal, S.; Chang, W.-S.; Link, S.; Nordlander, P. Plasmons in Strongly
13 Coupled Metallic Nanostructures. *Chemical Reviews* **2011**, *111* (6), 3913–3961.
14 <https://doi.org/10.1021/cr200061k>.
- 15 (4) Mie, G. Beiträge Zur Optik Trüber Medien, Speziell Kolloidaler Metallösungen.
16 *Ann. Phys.* **1908**.
- 17 (5) El-Sayed, M.; Link, S. OPTICAL PROPERTIES AND ULTRAFAST
18 DYNAMICS OF METALLIC NANOCRYSTALS. *Annu. Rev. Phys. Chem.* **2003**,
19 *54*, 331–366. <https://doi.org/10.1146/annurev.physchem.54.011002.103759>.
- 20 (6) El-Sayed, M.; Link, S. Spectral Properties and Relaxation Dynamics of Surface
21 Plasmon Electronic Oscillations in Gold and Silver Nanodots and Nanorods. *J.*
22 *Phys. Chem.* **1999**, *103*, 8410–8426.
- 23 (7) Lal, S.; Link, S.; Halas, N. J. Nano-Optics from Sensing to Waveguiding. In
24 *Nanoscience and Technology*; Co-Published with Macmillan Publishers Ltd, UK,
25 2009; pp 213–220. https://doi.org/10.1142/9789814287005_0022.
- 26 (8) Schuller, J. A.; Barnard, E. S.; Cai, W.; Jun, Y. C.; White, J. S.; Brongersma, M. L.
27 Plasmonics for Extreme Light Concentration and Manipulation. *Nature Materials*
28 **2010**, *9* (3), 193–204. <https://doi.org/10.1038/nmat2630>.
- 29 (9) Anker, J.; Hall, W.; Lyandres, O.; Shah, N.; Zhao, J.; Van Duyne, R. Biosensing
30 with Plasmonic Nanosensors. *nature materials* **2008**, *7*.

- 1 (10) Oldenburg, N., S. J. Averitt, R. D. Westcott, S. L. Halas. Nanoengineering of
2 Optical Resonances. *Chem. Phys. Lett.* **1998**, 288 (2–4), 243–247.
3 [https://doi.org/10.1016/S0009-2614\(98\)00277-2](https://doi.org/10.1016/S0009-2614(98)00277-2).
- 4 (11) Van Duyne, R.; Jeanmarie, D. L. Surface Raman Spectroelectrochemistry, Part
5 1: Heterocyclic, Aromatic, and Aliphatic Amines Adsorbed on the Anodized Silver
6 Electrode. *J. Electroanal. Chem.* **1977**, 84, 1–20.
- 7 (12) Baffou, G. Q. Thermo-Plasmonics: Using Metallic Nanostructures as Nano-
8 Sources of Heat. *Laser Photonic Rev.* **2012**, 1–17.
9 <https://doi.org/10.1002/lpor.201200003>.
- 10 (13) Baffou, G.; Quidant, R.; García de Abajo, F. J. Nanoscale Control of Optical
11 Heating in Complex Plasmonic Systems. *ACS Nano* **2010**, 4 (2), 709–716.
12 <https://doi.org/10.1021/nn901144d>.
- 13 (14) Zeng, Z.-C.; Wang, H.; Johns, P.; Hartland, G. V.; Schultz, Z. D. Photothermal
14 Microscopy of Coupled Nanostructures and the Impact of Nanoscale Heating in
15 Surface-Enhanced Raman Spectroscopy. *The Journal of Physical Chemistry C*
16 **2017**, 121 (21), 11623–11631. <https://doi.org/10.1021/acs.jpcc.7b01220>.
- 17 (15) Jain, P.; Huang, X.; El Sayed, I.; El Sayed, M. Noble Metals on the Nanoscale:
18 Optical and Photothermal Properties and Some Applications in Imaging, Sensing,
19 Biology, and Medicine. *Acc. Chem. Res.* **2008**, 1578–1586.
20 <https://doi.org/10.1021/ar7002804>.
- 21 (16) Govorov, A. O. R. Generating Heat with Metal Nanoparticles. *nanotoday* **2007**,
22 2, 30–38. [https://doi.org/10.1016/S1748-0132\(07\)70017-8](https://doi.org/10.1016/S1748-0132(07)70017-8).
- 23 (17) Govorov, A. O. Z. Gold Nanoparticle Ensembles as Heaters and Actuators:
24 Melting and Collective Plasmon Resonances. *Nanoscale Res Lett* **2006**, 84–90.
25 <https://doi.org/10.1007/s11671-006-9015-7>.
- 26 (18) Palermo, G.; Pagnotto, D.; Ricciardi, L.; Pezzi, L.; La Deda, M.; De Luca, A.
27 Thermoplasmonic Effects in Gain-Assisted Nanoparticle Solutions. *The Journal of*
28 *Physical Chemistry C* **2017**, 121 (43), 24185–24191.
29 <https://doi.org/10.1021/acs.jpcc.7b08186>.
- 30 (19) Lai, S.; Clare, S.; Halas, N. J. Nanoshell-Enabled Photothermal Cancer
31 Therapy: Impending Clinical Impact. *Acc Chem Res.* **2008**, 41, 1842–1851.
32 <https://doi.org/10.1021/ar800150g>.

- 1 (20) Neumann, O.; Urban, A. S.; Day, J.; Lal, S.; Nordlander, P.; Halas, N. J. Solar
2 Vapor Generation Enabled by Nanoparticles. *ACS Nano* **2013**, *7* (1), 42–49.
3 <https://doi.org/10.1021/nn304948h>.
- 4 (21) Baffou, G.; Quidant, R. Nanoplasmonics for Chemistry. *Chem Soc Rev* **2014**,
5 *43*, 3898–3907. <https://doi.org/10.1039/c3cs60364d>.
- 6 (22) Baffou, G.; Polleux, J.; Rigneault, H.; Monneret, S. Super-Heating and Micro-
7 Bubble Generation around Plasmonic Nanoparticles under Cw Illumination. *J.*
8 *Phys. Chem. C* **2014**, *118* (4890). <https://doi.org/dx.doi.org/10.1021/jp411519k>.
- 9 (23) Govorov, A. O.; Fan, Z.; Neiman, A. Photothermal Effect of Plasmonic
10 Nanoparticles and Related Bioapplications. **2012**.
- 11 (24) Kang, H.; Lee, G.-H.; Jung, H.; Lee, J. W.; Nam, Y. Inkjet-Printed
12 Biofunctional Thermo-Plasmonic Interfaces for Patterned Neuromodulation. *ACS*
13 *Nano* **2018**, *12* (2), 1128–1138. <https://doi.org/10.1021/acsnano.7b06617>.
- 14 (25) Sarhan, R. M.; Koopman, W.; Pudell, J.; Stete, F.; Rössle, M.; Herzog, M.;
15 Schmitt, C. N. Z.; Liebig, F.; Koetz, J.; Bargheer, M. Scaling Up Nanoplasmon
16 Catalysis: The Role of Heat Dissipation. *The Journal of Physical Chemistry C* **2019**,
17 *123* (14), 9352–9357. <https://doi.org/10.1021/acs.jpcc.8b12574>.
- 18 (26) Powell, A. W.; Stavrinadis, A.; de Miguel, I.; Konstantatos, G.; Quidant, R.
19 White and Brightly Colored 3D Printing Based on Resonant Photothermal
20 Sensitizers. *Nano Letters* **2018**, *18* (11), 6660–6664.
21 <https://doi.org/10.1021/acs.nanolett.8b01164>.
- 22 (27) Ricciardi, L.; Sancey, L.; Palermo, G.; Termine, R.; De Luca, A.; Szerb, E. I.;
23 Aiello, I.; Ghedini, M.; Strangi, G.; La Deda, M. Plasmon-Mediated Cancer
24 Phototherapy: The Combined Effect of Thermal and Photodynamic Processes.
25 *Nanoscale* **2017**, *9* (48), 19279–19289. <https://doi.org/10.1039/C7NR05522F>.
- 26 (28) Baffou, G.; Berto, P.; Urena, E. B.; Quidant, R.; Monneret, S.; Polleux, J.;
27 Rigneault, H. Photoinduced Heating of Nanoparticle Arrays. *ACS Nano* **2013**, *7*,
28 6478–6488.
- 29 (29) Baffou, G. *Thermoplasmonics: Heating Metal Nanoparticles Using Light*;
30 Cambridge University Press, 2017.
- 31 (30) El -Sayed, M. A.; Eustis, S. Why Gold Nanoparticles Are More Precious than
32 Pretty Gold: Noble Metal Surface Plasmon Resonance and Its Enhancement of the

- 1 Radiative and Nonradiative Properties of Nanocrystals of Different Shapes. *Chem.*
2 *Soc. Rev.* **2006**, *35*, 209–217.
- 3 (31) El-Sayed, M.; Neretina, S.; Huangm Xiaohua. Gold Nanorods: From Synthesis
4 and Properties to Biological and Biomedical Applications. *ADVANCED*
5 *MATERIALS* **2009**, *21*, 4880–4910. <https://doi.org/10.1002/adma.200802789>.
- 6 (32) Lalis, A.; Tessier, G.; Plain, J.; Baffou, G. Quantifying the Efficiency of
7 Plasmonic Materials for Near-Field Enhancement and Photothermal Conversion. *J.*
8 *Phys. Chem. C* **2015**, *119*, 28586–28596. <https://doi.org/10.1021/acs.jpcc.5b09294>.
- 9 (33) Palermo, G.; Cataldi, U.; Condello, A.; Caputo, R.; Bürgi, T.; Umeton, C.; De
10 Luca, A. Flexible Thermo-Plasmonics: An Opto-Mechanical Control of the Heat
11 Generated at the Nanoscale. *Nanoscale* **2018**, *10* (35), 16556–16561.
12 <https://doi.org/10.1039/C8NR04228D>.
- 13 (34) Pezzi, L.; Palermo, G.; Veltri, A.; Cataldi, U.; Bürgi, T.; Ritacco, T.; Giocondo,
14 M.; Umeton, C.; De Luca, A. Photo-Thermal Study of a Layer of Randomly
15 Distributed Gold Nanoparticles: From Nano-Localization to Macro-Scale Effects.
16 *Journal of Physics D: Applied Physics* **2017**, *50* (43), 435302.
17 <https://doi.org/10.1088/1361-6463/aa8618>.
- 18 (35) Sotiriou, G. A.; Blattmann, C. O.; Deligiannakis, Y. Nanoantioxidant-Driven
19 Plasmon Enhanced Proton-Coupled Electron Transfer. *Nanoscale* **2016**, 796–803.
- 20 (36) Shanthil, M.; Thomas, R.; Swathi, R. S.; George Thomas, K. Ag@SiO₂ Core–
21 Shell Nanostructures: Distance-Dependent Plasmon Coupling and SERS
22 Investigation. *The Journal of Physical Chemistry Letters* **2012**, *3* (11), 1459–1464.
23 <https://doi.org/10.1021/jz3004014>.
- 24 (37) Hanske, C.; Sanz-Ortiz, M. N.; Liz-Marzán, L. M. Silica-Coated Plasmonic
25 Metal Nanoparticles in Action. *Advanced Materials* **2018**, *30* (27), 1707003.
26 <https://doi.org/10.1002/adma.201707003>.
- 27 (38) Sotiriou, G.; Gass, S.; Pratsinis, S. Hermetically Coated Nanosilver: No Ag+
28 Ion Leaching. *Materials Research Society* **2012**, 1386.
- 29 (39) Panagiota, S.; Louludi, M.; Deligiannakis, Y. EPR Study of Phenolic Radical
30 Stabilization by Grafting on SiO₂. *Chemical Physics Letters* **2009**, *472* (1–3), 85–
31 89. <https://doi.org/10.1016/j.cplett.2009.02.080>.
- 32 (40) Stathi, P.; Deligiannakis, Y.; Avgouropoulos, G.; Louludi, M. Efficient H₂
33 Production from Formic Acid by a Supported Iron Catalyst on Silica. *Applied*

- 1 *Catalysis A: General* **2015**, 498, 176–184.
2 <https://doi.org/10.1016/j.apcata.2015.03.029>.
- 3 (41) Stathi, P.; Louloudi, M.; Deligiannakis, Y. Efficient Low-Temperature H₂
4 Production from HCOOH/HCOO⁻ by [Pd⁰@SiO₂-Gallic Acid] Nanohybrids:
5 Catalysis and the Underlying Thermodynamics and Mechanism. *Energy & Fuels*
6 **2016**, 30 (10), 8613–8622. <https://doi.org/10.1021/acs.energyfuels.6b01729>.
- 7 (42) Madler, L.; Amal, R.; Teoh, W. Y. Flame Spray Pyrolysis: An Enabling
8 Technology for Nanoparticles Design and Fabrication. *Nanoscale* **2010**, 2, 1324–
9 1347. <https://doi.org/10.1039/c0nr00017e>.
- 10 (43) Pratsinis, S. Flame Aerosol Synthesis of Ceramic Powders. *Prog. Energy*
11 *Combust. Sci.* **1998**, 24, 197–219.
- 12 (44) Pratsinis, S.; Mueller, R.; Kammler, H. K.; Madler, L. Controlled Synthesis of
13 Nanostructured Particles by Flame Spray Pyrolysis. *Aerosol Science* **2002**, 33, 369–
14 389.
- 15 (45) Pratsinis, S.; Madler, L.; Mueller, R. Nanoparticle Synthesis at High Production
16 Rates by Flame Spray Pyrolysis. *Chemical Engineering Science* **2002**, 58, 1969–
17 1976.
- 18 (46) Pratsinis, S.; Mueller, R.; Kammler, H. K.; Madler, L. Controlled Synthesis of
19 Nanostructured Particles by Flame Spray Pyrolysis. *Aerosol Science* **2002**, 33, 369–
20 389.
- 21 (47) Goudeli, E.; Eggersdorfer, M. L.; Pratsinis, S. E. Coagulation–Agglomeration
22 of Fractal-like Particles: Structure and Self-Preserving Size Distribution. *Langmuir*
23 **2015**, 31 (4), 1320–1327. <https://doi.org/10.1021/la504296z>.
- 24 (48) Sotiriou, G.; Blattmann, C. O.; Pratsinis, S. Composite Nanosilver Structures
25 Suitable for Plasmonic Biosensors. *Materials Research Society* **2012**, 1416.
- 26 (49) Sotiriou, G.; Sannomiya, T.; Teleki, A.; Krumeich, F.; Pratsinis, S. Non-Toxic
27 Dry-Coated Nanosilver for Plasmonic Biosensors. *ADVANCED MATERIALS*
28 **2010**.
- 29 (50) Teleki, A.; Heine, M.; Krumeich, F.; Akhtar, K.; Pratsinis, S. In Situ Coating of
30 Flame-Made TiO₂ Particles with Nanothin SiO₂ Films. *Langmuir* **2008**, 12553–
31 12558. <https://doi.org/10.1021/la801630z>.

- 1 (51) Teleki, A.; Akhtar, M. K.; Pratsinis, S. E. The Quality of SiO₂-Coatings on
2 Flame-Made TiO₂-Based Nanoparticles. *Journal of Materials Chemistry* **2008**, *18*
3 (30), 3547. <https://doi.org/10.1039/b803039a>.
- 4 (52) Kandilian, R.; Heng, R.-L.; Pilon, L. Absorption and Scattering by Fractal
5 Aggregates and by Their Equivalent Coated Spheres. *Journal of Quantitative*
6 *Spectroscopy and Radiative Transfer* **2015**, *151*, 310–326.
7 <https://doi.org/10.1016/j.jqsrt.2014.10.018>.
- 8 (53) Goudeli, E.; Eggersdorfer, M. L.; Pratsinis, S. E. Aggregate Characteristics
9 Accounting for the Evolving Fractal-like Structure during Coagulation and
10 Sintering. *Journal of Aerosol Science* **2015**, *89*, 58–68.
11 <https://doi.org/10.1016/j.jaerosci.2015.06.008>.
- 12 (54) Cole, J. R.; Mirin, N. A.; Knight, M. W.; Goodrich, G. P.; Halas, N. J.
13 Photothermal Efficiencies of Nanoshells and Nanorods for Clinical Therapeutic
14 Applications. *The Journal of Physical Chemistry C* **2009**, *113* (28), 12090–12094.
15 <https://doi.org/10.1021/jp9003592>.
- 16 (55) Chen, H.; Shao, L.; Ming, T.; Sun, Z.; Zhao, C.; Yang, B.; Wang, J.
17 Understanding the Photothermal Conversion Efficiency of Gold Nanocrystals.
18 *Small* **2010**, *6* (20), 2272–2280. <https://doi.org/10.1002/sml.201001109>.
- 19 (56) Govorov, A. O.; Hernandez, P.; Tandler, P. J.; Carlson Michael T;
20 Richardson, H. H. Experimental and Theoretical Studies of Light-to-Heat
21 Conversion and Collective Heating Effects in Metal Nanoparticle Solutions. *NANO*
22 *LETTERS* **2009**, *9*, 1139–1146.
- 23 (57) Das, S. K.; Khan, Md. M. R.; Parandhaman, T.; Laffir, F.; Guha, A. K.; Sekaran,
24 G.; Mandal, A. B. Nano-Silica Fabricated with Silver Nanoparticles: Antifouling
25 Adsorbent for Efficient Dye Removal, Effective Water Disinfection and Biofouling
26 Control. *Nanoscale* **2013**, *5* (12), 5549. <https://doi.org/10.1039/c3nr00856h>.
- 27 (58) Mulvaney, P. Surface Plasmon Spectroscopy of Nanosized Metal Particles.
28 *Langmuir* **1996**, *12*, 788–800.
- 29 (59) Romero, I.; Aizpurua, J.; Bryant, G. W.; García De Abajo, F. J. Plasmons in
30 Nearly Touching Metallic Nanoparticles: Singular Response in the Limit of
31 Touching Dimers. *Optics Express* **2006**, *14* (21), 9988.
32 <https://doi.org/10.1364/OE.14.009988>.
- 33

Chapter 4

Detection and Harvesting of Hot Electrons in Plasmon-driven Redox Reactions

Case Study #1: Photocatalytic Reduction of Hexavalent Chromium²

4.1 Introduction

Remediation of hexavalent chromium Cr⁶⁺ in environmental water sources is a key-priority to assure protection of public health¹. So far, the most efficient route of Cr⁶⁺ removal is the reduction to the inert trivalent chromium Cr³⁺, with the photocatalytic reduction route being the most effective, low-cost and hazardous-free procedure². During last decade, metal nanoparticles have been emerged as highly potent, promising photocatalysts and plasmon-assisted photochemistry is considered the next step in boosting challenging solar-to-chemical processes³⁻⁶. However, the evaluation of plasmonic photocatalysts in Cr⁶⁺ removal using solar light remains to be investigated.

In particular, the excitation of local surface plasmon resonance (LSPR) phenomena drives two distinct mechanisms: Upon irradiation, surface plasmons form

² Part of this chapter is published in *J. Phys. Chem. C* 2023, 127 (4), 2045–2057 and *ACS Catal.* 2022, 12 (16), 9908–9921.

1 and decay^{7,8}, initiating either [i] heat generation *via* thermal relaxation of photoinduced
2 carriers^{9,10} or [ii] energetic “hot” electron transfer to an appropriate acceptor^{11,12}. So far,
3 there is converging evidence that hot electrons, despite the short lifetime, can be
4 efficiently utilized in challenging chemical processes of immediate technological
5 importance, such as H₂ production^{13–15} and CO₂ reduction^{16–18}, to name a few.

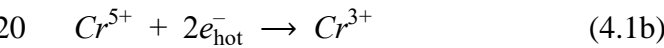
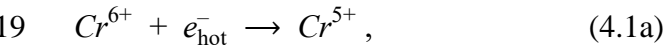
6 So far, however the transfer of plasmonic hot-electrons to redox-active metals has
7 not been thoroughly addressed. An interesting case is hexavalent Cr⁶⁺ since its
8 reduction to Cr³⁺ is the key-technology to remediate its toxicity. Detection of the hot-
9 carrier transfer in {plasmonic}-{electron-acceptor} interfaces is by itself a primary
10 challenge, both from the technical point of view by establishing a widely usable
11 technique for quantitative monitoring of hot electrons in such systems, as well as from
12 the theoretical point of view by understanding/disentangling which mechanism
13 predominates among plasmonic excitation, hot-electron generation, thermal dissipation
14 and near fields. Transferring these to realistic, non-monodispersed nanoaggregates is a
15 forward-looking realm also.

16 Based on estimates from ultrafast kinetics/non-equilibrium studies, so far we
17 understand that key-factors that determine the transfer efficiency of hot electrons to a
18 near acceptor, can be conceptually separated as: [i] processes occurring inside the
19 metallic particle, i.e. photoexcitation of plasmon modes, hot-carrier generation and
20 relaxation, and [ii] factors related to the particle-acceptor interface, i.e. the probability
21 of the hot electron reaching the particle surface and injected to the acceptor. Typically,
22 processes [i] are transient, characterized by ultrafast kinetics, while phenomena in [ii]
23 tend to relate to equilibrium states. In this case, interfacial or quasi-equilibrium
24 reactions are the slowest, thus determining the rate-limiting steps of the entire process.
25 However, a quantitative capturing and monitoring of plasmon-induced hot electrons
26 under chemical equilibrium remains highly challenging. Seemala *et al.*¹⁹ have
27 demonstrated that Ag nanoparticles can achieve plasmon-mediated O₂ dissociation,
28 with the dominant mechanism assigned to intense surface electric fields, while the hot
29 carriers had no effect on this particular reaction. In monodisperse spherical Ag
30 nanoparticles, the theoretical hot-electron lifetime is in the range of picoseconds, while
31 the optimal range of particle size for maximizing the hot-electron yield lies between 10-
32 20 nm²⁰. In practical applications, where non-monodisperse nanoaggregates are often
33 used, tuning the interparticle distance (plasmonic coupling) through aggregation

1 degree, promotes the generation of hot carriers due to enhanced electric fields localized
2 between neighboring particles^{21–23}. Thus, in the case of a non-monodisperse Ag
3 nanoensemble, the hot-electron generation rate becomes both size- and aggregation-
4 dependent²⁴.

5 In this context, the development of the appropriate method for monitoring the
6 generation and harvesting of hot carriers still poses a challenge by itself. The methods
7 used so far can be classified as (i) fast-kinetic spectroscopies, reviewed by Hartland¹⁰
8 and Besteiro *et al.*²⁵, (ii) imaging methods^{26–32} or (iii) monitoring the products of a
9 selected chemical process. Despite the first two methods provide fundamental elements
10 for the understanding of the process, approach (iii) is of key-importance to understand
11 the process under chemical equilibrium. However, despite the great progress achieved
12 so far^{33–36}, a direct quantitative monitoring of the energetic carriers remains elusive.
13 Herein, we used Electron Paramagnetic Resonance as a state-of-the-art spectroscopy to
14 study the transfer of hot-electrons from photoexcited core-shell Ag@SiO₂
15 nanoaggregates to Cr⁶⁺-atoms. {Cr-oxalate} is employed as a well-studied, electron-
16 accepting system.^{37–40} One-electron reduction of Cr⁶⁺ results to Cr⁵⁺ (1a), and a
17 subsequent two-electron reduction of Cr⁵⁺ results to Cr³⁺ formation (1b),

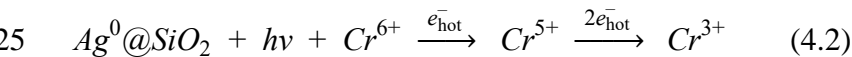
18



21

22 In the presence of illuminated Ag@SiO₂ nanoaggregates, the overall electron transfer
23 is described by reaction (2),

24



26

27 Hence, quantitative monitoring of the {Cr⁶⁺-, Cr⁵⁺- and Cr³⁺-oxalate} species offers
28 complete mass-balance control, which allows a direct electron counting.

1 EPR is eminently suited to detect and quantify unpaired electrons in metal
2 centers^{41,42}, as well as unpaired spins in small Ag nanoparticles,^{43,44} and photo-induced
3 trapped carriers.⁴⁵ Quantitative EPR analysis should take into account the spin-state of
4 the studied system^{41,42}. More specifically, for $S > 1/2$ systems, the work of Chasteen had
5 clearly exemplified the way to quantify EPR signals for high-spin $\text{Fe}^{3+}(5/2)$.⁴⁶ Herein
6 we use the Spin-Hamiltonian for the $S=3/2$ { Cr^{3+} -oxalate} system and we account a
7 spin-state-corrected spin quantitation protocol. In the same context, the $S=1/2$ { Cr^{5+} -
8 oxalate} system was analyzed and spin-quantified. In this way, we use EPR spectra as
9 quantitative indexes of the number of electrons transferred to Cr-species according to
10 reactions (1a, 1b)

11 The plasmonic Ag^0/SiO_2 nanoaggregates studied herein were synthesized using
12 Flame Spray Pyrolysis (FSP) whose photothermal profile has been thoroughly
13 characterized in our previous work⁴⁷. Ag is the chosen material here, since it displays
14 superior plasmon resonance in the optical region and thus the capability to excite higher
15 energetic carriers.⁴⁸ Herein, three core@shell Ag^0/SiO_2 configurations were employed
16 (see Table S1), with a 15 nm Ag core, and varying SiO_2 thickness of 1-5 nm. Using
17 EPR spectroscopy, we established a spin-state-calibrated EPR methodology to
18 quantitatively monitor the one-, two- and three-electron transfer steps from
19 photoexcited Ag^0/SiO_2 towards the reduction of {oxalate- Cr^{6+} } to {oxalate- $\text{Cr}^{5+}/\text{Cr}^{3+}$ }
20 species respectively. Moreover, in such quantitative study, it was important to assess
21 the possible direct Cr^{6+} reduction i.e. due to oxidation of non-coated Ag surface. Thus,
22 using FSP we have synthesized non-coated Ag-particles that were simply deposited on
23 SiO_2 . We show that in the core-shell Ag^0/SiO_2 , the SiO_2 shell plays a key role in hot-
24 electron transfer. In a wider context, the present study, exemplify the possibility of
25 plasmon-enhanced reduction of toxic Cr^{6+} ions towards inert Cr^{3+} within the picture of
26 environmental chromium remediation.

27

28 4.2 Materials & Methods

29 *Flame spray pyrolysis (FSP) synthesis of Ag particles:* The nanoparticles were
30 synthesized using a flame spray pyrolysis (FSP) set-up as already reported.⁴⁷ The
31 precursor solution was prepared by dissolving silver acetate (Sigma-Aldrich, purity >
32 99%) in 2-ethylhexanoic acid (EHA) and acetonitrile (ACN) (both Sigma-Aldrich,

1 purity > 97%), volume ratio 1:1 at varying concentrations 0.4–0.5 M. Then, the solution
2 was fed through a capillary at 5–7 mL min⁻¹ into the flame and atomized into fine
3 droplets by 5 L min⁻¹ dispersed O₂ (Linde, purity > 99%). Pressure drop at the nozzle
4 tip was maintained at 1.5 bar. A supporting O₂/CH₄ (5 L min⁻¹, 2.5 L min⁻¹) pilot flame
5 ignites the droplets, initiates combustion, and supports the spray flame. The high
6 temperature inside the flame field triggers the metal vapor to form nuclei through the
7 gas-to-particle formation.^{49,50} Particle coalescence, sintering and agglomeration result
8 in the final powder collected using a vacuum pump (Busch V40) on glass microfiber
9 filters (Albet). Nanoparticles were collected by scraping of the powder from the filter.

10 *Synthesis of core@shell Ag@SiO₂*: The *in situ* SiO₂ encapsulation of Ag NPs was
11 engineered in an enclosed FSP reactor, originally described by Sotiriou *et al.*^{43,51} In our
12 study, the desired SiO₂ shell thickness was adjusted in the range 1 to 5 nm as detailed
13 in our recent work. Specifically, the flame was enclosed by a metallic tube (9 cm
14 diameter, 20 cm height), to prolong the high temperature residence time and thus
15 control the particle size and crystallinity. A toroidal ring, equipped with 16 equidistant
16 holes, 500 μm diameter, was placed above the metallic tube, and used to radially spray
17 the SiO₂ precursor vapor on the Ag particles. 0.5–3 L min⁻¹ N₂ was used as carrier gas
18 (Linde, purity > 99%) bubbled through hexamethyldisiloxane (HMDSO, Aldrich,
19 purity 98%), fixed at 10 °C. The N₂-HMDSO stream was injected into the particle field,
20 along with an additional N₂ stream used to enforce the radial convection of the HMDSO
21 vapor, according to the methodology developed by Teleki *et al.*^{52,53} In addition, co-
22 agglomerated Ag/SiO₂ materials were prepared in a single-nozzle FSP reactor by
23 spraying a mixture of silver acetate/HMDSO. The FSP settings and characteristics of
24 the Ag@SiO₂ materials are listed in Table S1.

25 *Sample preparation for EPR measurements*: Potassium dichromate (K₂Cr₂O₇, purity >
26 99%) and oxalic acid (C₂H₂O₄, purity > 98%) were purchased from Sigma-Aldrich.
27 Stock Cr-oxalate solutions were prepared in degassed ultrapure Milli-Q water
28 (Millipore) at pH = 3, using 10 mM K₂Cr₂O₇ and 40 mM C₂H₂O₄, purchased from
29 Sigma-Aldrich. At fixed stoichiometry Cr:Oxalate = 1:2, stable [Cr-{oxalate}₃]
30 complexes are formed, as verified by EPR spectroscopy. Exhaustive degassing of each
31 sample was performed to remove ambient O₂, using a Leybold vacuum pump (10⁻⁵ bar).
32 For each experiment, fresh Cr-oxalate was used. Every sample was prepared by adding
33 the appropriate amount from the stock Cr-oxalate solution to a freshly prepared

1 suspension of Ag⁰@SiO₂ in dark conditions. Before irradiation, the system was allowed
2 to equilibrate under mild stirring, at room temperature for 15 minutes. Degassing was
3 an important step to remove ambient O₂ that, otherwise, might act as an adventitious
4 electron acceptor in this type of experiments.

5 *Irradiation Set-up:* Irradiation of the samples was performed using an arc xenon lamp
6 (Oriel 6293) operating at 450 W (Figure S1). The power intensity was kept constant
7 and recorded at 150 mW cm⁻² by a power meter (Newport). To eliminate heating effects
8 by the IR photons, a water filter was inserted before the focusing lens. The particle
9 suspensions were irradiated via a 90°-reflector mirror holder (model: 62245).

10 *Monitoring ΔT Variations:* The temperature was recorded by an infrared thermal imager
11 (Fluke, TiS40). Considering the SiO₂ surface, the emissivity was set at 0.7 and the
12 background temperature at room temperature, 22 °C. The camera-data analysis is
13 accomplished by the SmartView software. The standard error values shown at
14 temperature curves are obtained according to thermal camera's range (± 1 °C). Constant
15 stirring during the experiment downgrades the existence of thermal gradients in the
16 surrounding medium.

17 *Electron Paramagnetic Resonance (EPR):* The X-band electron paramagnetic
18 resonance (EPR) spectra were recorded with a Bruker ER200D spectrometer at liquid-
19 nitrogen temperature (77 K), equipped with an Agilent 5310A frequency counter. The
20 spectrometer was running under a custom-made software based on LabView.⁵⁴
21 Adequate signal to noise ratio was obtained after 10 scans, with a microwave power
22 fixed at 8 mW. The EPR instrumental conditions were as follows: microwave frequency
23 9.54 GHz, modulation frequency = +50.00 kHz, and modulation amplitude = 10 Gauss
24 peak-to-peak.

25 *Cr Mass-balance Monitoring:* The mass-balance of the Cr species was monitored
26 according to relation (3). Cr⁶⁺ was quantified by the well-established diphenylcarbazide
27 (DPC) method using UV-Vis spectroscopy⁵⁵, and Cr⁵⁺/Cr³⁺ species were quantified
28 using EPR.

29 *Validation of the Methodology:* The present methodology for quantitative monitoring
30 of the hot electrons transferred to the Cr-acceptors requires diligent control of eventual
31 side reactions, as follows: the direct photochemical reduction of the Cr⁶⁺ ions, has been

1 estimated in control experiments by irradiating the {Cr⁶⁺-oxalate} solution, in the
2 absence of Ag@SiO₂ nanoparticles. In our irradiation set up, in the absence of NPs, a
3 maximum of ~10% Cr⁶⁺ was reduced by direct photolysis, in accordance with Testa *et*
4 *al.*³⁷ (see Figure S15). Cr⁶⁺, due to the highly oxidizing potential ($E_0 = +1.33$ V) for the
5 redox couple Cr⁶⁺(ox)₃/Cr³⁺(ox)₃, is a very efficient electron acceptor which renders it
6 a strongly oxidizing agent. Thus, direct Ag oxidation might lead to Cr⁶⁺ reduction
7 without the intervention of light, forming Ag ions released in the solution. Sotiriou *et*
8 *al.* have investigated in detail the redox stability of flame-made SiO₂-coated Ag
9 nanoparticles and demonstrated that SiO₂ encapsulation can eliminate the Ag⁺ leaching
10 in aqueous suspensions.⁵⁶ Therein, the release of Ag⁺ ions by an Ag@SiO₂/ {Cr-
11 oxalate} suspension was found to account for ~7% of total Cr-reduction, for the 1 nm
12 SiO₂ shell, see Figure S10. As a reference, in co-agglomerated Ag/50SiO₂, Cr⁶⁺ ions
13 were able to oxidize ~30% of the Ag, amplifying the superior stability of the core@shell
14 structure studied in this work. Furthermore, considering the case of eg. 0.08 g L⁻¹
15 Ag@1SiO₂ (Figure 2), the decrease of Cr⁶⁺ concentration by ~1.6 mM cannot be
16 assigned to 0.7 mM Ag in the solution since post-catalysis XPS measurements show no
17 oxidized species at all. Hence Ag⁺ release cannot be the prevailing mechanism of Cr⁶⁺
18 reduction. Cr species related to the oxidation mechanism have been subtracted from the
19 total yield.

20 *Ag@SiO₂ Characterization:* The morphology and phase composition of the [Ag@SiO₂-
21 Cr] system were studied using a scanning electron microscope (SEM, Quanta Inspect,
22 FEI, Eindhoven, Netherlands) coupled with energy-dispersive X-ray spectroscopy
23 (EDXDX4, EDAX, Mahwah, NJ, USA) and a FEI Talos F200i field-emission
24 (scanning) transmission electron microscope (Thermo Fisher Scientific Inc., Waltham,
25 MA, USA) operating at 200 kV, equipped with a windowless energy-dispersive
26 spectroscopy microanalyzer (6T/100 Bruker, Hamburg, Germany). XRD data were
27 acquired at room temperature using a Bruker D8 Advance 2theta diffractometer with
28 copper radiation (Cu K α , $\lambda = 1.5406$ Å) and a secondary monochromator operating (40
29 kV, 40 mA), whereby samples were measured between 10° and 80° (Figure S6). Crystal
30 size was evaluated by using the Scherrer formula. UV-Vis spectra were collected by a
31 PerkinElmer Lambda 35 Spectrometer by dispersing particles in aqueous solvents and
32 placing them in quartz cuvettes. XPS spectra were acquired in a surface analysis
33 ultrahigh vacuum system (SPECS GmbH) equipped with a twin Al–Mg anode X-ray

1 source and a multi-channel hemispherical sector electron analyzer (HSAPhoibos 100).
2 The base pressure was $1-3 \times 10^{-9}$ mbar. A monochromatized Mg K α line at 1253.6 eV
3 and analyzer pass energy of 15 eV was used in all XPS measurements. The binding
4 energies were calculated regarding the binding energy (BE) of C 1s peak of adventitious
5 carbon at 284.8 eV. The peak deconvolution was calculated using a Shirley background.
6 The powder specific surface area (SSA) was determined from Brunauer–Emmett–
7 Teller (BET) method and the adsorption and desorption isotherms of nitrogen at 196 °C
8 using a TriStar 3000 Micromeritics instrument. Prior the measurements, the samples
9 were outgassed at 150 °C for 10 h under N₂ flow.

10 *Quantitative Electron Paramagnetic Resonance:* Cu²⁺(NO₃)₂(S=1/2) and {Fe³⁺-
11 EDTA} (S= 5/2) in ethanol, were used as spin standards for the quantitation of the Cr-
12 species according to the quantitation method of Chasteen.⁴⁶ Specifically, Cu²⁺(S= 1/2)
13 is appropriate for quantitation of the Cr⁵⁺(S=1/2) since both have similar spin-relaxation
14 profiles, and $g \sim 2$. On the other hand, {Cr³⁺-oxalate} and Fe³⁺-EDTA both have broad
15 EPR spectra extending in the same region of magnetic fields, from $g \sim 4$ to $g \sim 2$, thus
16 {Fe³⁺-EDTA} (S = 5/2) provides a reliable spin-standard for EPR quantitation of high
17 spin Cr³⁺(S=3/2) species. It is underlined that the EPR microwave-saturation profile of
18 the spin systems was measured, as in due, and spin quantification was done under non-
19 saturating conditions. In the experimental EPR spectra of the samples irradiated at
20 various times, contained a mixture of Cr⁵⁺ and Cr³⁺ species, the quantitative analysis of
21 Cr⁵⁺ and Cr³⁺ consisted of two steps:

22 [i] deconvolution of the total experimental EPR spectrum to the Cr⁵⁺ and Cr³⁺ EPR sub-
23 spectra. This was done by computer simulation of the Cr⁵⁺- and Cr³⁺-EPR signals, as
24 exemplified in Figure 1.

25 [ii] then, the double integral of the simulated Cr⁵⁺ and Cr³⁺ EPR spectra were used to
26 estimate the spin concentration, by comparison with the Cu²⁺(S = 1/2) and Fe³⁺ (S =
27 5/2) calibration, respectively.

28 *EPR simulation:* To simulate the EPR spectrum of Cr⁵⁺ (S = 1/2) spin system we have
29 used a Zeeman spin-Hamiltonian

30
$$H = \beta \mathbf{B} \cdot \tilde{g} \cdot \mathbf{S} \quad (4.3)$$

31

1 where \tilde{g} is the g-tensor and $S = 1/2$.

2 The Cr^{3+} ($S = 3/2$) spin system, was simulated using the Spin-Hamiltonian (eq. 4.4)¹⁰

3

$$4 \quad H = \beta \mathbf{B} \cdot \tilde{g} \cdot \mathbf{S} + \mathbf{S} \cdot \tilde{D} \cdot \mathbf{S}$$

$$5 \quad = \frac{\mu_B}{h} (\vec{B} \cdot \tilde{g} \cdot \vec{S}) + D \left(S_z^2 - \frac{1}{3} S(S+1) \right) + E (S_x^2 - S_y^2) \quad (4.4)$$

6

7 with $S = 3/2$. The values of the components of the zero-field splitting tensor \tilde{D} (D and
8 E) are related to the electronic configuration symmetry and spin-ligand interactions
9 strength. Specific attention is required when using the $S = 5/2$ system of Fe^{3+} to quantify
10 the $S = 3/2$ system of Cr^{3+} , as detailed by Eaton *et al.*⁴¹ The equation that describes the
11 double integral of an experimental EPR spectrum and how it relates to the number of
12 spins in the sample is given by

13

$$14 \quad DI = c [G_R C_t n] \left(\frac{\sqrt{P} B_m Q n_B S(S+1) n_S}{f(B_1, B_m)} \right) \propto S(S+1), \quad (5)$$

15

16 where c is a constant input to the software from a sample with known number of spins,
17 G_R the receiver gain, C_t the conversion time, n is the number of scans, P the microwave
18 power in W, B_m the modulation amplitude in Gauss, Q is the quality factor of resonator,
19 n_B the Boltzmann factor for temperature dependence, S with n_S are the total electron
20 spin and the number of spins, respectively, and $f(B_1, B_m)$ is the spatial distribution of
21 the microwave field and the modulation field experienced by the sample.

22 Thus, when we use the $\text{Fe}^{3+}(5/2)$ spins to quantify the $\text{Cr}^{3+}(S=3/2)$ system, a spin-
23 dependent correction factor is applied, see eq. 4.6.

24

$$25 \quad \frac{DI(\text{Cr}^{3+}: S_1 = 3/2)}{DI(\text{Fe}^{3+}: S_2 = 5/2)} \sim \frac{S_1(S_1 + 1)}{S_2(S_2 + 1)} = \frac{3}{7}, \quad (4.6)$$

26

1 where DI is the double integrated area of an EPR signal, recorded under non-saturating
 2 microwave power. Finally, attention should be paid to the fact that to convert the
 3 amount of Cr³⁺ to the number of electrons, a factor of (×3) must be used since Cr⁶⁺ →
 4 Cr³⁺ reduction is a 3-electron event.

5 Overall, a precise quantitative assessment of the hot-electron transfer to Cr⁶⁺, can be
 6 done based on the control of the mass balance of all Cr species, as described in the
 7 mass-balance relation (eq. 4.7)

8

$$9 \quad [\text{Cr}]_{\text{TOTAL}} = [\text{Cr}^{6+}] + [\text{Cr}^{5+}] + [\text{Cr}^{3+}] \quad (4.7)$$

10

11 Cr⁶⁺ was quantified by UV-Vis spectroscopy, while Cr⁵⁺ and Cr³⁺ were quantified by
 12 EPR.

13

14 4.3 Results/Discussion

15 4.3.1 Ag@SiO₂ Characterization

16

Table 4.1. Flame spray pyrolysis (FSP) synthesis parameters and particle characteristics.

Ag@XSiO ₂ *	FSP Parameters			Particle Characteristics			
	Precursor Molarity (M)	P/D**	Si Precursor Flow Rate (L min ⁻¹)	wt% SiO ₂	d _{XRD} (nm)	d _{TEM} (nm)	SSA (m ² g ⁻¹)
Ag@1SiO ₂	0.4	5/5	0.6	10	14 ± 0.5	15 ± 3.5	29 ± 3
Ag@3SiO ₂	0.4	5/5	1.2	20	15 ± 0.5	15 ± 3.5	62 ± 5
Ag@5SiO ₂	0.5	7/5	2.0	27	16 ± 0.5	14 ± 4.0	61 ± 5
Ag/50SiO ₂ ***	0.4	5/5	–	50	18 ± 0.5	–	245 ± 5

17 *X denotes the shell thickness (nm). **P/D: Precursor Feed Rate (ml
 18 min⁻¹)/Dispersion O₂ (L min⁻¹). ***50% wt SiO₂ (co-agglomerated).

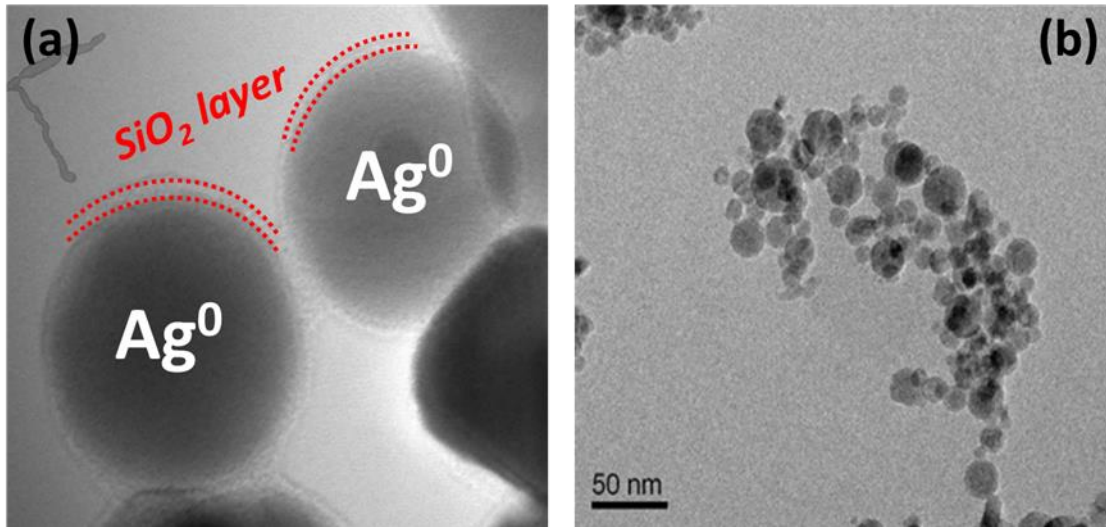


Figure 4.1. TEM images of (a) coupled Ag@1SiO₂ NPs with 1nm SiO₂ shell, (b) fractal-like ($D_f = 1.8$) Ag@SiO₂ nanoaggregates, a typical FSP-derived morphology.

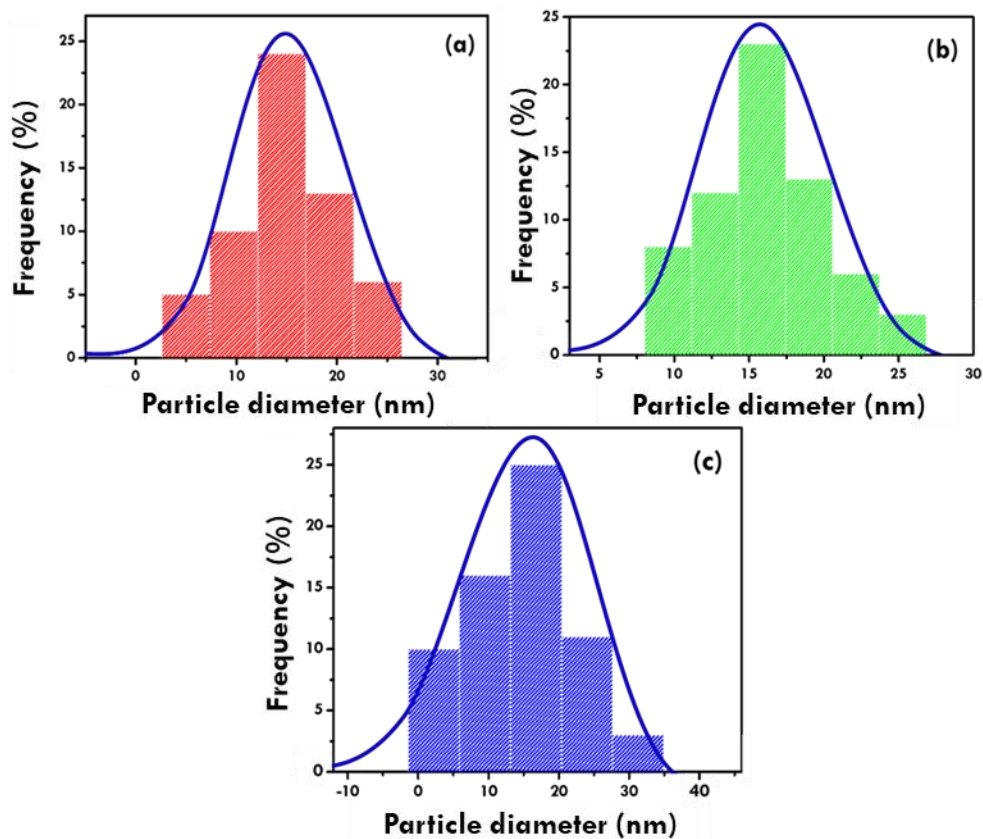


Figure 4.2. TEM-derived particle size distribution of (a) Ag@1SiO₂, (b) Ag@3SiO₂ and (c) Ag@5SiO₂ NPs.

Table 1 summarizes the structural characteristics of the Ag@SiO₂ particles used in the present study. FSP settings such as precursor molarity, P/D ratio and HMDSO flow rate are adjusted accordingly, so that the Ag particle size and SiO₂ shell thickness can be precisely controlled. Figure 1-3 depict the efficient SiO₂ coating and, the controlled size distribution and crystallinity of Ag@SiO₂ nanoparticles using TEM and XRD respectively. In all materials, the Ag⁰ core diameter was ~15 nm, while the SiO₂ layer thickness was adjusted in the range of 1-5 nm, established by other FSP-based studies.^{43,47} The SiO₂ shell thickness controls the interparticle distance, as evidenced in the UV/Vis profile (see Chapter II), with the resonance at 590 nm assigned to coupled plasmonic particles.⁵⁷ XPS study certifies the absence of oxidized Ag species, thus SiO₂ shell acts as an aggregation tuner and a particle protector as well (see Chapter II).⁵⁸

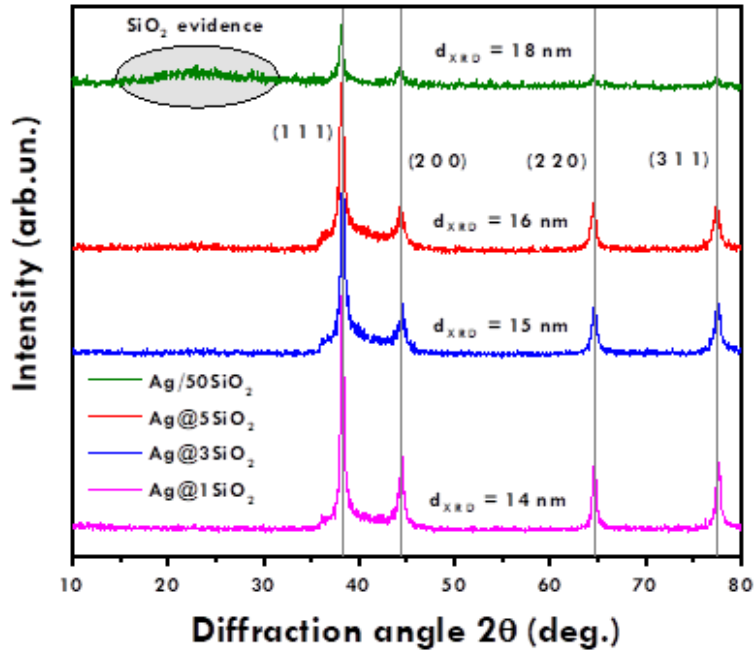


Figure 4.3. XRD patterns of the as-prepared Ag⁰@XSiO₂ NPs.

4.3.2 Plasmon-mediated hot carriers vs direct electron transfer in dark (DETD): Evaluation of Ag⁺ leaching

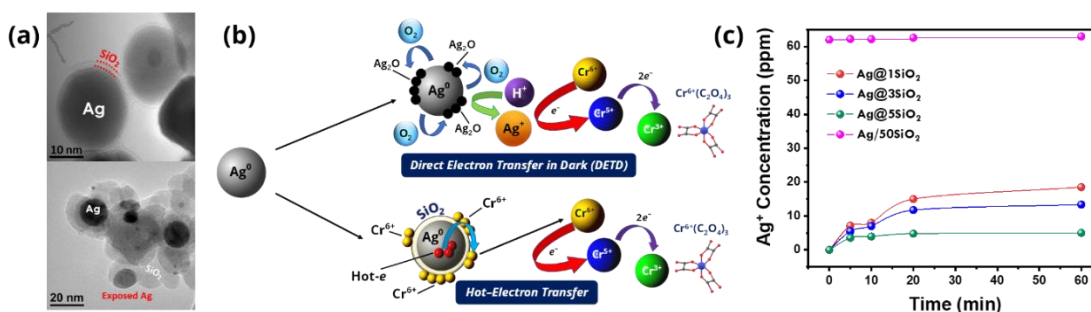


Figure 4.4. (a) TEM images of core-shell Ag@SiO₂ coated with a 1nm SiO₂ shell (upper) and Ag particles deposited on SiO₂ with exposed areas. (b) Schematic illustration of possible Cr⁶⁺ reduction paths: [i] Direct reduction of Cr⁶⁺ *via* oxidation of the non-coated Ag, results in release of oxidized Ag⁺ ions, and [ii] the plasmon-induced hot-electron transfer from plasmonic Ag@SiO₂ where the oxidative path is suppressed. (c) Evolution of Ag⁺ release by bare/non-coated Ag or SiO₂-coated Ag (0.5 g L⁻¹): The ultrathin 1nm SiO₂ shell hinders the contribution of oxidative Ag⁺ release to Cr⁶⁺ reduction to 13%, while the 3nm and 5nm shells suppresses it to 9% and 4%.

Before starting to consider plasmon-driven phenomena in Cr⁶⁺ reduction, other mechanisms should be elucidated in presence of Ag@SiO₂. Besides thermal effects, Figure 4b depicts the two possible mechanisms that contribute to Cr⁶⁺ reduction, the hot electrons and the direct Ag-oxidation by Cr⁶⁺. Oxidation of Ag particles occurs in the case of non-coated, exposed Ag surfaces.⁵⁹ This oxidative step results in release of the Ag⁺ ions in solution, thus monitoring them provides a quantitative measure of the eventual core oxidation. Thus, the SiO₂ coating provides an efficient shield, suppressing Ag⁺ release. Under ultrathin SiO₂ coating ~1-5nm, some Ag surface can be exposed to Cr⁶⁺. This Cr⁶⁺ reduction *via* the “dark/oxidative” path, is not related to hot-electron transfer thus it has to be properly accounted for. Herein, to take this into account we have carried out a diligent control of the Ag⁺ release, depicted in Figure 4c. The thinner 1 nm SiO₂ layer permits 15 ppm Ag⁺ leaching in the first 60 minutes. Regarding the Cr⁶⁺ reduction kinetics shown

hereafter, this release accounts for 13% of reduced Cr^{6+} , indicating a small portion of bare Ag surface in the $\text{Ag}@1\text{SiO}_2$. For reference, the Ag^+ leaching of the non-coated Ag/SiO_2 particles reaches 56% in the same time interval, as expected for the exposed Ag particles⁵⁹. Hereafter, taking these data into account, we show that the observed photoinduced Cr^{6+} reduction by core@shell $\text{Ag}@\text{SiO}_2$ originates from plasmon-induced hot electrons, while direct Cr^{6+} reduction *via* Ag oxidation is marginal.

4.3.3 Quantitative monitoring of hot-electron transfer to {Cr-oxalate} species by EPR spectra

Table 4.2. Spin Hamiltonian parameters for the {Cr³⁺-oxalate} and {Cr⁵⁺-oxalate} species.

{Cr ⁵⁺ -oxalate} species (S = 1/2)			{Cr ³⁺ -oxalate} species (S = 3/2)					
g_x	g_y	g_z	g_x	g_y	g_z	D (cm ⁻¹)	E (cm ⁻¹)	E/D
± 0.002	± 0.002	± 0.002	± 0.002	± 0.002	± 0.002	± 0.001	± 0.001	± 0.001
1.965	1.957	1.920	1.915	1.925	1.910	0.417	0.038	0.258

According to reaction (2), upon irradiation, hot electrons are stimulated generating {Cr⁵⁺-oxalate} and {Cr³⁺-oxalate} by a sequential one- and two-electron transfer. In this methodology, the EPR fingerprints of {Cr⁵⁺-oxalate} and {Cr³⁺-oxalate} species are identified by the distinct EPR signals, shown in Figure 5. The {Cr³⁺-oxalate}, i.e. $[\text{Cr}(\text{C}_2\text{O}_4)_3]^{3-}$ can be easily identified by the characteristic axial g-components in the $g \sim 5$ region, see theoretical spectrum in Figure 5b (blue trace). Similarly, {Cr⁵⁺-oxalate} can be identified by the sharp EPR signal at $g \sim 1.9$ in Figure 5a (green trace). In Figure 2b, the total experimental EPR signal (black) contains both {Cr-oxalate} species, evidenced by the sharp feature at ~ 1200 G and the derivative at ~ 3500 G. The detailed spin Hamiltonian parameters of {Cr⁵⁺/Cr³⁺-oxalate} species are listed in Table 2.

We underline that the EPR spectrum of Cr^{3+} in Figure 5b corresponds to monomeric *bis*-oxalate Cr^{3+} , i.e. $\{\text{Cr}^{3+}-(\text{oxalate})_2\}[\text{H}_2\text{O}]_2$ complex with a distinct EPR fingerprint.⁶⁰ In brief, the zero-field splitting $D = 0.417 \text{ cm}^{-1}$, estimated by the numerical simulation of the

EPR spectrum of $\{\text{Cr}^{3+}\text{-(oxalate)}_3\}$, is in very good agreement with literature for this type of complexes.³⁹ This D-component gives rise to characteristic effective g-values near $g \sim 5.2\text{--}5.4$, which are higher than the typically observed $g \sim 4$ values. Control experiments, in the absence of Ag particles or light, show absence of any EPR signal. Thus, the EPR spectra display the $\text{Ag}^0\text{@SiO}_2\text{/Cr-oxalate}$ system produces monomeric $\{\text{Cr}^{5+}\text{-oxalate}\}$ and $\{\text{Cr}^{3+}\text{-oxalate}\}$ complexes according to the plasmon-driven electron-transfer reaction (2). Formation of monomeric species is underlined, since it allows more precise quantitation of the detected $\{\text{Cr}^{5+}\text{-oxalate}\}$ and $\{\text{Cr}^{3+}\text{-species}\}$, thus the hot-electron population according to relation (4.8)

$$N_{\text{hot-e}} = 1 \times [\text{Cr}^{5+}] + 3 \times [\text{Cr}^{3+}], \quad (4.8)$$

where $N_{\text{hot-e}}$ is the concentration of hot electrons transferred to $\{\text{Cr-oxalate}\}$ acceptors, and $[\text{Cr}^{5+}]$ and $[\text{Cr}^{3+}]$ are the concentrations of the Cr-species in $\mu\text{moles L}^{-1}$, determined by EPR. For completeness, the non-recombined holes in the photo excited $\text{Ag}^0\text{@SiO}_2$ system were also detected by monitoring the formation of OH radicals using spin-trapping EPR.

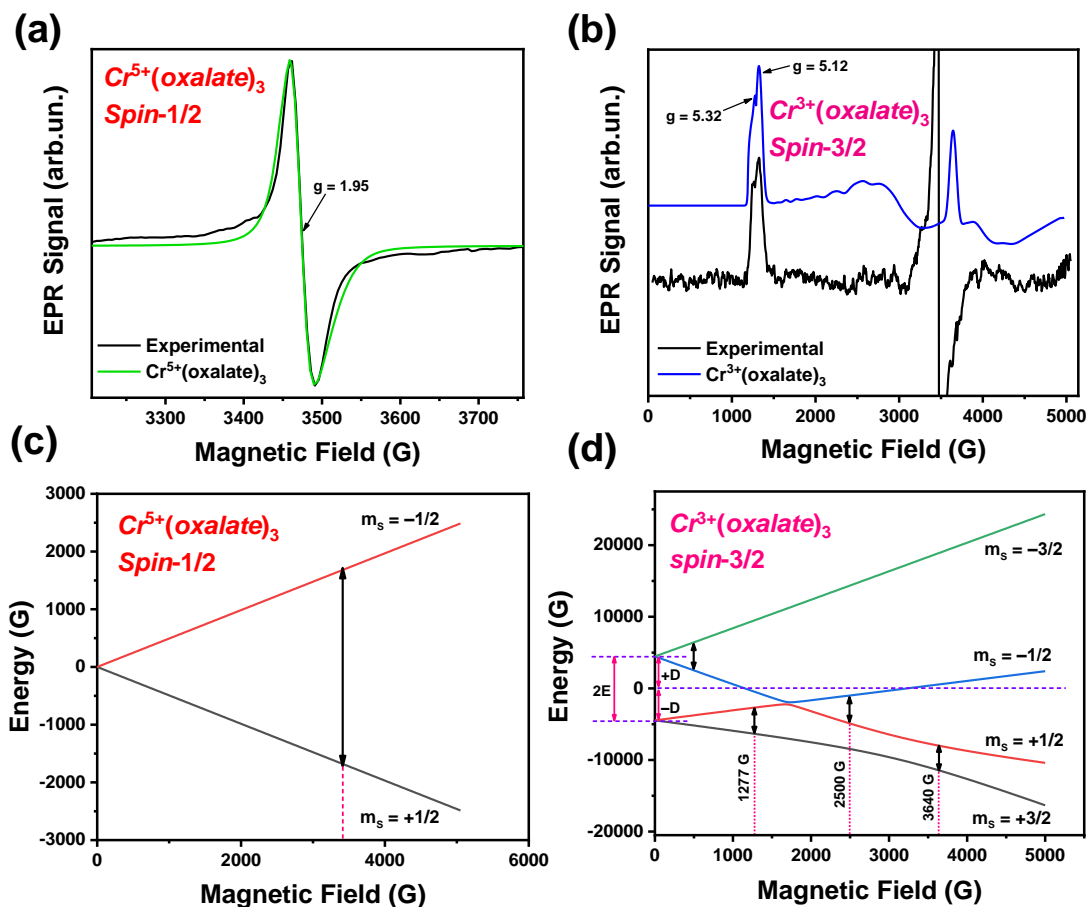


Figure 4.5. Experimental and simulated EPR signals of (a) Cr⁵⁺(oxalate)₃ species of spin system $S = 1/2$ and (b) Cr³⁺(oxalate)₃ species of spin system $S = 3/2$, displaying the characteristic axial g-components, i.e. $g \sim 2$ and $g \sim 5$, respectively. The detailed spin-Hamiltonian parameters are listed in Table 1. These graphs refer to a 500 mg L^{-1} Ag@SiO₂ NP concentration. (c, d) Calculated energy levels for the Cr⁵⁺(oxalate)₃ and Cr³⁺(oxalate)₃ species displaying the possible EPR resonances for the given X-band ($B_0 = 3400$ Gauss), obeying the selection rule for transitions $\Delta m_s = \pm 1$. These resonances verify the observed EPR signals of Cr⁵⁺(oxalate)₃ and Cr³⁺(oxalate)₃ species. For the Cr³⁺(oxalate)₃ system, the Euler angles (orientations) of the magnetic field were equivalent to $[\varphi, \theta] = [\pi/15, 0]$ relative to the molecular frame of the spin system ($S = 3/2$).

4.3.4 Monitoring hot-electron transfer to Cr⁶⁺/Cr⁵⁺/Cr³⁺

An independent route to confirm the injection of hot electrons is to monitor the population of Cr⁶⁺ species using the well-established diphenylcarbazide (DPC) method.⁵⁵

Figures 6a-b present the kinetics of the Cr^{6+} photo-reduction in presence of Ag@SiO_2 NPs. The Ag@SiO_2 NPs concentration affects drastically the reduction rate. Specifically, at low concentration (80 mg L^{-1}), at least 80% of Cr^{6+} was photo-reduced within $t \sim 60$ minutes, while at 500 mg L^{-1} the fastest kinetic rate of Cr^{6+} reduction was observed. Further analysis of the kinetic profile of Cr^{6+} reduction in Figure 6c, reveals that upon increasing NP concentration, the reaction pathway changes. At 80 mg L^{-1} the quasi-linear profile indicates that the Cr^{6+} photoreduction is a first-order reaction, which concurs with a one-electron transfer process i.e. as described by reaction (1a). Interestingly, increasing the particle concentration leads to apparent parabolic kinetics of Cr^{6+} reduction, indicating that second order effects occur as well (Cr^{3+} formation). This can be attributed to the enhanced plasmonic coupling of neighboring NPs that can increase the number of hot electrons and trigger the subsequent two-electron transfer (1b). The concentrations of 240 and 500 mg L^{-1} in Figure 6c can be fitted by a pseudo-first-order reaction expression, indicating that multi-electron transfer takes place (see reaction 2). Considering the photocatalytic rates per SiO_2 shell-thickness and particle concentration, the enhanced plasmonic coupling of 500 mg L^{-1} Ag@1SiO_2 promotes the elevated electron transfer and yields the superior performance, therefore this case will be further studied. It is underlined that three types of control experiments were carried out: [i] in the absence of Ag@SiO_2 under dark conditions, no Cr-reduction was observed at all. [ii] negligible presence i.e. $\sim 3.5\%$ of $\{\text{Cr}^{5+}\text{-oxalate}\}$ was obtained during the 10min mixing of Ag@1SiO_2 NPs and Cr^{6+} in the dark. This is a marginal Cr-reduction *via* Ag-oxidation in the dark, that correlates to Ag^+ leaching as shown in Figure 4c, where 14 ppm in the first 10 minutes accounts for $\sim 3\%$ reduced Cr^{6+} . Hence, the contribution of Ag oxidation in the total reaction is diminished compared to the plasmon-driven phenomena. [iii] Under UV/Vis irradiation without particles, $\sim 10\%$ of the $\{\text{Cr-oxalate}\}$ was reduced due to direct photolysis that is well known to occur by $<300 \text{ nm}$ UV-photons.⁶¹ In our analysis this fraction has been deducted from the total yield. Under visible-light photons $\lambda > 340 \text{ nm}$, the photolysis of $\{\text{Cr-oxalate}\}$ was almost zero, thus the dominant contribution to the observed Cr reduction is the plasmon-induced electron transfer.

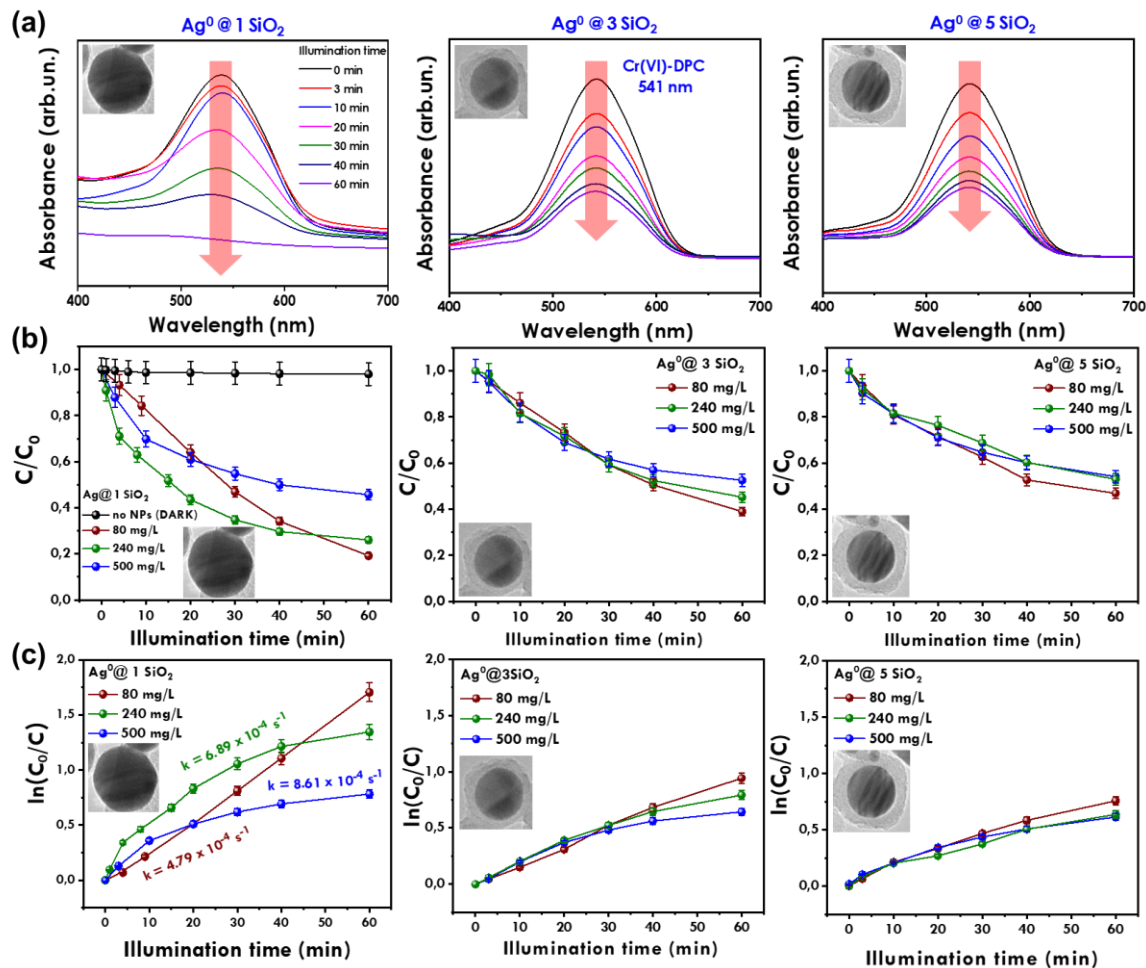


Figure 4.6. Monitoring of Cr^{6+} photo-reduction by Ag@SiO_2 nanoparticles of shell thickness 1, 3 and 5 nm. The SiO_2 shell can be seen in the inset TEM images. (a) UV-Vis monitoring of Cr^{6+} reduction by photoinduced hot-electrons using the Ag@1SiO_2 , Ag@3SiO_2 and Ag@5SiO_2 , respectively. (b) Kinetics of Cr^{6+} reduction at varying Ag@SiO_2 concentrations. The C/C_0 values refer to absorbance at 541 nm normalized to its intensity before irradiation (C_0). (c) $[\ln(C_0/C)]$ vs. [illumination time] plot. *Insets:* TEM images of Ag@SiO_2 NPs for varying SiO_2 shell thickness.

4.3.5 Quantitative analysis of hot-electron transfer

Figure 7 presents the kinetics of EPR spectra for the $\{\text{Cr-oxalate}\}$ species formed in the presence of the superior Ag@1SiO_2 NPs under irradiation. In Figure 7c-d, the EPR spectra contained a negligible $\{\text{Cr}^{5+}\text{-oxalate}\}$ signal under dark. The Cr mass-balance

analysis (eq 3), for low Ag@SiO₂ concentration (80 mg L⁻¹) and for high concentration (500 mg L⁻¹), is presented in Figure 8a and 8b respectively. The correlation confirms that at low particle concentration, after 60 minutes of irradiation, ~80% of the initial Cr⁶⁺ atoms have been reduced to Cr⁵⁺, i.e. by a one-electron reduction process. At high particle concentration, the Cr⁵⁺ kinetics display a volcano behavior: initially, one-electron acceptor Cr⁵⁺ species are formed for irradiation time up to ~3 minutes at the expense of Cr⁶⁺. Then, at prolonged irradiation times up to 60 minutes, the 3-electron acceptors Cr³⁺-oxalates are accumulated at the expense of Cr⁵⁺, in agreement with previous EPR studies.^{37,38} Increased concentration of Ag@1SiO₂ promotes the Cr³⁺ formation as more energetic electrons become available plus the increased presence of the local electric fields, in a similar way to the DPC method.

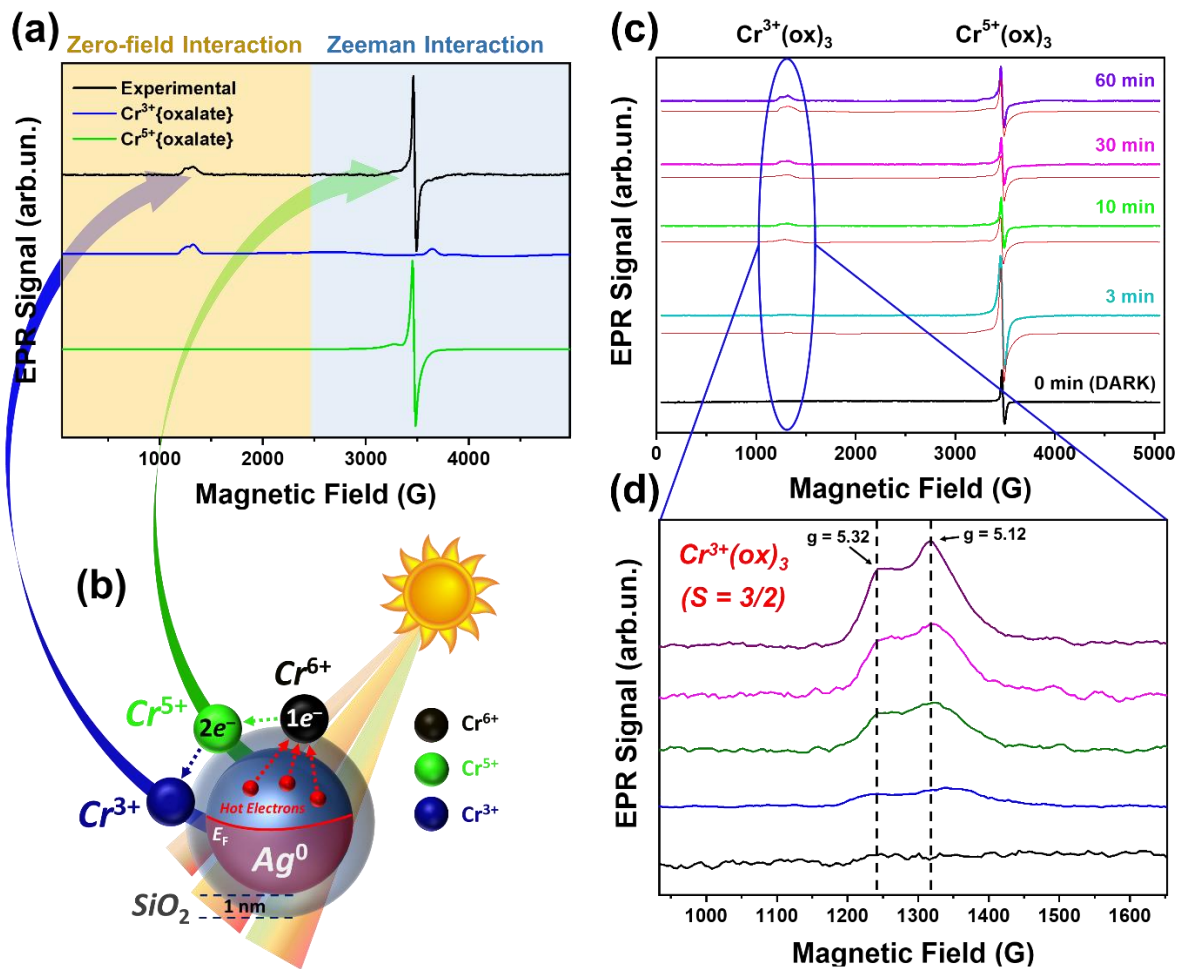


Figure 4.7. EPR spectra of {Cr⁵⁺-oxalate} and {Cr³⁺-oxalate} species formed via the hot-electron-driven reduction of Cr⁶⁺. (a) Experimental and simulated EPR signals of Ag@1SiO₂. The EPR spectra for the {Cr⁵⁺- and Cr³⁺-oxalate} species simulations are shown separated for clarity. The spin Hamiltonian parameters used are listed in Table S2. (b) A schematic representing the plasmon-induced Cr⁶⁺ reduction by the generated hot electrons. The arrows point to promoted reductions respectively. (c) EPR experimental (colored lines) and simulated (red lines) spectra of {Cr⁵⁺-oxalate} and {Cr³⁺-oxalate} various times of illumination of Ag@1SiO₂ NPs of concentration 500 mg L⁻¹ NP. (d) Magnified Cr³⁺ EPR region is presented, revealing the axial g-tensor of the {Cr³⁺-oxalate} species. In the absence of irradiation all these EPR signals were absent.

For completeness, the photoinduced hole formation has been monitored by EPR as well. The detection of OH radicals confirms that by tuning SiO₂-shell thickness, the generation and sufficient separation of hot carriers can be achieved in Ag@SiO₂ nanoaggregates.

The population of Cr⁵⁺ and Cr³⁺ normalized as [μmoles Cr] per [gram of Ag@SiO₂] after 10 minutes of illumination, for 500 mg L⁻¹ Ag⁰@SiO₂ is shown in Figure 8c. Regarding shell thickness, a rapid depletion of hot-electron population is observed by increasing the interparticle distance. The 1 nm shell allows a significant number of energetic electrons to be transferred, hence the superior performance, correlating in a similar way observed by increasing particle concentration. Again, the contribution of the increased number of hot spots should be noted for the thin-shell case, as they are known for promoting hot carrier generation.^{21,25}

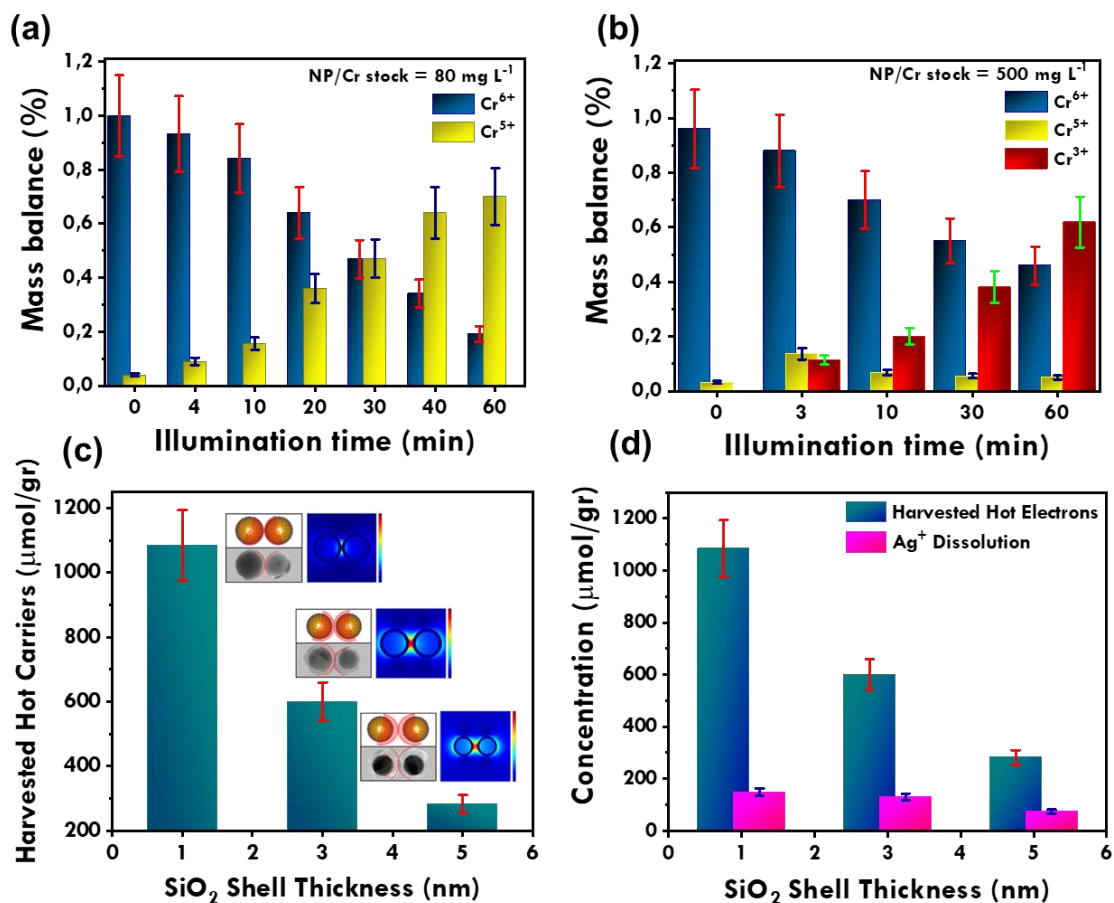


Figure 4.8. Mass balance (%) of Cr-species & hot-electrons. (a) Low Ag@1SiO₂ concentration 80 mg L⁻¹. (b) High Ag@1SiO₂ concentration of 500 mg L⁻¹. In both graphs, as Cr⁶⁺ is reduced, Cr⁵⁺ or/and Cr³⁺ increase. (c) Quantitation of hot electrons and the apparent quantum yield vs. the thickness of SiO₂ coating in 500 mg L⁻¹Ag@SiO₂ after 10 minutes of illumination. *Insets*: schematic figures of NP-NP vicinity and TEM images. The calculated near-field mapping profile of each NP configuration. (d) Ag⁺ leaching concentrations (DETD mechanism) remained far below the amounts of Cr⁵⁺/Cr³⁺-oxalates, thus the harvested hot electrons.

4.3.6 Disentangling the role of hot-electron transfer and thermal effects on plasmon-enhanced Cr-reduction mechanism

In our recent work, we have discussed in detail the photothermal effects implicated in irradiation of Ag⁰@SiO₂ NPs.⁴⁷ Hereafter, we have further investigated the role of bulk-medium temperature and wavelength irradiation in the hot-electron transfer efficiency,

shown in Figure 9. Strikingly, the charge-transfer kinetics at $T = 7.5\text{ }^{\circ}\text{C}$, $33\text{ }^{\circ}\text{C}$ and $57.5\text{ }^{\circ}\text{C}$ show a rather low sensitivity to temperature changes of the bulk medium, thus the estimated first-order reaction rates k , calculated in Figures 9a-b, were in the range 3.2 to $4.8 \times 10^{-4}\text{ s}^{-1}$. Figure 9c depicts that the activation energy for illuminated Ag@1SiO₂ was $E_a = 6.2\text{ kJ mol}^{-1}$ which is much lower than the observed $E_a = 25.4\text{ kJ mol}^{-1}$ in dark conditions, in the typical range for reactions involving redox-induced electron transfer ($20\text{--}90\text{ kJ mol}^{-1}$)^{62,63}. Recently, Halas's group^{64–66} reported that a substantial light-induced reduction of the activation barrier takes place in plasmon-enhanced photocatalytic processes when hot carriers are involved. This corroborates our present findings of a decreased activation energy in photocatalytic Cr⁶⁺ reduction by Ag@SiO₂.

However, the debate that emerged by the aforementioned work,^{67,68} necessitates the careful measurement of the photothermal effects as well.^{69,70} Herein, to further peer into the plasmon-driven mechanism, the role of excitation wavelength in Ag@1SiO₂ was studied where visible-light filters were employed during the Cr⁶⁺ photo-reduction, as shown in Figures 9d-e. As expected, cutting-off the plasmon resonance at $\lambda \sim 400\text{ nm}$, resulted in diminished efficiency. Further cutting-off the optical region while maintaining the same power intensity (150 mW cm^{-2}), Cr⁶⁺ reduction was further decreased indicating that photon energy away than the LSPR peak, has lower contribution in the reaction. The profile of thermal effects in Figure 6f shows that by cutting-off the plasmon resonance wavelength has a less severe impact on the photothermal performance, compared to the reaction yield. Specifically, the steep diminution of the Cr⁵⁺/Cr³⁺ species when $\lambda < 400\text{ nm}$ region was cut-off resembles to electronic transitions, while the linear decrease of photothermal heating tends to follow the absorption spectrum as expected. On a similar note to the light-induced decreased activation barrier, this observation strengthens the claim that hot-electron transfer is the prevailing mechanism since the role of thermal effects is minimized.

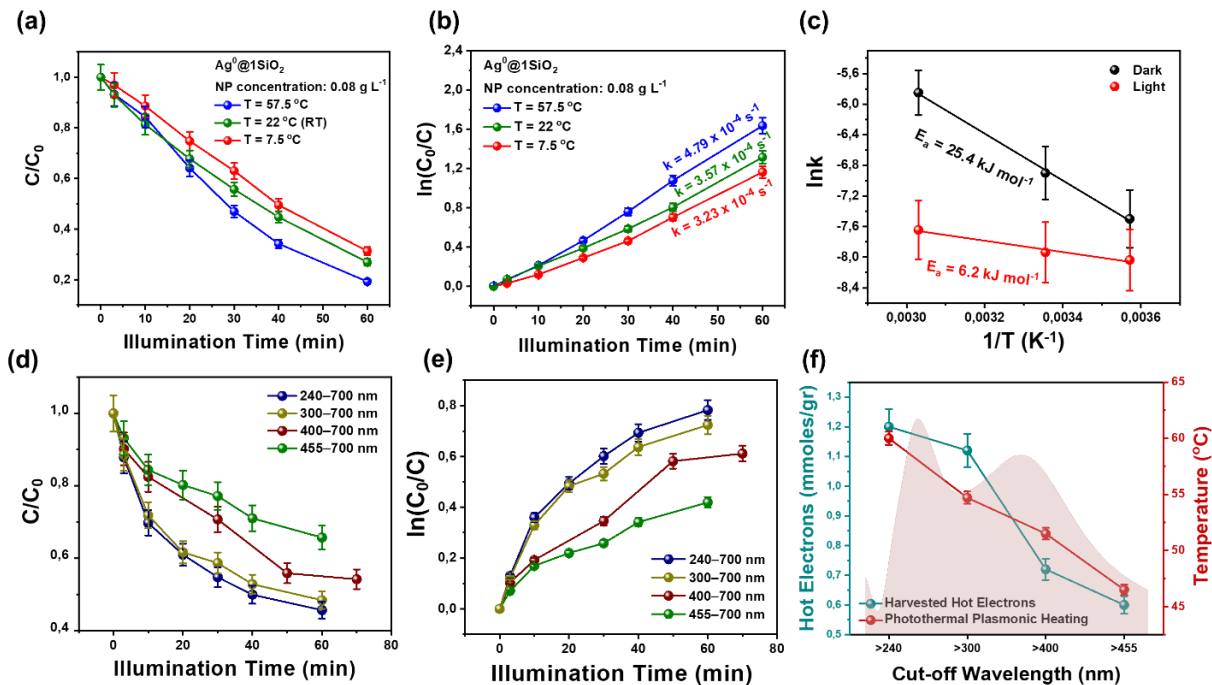


Figure 4.9. (a–c) Temperature dependence of Cr-reduction, by 0.08 g L^{-1} Ag@1SiO₂. (a) Reaction-order graph [$\ln(C/C_0)$ vs T] indicates that all temperatures, the process is first-order. Bulk-temperature change from 7.5 to 57.5 °C has limited effect on the kinetic rates. (b) Kinetics graph for Cr⁶⁺ reduction by Ag@1SiO₂ NPs for three different solution temperatures (7.5, 22, and 57.5 °C). (c) Arrhenius plot of Ag@1SiO₂/Cr-oxalate under dark and light. The activation energy is $E_a = 25 \text{ kJ mol}^{-1}$ and 6 kJ mol^{-1} respectively. Under light, the temperature was fixed at the same values measured under dark. (d, e) Effect of excitation wavelength on the Cr⁵⁺ production, using various light long-pass filters (240–700, 300–700, 400–700, and 455–700 nm). (f) Cr⁵⁺/Cr³⁺ species (hot electrons) and plasmon-induced bulk temperature using various light cut-off filters. (The UV-vis absorption spectrum of Ag@1SiO₂ is indicated as brown-shade).

Overall, based on the above findings, a conceptual energy diagram is proposed in Figure 10a. Hot electrons can be transferred to the external electron acceptor {Cr-oxalate} directly overcoming the barrier posed by the SiO₂ shell. Engineering the shell thickness, the interparticle nanogaps can be tuned determining the hot spot intensity and thus the

enhanced transfer of these energetic electrons to the {Cr-oxalates}. In this scheme, hot spots are seemingly promoters of hot-electron generation, as indicated by the enhanced performance of 1 nm shell (i.e. the closely coupled particles). STEM images, Figure 10b-d depicts that Cr-species are accumulated on the Ag@SiO₂ particles after irradiation. These are attributed to Cr³⁺, species that are known to have strong tendency to precipitate in aqueous solutions. Probably, the accumulation on the Ag@SiO₂ surface, as seen in STEM, can be higher at the interface of coupled particles where the hot spots prevail. This is an interesting possibility that deserves further study. In any case, from the environmental-remediation point of view, the present results indicate that the plasmonic Ag@SiO₂ nanoaggregates may play a double role i.e. to reduce Cr⁶⁺ to Cr³⁺ *via* highly energetic hot electrons, plus to attract them on the particle surface.

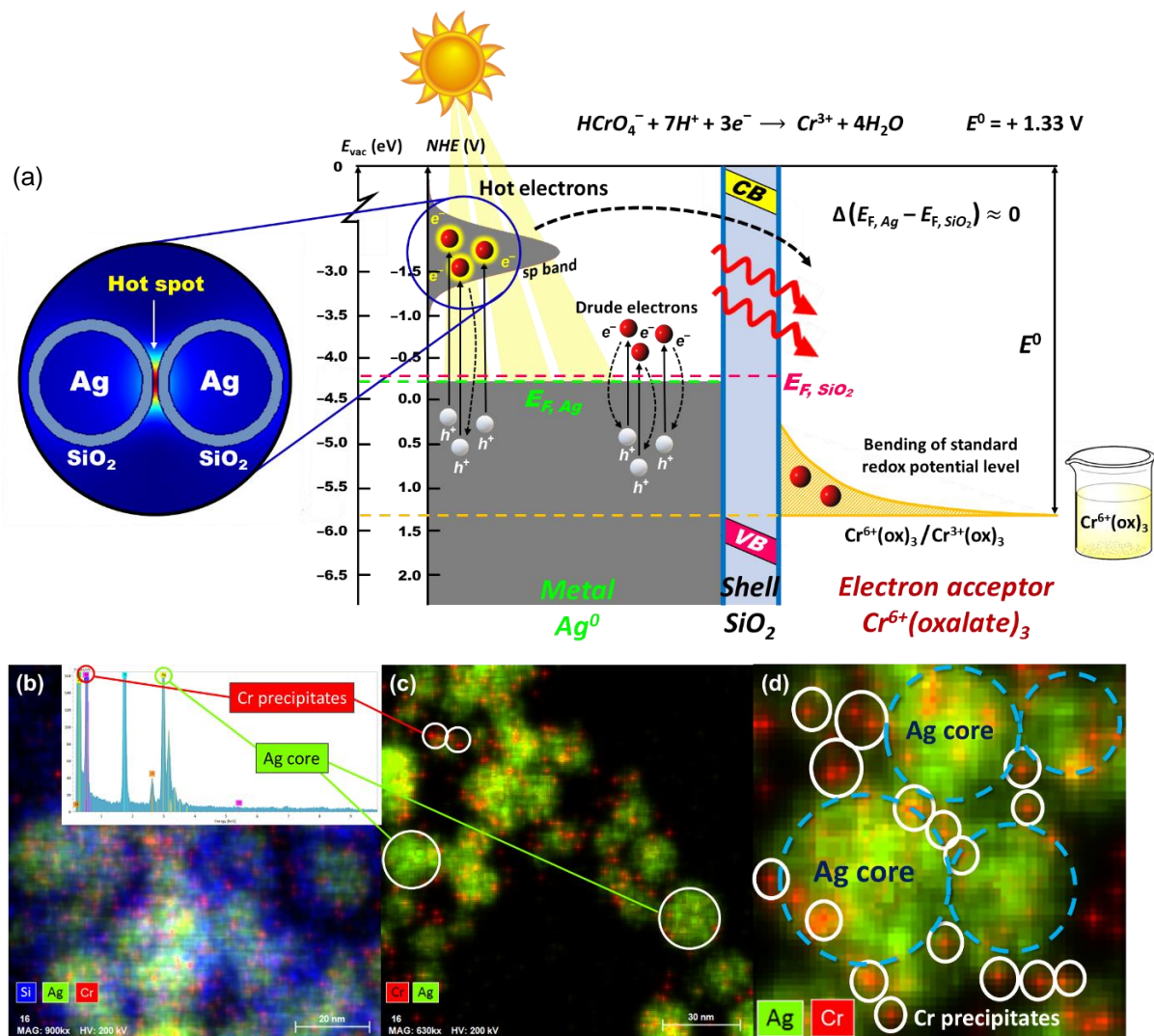


Figure 4.10. (a) Schematic illustration of energy diagram of core@shell–adsorbate [Ag⁰@SiO₂/{Cr⁶⁺-oxalate}] system demonstrating the bending of redox potential level of adsorbate {Cr⁶⁺(ox)₃/Cr³⁺(ox)₃} during illumination. STEM images of Ag@1SiO₂/{Cr-oxalate} system post-illumination, (b) showing Ag, Si and Cr (in green, blue and red color, respectively), (c) Ag and Cr precipitates (in green and red color), and (d) an indicative magnified region of (c), showing the Cr precipitates (red color, marked in white circles) at the interface of Ag nanoparticles. *Inset:* Energy-dispersive X-ray spectroscopy (EDS/EDX) spectrum for Ag@1SiO₂ (500 mg L⁻¹) post-photocatalysis. The Ag, Si and Cr peaks are detected. The Cr precipitates are expected to be Cr(OH)₃ during Cr⁶⁺ reduction in acidic environment.

Case Study #2: Plasmonic Switch in Oxidation Catalysis

In the same context of plasmon-enhanced redox reactions, the contribution of Ag@SiO₂ nanoaggregates in an oxidative process was explored as well. In particular, an alkene epoxidation performed by a molecular catalyst LMn^{II}, where L is a Schiff base ligand, in the presence of the plasmonic nanoparticles. Again, the scope is the proper disentanglement of the associated plasmonic mechanisms, such as hot carrier generation, the intense local electric fields and the thermal effects, on a similar manner to the case of Cr⁶⁺ photocatalytic reduction studied in the previous section.

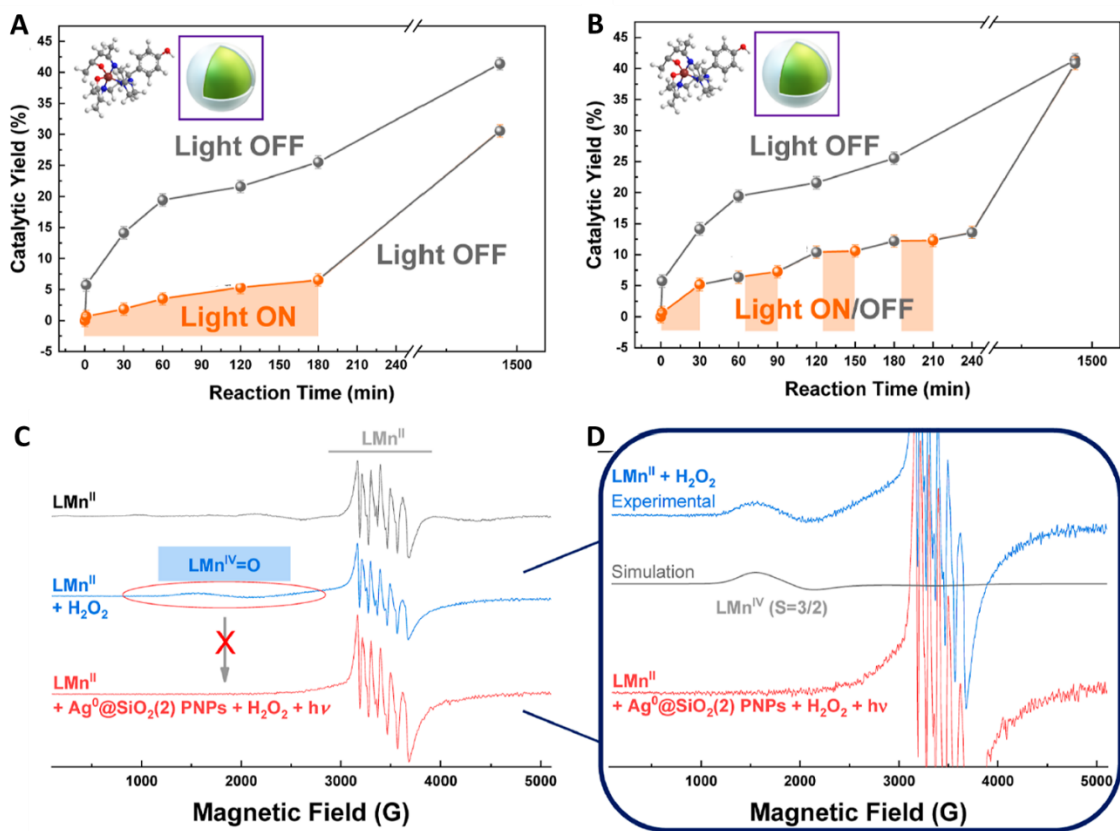


Figure 4.11. Reaction kinetics in the presence of Ag@3SiO₂ nanoaggregates without illumination and with (a) continuous illumination and (b) subsequent 30-minute light on/off. (c) EPR spectra of the LMn^{II} catalyst and the evolution after the addition of H₂O₂ (reference) and in presence of Ag@3SiO₂ while the sample is being exposed to light. (d) Magnified EPR spectra of the LMn^{II} after the addition of H₂O₂ in the absence of PNPs (reference) and in presence of PNPs while the sample is being exposed to light.

Surprisingly, upon irradiation of the Ag/SiO₂/LMn^{II} system, a reversible phenomenon that pauses the reaction kinetics was observed. Figures 11a-b depict that significant changes in the reaction kinetics are observed when the system is illuminated in the presence of Ag@3SiO₂, regardless of the illumination regime as follows: in the case of continuous illumination for 3h, a clear inhibition of the oxidation process was observed, reflected in a significant drop of the catalytic yield after 3 h, from 25% for the non-illuminated sample to 6.6%. In control experiment, without PNPs and no illumination treatment, after 3 h, a catalytic yield of 25.5% was achieved, which is typical for this catalytic reaction. This reaction hindering can be attributed to the presence of the plasmonic nanoparticles and can be reversible, with the catalytic yield approaching the typical values when the light is switched off.

Figures 11c-d show the EPR spectra of the LMn^{II} catalyst, the LMn^{II}+H₂O₂ and the Ag@2SiO₂/LMn^{II}+H₂O₂ under illumination. The LMn^{II} spectrum shows the typical signal of monomeric Mn^{II} ions ($S = 5/2, I = 5/2$) coordinated by the N- and O-atoms of the Schiff-base ligand. Shortly after the addition of H₂O₂, a new broad signal centered at $g \sim 4$ arises. This signal is typical of the LMn^{IV}=O species with $S = 3/2$. Figure 11d includes the theoretical simulation of LMn^{IV} ($S=3/2$). Thus, based on our EPR data, we conclude that in the presence of PNPs under illumination, the formation of the LMn^{IV}=O transient is inhibited, thus the “on demand” pause of the catalytic process, with the process of LMn^{IV}=O formation to be analyzed in detail elsewhere.

4.4 Conclusions

The efficient photoreduction of hexavalent Cr⁶⁺ can be achieved by photoexcited Ag@SiO₂ plasmonic nanoaggregates. The present work introduces a novel experimental concept and methodology for trapping and quantitative assessment of plasmon-induced hot electrons generated by core@shell plasmonic nanoaggregates, based on EPR spectroscopy. Cr species are efficient electron acceptors, and progressive one- and three-electron events are mapped *via* monitoring of intermediate states Cr⁵⁺($S=1/2$) and Cr³⁺($S= 3/2$). Plasmonic coupling is the key parameter for successful transfer of the energetic carriers from the

interior of the plasmonic nanocrystal to the exterior/interfacial Cr-acceptor. FSP provides a state-of-the-art technology to control interparticle distance by engineering the shell thickness. The case of ultrathin SiO₂ shell allows a considerable hot-electron transfer and a light-induced lowering of the activation barrier, while the role of thermal effects and Ag oxidation phenomena are minimized. The present findings offer a new dimension on plasmon-driven photoreduction of hexavalent Cr⁶⁺, in terms of the solar-driven environmental remediation.

References

- (1) Järup, L. Hazards of Heavy Metal Contamination. *British Medical Bulletin* **2003**, *68* (1), 167–182. <https://doi.org/10.1093/bmb/ldg032>.
- (2) Yang, L.; Xiao, Y.; Liu, S.; Li, Y.; Cai, Q.; Luo, S.; Zeng, G. Photocatalytic Reduction of Cr(VI) on WO₃ Doped Long TiO₂ Nanotube Arrays in the Presence of Citric Acid. *Applied Catalysis B: Environmental* **2010**, *94* (1–2), 142–149. <https://doi.org/10.1016/j.apcatb.2009.11.002>.
- (3) Linic, S.; Christopher, P.; Ingram, D. B. Plasmonic-Metal Nanostructures for Efficient Conversion of Solar to Chemical Energy. *Nature Materials* **2011**, *10* (12), 911–921. <https://doi.org/10.1038/nmat3151>.
- (4) Zhang, Y.; He, S.; Guo, W.; Hu, Y.; Huang, J.; Mulcahy, J. R.; Wei, W. D. Surface-Plasmon-Driven Hot Electron Photochemistry. *Chemical Reviews* **2018**, *118* (6), 2927–2954. <https://doi.org/10.1021/acs.chemrev.7b00430>.
- (5) Christopher, P.; Xin, H.; Linic, S. Visible-Light-Enhanced Catalytic Oxidation Reactions on Plasmonic Silver Nanostructures. *Nature Chem* **2011**, *3* (6), 467–472. <https://doi.org/10.1038/nchem.1032>.
- (6) Cortés, E.; Besteiro, L. V.; Alabastri, A.; Baldi, A.; Tagliabue, G.; Demetriadou, A.; Narang, P. Challenges in Plasmonic Catalysis. *ACS Nano* **2020**, *14* (12), 16202–16219. <https://doi.org/10.1021/acsnano.0c08773>.

- (7) Halas, N. J.; Lal, S.; Chang, W.-S.; Link, S.; Nordlander, P. Plasmons in Strongly Coupled Metallic Nanostructures. *Chemical Reviews* **2011**, *111* (6), 3913–3961. <https://doi.org/10.1021/cr200061k>.
- (8) Schuller, J. A.; Barnard, E. S.; Cai, W.; Jun, Y. C.; White, J. S.; Brongersma, M. L. Plasmonics for Extreme Light Concentration and Manipulation. *Nature Materials* **2010**, *9* (3), 193–204. <https://doi.org/10.1038/nmat2630>.
- (9) Baffou, G. Q. Thermo-Plasmonics: Using Metallic Nanostructures as Nano-Sources of Heat. *Laser Photonic Rev.* **2012**, 1–17. <https://doi.org/10.1002/lpor.201200003>.
- (10) Hartland, G. V. Optical Studies of Dynamics in Noble Metal Nanostructures. *Chem. Rev.* **2011**, *111*, 3858–3887. <https://doi.org/dx.doi.org/10.1021/cr1002547>.
- (11) Brongersma, M. L.; Halas, N. J.; Nordlander, P. Plasmon-Induced Hot Carrier Science and Technology. *Nature Nanotechnology* **2015**, *10* (1), 25–34. <https://doi.org/10.1038/nnano.2014.311>.
- (12) Hartland, G. V.; Besteiro, L. V.; Johns, P.; Govorov, A. O. What’s so Hot about Electrons in Metal Nanoparticles? *ACS Energy Letters* **2017**, *2* (7), 1641–1653. <https://doi.org/10.1021/acsenergylett.7b00333>.
- (13) Warren, S. C.; Thimsen, E. Plasmonic Solar Water Splitting. *Energy Environ. Sci.* **2012**, *5* (1), 5133–5146. <https://doi.org/10.1039/C1EE02875H>.
- (14) Ingram, D. B.; Linic, S. Water Splitting on Composite Plasmonic-Metal/Semiconductor Photoelectrodes: Evidence for Selective Plasmon-Induced Formation of Charge Carriers near the Semiconductor Surface. *J. Am. Chem. Soc.* **2011**, *133* (14), 5202–5205. <https://doi.org/10.1021/ja200086g>.
- (15) Lee, J.; Mubeen, S.; Ji, X.; Stucky, G. D.; Moskovits, M. Plasmonic Photoanodes for Solar Water Splitting with Visible Light. *Nano Letters* **2012**, *12* (9), 5014–5019. <https://doi.org/10.1021/nl302796f>.
- (16) Zhou, L.; Martirez, J. M. P.; Finzel, J.; Zhang, C.; Swearer, D. F.; Tian, S.; Robotjazi, H.; Lou, M.; Dong, L.; Henderson, L.; Christopher, P.; Carter, E. A.; Nordlander, P.; Halas, N. J. Light-Driven Methane Dry Reforming with Single Atomic Site Antenna-Reactor Plasmonic Photocatalysts. *Nat Energy* **2020**, *5* (1), 61–70. <https://doi.org/10.1038/s41560-019-0517-9>.

- (17) Hou, W.; Hung, W. H.; Pavaskar, P.; Goeppert, A.; Aykol, M.; Cronin, S. B. Photocatalytic Conversion of CO₂ to Hydrocarbon Fuels via Plasmon-Enhanced Absorption and Metallic Interband Transitions. *ACS Catalysis* **2011**, *1* (8), 929–936. <https://doi.org/10.1021/cs2001434>.
- (18) Robotjazi, H.; Bao, J. L.; Zhang, M.; Zhou, L.; Christopher, P.; Carter, E. A.; Nordlander, P.; Halas, N. J. Plasmon-Driven Carbon–Fluorine (C(Sp³)-F) Bond Activation with Mechanistic Insights into Hot-Carrier-Mediated Pathways. *Nat Catal* **2020**, *3* (7), 564–573. <https://doi.org/10.1038/s41929-020-0466-5>.
- (19) Seemala, B.; Therrien, A. J.; Lou, M.; Li, K.; Finzel, J. P.; Qi, J.; Nordlander, P.; Christopher, P. Plasmon-Mediated Catalytic O₂ Dissociation on Ag Nanostructures: Hot Electrons or Near Fields? *ACS Energy Lett.* **2019**, *4* (8), 1803–1809. <https://doi.org/10.1021/acsenergylett.9b00990>.
- (20) Manjavacas, A.; Liu, J. G.; Kulkarni, V.; Nordlander, P. Plasmon-Induced Hot Carriers in Metallic Nanoparticles. *ACS Nano* **2014**, *8* (8), 7630–7638. <https://doi.org/10.1021/nn502445f>.
- (21) Besteiro, L. V.; Govorov, A. O. Amplified Generation of Hot Electrons and Quantum Surface Effects in Nanoparticle Dimers with Plasmonic Hot Spots. *The Journal of Physical Chemistry C* **2016**, *120* (34), 19329–19339. <https://doi.org/10.1021/acs.jpcc.6b05968>.
- (22) Harutyunyan, H.; Martinson, A. B. F.; Rosenmann, D.; Khorashad, L. K.; Besteiro, L. V.; Govorov, A. O.; Wiederrecht, G. P. Anomalous Ultrafast Dynamics of Hot Plasmonic Electrons in Nanostructures with Hot Spots. *Nature Nanotechnology* **2015**, *10* (9), 770–774. <https://doi.org/10.1038/nnano.2015.165>.
- (23) Kong, X.-T.; Wang, Z.; Govorov, A. O. Plasmonic Nanostars with Hot Spots for Efficient Generation of Hot Electrons under Solar Illumination. *Advanced Optical Materials* **2017**, *5* (15). <https://doi.org/10.1002/adom.201600594>.
- (24) Santiago, E. Y.; Besteiro, L. V.; Kong, X.-T.; Correa-Duarte, M. A.; Wang, Z.; Govorov, A. O. Efficiency of Hot-Electron Generation in Plasmonic Nanocrystals with Complex Shapes: Surface-Induced Scattering, Hot Spots, and Interband Transitions. *ACS Photonics* **2020**, *7* (10), 2807–2824. <https://doi.org/10.1021/acsp Photonics.0c01065>.

- (25) Besteiro, L. V.; Yu, P.; Wang, Z.; Holleitner, A. W.; Hartland, G. V.; Wiederrecht, G. P.; Govorov, A. O. The Fast and the Furious: Ultrafast Hot Electrons in Plasmonic Metastructures. Size and Structure Matter. *Nano Today* **2019**, *27*, 120–145. <https://doi.org/10.1016/j.nantod.2019.05.006>.
- (26) Jang, Y. J.; Chung, K.; Lee, J. S.; Choi, C. H.; Lim, J. W.; Kim, D. H. Plasmonic Hot Carriers Imaging: Promise and Outlook. *ACS Photonics* **2018**, *5* (12), 4711–4723. <https://doi.org/10.1021/acsp Photonics.8b01021>.
- (27) Besteiro, L. V.; Kong, X.-T.; Wang, Z.; Hartland, G.; Govorov, A. O. Understanding Hot-Electron Generation and Plasmon Relaxation in Metal Nanocrystals: Quantum and Classical Mechanisms. *ACS Photonics* **2017**, *4* (11), 2759–2781. <https://doi.org/10.1021/acsp Photonics.7b00751>.
- (28) Lock, D.; Rusimova, K. R.; Pan, T. L.; Palmer, R. E.; Sloan, P. A. Atomically Resolved Real-Space Imaging of Hot Electron Dynamics. *Nature Communications* **2015**, *6* (1), 8365. <https://doi.org/10.1038/ncomms9365>.
- (29) Hu, M.; Novo, C.; Funston, A.; Wang, H.; Staleva, H.; Zou, S.; Mulvaney, P.; Xia, Y.; Hartland, G. V. Dark-Field Microscopy Studies of Single Metal Nanoparticles: Understanding the Factors That Influence the Linewidth of the Localized Surface Plasmon Resonance. *Journal of Materials Chemistry* **2008**, *18* (17), 1949. <https://doi.org/10.1039/b714759g>.
- (30) Giugni, A.; Torre, B.; Toma, A.; Francardi, M.; Malerba, M.; Alabastri, A.; Proietti Zaccaria, R.; Stockman, M. I.; Di Fabrizio, E. Hot-Electron Nanoscopy Using Adiabatic Compression of Surface Plasmons. *Nature Nanotechnology* **2013**, *8* (11), 845–852. <https://doi.org/10.1038/nnano.2013.207>.
- (31) Segal, E.; Galanty, M.; Aharon, H.; Salomon, A. Visualization of Plasmon-Induced Hot Electrons by Scanning Electron Microscopy. *The Journal of Physical Chemistry C* **2019**, *123* (50), 30528–30535. <https://doi.org/10.1021/acspjcc.9b08202>.
- (32) Reddy, H.; Wang, K.; Kudyshev, Z.; Zhu, L.; Yan, S.; Vezzoli, A.; Higgins, S. J.; Gavini, V.; Boltasseva, A.; Reddy, P.; Shalaev, V. M.; Meyhofer, E. Determining Plasmonic Hot-Carrier Energy Distributions via Single-Molecule Transport Measurements. *Science* **2020**, *369* (6502), 423–426. <https://doi.org/10.1126/science.abb3457>.

- (33) Cortés, E.; Xie, W.; Cambiasso, J.; Jermyn, A. S.; Sundararaman, R.; Narang, P.; Schlücker, S.; Maier, S. A. Plasmonic Hot Electron Transport Drives Nano-Localized Chemistry. *Nature Communications* **2017**, *8* (1), 14880. <https://doi.org/10.1038/ncomms14880>.
- (34) Simoncelli, S.; Li, Y.; Cortés, E.; Maier, S. A. Nanoscale Control of Molecular Self-Assembly Induced by Plasmonic Hot-Electron Dynamics. *ACS Nano* **2018**, *12* (3), 2184–2192. <https://doi.org/10.1021/acsnano.7b08563>.
- (35) Zhai, Y.; DuChene, J. S.; Wang, Y.-C.; Qiu, J.; Johnston-Peck, A. C.; You, B.; Guo, W.; DiCiaccio, B.; Qian, K.; Zhao, E. W.; Ooi, F.; Hu, D.; Su, D.; Stach, E. A.; Zhu, Z.; Wei, W. D. Polyvinylpyrrolidone-Induced Anisotropic Growth of Gold Nanoprisms in Plasmon-Driven Synthesis. *Nature Materials* **2016**, *15* (8), 889–895. <https://doi.org/10.1038/nmat4683>.
- (36) Yu, Y.; Wijesekara, K. D.; Xi, X.; Willets, K. A. Quantifying Wavelength-Dependent Plasmonic Hot Carrier Energy Distributions at Metal/Semiconductor Interfaces. *ACS Nano* **2019**, *13* (3), 3629–3637. <https://doi.org/10.1021/acsnano.9b00219>.
- (37) Testa, J. J.; Grela, M. A.; Litter, M. I. Heterogeneous Photocatalytic Reduction of Chromium(VI) over TiO₂ Particles in the Presence of Oxalate: Involvement of Cr(V) Species. *Environ. Sci. Technol.* **2004**, *38* (5), 1589–1594. <https://doi.org/10.1021/es0346532>.
- (38) Giannakas, A. E.; Seristatidou, E.; Deligiannakis, Y.; Konstantinou, I. Photocatalytic Activity of N-Doped and N–F Co-Doped TiO₂ and Reduction of Chromium(VI) in Aqueous Solution: An EPR Study. *Applied Catalysis B: Environmental* **2013**, *132–133*, 460–468. <https://doi.org/10.1016/j.apcatb.2012.12.017>.
- (39) Pattison, D. I.; Lay, P. A.; Davies, M. J. EPR Studies of Chromium(V) Intermediates Generated via Reduction of Chromium(VI) by DOPA and Related Catecholamines: Potential Role for Oxidized Amino Acids in Chromium-Induced Cancers. *Inorg. Chem.* **2000**, *39* (13), 2729–2739. <https://doi.org/10.1021/ic991443a>.
- (40) Farrell, R. P.; Lay, P. A.; Levina, A.; Maxwell, I. A.; Bramley, R.; Brumby, S.; Ji. An EPR Spectroscopic Study of Chromium(V) Oxalato Complexes in Aqueous

- Solutions. Mechanism of the Chromium(VI) Oxidation of Oxalic Acid. *Inorg. Chem.* **1998**, *37* (13), 3159–3166. <https://doi.org/10.1021/ic971070i>.
- (41) Eaton, G. R.; Eaton, S. S.; Barr, D. P.; Weber, R. T.; (Wiedeń), S.-V. *Quantitative EPR*; Springer: Wien; New York, 2014.
- (42) Deligiannakis, Y.; Louloudi, M.; Hadjiliadis, N. Electron Spin Echo Envelope Modulation (ESEEM) Spectroscopy as a Tool to Investigate the Coordination Environment of Metal Centers. *Coordination Chemistry Reviews* **2000**, *204* (1), 1–112. [https://doi.org/10.1016/S0010-8545\(99\)00218-0](https://doi.org/10.1016/S0010-8545(99)00218-0).
- (43) Sotiriou, G. A.; Blattmann, C. O.; Deligiannakis, Y. Nanoantioxidant-Driven Plasmon Enhanced Proton-Coupled Electron Transfer. *Nanoscale* **2016**, *8* (2), 796–803. <https://doi.org/10.1039/C5NR04942C>.
- (44) Mitrikas, G.; Deligiannakis, Y.; Trapalis, C. C.; Boukos, N.; Kordas, G. CW and Pulsed EPR Study of Silver Nanoparticles in a SiO₂ Matrix. *Journal of Sol-Gel Science and Technology* **1998**, *13* (1/3), 503–508. <https://doi.org/10.1023/A:1008654102264>.
- (45) Moularas, C.; Psathas, P.; Deligiannakis, Y. Electron Paramagnetic Resonance Study of Photo-Induced Hole/Electron Pairs in NaTaO₃ Nanoparticles. *Chemical Physics Letters* **2021**, *782*, 139031. <https://doi.org/10.1016/j.cplett.2021.139031>.
- (46) Bou-Abdallah, F.; Chasteen, N. D. Spin Concentration Measurements of High-Spin ($G' = 4.3$) Rhombic Iron(III) Ions in Biological Samples: Theory and Application. *J Biol Inorg Chem* **2007**, *13* (1), 15–24. <https://doi.org/10.1007/s00775-007-0304-0>.
- (47) Moularas, C.; Georgiou, Y.; Adamska, K.; Deligiannakis, Y. Thermoplasmonic Heat Generation Efficiency by Nonmonodisperse Core–Shell Ag⁰@SiO₂ Nanoparticle Ensemble. *J. Phys. Chem. C* **2019**, *123* (36), 22499–22510. <https://doi.org/10.1021/acs.jpcc.9b06532>.
- (48) Naik, G. V.; Shalaev, V. M.; Boltasseva, A. Alternative Plasmonic Materials: Beyond Gold and Silver. *Adv. Mater.* **2013**. <https://doi.org/10.1002/adma.201205076>.
- (49) Pratsinis, S.; Mueller, R.; Kammler, H. K.; Madler, L. Controlled Synthesis of Nanostructured Particles by Flame Spray Pyrolysis. *Aerosol Science* **2002**, *33*, 369–389.

- (50) Madler, L.; Amal, R.; Teoh, W. Y. Flame Spray Pyrolysis: An Enabling Technology for Nanoparticles Design and Fabrication. *Nanoscale* **2010**, *2*, 1324–1347. <https://doi.org/10.1039/c0nr00017e>.
- (51) Sotiriou, G.; Sannomiya, T.; Teleki, A.; Krumeich, F.; Pratsinis, S. Non-Toxic Dry-Coated Nanosilver for Plasmonic Biosensors. *ADVANCED MATERIALS* **2010**.
- (52) Teleki, A.; Heine, M.; Krumeich, F.; Akhtar, K.; Pratsinis, S. In Situ Coating of Flame-Made TiO₂ Particles with Nanothin SiO₂ Films. *Langmuir* **2008**, 12553–12558. <https://doi.org/10.1021/la801630z>.
- (53) Teleki, A.; Akhtar, M. K.; Pratsinis, S. E. The Quality of SiO₂-Coatings on Flame-Made TiO₂-Based Nanoparticles. *Journal of Materials Chemistry* **2008**, *18* (30), 3547. <https://doi.org/10.1039/b803039a>.
- (54) Grigoropoulou, G.; Christoforidis, K. C.; Louloudi, M.; Deligiannakis, Y. Structure-Catalytic Function Relationship of SiO₂-Immobilized Mononuclear Cu Complexes: An EPR Study. *Langmuir* **2007**, *23* (20), 10407–10418. <https://doi.org/10.1021/la700815d>.
- (55) Stover, N. M. DIPHENYLCARBAZIDE AS A TEST FOR CHROMIUM. *J. Am. Chem. Soc.* **1928**, *50* (9), 2363–2366. <https://doi.org/10.1021/ja01396a007>.
- (56) Sotiriou, G.; Gass, S.; Pratsinis, S. Hermetically Coated Nanosilver: No Ag⁺ Ion Leaching. *Materials Research Society* **2012**, 1386.
- (57) Jiang, M.-M.; Chen, H.-Y.; Li, B.-H.; Liu, K.-W.; Shan, C.-X.; Shen, D.-Z. Hybrid Quadrupolar Resonances Stimulated at Short Wavelengths Using Coupled Plasmonic Silver Nanoparticle Aggregation. *J. Mater. Chem. C* **2014**, *2* (1), 56–63. <https://doi.org/10.1039/C3TC31910E>.
- (58) Das, S. K.; Khan, Md. M. R.; Parandhaman, T.; Laffir, F.; Guha, A. K.; Sekaran, G.; Mandal, A. B. Nano-Silica Fabricated with Silver Nanoparticles: Antifouling Adsorbent for Efficient Dye Removal, Effective Water Disinfection and Biofouling Control. *Nanoscale* **2013**, *5* (12), 5549. <https://doi.org/10.1039/c3nr00856h>.
- (59) Sotiriou, G. A.; Meyer, A.; Knijnenburg, J. T. N.; Panke, S.; Pratsinis, S. E. Quantifying the Origin of Released Ag⁺ Ions from Nanosilver. *Langmuir* **2012**, *28* (45), 15929–15936. <https://doi.org/10.1021/la303370d>.

- (60) Andriessen, W. T. M.; Groenewege, M. P. Electron Paramagnetic Resonance of Chromium(III) Complexes of the Type Cis-[Cr(2,2'-Bpy)2XY]Z, Cis-[Cr(1,10-Phen)2XY]Z, and Cis-[Cr(Ox)2XY]Z in Frozen Solutions and Powders. *Inorg. Chem.* **1976**, *15* (3), 621–626. <https://doi.org/10.1021/ic50157a024>.
- (61) Mytych, P.; Cieřla, P.; Stasicka, Z. Photoredox Processes in the Cr(VI)–Cr(III)–Oxalate System and Their Environmental Relevance. *Applied Catalysis B: Environmental* **2005**, *59* (3–4), 161–170. <https://doi.org/10.1016/j.apcatb.2004.12.015>.
- (62) Psathas, P.; Georgiou, Y.; Moularas, C.; Armatas, G. S.; Deligiannakis, Y. Controlled-Phase Synthesis of Bi₂Fe₄O₉ & BiFeO₃ by Flame Spray Pyrolysis and Their Evaluation as Non-Noble Metal Catalysts for Efficient Reduction of 4-Nitrophenol. *Powder Technology* **2020**. <https://doi.org/10.1016/j.powtec.2020.04.059>.
- (63) Peng, H.; Guo, J. Reduction Behavior of Chromium(VI) with Oxalic Acid in Aqueous Solution. *Sci Rep* **2020**, *10* (1), 17732. <https://doi.org/10.1038/s41598-020-74928-7>.
- (64) Zhou, L.; Swearer, D. F.; Zhang, C.; Robotjazi, H.; Zhao, H.; Henderson, L.; Dong, L.; Christopher, P.; Carter, E. A.; Nordlander, P.; Halas, N. J. Quantifying Hot Carrier and Thermal Contributions in Plasmonic Photocatalysis. *Science* **2018**, *362* (6410), 69–72. <https://doi.org/10.1126/science.aat6967>.
- (65) Swearer, D. F.; Robotjazi, H.; Martirez, J. M. P.; Zhang, M.; Zhou, L.; Carter, E. A.; Nordlander, P.; Halas, N. J. Plasmonic Photocatalysis of Nitrous Oxide into N₂ and O₂ Using Aluminum–Iridium Antenna–Reactor Nanoparticles. *ACS Nano* **2019**, *13* (7), 8076–8086. <https://doi.org/10.1021/acsnano.9b02924>.
- (66) Yuan, L.; Lou, M.; Clark, B. D.; Lou, M.; Zhou, L.; Tian, S.; Jacobson, C. R.; Nordlander, P.; Halas, N. J. Morphology-Dependent Reactivity of a Plasmonic Photocatalyst. *ACS Nano* **2020**, *14* (9), 12054–12063. <https://doi.org/10.1021/acsnano.0c05383>.
- (67) Sivan, Y.; Baraban, J.; Un, I. W.; Dubi, Y. Comment on “Quantifying Hot Carrier and Thermal Contributions in Plasmonic Photocatalysis.” *Science* **2019**, *364* (6439), eaaw9367. <https://doi.org/10.1126/science.aaw9367>.
- (68) Zhou, L.; Swearer, D. F.; Robotjazi, H.; Alabastri, A.; Christopher, P.; Carter, E. A.; Nordlander, P.; Halas, N. J. Response to Comment on “Quantifying Hot Carrier

and Thermal Contributions in Plasmonic Photocatalysis.” *Science* **2019**, *364* (6439), eaaw9545. <https://doi.org/10.1126/science.aaw9545>.

- (69) Mascaretti, L.; Naldoni, A. Hot Electron and Thermal Effects in Plasmonic Photocatalysis. *Journal of Applied Physics* **2020**, *128* (4), 041101. <https://doi.org/10.1063/5.0013945>.
- (70) Baffou, G.; Bordacchini, I.; Baldi, A.; Quidant, R. Simple Experimental Procedures to Distinguish Photothermal from Hot-Carrier Processes in Plasmonics. *Light Sci Appl* **2020**, *9* (1), 108. <https://doi.org/10.1038/s41377-020-00345-0>.

Chapter 5

Photo-induced Electron/Hole Dynamics in Flame-made NaTaO₃ Nanoparticles

5.1 Introduction

Alkali tantalates, particularly NaTaO₃, are promising photocatalytic perovskites under UV excitation,¹⁻⁴ due to highly negative conduction-band energy, determined primarily by the *d*-orbitals of tantalum, and the effect of alkaline atoms. Despite major research focus on NaTaO₃, there is currently less understanding of key-aspects of photo-generated holes and electrons. Photocatalytic activation of semiconductive metal oxides, leads to rapid {h⁺/e⁻} separation, thus appropriate *in situ* spectroscopies are required to trap, identify and monitor such elusive species. In this context, Electron Paramagnetic Resonance (EPR) has provided valuable information for direct detection of holes and electrons in colloidal TiO₂^{5,6}, and nano-TiO₂ with emphasis on P25-TiO₂⁷⁻⁹. Specifically

³Part of this work is published in *Chem. Phys. Lett.* 2021, 782, 36, 139031 and *ACS Appl. Nano Mater.* 2023, 6, 4, 2658–2671

Nakaoka et al.¹⁰ has shown that hole-related EPR signals originate from $\{\text{Ti}^{4+}\cdot\text{O}\cdot\text{Ti}^{4+}\cdot\text{O}(\text{H})\}$ units in TiO_2 , while a detailed EPR study of $\{\text{h}^+/\text{e}^-\}$ pairs in Anatase/Rutile TiO_2 ¹¹ and the understanding of photoactive centers in N-doped TiO_2 by Giamello's group¹² have further refined our comprehension of carrier dynamics in TiO_2 semiconductors. So far, only a few EPR studies exist on photoactive NaTaO_3 , however none on photogenerated $\{\text{h}^+/\text{e}^-\}$ pairs. Wang et al. have reported a single derivative EPR signal at $g\sim 2$ detected in self-doped NaTaO_3 , attributed to reduced Ta^{4+} centers, however no further information related to structure, kinetics and relation to H_2 production was provided¹³. Although Meyer et al. detected photo-induced EPR signals of surface-anchored oxygen species in relatively small NaTaO_3 (25nm), no direct detection of trapped electrons was verified¹⁴.

Control of NaTaO_3 particle size at the nanoscale, appears as an interesting bottleneck by itself, since the majority of the reported NaTaO_3 displays (sub)micrometric size^{13,15}. Herein, we made the hypothesis that synthesis of smaller nano- NaTaO_3 , would facilitate the elusive photo-induced $\{\text{h}^+/\text{e}^-\}$ pairs. Thus, NaTaO_3 nanoparticles were synthesized using flame spray pyrolysis (FSP)¹⁶, with the lowest achieved, to our knowledge, particle size of 14nm. FSP is a well-established flame-combustion process, suitable for engineering nanomaterials of controlled size and phase^{17,18}. To understand the role of the particle size in $\{\text{h}^+/\text{e}^-\}$ dynamics, two NaTaO_3 sizes (14 and 26nm) were studied. The aim of the present work was the [i] development of flame-made small NaTaO_3 nanoparticles, [ii] *in situ* trapping and identification of the photo-generated $\{\text{h}^+/\text{e}^-\}$ pairs by low-temperature CW-EPR (77K) and [iii] study of recombination dynamics of the $\{\text{h}^+/\text{e}^-\}$ pairs, in conjunction with photocatalytic H_2 production performance.

5.2 Materials & Methods

Synthesis of NaTaO_3 by Flame Spray Pyrolysis: The nanoparticles were produced in a single-nozzle enclosed FSP reactor, described previously¹⁸. The precursor solution contained Tantalum(V) chloride (anhydrous 99.9%, STREM) and sodium 2-ethylhexanoate (98%, TCI) of molar ratio 1:1, dissolved in ethanol. The FSP parameters comprised of a dispersion oxygen flow rate of 5 L/min (Linde 99%) and a precursor flow rate of 5 mL/min. To control the particle size, the low molarity of 60mM for 14 nm particles was used and a high concentration of 240mM for the 26nm particles. The flame was

enclosed by a quartz tube of 20 cm height. The produced particles were deposited on a glass microfibre filter with a binder (Albet Labscience GF_6_257), assisted by a vacuum pump (BUSCH) and collected by scraping of the powder. The nanomaterials were stored in glass vials under an inert Argon atmosphere, until use.

Synthesis of Ag/NaTaO₃ by Flame Spray Pyrolysis: Ag/TiO₂@TiO_x heterostructures have been prepared by flame spray pyrolysis using a dual nozzle configuration shown in Figure 1 and described in previous work. Precursor molarity, precursor fuel feed rate to dispersion gas rate (P/D ratio) and the internozzle distance was adjusted accordingly so that the desired particle size of each element can be controlled independently. For the NaTaO₃ case, the setup parameters are described, while for Ag, silver acetate (sigma aldrich, >99%) was dissolved in acid/acetonitrile (1:1). The detailed parameters are demonstrated in Table 2. The powder product was collected, using a vacuum pump (Busch V40), on a glass microfiber filter (Albet) placed 66 cm above the flame mixing point.

Powder X-Ray Diffractions (pXRD): The powder crystal structures were analyzed with a D8 Advance Bruker diffractometer, radiation source Cu (K α , $\lambda=1,5418$), with operation parameters of 40 mA current and 40 KV generator voltage.

Transmission Electron Microscopy: Morphology, nanostructure and chemical composition of nanoparticles was examined using FEI Titan 80-300 S/TEM microscope at 300 kV accelerating voltage. STEM images were obtained with beam convergence semi angle of 21.5 mrad. Sample preparation consisted of sonicating powdered samples in ethanol and depositing the homogeneous suspension in the form of a single droplet on a TEM copper grid covered by a carbon-fiber film. Before imaging, to remove any organic contamination, samples were treated for 3 seconds in argon plasma using Fischione Instruments 1020 Plasma Cleaner.

Electron Paramagnetic Resonance Spectroscopy: The X-band electron paramagnetic resonance (EPR) spectra of NaTaO₃ nanoaggregates were recorded with a Bruker ER200D spectrometer at 77 K, equipped with an Agilent 5310A frequency counter. The spectrometer was running under a home-made software based on LabView¹⁹. Adequate signal to noise ratio was obtained after 30-50 scans, with a microwave power fixed at 6 dB.

The EPR instrumental conditions were as follows: microwave frequency = 9.55 GHz, modulation frequency = +50.00 kHz, and modulation amplitude = 10 Gauss peak-to-peak. The spectra of photo-induced species were obtained by subtracting the EPR data in dark conditions from the data recorded under illumination. Irradiation of the samples was performed *in-situ* using an arc Xenon lamp (model: Oriel 6293, 1000 W) operating with 750 W input power. To eliminate heating effects, a water-filter was inserted before the focusing lens to eliminate the infrared contribution. 15mg of NaTaO₃ powder was placed in a 5mm EPR tube (Wilmad) and then frozen at 77K. After obtaining each light-minus-dark spectra, the tube was thawed for 5 seconds at RT in the dark, and frozen instantly at 77K, to examine the photo-excited carrier kinetics. Once measurement is done, this process was repeated for various time intervals in RT-dark.

Simulation of the EPR spectra: The photo-induced EPR signals obtained experimentally, were simulated using the Easyspin Matlab package. For all samples, the electron- and hole-related signals display axial and rhombic g-tensors assigned to Ta⁴⁺ centers and oxygen anion radicals respectively, as listed in Table 1. In the case of a NaTaO₃ nanocrystal, the nuclei contributions should be considered as well, specifically the ¹⁸¹Ta (I=7/2) and ²³Na(I=3/2) isotopes of 100% natural abundance. In general, the spin Hamiltonian (H_s) for a spin system is expressed as:

$$H_s = H_{SZ} + H_{SN} + H_{NZ} + H_{NN} + H_{NQ} + H_{ZFS} \quad (5.1),$$

where the six energy terms describe the spin-magnetic field (SZ), spin-nucleus (SN), nucleus-magnetic field (NZ), nucleus-nucleus (NN), nucleus-quadrupolar moment (NQ) and spin-spin (ZFS) interactions respectively. The (NZ) and (NN) interactions are negligible in CW-EPR. Although the NaTaO₃ spin system contains a non-zero nuclear quadrupole moment (I>1/2), (NQ) interaction has a minor contribution due to broadenings in field-swept EPR spectra. Thus, in this work, the spin Hamiltonian is given by:

$$H_s = \beta_e \mathbf{B}_0 \mathbf{g}_{e1} \mathbf{S} + \beta_e \mathbf{B}_0 \mathbf{g}_{e2} \mathbf{S} + \beta_e \mathbf{B}_0 \mathbf{g}_{h1} \mathbf{S} + \beta_e \mathbf{B}_0 \mathbf{g}_{h2} \mathbf{S} + \mathbf{S} \mathbf{A}_{Ta} \mathbf{I} + \mathbf{S} \mathbf{A}_{Na} \mathbf{I} \quad (5.2),$$

where g_{e1}, g_{e2}, g_{h1}, g_{h2} and A_{Ta} are listed in Table 1 for the case of 14NaTaO₃ under N₂ atmosphere. The A-values for ¹⁸¹Ta are expected to be highly anisotropic, with the isotropic hyperfine coupling A_{iso} estimated as:

$$A_{\text{iso}}[^{181}\text{Ta}(I=7/2)] = (1/3)[A_x+A_y+A_z] \quad (5.3)$$

For one s-electron spin 100% localized on a $^{181}\text{Ta}(I=7/2)$ nucleus, the reference value of the isotropic hyperfine constant is 5359 Gauss.¹ Thus, the fraction of the spin localized on the Ta atom in NaTaO_3 crystal has been estimated from the ratio

$$\% \text{spin on Ta} = A_{\text{iso}}/5359 \quad (5.4)$$

Regarding the hyperfine coupling due to ^{23}Na , The CW-EPR resolution was not sufficient for detecting the distortions due to hyperfine splitting $A_{\text{iso}}[^{23}\text{Na}(I=3/2)]$ coupled to trapped electrons, while in the case of holes, we have retained the term in the spin Hamiltonian with $A_{\text{iso}}[^{23}\text{Na}(I=3/2)]=7\text{Gauss}$. A detailed survey of g- and A- tensors allowed us to successfully simulate all the experimental EPR spectra for the detected $\{h^+/e^-\}$ pairs in NaTaO_3 particles.

Photocatalytic Hydrogen Evolution (HER): Experiments were done using a photoreactor (Toption instrument co. Ltd., volume 340 ml) connected to a cooling system, with controlled temperature of $26\pm 3^\circ\text{C}$. The irradiation source was a 250W Hg lamp, inserted into the Quartz-immersion well. Gas Chromatography with a Thermal-Conductivity Detector (TCD- Shimadzu GC-2014, Carboxen 1000 column, Ar carrier gas) was used for quantitative monitoring of produced gases. In each experiment, 69 mg of catalyst was suspended in 220 mL Milli-Q water and 55mL methanol (20% per volume). 0.5% per weight Ni^{2+} was used as electron acceptor. The average experimental pH was fixed at 4.6.

5.3 Results & Discussion

5.3.1 Photo-excitation of electron/hole pairs in NaTaO_3

Figures 5.1a,b present XRD and TEM data for FSP-made 14nm and 26nm NaTaO_3 (codenamed 14 NaTaO_3 and 26 NaTaO_3). According to TEM images, the FSP- NaTaO_3 particles are quasi-spherical, forming soft agglomerates, as expected for flame-made materials. Fitting of XRD data shows that their crystal structure is close to either orthorhombic ($a = 5.5213\text{\AA}$, $b = 7.7952\text{\AA}$, $c = 5.4842\text{\AA}$; JCPDS 73-0878) or cubic phase ($a = b = c = 3.929\text{\AA}$; JCPDS 74-2488). From the resolved TEM fringes in Fig. 5.1b, we discern interlattice distance of 3.95\AA for 14 NaTaO_3 and 4.05\AA for 26 NaTaO_3 in agreement

with the {101} spacings of cubic-NaTaO₃ phase¹³. Both FSP-made NaTaO₃ catalysts are highly active in H₂ production from H₂O, as shown in Figure 5.1c, achieving rates of 1620 μmol H₂ g⁻¹h⁻¹ and 645 μmol H₂ g⁻¹h⁻¹ respectively. The initial delay observed in the production of H₂ is attributed to the time required for photo deposition of NiO particles onto the NaTaO₃ surface. Considering SSA normalization (Table 5.S1), the enhanced photocatalytic performance of 14NaTaO₃ compared to 26NaTaO₃ is not only attributed to surface area contribution.

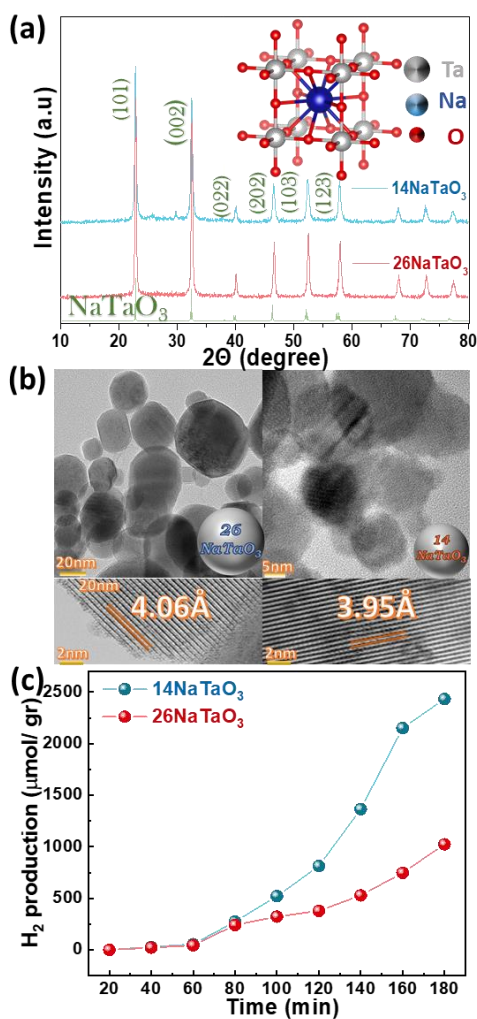


Figure 50. (a) XRD pattern of 14NaTaO₃ and 26NaTaO₃. (b) HR-TEM images of 26NaTaO₃ (left) and 14NaTaO₃ (right) showing the lattice fringes. (c) H₂ evolution rates of 14NaTaO₃ and 26NaTaO₃ in a time interval of 3 hours.

EPR signals of holes & electrons in $^{14}\text{NaTaO}_3$ under N_2 . The photo-induced [light-minus-dark] 77K EPR spectra for $^{14}\text{NaTaO}_3$ shown in Figure 5.2a(ii), is dominated by a sharp feature, plus weaker lines better resolved in Figure 5.2b. All these signals rapidly decayed after switching off the light and short annealing at RT-dark (Figure 5.2a(iii)). Subsequent 77K-irradiation fully restored all light-induced EPR signals (Figure 5.2a(iv)) with a detailed kinetics profile shown in Figure 5.2a(inset). Accordingly, these EPR signals are assigned to photo-induced $\{\text{h}^+/\text{e}^-\}$ pairs in $^{14}\text{NaTaO}_3$ nanoparticles, where the illuminated particles are under N_2 atmosphere, thus the disappearance at RT/dark should be mainly attributed to $\{\text{h}^+/\text{e}^-\}$ pair recombination, not to photocatalytic events. The experimental EPR spectra can be fully simulated with four sub spectra, (e1, e2, h1 and h2 in Figure 5.2b) using the Spin-Hamiltonian parameters listed in Table 5.1. The prominent, derivative-like component (h1) is described by a g-tensor $g^{\text{h1}}=[2.028, 2.018, 2.005]$. Typically, in semiconductors such as TiO_2 ¹⁰, ZrTiO_4 and ZnO ²⁰, photoinduced holes are localized on an oxygen radical anion of the lattice $\text{h}^+ = \{\text{M}-\text{O}^{\cdot-}-\text{M}\}$ and are detected in EPR at the low-field region ($g > g_e$) with a slight g-anisotropy. Accordingly, we assign holes (h1) in NaTaO_3 to $\{\text{Ta}^{5+}-\text{O}^{\cdot-}-\text{Ta}^{5+}\}$ and the g-values are determined by the spin-orbit coupling and local environment of the oxygen radical-anion²¹. In crystals, the local environment of $\text{O}^{\cdot-}$ is expected to position at $2p_z$ orbital at higher energy vs. $2p_x, 2p_y$ orbitals, thus the g-values of the holes are determined by the energy difference $[\text{E}(2p_z)-\text{E}(2p_x, 2p_y)]$ ²². A second type of hole (h2), evidenced as a shoulder on the (h1) signal, with a g^{h2} -tensor $[2.007, 2.019, 2.037]$, is resolved in Figure 5.2b as well. The higher g-anisotropy of (h2) might indicate a more distorted local environment, concurring with (h2) being more exposed to the surface atoms, while (h1) being more in the bulk of NaTaO_3 lattice. We notice that the low g-value for the holes in NaTaO_3 deviates from the free-electron $g_e=2.0023$, in agreement with similar results consistently observed for holes in TiO_2 nanoparticles^{7,10}. Moreover, the high g-value for (h2) in NaTaO_3 indicates that the spin-orbit coupling terms for the holes in the nano-oxide lattice had a severe impact on the g-shift.

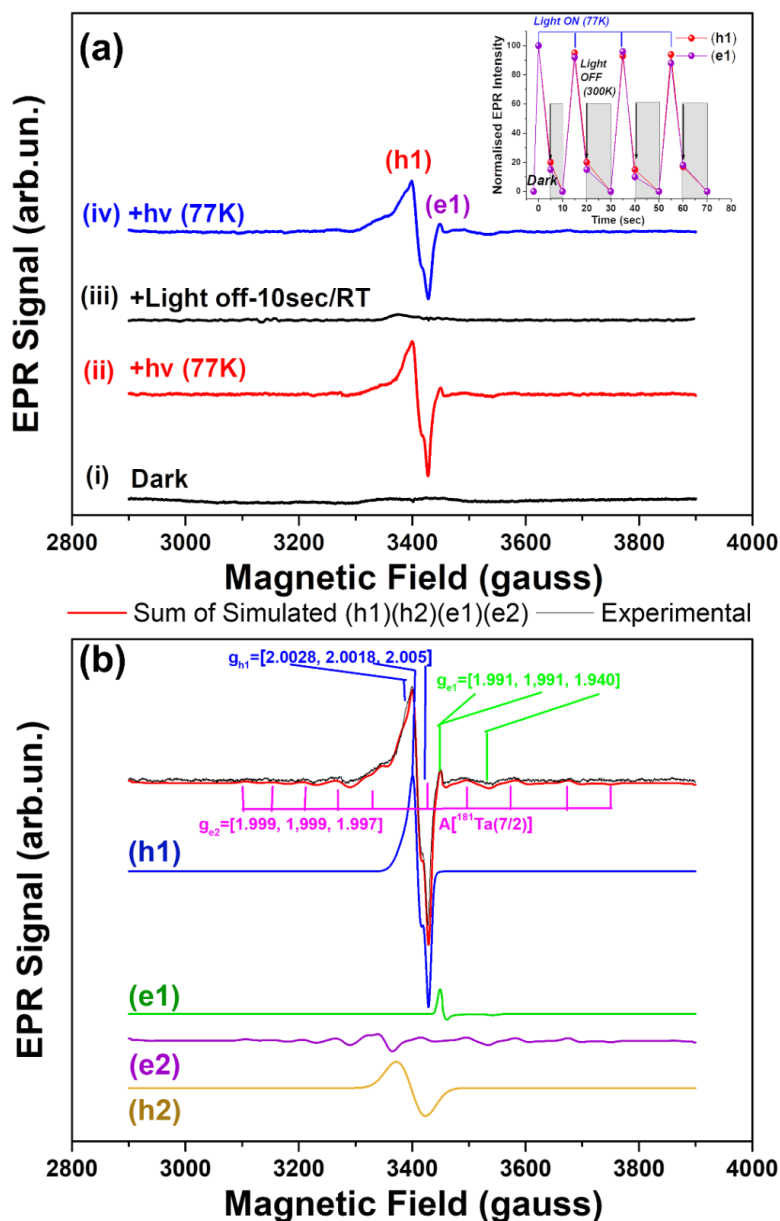


Figure 5.2. (a) Light-minus-dark EPR spectra of $^{14}\text{NaTaO}_3$ under N_2 atmosphere (i) dark, (ii): as in (i) plus illumination at 77K, (iii): as in (ii) plus 10sec/dark/RT and (iv): as in (iii) plus illumination at 77K. **Inset:** Kinetics of holes (h1) and electrons (e1) in $^{14}\text{NaTaO}_3$, derived from thaw-freeze cycles. (b) Experimental (black) and simulated (red) EPR spectra (holes=h1,h2 & electrons=e1,e2) of $^{14}\text{NaTaO}_3$ under N_2 atmosphere.

Regarding the photo-generated electrons, they can be localized on the metal atom, giving rise to EPR fingerprints at $g < g_e$ region²³. EPR detectable paramagnetic centers in NaTaO₃ can originate from Ta⁴⁺ centers with a 5d¹(S=1/2) configuration, as shown in Figure 5.2b. Specifically, two signals assigned to electrons are resolved: a sharp EPR feature (e1) described by an axial g-tensor $g^{e1}=[1.991, 1.991, 1.940]$ and, more interestingly, a riddle-like broad signal (e2) described with $g^{e2}=[1.997, 1.997, 1.999]$. The identity of the (e1) signal can be assigned to an electron trapped in the lattice, however due to limited spectral resolution, it is not clear if this is localized on a Ta⁴⁺ atom or on a lattice defect. The (e2) signal is assigned to an electron coupled with one ¹⁸¹Ta[I=7/2] nucleus (100% nat. abundance). The $\mathbf{A}({}^{181}\text{Ta}[I=7/2])$ tensor, see Table 5.1, is strongly anisotropic, giving rise to the riddle-like signal, distributing the resonance magnetic fields over 2I+1 values for each g-component. The g-tensor and $\mathbf{A}({}^{181}\text{Ta}[I=7/2])$ in 14NaTaO₃ are in accordance of previously reported values for synthetic (π -C₅H₅),Ta⁴⁺Cl₂ complexes²⁴. In distorted tetrahedral symmetry, Ta⁴⁺ has 5d¹ configuration, with the unpaired electron residing in a [$c_1 dx^2-y^2 + c_2 dz^2$] molecular orbital, with mainly dx²-y² character and small dz² admixture, i.e. $c_1 \gg c_2$. The 5s,6s character of Ta⁴⁺ is expected to be negligible. The $A_{iso}({}^{181}\text{Ta}[I=7/2]) = 119$ G (eq. 3) is attributed mainly to indirect spin-polarization effects by d-spins, hence the low s-character 119/5359~2% of unpaired spin on a Ta-atom. For completeness, we state that the hyperfine coupling with ²³Na(I=3/2) atoms in NaTaO₃ could not be reliably resolved in our spectra.

Effect of H₂O: After exposure to H₂O or ambient humidity, the photogenerated EPR signals of 14NaTaO₃ show some changes, demonstrated in Figures 5.3a,b. In Figure 5.3c, two hole species (h1), (h2) are resolved with g-tensors listed in Table 5.1. The g^{h2} for 14NaTaO₃(H₂O), shows small, but resolvable, differences compared to (h2) holes of 14NaTaO₃(N₂). The g^{h1} are rather comparable for both cases, which might imply that the differences in g^{h2} reflect the effect of H₂O adsorbed on 14NaTaO₃ surface, thus the (h2)-states are promoted by the presence of H₂O. Altogether, we suggest that (h1) are trapped holes inside the lattice while (h2) are exposed near to surface. An analogous phenomenon occurs in TiO₂ where two hole configurations can be resolved by EPR, i.e. {Ti⁴⁺-O^{•-}-Ti⁴⁺}

or $\{\text{Ti}^{4+} - \text{O} - \text{Ti}^{4+} - \text{O} \cdot \text{H}\}$ depending on the state of surface-occupation by H_2O^{10} . Thus, we suggest that

$$\text{Bulk Holes (h1)} = \{\text{Ta}^{5+} - \text{O}^{\cdot-} - \text{Ta}^{5+}\}$$

$$\text{Surface Holes (h2)} = \{\text{Ta}^{5+} - \text{O} - \text{Ta}^{5+} - \text{O} \cdot \text{H}\}$$

Table 5.1. Spin Hamiltonian parameters of $^{14}\text{NaTaO}_3$ under N_2 or exposed to H_2O .

	g-tensor [#]			$A^{181}\text{Ta}(I=7/2)$ Hyperfine		
	g ₁	g ₂	g ₃	Tensor (gauss (± 1))		
$^{14}\text{NaTaO}_3$ (under N_2 atmosphere)						
(h1) $\{\text{Ta}^{5+} - \text{O}^{\cdot-} - \text{Ta}^{5+}\}$	2.005(2)	2.018(2)	2.028(2)	-	-	-
(h2) $\{\text{Ta}^{5+} - \text{O} - \text{Ta}^{5+} - \text{O} \cdot \text{H}\}$	2.007(4)	2.019(2)	2.037(2)	-	-	-
(e2) lattice electron	1.940(2)	1.991(2)	1.991(2)	-	-	-
(e1) Ta^{4+} (lattice electron)	1.997(2)	1.997(2)	1.999(2)	71	71	214
$^{14}\text{NaTaO}_3$ (exposed to H_2O)						
(h1) $\{\text{Ta}^{5+} - \text{O}^{\cdot-} - \text{Ta}^{5+}\}$	2.003(2)	2.018(2)	2.022(2)	-	-	-
(h2) $\{\text{Ta}^{5+} - \text{O} - \text{Ta}^{5+} - \text{O} \cdot \text{H}\}$	2.004(4)	2.022(2)	2.035(2)	-	-	-
(e3) Ta^{4+} (lattice electron)	1.946(2)	1.993(2)	1.993(2)	-	-	-
(e4) Ta^{4+} (surface electron)	1.933(2)	1.933(2)	1.973(2)	-	-	-
(e5) Ta^{4+} (surface electron)	1.930(2)	1.960(2)	1.960(2)	-	-	-

error-bars in parentheses.

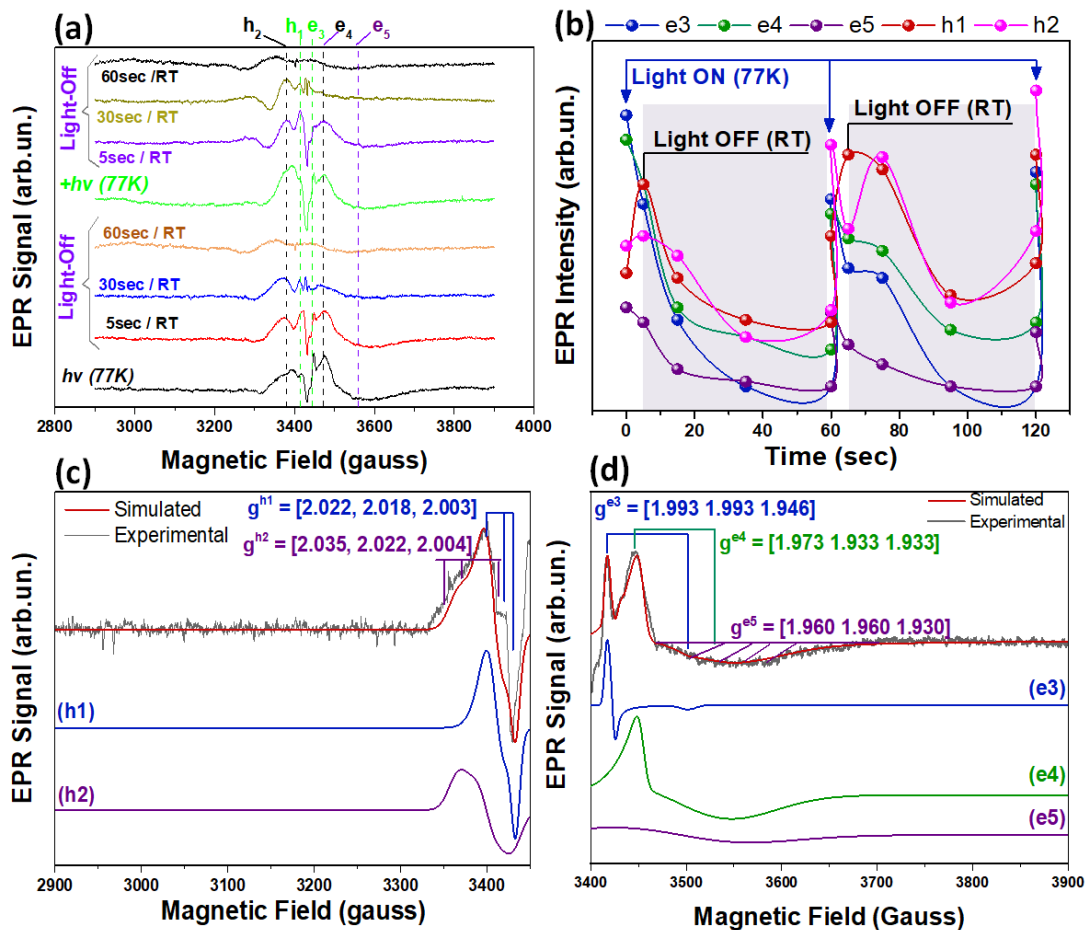


Figure 5.3. (a) Light-minus-dark EPR spectra of $^{14}\text{NaTaO}_3$ exposed to H_2O . (b) kinetics of the EPR signals under light/dark-RT cycles. (c) Experimental (black) and simulated (red) EPR spectra (holes=h₁,h₂) of $^{14}\text{NaTaO}_3$ exposed to H_2O and (d) EPR signals (electrons=e₃,e₄,e₅), detected in degassed $^{14}\text{NaTaO}_3$ plus 2-propanol as a hole scavenger.

Addition of 2-propanol as hole scavenger, diminishes the h₁, h₂ signals (not shown), further confirming their assignments to photoinduced holes. In Figure 5.3d, the presence of 2-propanol promotes the intensity of the Ta^{4+} -electron EPR signals. Two types of electrons are well-resolved, (see Table 5.1). The sharp lineshape of (e₃) indicates that is probably localized inside the $^{14}\text{NaTaO}_3$ lattice, similar to lattice Ti^{3+} electrons in Anatase TiO_2 ⁵. The axial tensor $g^{e4} = [1.933, 1.933, 1.973]$ along with the broad g-component, dominates the EPR spectrum of $^{14}\text{NaTaO}_3(\text{H}_2\text{O})$, even without 2-propanol. The strong broadening of the g-component indicates a severe heterogeneity of the local environment of these (e₄)

centers in $14\text{NaTaO}_3(\text{H}_2\text{O})$. A third broad component (e5) can be resolved at intermediate kinetic times in the dark. It can be considered that (e4) and (e5) are attributed to trapped Ta^{4+} electrons close to the surface of 14NaTaO_3 , in accordance to the well-known surface Ti^{3+} species in TiO_2 . Noticeably, strong ^{181}Ta -hyperfine coupling as resolved in $14\text{NaTaO}_3(\text{N}_2)$, is not observed in the case of $14\text{NaTaO}_3(\text{H}_2\text{O})$.

Size effect: When the size of the NaTaO_3 particles was increased from 14 to 26 nm, the population of photoinduced $\{\text{h}^+/\text{e}^-\}$ detected by EPR at 77K was significantly lower. Figure 5.4 demonstrates, for the case of H_2O -exposed particles, (e4)-type electrons are resolved and the (h1)(h2) holes display diminished intensity in 26NaTaO_3 . Thus, decreasing the particle size is an efficient route to mitigate the carrier separation in a NaTaO_3 crystal and, by correlating the EPR findings with H_2 production, achieve enhanced photocatalytic rates.

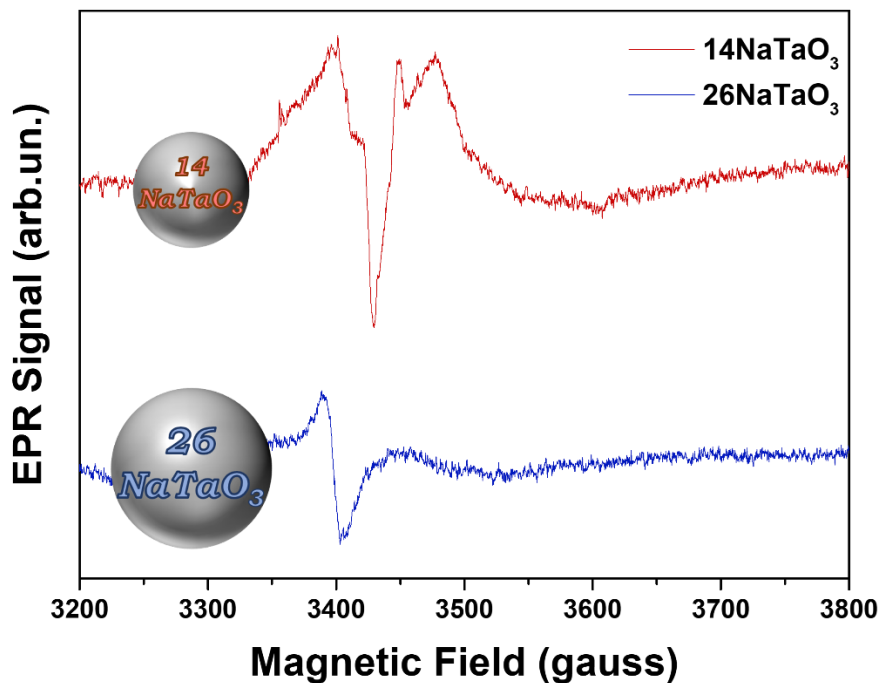


Figure 5.4. Light-minus-dark EPR spectra for (i) 14NaTaO_3 and (ii) 26NaTaO_3 particles.

5.3.2 Synthesis and Characterization of Ag/NaTaO₃

Table 5.2. FSP parameters of Ag/NaTaO₃ heterostructures.

#	FSP Parameters				NaTaO ₃ d _{XRD} (nm)	Energy Gap E _g (eV)
	Na+Ta Molarity	%wt Ag	Flame #1 P/D	Flame #2 P/D		
13NTO	0.2	0	5/5	-	13	3.95
2Ag/13NTO	0.2	2	5/5	5/5	12	3.95
20Ag/13NTO	0.2	20	5/5	3/5	12	4.1
20NTO	0.6	0	7/5	-	18	4
2Ag/20NTO	0.6	2	7/5	5/5	20	4.05
20Ag/20NTO	0.6	20	7/5	3/5	20	3.96

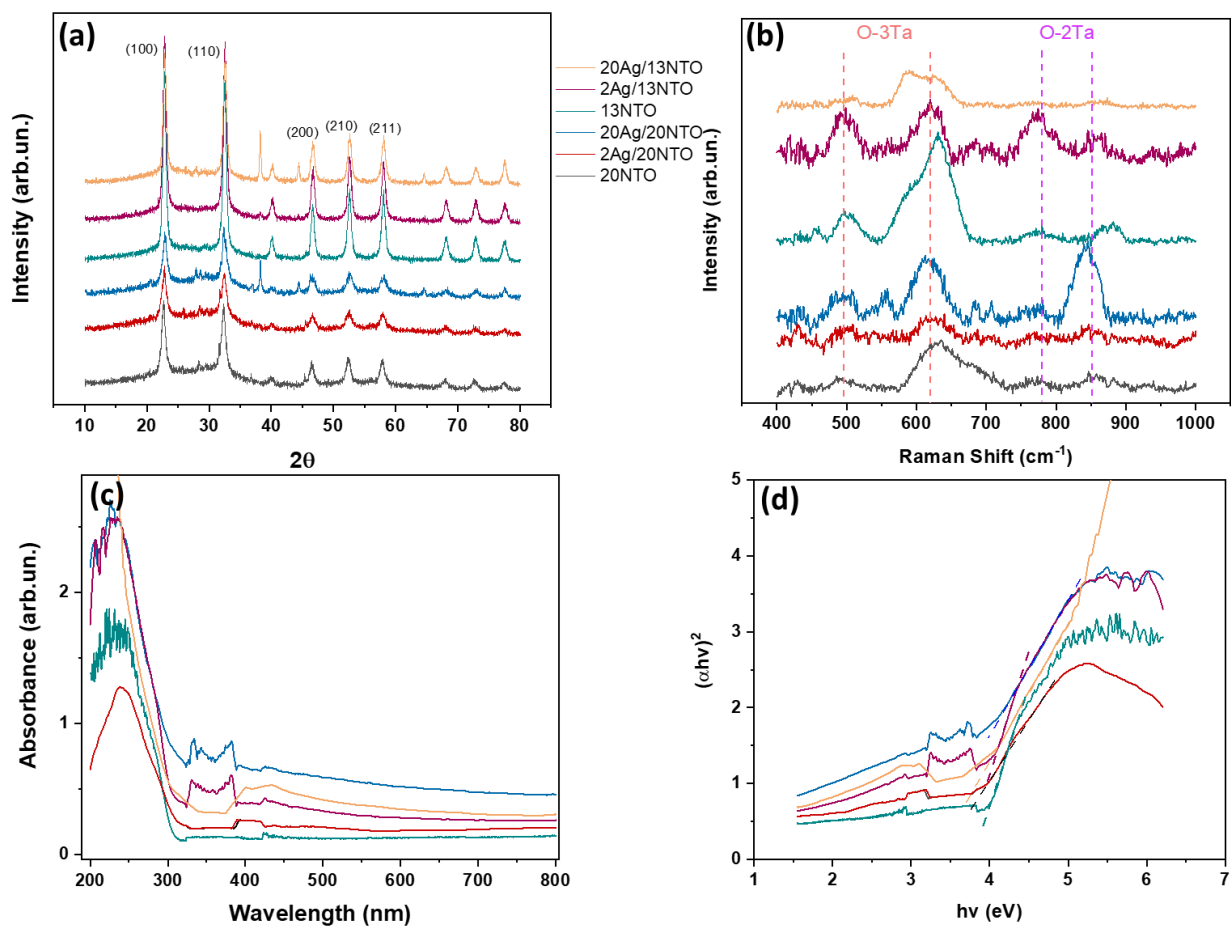


Figure 5.5 (a) XRD patterns, (b) Raman spectra, (c) DRS-UV-Vis spectra and (d) Tauc plots of Ag/NaTaO₃ nanostructures.

Figure 5.5 depicts the characterizations of Ag/NaTaO₃ hetero-nanostructures varying Ag content and NaTaO₃ particle size, as listed in Table 5.2. Specifically, the effective particle size was determined by XRD measurements, shown in Figure 5.5a for all the materials, where the characteristic peaks of NaTaO₃ are clearly evident. The presence of crystalline Ag become evident for the case of 20% Ag/NaTaO₃ nanostructures, while for the case of 2% Ag, the Ag crystals are rather small to be detected by XRD. Figure 5.5b shows the Raman spectra of Ag/NaTaO₃, where the peaks at 500-620 cm⁻¹ and 800-900 cm⁻¹ are attributed to O-3Ta and O-2Ta stretching vibrations respectively. For the case of Ag/NaTaO₃, the high-intensity broad background due to SERS phenomena was deducted. Interestingly, the Tauc plots in Figure 5.5d reveal the presence of energy states in the sub-gap area, thus the formation of an Urbach tail, upon increasing the Ag content. However, this cannot be conclusively assigned to reduced NaTaO_x species, because the plasmon resonance of silver is in the same region, thus the broadened absorption band of 20Ag/NaTaO₃ nanostructures can be due the mixing of Ag and NaTaO₃ energy states.

5.4 Conclusions

Overall, the present study elucidates that [i] small 14NaTaO₃ particles reveal a rich EPR landscape regarding the electronic configuration and kinetics of photoinduced {h⁺/e⁻} pairs, and [ii] increased NaTaO₃ particle size diminishes the yield of stable photo-excited carriers significantly, due to rapid recombination events. This observation might explain the fact that despite the intense study of NaTaO₃ so far, there was no successful detection of photoinduced centers by EPR, most likely because large NaTaO₃ particles were used in previous works. Thus, the direct detection and comprehension of the photo-active species in NaTaO₃ can lead to a fundamental understanding of their promising contribution in challenging photocatalytic reactions, with a significant impact on the energy and environmental fields. Furthermore, in order to study the plasmonic/semiconducting interface, Ag/NaTaO₃ nanostructures were engineering using flame spray pyrolysis of controlled Ag content and NaTaO₃ particle size. However, according to XRD, Raman and UV-Vis measurements, there is no conclusive evidence of plasmon-induced charge-transfer phenomena.

5.5 Supplementary Information

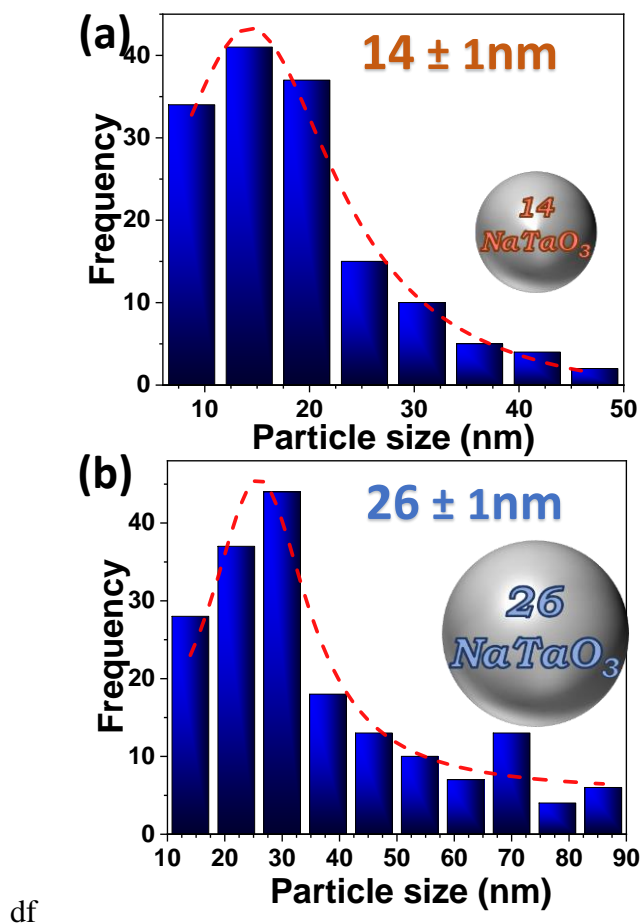


Figure 5.S1. Size distribution of (a) 14NaTaO_3 and (b) 26NaTaO_3 , derived by TEM analysis.

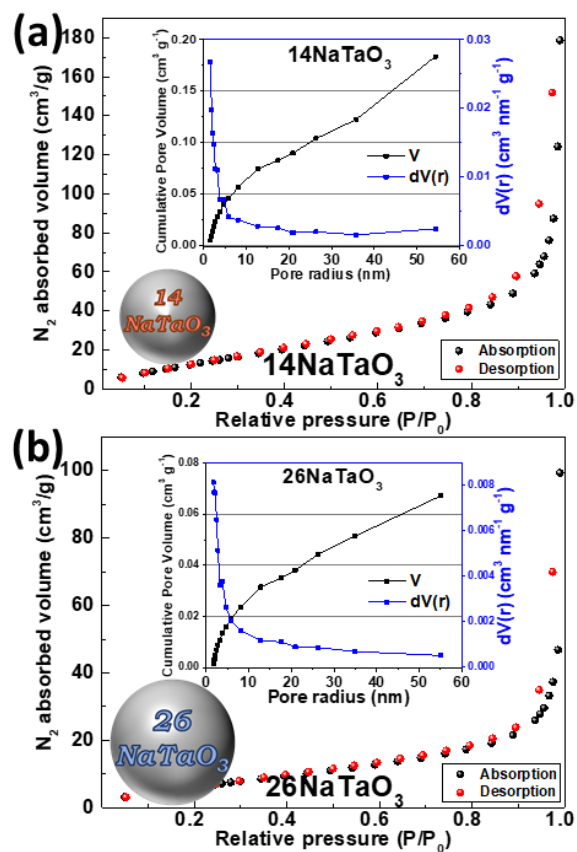


Figure 5.S2. Adsorption/desorption isotherms of (a) 14NaTaO_3 and (b) 26NaTaO_3 . **Inset:** $dV(r)$ vs pore radius plot.

Table 5.S1. Structural characteristics of the NaTaO₃ nanoparticles.

Materials	Crystallite size		SSA (m ² g ⁻¹)	Total pore volume (cm ³ g ⁻¹)	H ₂ evolution (μmol g ⁻¹ h ⁻¹)
	(nm)				
	dTEM*	dBET**			
14NaTaO₃	14 ± 1	20	37.5	18 × 10 ⁻²	1621
26NaTaO₃	26 ± 1	27	27.5	7 × 10 ⁻²	645

*estimated by TEM analysis **d_{BET}=6000/(SSA*p), where p is the NaTaO₃ density (7.13 g/ml).

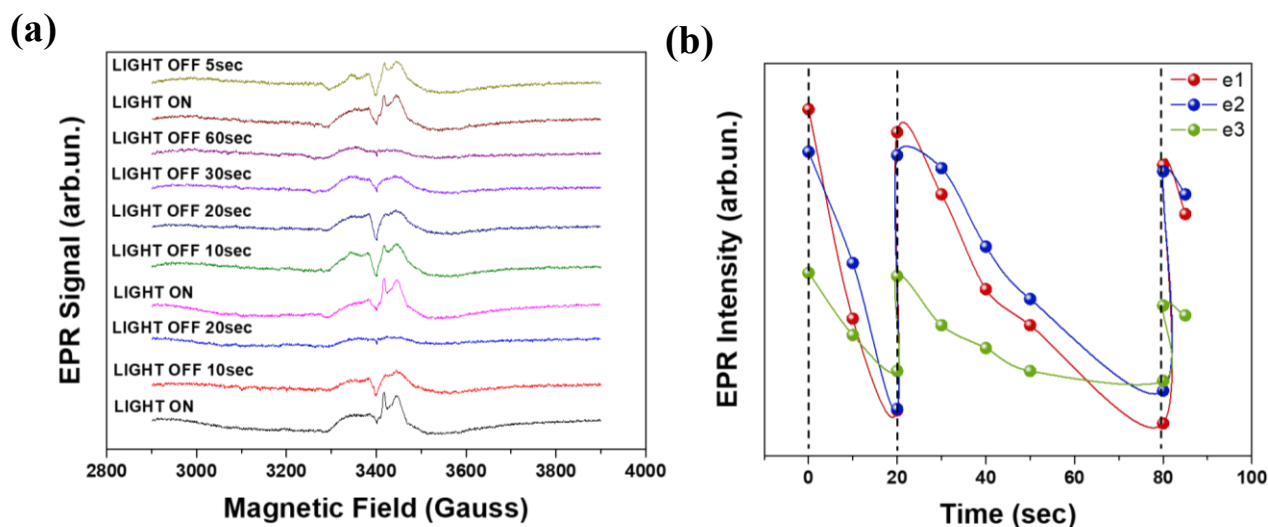


Figure 5.S3. (a) Light-minus-dark EPR spectra of 14NaTaO₃ exposed to H₂O, with the addition of isopropanol as a hole scavenger varying time in RT after illumination. (b) Correlation plots of electron kinetics, derived by the EPR signals. The assignment of electron signals is included in Table 1. The narrow signal (red line) displays a rapid decrease when light is off, assigned to an electron localised in the interior of the NaTaO₃ crystal. In contrast, the slow decrease of the broader signal (green line) indicates the existence of delocalised electrons in the particle surface.

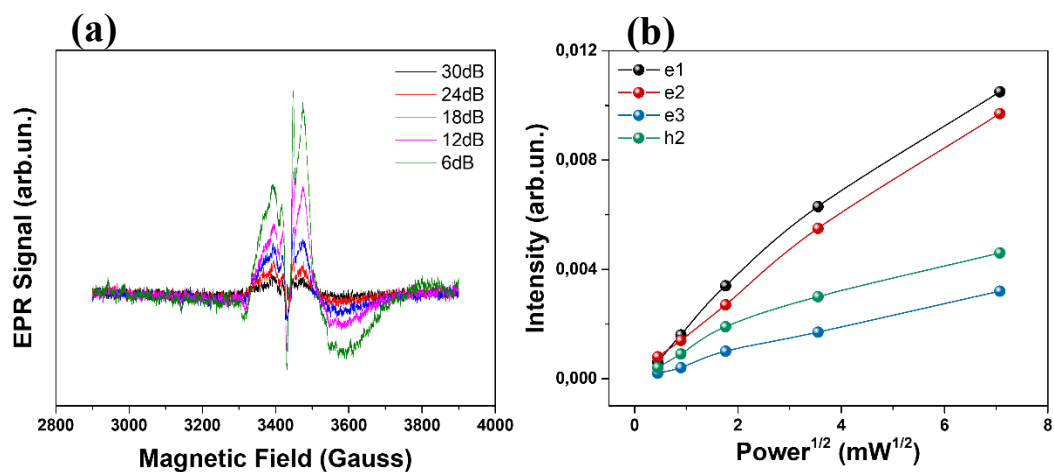


Figure 5.S4. (a) Light-minus-dark EPR spectra of $14\text{NaTaO}_3(\text{H}_2\text{O})$, varying microwave power. (b) Saturation plot of $14\text{NaTaO}_3(\text{H}_2\text{O})$. Localised electrons (e1) and (e2) display more intense spin-lattice interactions compared to delocalised surface electrons (e3). The almost-saturation of h2 signal indicates that the hole is trapped in an oxygen anion radical near the surface.

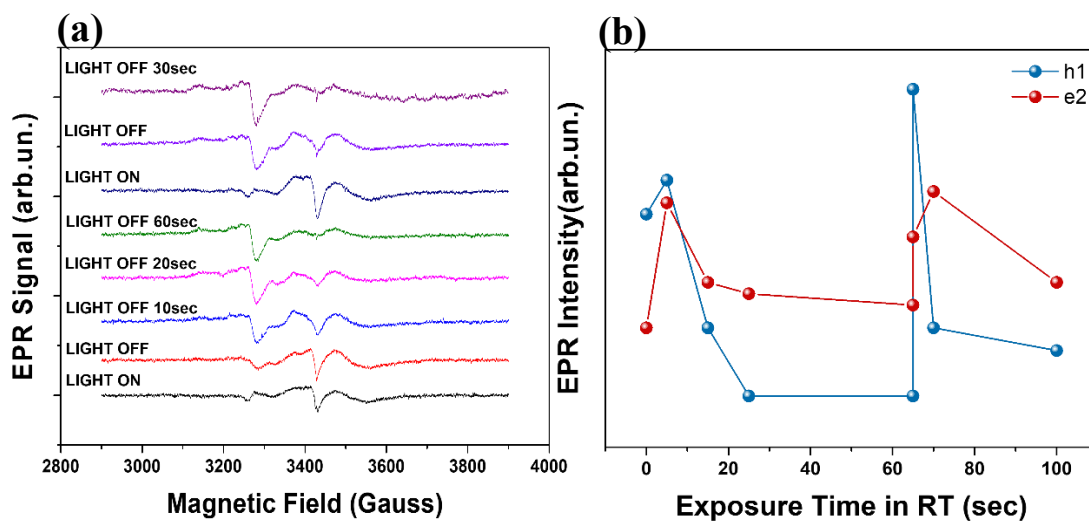


Figure 5.S5. (a) Light-minus-dark EPR spectra of 26NaTaO_3 exposed to H_2O , varying irradiance conditions. (b) Correlation plot of carrier kinetics in 26NaTaO_3 , derived by the EPR signals.

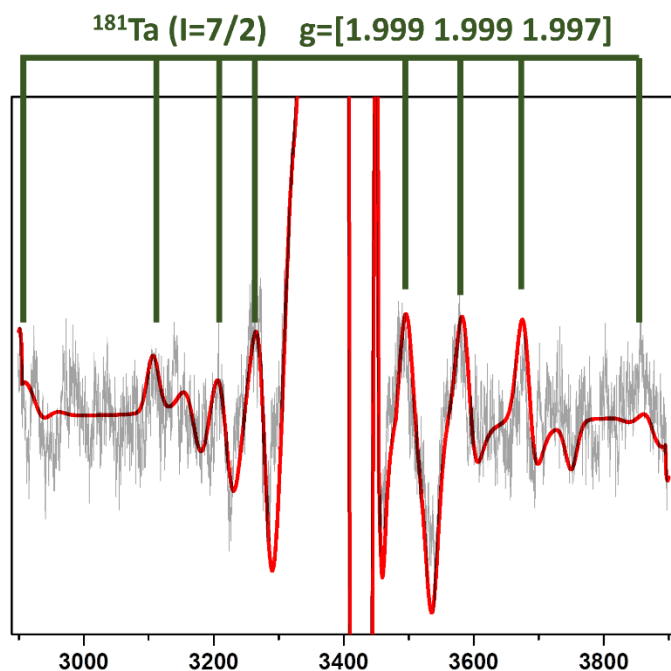


Figure 5.S6. Magnified EPR spectra of $14\text{NaTaO}_3(\text{N}_2)$ atmosphere showing the simulated hyperfine splitting due to electron (e_2)- ^{181}Ta coupling. Spin Hamiltonian parameters are listed in Table 1.

References

- (1) Kato, H.; Kudo, A. Photocatalytic Water Splitting into H_2 and O_2 over Various Tantalate Photocatalysts. *Catalysis Today* **2003**, *78* (1–4), 561–569. [https://doi.org/10.1016/S0920-5861\(02\)00355-3](https://doi.org/10.1016/S0920-5861(02)00355-3).
- (2) Kato, H.; Kudo, A. Water Splitting into H_2 and O_2 on Alkali Tantalate Photocatalysts ATaO_3 (A = Li, Na, and K). *J. Phys. Chem. B* **2001**, *105* (19), 4285–4292. <https://doi.org/10.1021/jp004386b>.
- (3) Kudo, A.; Kato, H.; Nakagawa, S. Water Splitting into H_2 and O_2 on New $\text{Sr}_2\text{M}_2\text{O}_7$ (M = Nb and Ta) Photocatalysts with Layered Perovskite Structures: Factors Affecting the Photocatalytic Activity. *J. Phys. Chem. B* **2000**, *104* (3), 571–575. <https://doi.org/10.1021/jp9919056>.

- (4) Zhang, P.; Zhang, J.; Gong, J. Tantalum-Based Semiconductors for Solar Water Splitting. *Chem. Soc. Rev.* **2014**, *43* (13), 4395–4422. <https://doi.org/10.1039/C3CS60438A>.
- (5) Howe, R. F.; Gratzel, M. EPR Observation of Trapped Electrons in Colloidal Titanium Dioxide. *J. Phys. Chem.* **1985**, *89* (21), 4495–4499. <https://doi.org/10.1021/j100267a018>.
- (6) Howe, R. F.; Gratzel, Michael. EPR Study of Hydrated Anatase under UV Irradiation. *J. Phys. Chem.* **1987**, *91* (14), 3906–3909. <https://doi.org/10.1021/j100298a035>.
- (7) Micic, O. I.; Zhang, Y.; Cromack, K. R.; Trifunac, A. D.; Thurnauer, M. C. Trapped Holes on Titania Colloids Studied by Electron Paramagnetic Resonance. *J. Phys. Chem.* **1993**, *97* (28), 7277–7283. <https://doi.org/10.1021/j100130a026>.
- (8) Micic, O.; Zhang, Y.; Cromack, K. R.; Trifunac, A.; Thurnauer, M. Photoinduced Hole Transfer from Titanium Dioxide to Methanol Molecules in Aqueous Solution Studied by Electron Paramagnetic Resonance. *J. Phys. Chem.* **1993**, *97* (50), 13284–13288. <https://doi.org/10.1021/j100152a036>.
- (9) Hurum, D. C.; Agrios, A. G.; Gray, K. A.; Rajh, T.; Thurnauer, M. C. Explaining the Enhanced Photocatalytic Activity of Degussa P25 Mixed-Phase TiO₂ Using EPR. *J. Phys. Chem. B* **2003**, *107* (19), 4545–4549. <https://doi.org/10.1021/jp0273934>.
- (10) Nakaoka, Y.; Nosaka, Y. ESR Investigation into the Effects of Heat Treatment and Crystal Structure on Radicals Produced over Irradiated TiO₂ Powder. *Journal of Photochemistry and Photobiology A: Chemistry* **1997**, *110* (3), 299–305. [https://doi.org/10.1016/S1010-6030\(97\)00208-6](https://doi.org/10.1016/S1010-6030(97)00208-6).
- (11) Kumar, C. P.; Gopal, N. O.; Wang, T. C.; Wong, M.-S.; Ke, S. C. EPR Investigation of TiO₂ Nanoparticles with Temperature-Dependent Properties. *J. Phys. Chem. B* **2006**, *110* (11), 5223–5229. <https://doi.org/10.1021/jp057053t>.
- (12) Livraghi, S.; Paganini, M. C.; Giamello, E.; Selloni, A.; Di Valentin, C.; Pacchioni, G. Origin of Photoactivity of Nitrogen-Doped Titanium Dioxide under Visible Light. *J. Am. Chem. Soc.* **2006**, *128* (49), 15666–15671. <https://doi.org/10.1021/ja064164c>.
- (13) Wang, J.; Su, S.; Liu, B.; Cao, M.; Hu, C. One-Pot, Low-Temperature Synthesis of Self-Doped NaTaO₃ Nanoclusters for Visible-Light-Driven Photocatalysis. *Chem. Commun.* **2013**, *49* (71), 7830. <https://doi.org/10.1039/c3cc42487a>.

- (14) Meyer, T.; Priebe, J. B.; da Silva, R. O.; Peppel, T.; Junge, H.; Beller, M.; Brückner, A.; Wohlrab, S. Advanced Charge Utilization from NaTaO₃ Photocatalysts by Multilayer Reduced Graphene Oxide. *Chem. Mater.* **2014**, *26* (16), 4705–4711. <https://doi.org/10.1021/cm500949x>.
- (15) Farooq, U.; Ahmed, J.; Alshehri, S. M.; Ahmad, T. High-Surface-Area Sodium Tantalate Nanoparticles with Enhanced Photocatalytic and Electrical Properties Prepared through Polymeric Citrate Precursor Route. *ACS Omega* **2019**, *4* (21), 19408–19419. <https://doi.org/10.1021/acsomega.9b02830>.
- (16) Teoh, W. Y.; Amal, R.; Mädler, L. Flame Spray Pyrolysis: An Enabling Technology for Nanoparticles Design and Fabrication. *Nanoscale* **2010**, *2* (8), 1324. <https://doi.org/10.1039/c0nr00017e>.
- (17) Pratsinis, S.; Mueller, R.; Kammler, H. K.; Madler, L. Controlled Synthesis of Nanostructured Particles by Flame Spray Pyrolysis. *Aerosol Science* **2002**, *33*, 369–389.
- (18) Psathas, P.; Georgiou, Y.; Moularas, C.; Armatas, G. S.; Deligiannakis, Y. Controlled-Phase Synthesis of Bi₂Fe₄O₉ & BiFeO₃ by Flame Spray Pyrolysis and Their Evaluation as Non-Noble Metal Catalysts for Efficient Reduction of 4-Nitrophenol. *Powder Technology* **2020**, *368*, 268–277. <https://doi.org/10.1016/j.powtec.2020.04.059>.
- (19) Grigoropoulou, G.; Christoforidis, K. C.; Louloudi, M.; Deligiannakis, Y. Structure-Catalytic Function Relationship of SiO₂-Immobilized Mononuclear Cu Complexes: An EPR Study. *Langmuir* **2007**, *23* (20), 10407–10418. <https://doi.org/10.1021/la700815d>.
- (20) Polliotto, V.; Albanese, E.; Livraghi, S.; Indyka, P.; Sojka, Z.; Pacchioni, G.; Giamello, E. Fifty–Fifty Zr–Ti Solid Solution with a TiO₂-Type Structure: Electronic Structure and Photochemical Properties of Zirconium Titanate ZrTiO₄. *J. Phys. Chem. C* **2017**, *121* (10), 5487–5497. <https://doi.org/10.1021/acs.jpcc.6b12892>.
- (21) Brailsford, J. R.; Morton, J. R. Paramagnetic Resonance Spectrum of O⁻ Trapped in KCl, RbCl, and KBr. *The Journal of Chemical Physics* **1969**, *51* (11), 4794–4798. <https://doi.org/10.1063/1.1671869>.

- (22) Gionco, C.; Livraghi, S.; Maurelli, S.; Giamello, E.; Tosoni, S.; Di Valentin, C.; Pacchioni, G. Al- and Ga-Doped TiO₂, ZrO₂, and HfO₂: The Nature of O 2p Trapped Holes from a Combined Electron Paramagnetic Resonance (EPR) and Density Functional Theory (DFT) Study. *Chem. Mater.* **2015**, *27* (11), 3936–3945. <https://doi.org/10.1021/acs.chemmater.5b00800>.
- (23) Chiesa, M.; Giamello, E.; Livraghi, S.; Paganini, M. C.; Polliotto, V.; Salvadori, E. Electron Magnetic Resonance in Heterogeneous Photocatalysis Research. *J. Phys.: Condens. Matter* **2019**, *31* (44), 444001. <https://doi.org/10.1088/1361-648X/ab32c6>.
- (24) Al-Mowali, A. H.; Kuder, W. A. A. An Electron Paramagnetic Resonance Study of Dichlorobis-(π -Cyclopentadienyl)Tantalum(IV), (π -C₅H₅)₂TaCl₂. *J. Mol. Struct.* **1979**, *57*, 141–147. [https://doi.org/10.1016/0022-2860\(79\)80239-2](https://doi.org/10.1016/0022-2860(79)80239-2).

Chapter 6

Understanding the Electron Storage in Interfacial Magnéli Islands on Flame-made Black Ag/TiO₂ Nanostructures

6.1 Introduction

Fueled by the necessity for energy independence and climate neutrality, photocatalysis is established as the corner stone providing a way to develop “green” energy supply harvesting the abundant sunlight. However, the ongoing energy crisis urges photocatalysts to react under non optimal situations, i.e. when illumination is stopped, giving birth to the term of “memory catalysis” (MC) or dark photocatalysis, where photo-induced performance is preserved in the dark.¹⁻³ In particular, the sufficient electron storage and discharge is a prerequisite, a term often fulfilled by noble metals such as Ag, Au and Pt due to high conductivity and capacitive nature. In this context, metal/semiconductor nanocomposites are an efficient way to mitigate photocatalytic

activity by introducing a Schottky barrier in the interface, that facilitates carrier separation and hindering back-transfer events if optimized accordingly.⁴ Although the first examples of MC effect were rather weak for the case of PdO/TiO₂⁵ and CuO/TiO₂⁶, Kamat et al. was the first to report the superior MC performance of Ag/TiO₂ interface compared to Pt/TiO₂ and Au/TiO₂ and attributed it to the Fermi equilibrium that allows the sufficient electron trap both in Ag particle and in Ti³⁺ sites on TiO₂ CB.⁷ Notably, the ohmic contact of metals such as Pt and Pd renders the rapid charge discharge on the solid/liquid interface, thus they are preferred as electron acceptors for reactions such as water splitting.^{8,9} On the same note, Choi et al. demonstrated the usage of Ag/TiO₂ interface for pollutant removal using MC.¹⁰ During illumination, the photo-excited holes drives the oxidation of 4-chlorophenol (daytime) and when light is switched off, the reduction of hexavalent chromium Cr(VI) was investigated (night time) by the trapped electrons during pre-irradiation.

Despite the chosen reaction, the light conditions and the interfacial engineering of the metal/semiconductor hetero-junctions, MC activity depends on metallic particle size as well. In particular, smaller particles tend to provide higher capacitive capabilities, an observation that renders common deposition methods such as impregnation and photo-deposition ineffectual, since the particle size cannot be precisely controlled.⁷ On this regard, Cai et al. proposed the novel concept of dark deposition, where the pre-illuminated stored electrons reduce the Ag⁺ ions into particles of ~10 nm on TiO₂ without the undesired growth due to the constant light dose.^{11,12} Similarly, efficient semiconductors such as TiO₂ are modified in numerous ways in order to impede the limited visible photon absorption and harness the sunlight energy preserving the high chemical-to-solar efficiency. In the case of the widely reported black TiO₂¹³, the introduction of Ti³⁺ centers in the disordered TiO₂ surface modifies the electronic structure.^{14,15} However, when these randomly distributed defects obtain periodicity, crystalline Ti_xO_{x-1} suboxides are formed called Magnéli¹⁶⁻¹⁸ and can be utilized to mitigate charge separation and reactivity resulting to enhanced photocatalytic performance.¹⁹⁻²¹ However, the synthesis of Magnéli suboxide phases remain a bottleneck due to the high-temperature treatments under reducing conditions.²²⁻²⁴ On this regard, Kakeru et al. reported the formation of stable crystalline Magnéli interface can be attained in situ during the TiO₂ synthesis in flame aerosol

processes in the presence of Ag nanoparticles.²⁵ The initial hypothesis was that the reducing atmosphere in the flame induced by combustion intermediates promotes the Magnéli formation and the role of Ag is purely catalytic due to strong-metal-support-interaction phenomena (SMSI).

These visible-active black Ag/TiO₂@TiO_x nanocomposites, exclusively prepared in a single-step procedure by flame spray pyrolysis (FSP)²⁶, provide two beneficial factors for amplified electron storage and MC effect; [i] the presence of Magnéli suboxides nanoislands increase the population of electron traps in the Ag/TiO₂ interface and [ii] the in situ deposition of Ag particles during their simultaneous formation with another nano-oxide in flames, result to homogeneous Ag size smaller than 8nm, inaccessible with the traditional methods, thus displaying superior capacitance.

Herein, black Ag/TiO₂@TiO_x nanocomposites were prepared by FSP varying Ag content, TiO₂ particle size and Magnéli mass fraction, in order to investigate the contribution of the distorted suboxide interface in electron storage and discharge. Furthermore, MC effect was observed in the reduction of Cr(VI) in the presence of the pre-irradiated black Ag/TiO₂@TiO_x nanocomposites, verifying their superior capacitance.

6.2 Materials & Methods

Ag/TiO₂ heterostructures have been prepared by flame spray pyrolysis using either a single or a dual nozzle configuration shown in Figure 6.1 and described in detail previously.²⁷ Precursor molarity, precursor fuel feed rate to dispersion gas rate (P/D ratio) and the internozzle distance were adjusted accordingly so that the desired properties of each element can be controlled independently. The detailed parameters are demonstrated in Table 6.1. Specifically, titanium iso-propoxide (TTIP, Sigma Aldrich) and silver acetate (sigma aldrich, >99%) were dissolved in ethylhexanoic acid/acetonitrile (1:1) for the case of the single flame, or dissolved in mixtures of xylene/acetonitrile (2.2:1) and ethylhexanoic acid/acetonitrile (1:1) respectively for the case of dual-flame setup. A O₂/CH₄ premixed gas (3.2/1.5 L min⁻¹, Linde >99.9%) provided the supporting flame and the initial ignition. The powder product was collected, using a vacuum pump (Busch V40), on a glass microfiber filter (Albet) placed 66 cm above the flame mixing point. In

sequential FSP, the Ag precursor was fed to the flame after the already formed TiO₂ particles have been collected and the Ag particles deposition takes place in cooler temperature gradients outside the hotter flame zone.

The morphology, nanostructure, and chemical composition of nanoparticles were examined using an FEI Titan 80–300 S/TEM microscope at a 300 kV accelerating voltage. STEM images were obtained with a beam convergence semiangle of 21.5 mrad. Sample preparation consisted of sonicating powdered samples in ethanol and depositing the homogeneous suspension in the form of a single droplet on a TEM copper grid covered by a lacey carbon film. Before the observations, to remove any organic contamination, samples were treated for 3 s in argon plasma using a Fischione Instruments 1020 Plasma Cleaner. Powder X-ray diffraction (pXRD) data were collected at room temperature using a Bruker D8 Advance 2theta diffractometer with copper radiation (Cu K α , $\lambda = 1.5406 \text{ \AA}$) and a secondary monochromator operating (40 kV, 40 mA). Raman spectroscopy was performed with a HORIBA Xplora Plus Raman coupled to an Olympus BX41 microscope, equipped with a 785 nm diode laser as an excitation source focused with the microscope. The spectra were obtained at laser power of 1 mW, integration time to 5 sec for 20 accumulations. X-ray photoelectron spectroscopy (XPS) were acquired in a surface analysis ultrahigh vacuum system (SPECS GmbH) equipped with a twin Al-Mg anode X-ray source and a multichannel hemispherical sector electron analyzer (HSA-Phoibos 100). The base pressure was $2\text{-}5 \times 10^{-9}$ mbar. A monochromatized Mg K α line at 1253.6 eV and analyzer pass energy of 15 eV were used in all measurements. The binding energies were calculated with reference to the energy of C 1s peak of contaminant carbon at 284.5 eV. The peak deconvolution was calculated using a Shirley background. Photoluminescence (PL) spectra were obtained at room temperature with 320 nm wavelength excitation, using an Edinburgh FS5 spectrofluorometer (Edinburgh Ltd., Livingston, UK) equipped with a 150 W CW Ozone-free xenon arc lamp.

The electrochemical measurements, including impedance and Mott–Schottky, were collected with a Corrtest potentiostat. A three-electrode cell, consisted of a Pt counter electrode, an Ag/AgCl (saturated KCl) reference electrode and a particle-coated FTO working electrode (25 cm²) was used to carry out all electrochemical measurements. The

capacitance of the semiconductor/electrolyte interface was obtained using 10 mV AC voltage amplitude at 1 kHz, in 0.2 M Na₂SO₄ solution (pH = 7.1). The measured flat-band potentials were converted to the reversible hydrogen electrode (RHE) scale using the Nernst equation:

$$E_{RHE} = E_{Ag/AgCl} + 0.197 + 0.059 * pH \quad (6.1)$$

The flat-band potential (E_{FB}) and carrier density (N_D) were determined from the C^2 versus E plots using the standard relationship with the surface area of the electrodes (25 cm²).²⁸

$$\frac{1}{C^2} = \frac{2}{A^2 N_D e \epsilon \epsilon_0} \left(E - E_{FB} - \frac{kT}{e} \right) \quad (6.2)$$

where C is the space charge capacitance of the semiconductor, e is the elementary charge value, ϵ is the relative permittivity of the semiconductor (TiO₂ ~ 55 for anatase)²⁹, ϵ_0 is the permittivity in vacuum, E is the applied potential, T is the temperature, and k is the Boltzmann constant.

Electrochemical impedance spectroscopic (EIS) analysis was conducted using a 10 mV AC amplitude perturbation between 100 kHz and 0.01 Hz, under open-circuit potential conditions. The electrochemical impedance data were fitted to an equivalent circuit model using ZView software.

The working electrodes were prepared as follows: 15 mg of each sample was dispersed in 6 ml ethanol containing 120 μ l of 5% Nafion solution and the mixture was sonicated in a water bath until a uniform suspension is obtained. Then, the suspension was deposited on the surface of fluorine-doped tin oxide (FTO, 13 Ω /cm²), using the spin coating method (200 μ l, 10 cycles). The initial spin speed during the sample's dropcasting was 2000 rpm for 20 sec, proceeded by an increase to 5000 rpm for 30 sec. The obtained films were dried at 100° for 15 minutes for the removal of solvent residuals. FTO-coated glass substrates were initially rinsed in DI water, acetone and 2-propanol and subjected to sonication for 10 minutes.

The X-band electron paramagnetic resonance (EPR) spectra were recorded with a Bruker ER200D spectrometer at 77 K, equipped with an Agilent 5310A frequency counter.

The spectrometer was running under a home-made software based on LabView. The EPR instrumental conditions were as follows: microwave frequency = 9.55 GHz, modulation frequency = +50.00 kHz, modulation amplitude = 10 Gauss pp and microwave power = 10 dB. The spectra of photo-generated carriers were obtained by subtracting the EPR data in dark conditions from the data recorded under illumination. Irradiation of the samples was performed *in-situ* using a led lamp (Phoseon Firejet 100) operating at various wavelength regions keeping the power density constant (9 mW/cm^2). 15 mg of each sample was placed in a 5 mm EPR tube (Wilmad) and then frozen at 77K. The assignment of each carrier species was resolved by simulating the EPR spectra using EasySpin software.³⁰

The simulation of electromagnetic hot spots in Ag@SiO₂ particle proximity was conducted using Matlab work package MNPBEM based on the boundary element method (BEM), developed by Garcia de Abajo and Howie.³¹ The surrounding medium was the water ($n=1.33$) and the optical constants of silver were taken by Palik.³²

Dark photocatalysis preparation: At first, a Cr⁶⁺ stock of 1 mM potassium dichromate (K₂Cr₂O₇, Sigma Aldrich, >99%) or 2 mM Cr⁶⁺ is prepared (2.9 mg K₂Cr₂O₇ in 10 ml HPLC grade H₂O). Furthermore, Ag/TiO₂ NPs stock of 0.5 g/l (in 6 ml HPLC grade H₂O) are irradiated for 60 minutes by Phoseon FJ100 LED 405 nm with power density of 700 mW/cm² using a power meter (Newport). Post-illumination, we add 300 µl of Cr⁶⁺ stock to NPs stock in order to perform the dark Cr(VI) reduction kinetics by the stored hot electrons and it has been monitored by UV-Vis spectroscopy utilizing DPC method. For the DPC method, each time 0.5 ml of the Cr(VI)-NPs stock are mixed in a cuvette with 2.4 ml HPLC grade H₂O and 0.1 ml diphenylcarbazide (DPC) stock. The DPC stock consists of 218 mg (18 mM) 1,5-diphenylcarbazide (Sigma Aldrich, >98%) dissolved in 50 ml acetone. The absorbance at 541 nm from the Cr⁶⁺-DPC complex was used to quantify Cr⁶⁺ in the solution. The color of the solution became stable after 5 minutes. Before each UV-Vis measurement, the solution pH was adjusted to 3, by adding small amounts of HNO₃. Each catalytic run was repeated 3 times for verifying the experiment's credibility.

6.3 Results/Discussion

6.3.1 Structural Characterization of Black Ag/TiO₂@TiO_x nanocomposites

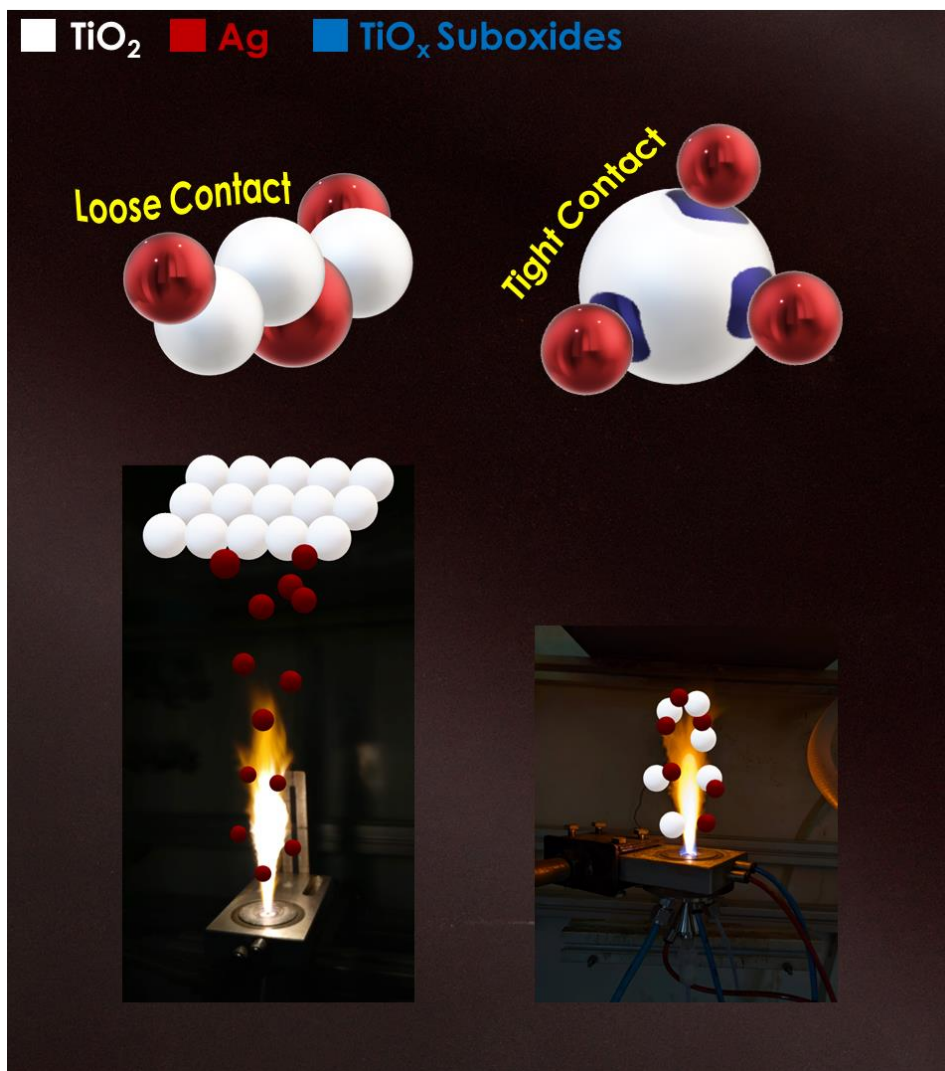


Figure 6.51. A schematic illustration depicting the two FSP setups and the synthetic procedure of black Ag/TiO₂@TiO_x: The sequential deposition of Ag on TiO₂ particles (left) and the single-combustion approach (TiO₂ and Ag formation in the same flame) (right).

Figure 6.1 shows the FSP reactor configurations used for the synthesis of Ag/TiO₂@TiO_x nanocomposites. The single-combustion approach yields TiO₂ particles of controlled size with Ag particles being kept small (< 8 nm), independent to Ag content in

the liquid precursor fed in the flame, in consistence to previous works.^{25,26} On the contrary, the sequential deposition provides the time required for the in-flight growth of Ag particles. The as-prepared particles are listed in Table 1. For the sake of distinction, TC and LC samples are attributed to the tight and loose contact between Ag and TiO₂ particles in the same flame and sequential deposition respectively. A thorough investigation of TiO₂ particle size, Ag content and mixing point can be found in Appendix 3.

Table 6.1. FSP parameters and particle characteristics of Ag/TiO₂ heterostructures.

¹ XAg/YTiO ₂	Molarity (M)	P/D ratio	d _{XRD} Ag (nm)	d _{XRD} TiO ₂ (nm) ²	TiO _x Mass Fraction	SSA (m ² /g) ³	Ti ₃₊ /Ti ₄₊ ⁴
18TiO ₂	0.6	5/5	-	18	0	100	0
TC-20Ag/18TiO ₂	0.6	7/5	6	5	13	83	0.33
TC-50Ag/18TiO ₂	0.6	7/5	5	5	20	62	0.42
LC-50Ag/18TiO ₂	0.6	7/5	28	18	0	85	0.11
TC-50Ag/11TiO ₂	0.16	7/5	4	18	23	127	0.4

¹ XAg/YTiO₂: X denotes for Ag content and Y for TiO₂ particle size respectively. ² derived by Scherrer equation for the Anatase peak. ³ calculated by BET analysis. ⁴ derived by XPS measurements.

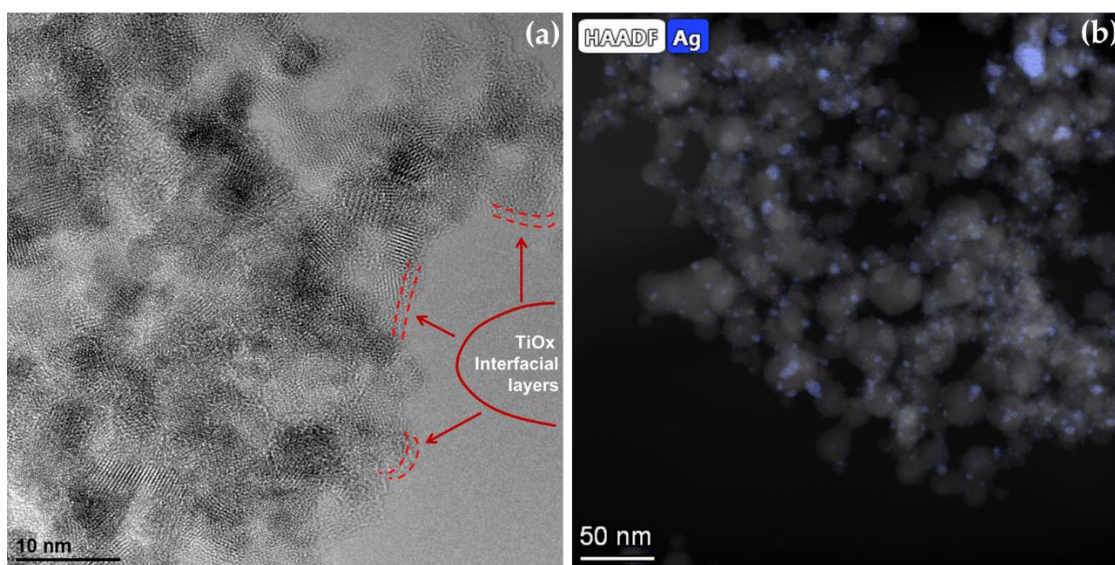


Figure 6.52. (a)(b) STEM images of TC-50Ag/TiO₂, displaying the color mapping of Ag particles dispersed in TiO₂ nanoparticles.

Figure 6.2a shows a high-angle annular dark-field scanning transmission electron microscopy (HAADF-STEM) image of TC-50Ag/TiO₂ nanocomposites, where a fractal-

like aggregated morphology is revealed, as expected for flame-made nanoparticles. The elemental composition depicted in Figure 6.2b exhibits the presence of Ag particles (blue) of size ~ 8 nm deposited in larger TiO_2 particles. Figure 2c shows the suboxide phases are detected as distortions in the Ag/ TiO_2 interface, even encapsulating partially some Ag particles, as reported in similar works. In the case of LC-50Ag/ TiO_2 , Figure 2d shows the much larger Ag spheres (~ 28 nm) co-agglomerated with TiO_2 particles and no distortion layers are observed at all.

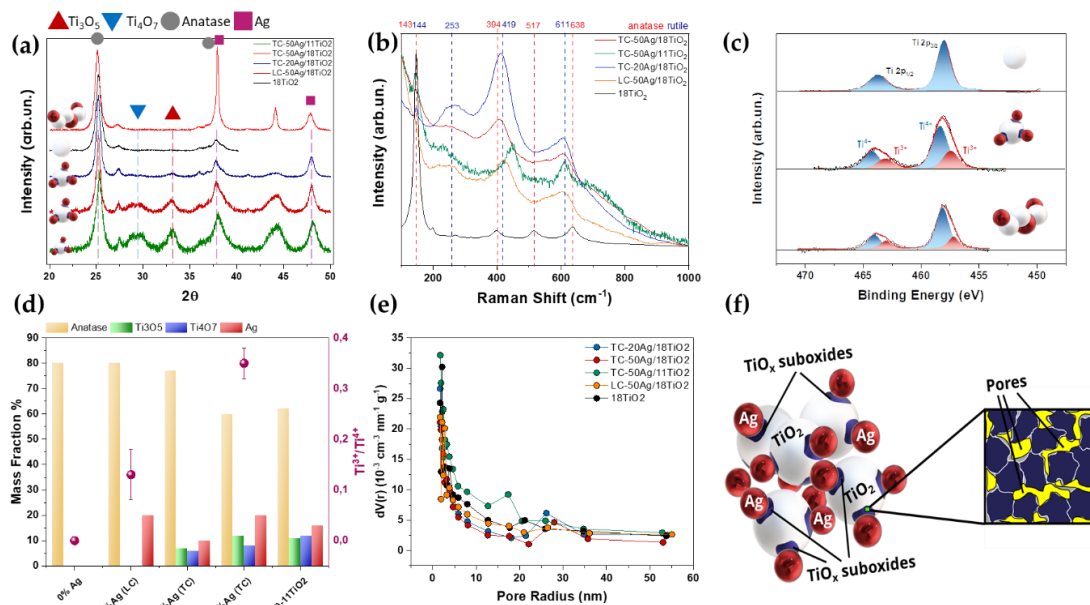


Figure 6.53. (a) XRD pattern of Ag/ TiO_2 nanocomposites varying Ag content, TiO_2 particle size and the type of interfacial Ag/ TiO_2 contact. The symbols correspond to the present crystal phases. (b) Raman spectra of Ag/ TiO_2 nanocomposites varying Ag content, TiO_2 particle size and the type of interfacial Ag/ TiO_2 contact. The typical peaks for Anatase and Rutile are marked. (c) XPS spectra of 18 TiO_2 , LC-50Ag/18 TiO_2 and TC-50Ag/18 TiO_2 (core levels of Ti $2p_{1/2}$ and $2p_{3/2}$ peaks). (d) Mass fractions of the crystal phases (derived by XRD) and the $\text{Ti}^{3+}/\text{Ti}^{4+}$ ratio (derived by XPS) for each Ag/ TiO_2 nanocomposite. (e) Pore size distribution (PSD) for each Ag/ TiO_2 nanocomposite (derived by N_2 porosimetry). (f) A schematic depicting the presence of larger pores in the distorted TC-Ag/ TiO_2 interface.

XRD analysis of the Ag/TiO₂ nanocomposites varying Ag content and synthesis setup are depicted in Figure 6.3a. Anatase and rutile TiO₂ phases are clearly evident in every sample, in agreement with existing literature. When the Ag content is increased, the broad humps at 29.5 and 33° arise, attributed to crystalline Ti₄O₇ and Ti₃O₅ Magneli phases respectively. Of course, the peaks correspond to Ag are detected as well, at 38 and 44°. Kakeru et al. reported that increasing the temperature and the reducing conditions inside the flame (eg. P/D ratio: 8/5), the TiO_x suboxide content is further increased. However, extreme conditions such as P/D ratio: 16/5 promotes Ag particle growth and hinders Ag-Ti SMSI. Herein, we obtain the maximum presence of Magneli suboxide phases for the case of 50% wt Ag content. The increased mass fraction of Magneli phases, i.e. Ti³⁺ sites is verified by XPS measurements as well, shown in Figure 6.3d for the case of TC-50Ag/TiO₂. Notably, no suboxide phases become evident for the LC-50Ag/TiO₂, i.e. the loose interaction of sequentially deposited Ag in the already formed and collected TiO₂ particles. This can be attributed to the colder thermal gradients (69 cm above the flame) the particles make contact, rendering the reducing conditions inside the flame, the pivotal factor for the successful formation of TiO_x suboxides in the Ag/TiO₂ interface.

Moreover, considering the TEM and XRD analysis, a limit in Ag particle growth (< 8 nm) is evident despite the increased Ag content and precursor feed rate, two major parameters for controlling the particle size in flame synthesis. This behavior has been noticed in similar flame-made hetero-structures, but these controllably small Ag particles, and the subsequent increased capacitance, have yet to be employed in electron storage. As expected, in the sequential deposition, the Ag nanoparticles are much larger, due to the increased in-flight growth until the contact with TiO₂. Another interesting aspect upon Ag/TiO₂ is revealed when the (111) and (200) crystal facets of Ag are compared. In the case of LC-50Ag/TiO₂, the preferred growth of (111) facet is observed, as known for flame-made Ag. However, for the TC-50Ag/TiO₂, where Ag and Ti are nano-mixed inside the flame, the dominant SMSI events induce facet distortions in Ag and the growth of (111) is hindered.

Figure 6.3b depicts the Raman spectra of the Ag/TiO₂ nanocomposites. The peaks at 143, 394, 517 and 638 cm⁻¹ are attributed to anatase, in agreement with literature. Increasing Ag

content in the LC-50Ag/18TiO₂ interface, the observed band broadening indicates a rutile formation where the peaks at 230 and 606 cm⁻¹ arise. The 30 nm Ag particles trigger intense SERS effect that drive in situ phase transformation upon measurement even using the lowest laser power. For the case of black TC-50Ag/18TiO₂ prepared by the single-flame setup, the broadened and shifted peaks reveal Ti-O bond stretching, indicative of the distorted interface and the presence of magneli suboxide phases, according to the existing literature in disordered black TiO₂.²⁵ XPS analysis of Ti 2p spectrum, as shown in Figure 2f, demonstrates two distinct surface Ti species in presence of Ag. Specifically, the binding energy at ## and ## correspond to Ti⁴⁺ and Ti³⁺ species respectively, verifying the distorted suboxide Ag/TiO₂ interface due to the Magneli phases. On a similar note, the O1s XPS spectra in Supporting Information show two distinct peaks, at 529 and 531.6 eV. The former one can be attributed to hydroxyl groups (OH), but the observed increase by adding more Ag, thus enhanced surface distortion, can be assigned to oxygen vacancies (V_o) as well. The XPS spectrum in SI shows that Ag particles preserve the metallic state and no oxidation events have been detected.

6.3.2 Storage and Transfer of Photo-generated Carriers in Distorted Suboxide Interface

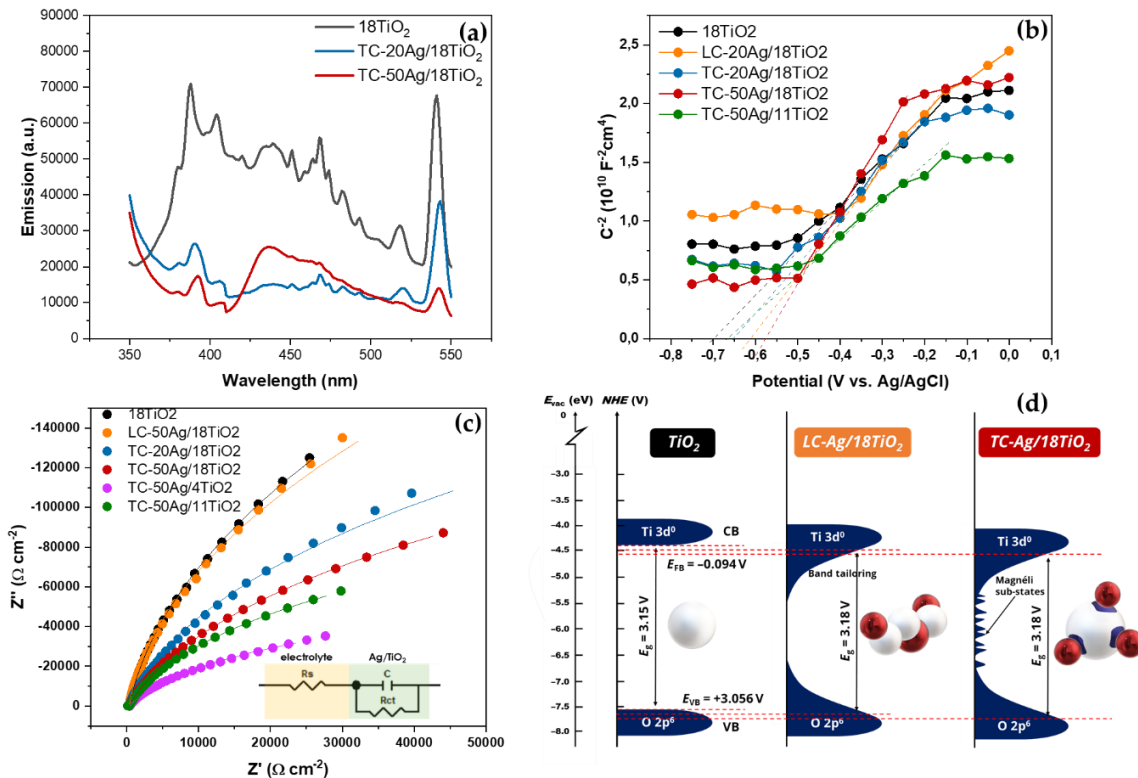


Figure 6.54. (a) Room-temperature PL emission spectra, (b) Mott-Schottky plots and (c) Nyquist plots of the Ag/TiO₂ nanocomposites. Inset: Equivalent circuit used for data analysis (R_s : electrolyte resistance, R_{ct} : charge-transfer resistance, C_{dl} : double-layer capacitance). (d) Schematic depicting the energy bands of ref. TiO₂ and distorted interface upon loose and tight Ag/TiO₂ contact. The CB edge is roughly equal to flat-band energy E_{FB} for n-type semiconductors and VB edge can be calculated using the band-gap energy.

Regarding electronic properties, the fraction of interfacial Magnéli phases provides additional energy states acting as efficient electron traps. In this context, Figure 6.4a depicts the photoluminescence (PL) spectra of Ag/TiO₂ nanocomposites. In general, heavy doping and/or high density of oxygen vacancies in semiconducting materials decrease the PL intensity, interpreted as slower electron/hole recombination rate. Similarly, the TiO_x suboxides in the distorted Ag/TiO₂ interface of TC-50Ag/18TiO₂, provide the electron/hole

separation acting as efficient electron traps. Hence it becomes clear, that increasing Ag content, thus promoting Magneli formation via the tight Ag/TiO₂ contact, the photo-excited electrons can be effectually harvested.

Table 6.2. Electrochemical impedance data of Ag/TiO₂ nanocomposites.

Ag/TiO ₂	E _{FB} (V vs RHE)	N _D (cm ⁻³)	R (Ω)	Energy Gap E _g (eV)	E _{VB} (V vs RHE)
18TiO ₂	-0,094	1.03 x 10 ¹⁷	970	3.15	3.056
TC-20Ag/18TiO ₂	-0,004	1 x 10 ¹⁷	450	3.18	3.176
TC-50Ag/18TiO ₂	0,026	7.1 x 10 ¹⁶	310	-	
LC-50Ag/18TiO ₂	-0,004	8.9 x 10 ¹⁶	790	3.18	3.176
TC-50Ag/11TiO ₂	-0,034	1.35 x 10 ¹⁷	217	-	

Band-gap energy derived by DRS measurements. E_{VB} = E_{FB} - E_g.

To better understand and interpret the relations between the distorted suboxide interface in black Ag/TiO₂ nanoaggregates and the electron storage, electrochemical impedance measurements were performed. Figure 6.4b shows the Mott-Schottky plots of Ag/TiO₂ electrodes (deposited on FTO-coated glass substrates), that is 1/C² as a function of applied voltage (E) curves. The flat band potentials (E_{FB}) of each sample can be obtained as extrapolation of the linear fits of 1/C² versus E curves to zero and the donor density (N_d) can be extracted from the slope. The positive slopes of the Mott-Schottky plots observed here, indicate a typical n-type semiconductor behavior, where electrons are the majority charge-carriers.³³ As listed in Table 6.2, increasing Ag content in Ag/TiO₂ nanocomposites induce an anodic offset of E_{FB} in the range from -0.09 to 0.03 V vs RHE, with TC-50Ag/18TiO₂ displaying the much higher shift compared to pristine TiO₂ and the rest Ag/TiO₂ nanostructures. Assuming that flat band position lies very close to CB edge (a typical case for heavily n-type doped semiconductors)³⁴, the observed anodic shift can be assigned to two factors: The metal/semiconductor junction and the interfacial Magneli presence. In the former case, considering the LC-50Ag/18TiO₂ sample, where no

suboxides are present, the electric field formed upon Ag/TiO₂ contact and the lower Fermi level of Ag compared to TiO₂, force the electrons to migrate from TiO₂ to Ag until Fermi level equilibrium, resulting to the subsequent band bending, as depicted in Figure 6.4d. In the latter case, the higher E_{FB} shift in TC-50Ag/18TiO₂ can be assigned to the presence of Magneli phases in the interface, that distort the TiO₂ band edges even further and create new sub-gap energy states. Interestingly, the higher donor density was observed in the case of TC-50Ag/11TiO₂. Hence, besides the presence of Ag and, thus the interfacial Magneli formation, the TiO₂ particle size influences the electron trap density and charge dissociation as well. This is most likely attributed to the n-type doping effect of the interfacial Magneli suboxides, improving the electron harvest and storage capabilities. These traps in the Ag/TiO₂ distorted interface can serve as electron donors to the CB of TiO₂, increasing the carrier density and mobility in the black Ag/TiO₂ nanocomposites. Furthermore, considering the DRS measurements in Figure S6.2 in Supporting Information and the electrochemical data presented above, the high visible-light absorption of the black Ag/TiO₂ nanoaggregates, are attributed to [i] the band gap narrowing due to Ag/TiO₂ junction and, more importantly, [ii] the formation of sub-gap energy states due to the high defect density in the interface induced by the Magneli phases (shown in Figure 6.4d), that act as electron traps improving significantly the carrier separation and light absorption.

To gain additional insight about the charge transfer and storage in the black Ag/TiO₂ nanoaggregates, electron impedance spectroscopy (EIS) measurements were conducted, as demonstrated in Figure 6.4c. Specifically, the Nyquist plots of each electrode recorded in a 0.2 M Na₂SO₄ electrolyte (pH 7.1) under open circuit potential conditions. A typical electric circuit (inset of Figure 6.4c) consisting of the electrolyte resistance (R_s), charge-transfer resistance at the electrode/electrolyte interface (R_{ct}) and double layer capacitance (C_{dl}) has been used to interpret the experimental data.³⁵ Fitting analysis indicates that R_{ct} values are lower when the Magneli fraction is increased, as shown in Table 6.2, suggesting an accelerated charge transfer rate at the interface between electrode and electrolyte. Considering both the increased donor density and the superior charge mobility, the TC-50Ag/11TiO₂ nanocomposite displays the superior carrier separation. However, TC-

50Ag/18TiO₂ demonstrates the highest E_{FB} shift, which is probably due to TiO₂ particle size affecting the Fermi level, thus diverting the band-edges alignment.

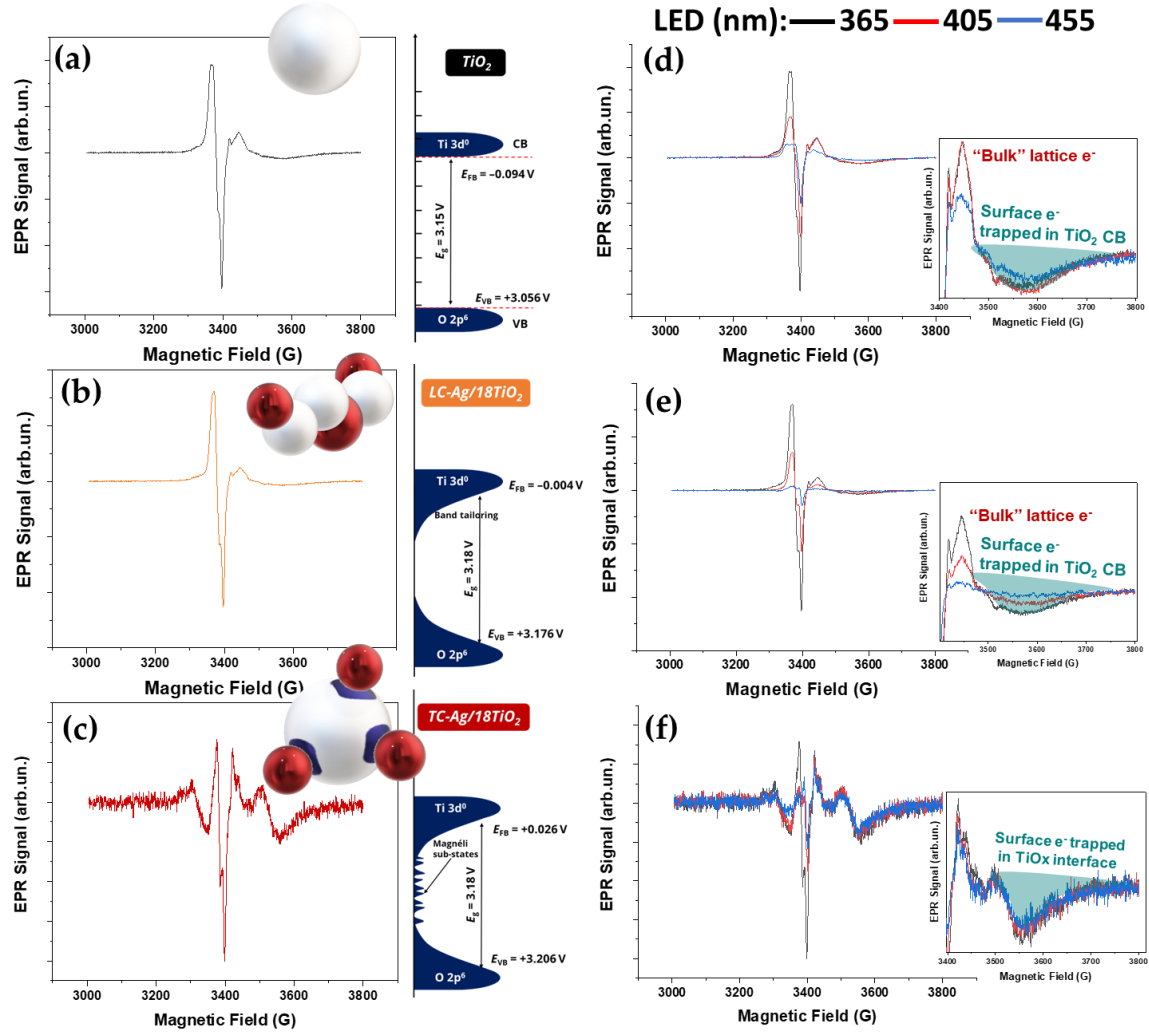


Figure 6.55. EPR spectra of (a) 18TiO₂, (b) LC-50Ag/18TiO₂ and (c) TC-50Ag/18TiO₂. The spectra depict photo-induced species and plotted by subtracting the spectrum obtained under light from the one under dark conditions. (d)(e)(f) EPR spectra of photo-induced electron/hole pairs varying the excitation wavelength under constant power density. Inset: The magnified region of the trapped photo-excited electrons.

The generation and dynamics of photo-excited carriers in the Ag/TiO₂ nanoaggregates is investigated using EPR spectroscopy, and the signals assigned to electron/hole pairs are presented in Figure 6.5. Specifically, the experimental EPR spectra

can be simulated with five subspectra, as seen in Figure 6.5a for the case of 18TiO₂ and using the Spin-Hamiltonian parameters listed in Table 6.3. As known for TiO₂, the prominent, derivative-like components h1 and h2, are assigned to photo-induced holes localized on lattice oxygen atoms near the surface with the g-tensor g_{h1} determined by the spin-orbit coupling and the local environment. Accordingly, the higher anisotropy of the other hole type h2, indicates a more distorted local environment, thus h2 are more exposed to the surface compared to the more localized in lattice h1, trapped at hydroxyl groups. On a similar note, the simulated e1, e2 and e3 species can be assigned to electrons trapping sites at Ti³⁺ surface and bulk centers, in anatase, rutile and surface sites respectively, with the Spin-Hamiltonian parameters (Table 6.3) being in agreement with the existing literature.

Interestingly, the simulated EPR spectra for TC-50Ag/18TiO₂ resolved in Figure 6.5c, shows that the photo-excited surface electrons act differently. In particular, the narrower linewidth of (e3) assigned to Ti³⁺ surface trapping sites, denotes the restricted mobility of the photo-generated electrons compared to pristine 18TiO₂. It becomes evident that increasing Ag content and, thus the formation of Magneli suboxides in the Ag/TiO₂ interface, the photo-induced electrons can be efficiently confined in these interfacial trapping sites, improving the carrier dissociation and storage. It is noteworthy that there is no evidence of these restricted electrons for LC-50Ag/18TiO₂, indicating the importance of the distorted interface.

Regarding the type of electrons stimulated, injected and trapped in the Ti³⁺ sites, it is paramount to understand where it originates. On this regard, EPR measurements were conducted using different excitation wavelength, as shown in Figure 6.4d-f for the 18TiO₂, LC-50Ag/18TiO₂ and TC-50Ag/18TiO₂ nanocomposites respectively. In particular, comparing the two former samples, a change in the population of photo-excited electrons is detected. For the case of 18TiO₂, the number of photo-induced electrons is similar for both 365 and 405 nm with the slight decrease when the 455 nm illumination is used. Interestingly, for the case of LC-50Ag/18TiO₂, the population of photo-excited electrons under 405 nm illumination, is almost zero, either for electrons trapped in the lattice or on the surface, as shown in the inset of Figure 6.5e. This indicates the migration of these

electrons to the coupled Ag nanoparticles, where the visible-light-excited electrons to be more favored for transfer. When the Ag/TiO₂ interface is further distorted due to the presence of the Magneli TiO_x suboxides, the total photo-excited population is diminished compared to the other two nanocomposites, probably because the Ag coverage of the TiO₂ surface prevents the proper illumination of TiO₂ particles, shown in Figure 6.5f. However, the relative number of photo-excited electrons are kept constant under varying excitation wavelength. This provides additional evidence of the increased number of sub-gap energy states, thus introducing an almost continuum energy distribution through the band gap, in agreement to DRS measurements and the black color.

6.3.3 Dark photocatalysis in Cr⁶⁺ reduction

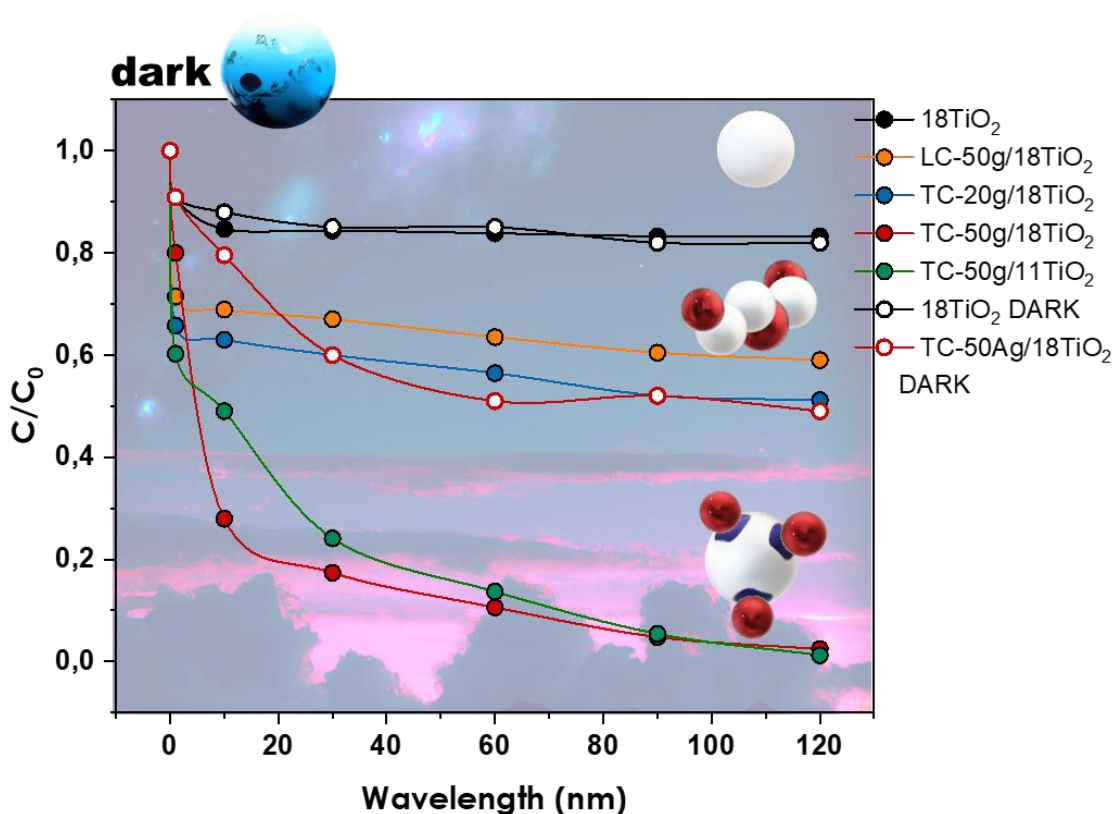


Figure 6.56. Kinetics of Cr⁶⁺ photo-reduction under 405 nm illumination in the presence of Ag/TiO₂ nanocomposites post-illumination under dark conditions. The open symbols describe catalytic runs where no light was used. Cr⁶⁺ is inserted into the system before and after illumination for the (a) and (b) procedure respectively.

Figure 6.6 demonstrates the photocatalytic reduction of hexavalent chromium (Cr^{6+}), enhanced by the presence of Ag/TiO₂ nanocomposites. In terms of dark photocatalysis, the contribution of the reference sample 18TiO₂ in the reaction is zero, as evidenced in Figure 6.6. The performance of LC-50Ag/18TiO₂ is anticipated, since the Ag/TiO₂ interface is the most efficient contact reported for efficient electron storage.⁷ Strikingly, the optimal catalytic yield is detected for the case of TC-50Ag/TiO₂ nanocomposites, independently of the TiO₂ particle size. Specifically, the reduction process is completed within 2 hours after light. This performance comes to agreement with the hypothesis that the Magneli TiO_x nano-islands present in the distorted Ag/TiO₂ interface, improve the capability of excite and storage electrons utilizing the visible region.

6.4 Conclusions

In this work, visible-light active Ag/TiO₂ nanocomposites were produced using flame spray pyrolysis, tuning both Ag content and TiO₂ particle size, with emphasis given to the interfacial contact (loose or tight). In the latter case, crystalline TiO_x suboxide phases (Magneli) are introduced as nano-islands upon Ag-TiO₂ contact, distorting the interface. Regarding the electronic structure, it was revealed that photo-excited electrons can be efficiently “trapped” near the surface, thus prolonging the electron/hole separation and their potential chemical activity. Therefore, the interfacial Magneli phases introduce sub-gap energy states, improving drastically both electron storage and visible-light activity. In terms of dark photocatalysis, the pre-irradiated black Ag/TiO₂ nanocomposites reduce hexavalent Cr^{6+} ions, providing electrons even after 2 hours under dark conditions, verifying the role of interfacial Magneli nano-islands to trap surface electrons in active sites utilising sunlight.

6.5 Supporting Information

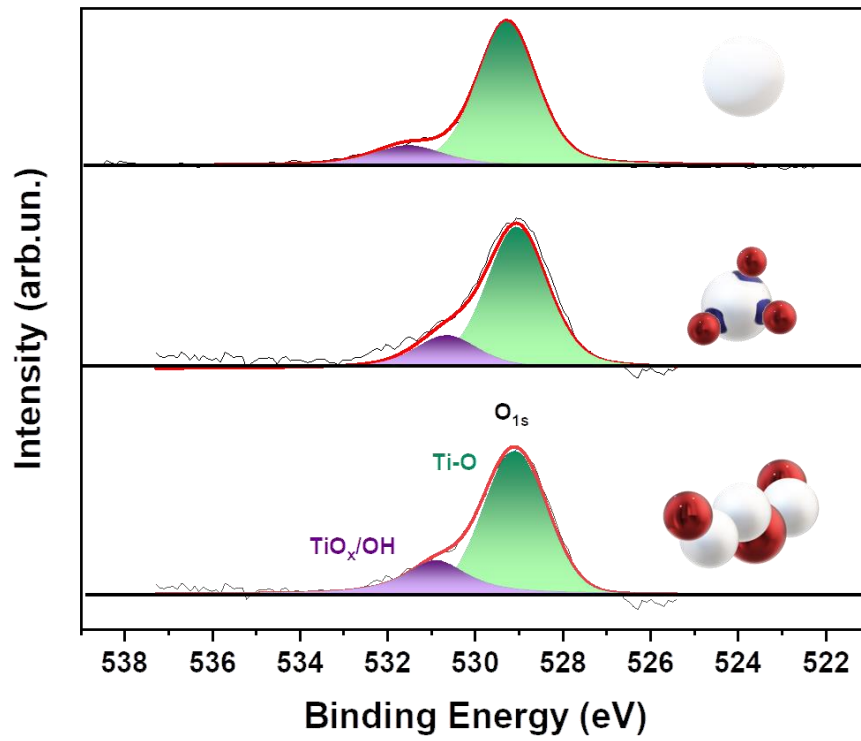


Figure 6.S1. Kinetics XPS spectra of O_{1s} for 18TiO₂, LC-50Ag/18TiO₂ and TC-50Ag/18TiO₂

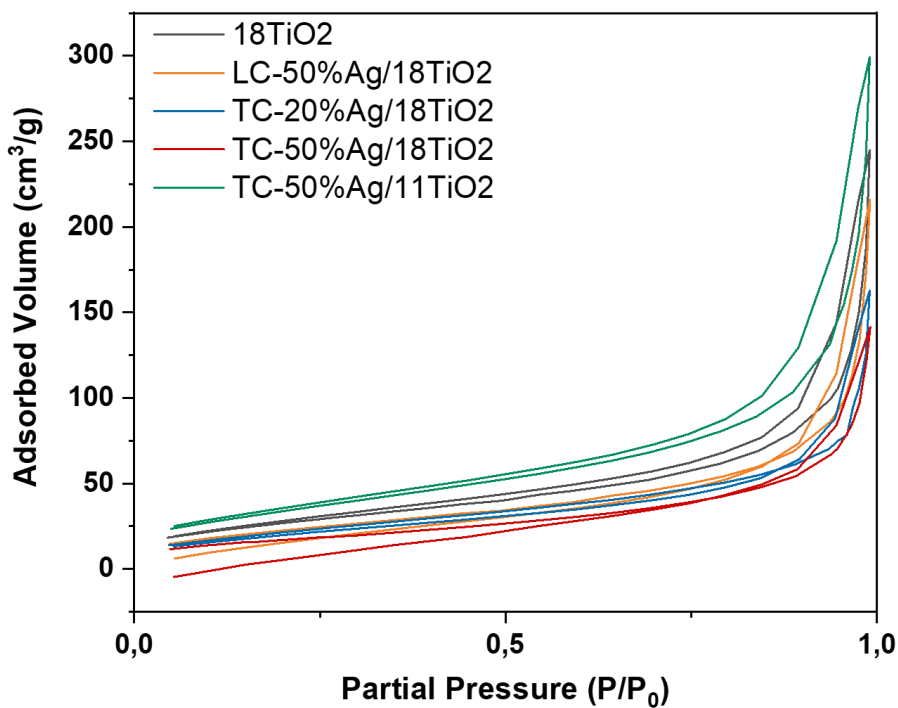


Figure 6.S2. Nitrogen adsorption isotherms for the Ag/TiO₂ nanocomposites.

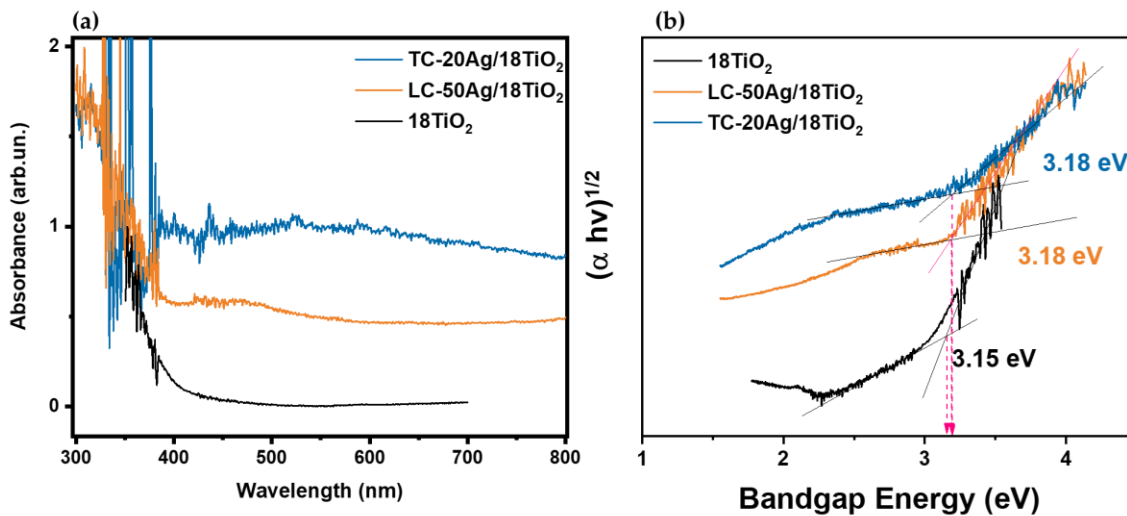


Figure 6.S3. (a) DRS measurements of Ag/TiO₂ nanostructures. (b) Tauc plot. The energy band gap is derived using Kubelka-Munk equation.

References

- (1) Li, Q.; Li, Y. W.; Liu, Z.; Xie, R.; Shang, J. K. Memory Antibacterial Effect from Photoelectron Transfer between Nanoparticles and Visible Light Photocatalyst. *J. Mater. Chem.* **2010**, *20* (6), 1068–1072. <https://doi.org/10.1039/B917239D>.
- (2) Yi, F.; Ma, J.; Lin, C.; Zhang, H.; Qian, Y.; Jin, H.; Zhang, K. Electronic and Thermal Transfer Actuating Memory Catalysis for Organic Removal by a Plasmonic Photocatalyst. *Chemical Engineering Journal* **2022**, *427*, 132028. <https://doi.org/10.1016/j.cej.2021.132028>.
- (3) Li, Y.; Li, H.; Lu, X.; Yu, X.; Kong, M.; Duan, X.; Qin, G.; Zhao, Y.; Wang, Z.; Dionysiou, D. D. Molybdenum Disulfide Nanosheets Vertically Grown on Self-Supported Titanium Dioxide/Nitrogen-Doped Carbon Nanofiber Film for Effective Hydrogen Peroxide Decomposition and “Memory Catalysis.” *Journal of Colloid and Interface Science* **2021**, *596*, 384–395. <https://doi.org/10.1016/j.jcis.2021.03.140>.
- (4) Zhang, Z.; Yates, J. T. Band Bending in Semiconductors: Chemical and Physical Consequences at Surfaces and Interfaces. *Chem. Rev.* **2012**, *112* (10), 5520–5551. <https://doi.org/10.1021/cr3000626>.
- (5) Li, Q.; Li, Y. W.; Wu, P.; Xie, R.; Shang, J. K. Palladium Oxide Nanoparticles on Nitrogen-Doped Titanium Oxide: Accelerated Photocatalytic Disinfection and Post-Illumination Catalytic “Memory.” *Adv. Mater.* **2008**, *20* (19), 3717–3723. <https://doi.org/10.1002/adma.200800685>.
- (6) Liu, L.; Yang, W.; Li, Q.; Gao, S.; Shang, J. K. Synthesis of Cu₂O Nanospheres Decorated with TiO₂ Nanoislands, Their Enhanced Photoactivity and Stability under Visible Light Illumination, and Their Post-Illumination Catalytic Memory. *ACS Appl. Mater. Interfaces* **2014**, *6* (8), 5629–5639. <https://doi.org/10.1021/am500131b>.
- (7) Takai, A.; Kamat, P. V. Capture, Store, and Discharge. Shuttling Photogenerated Electrons across TiO₂–Silver Interface. *ACS Nano* **2011**, *5* (9), 7369–7376. <https://doi.org/10.1021/nm202294b>.

- (8) Choi, H.; Chen, W. T.; Kamat, P. V. *Know Thy Nano Neighbor*. Plasmonic versus Electron Charging Effects of Metal Nanoparticles in Dye-Sensitized Solar Cells. *ACS Nano* **2012**, *6* (5), 4418–4427. <https://doi.org/10.1021/nm301137r>.
- (9) Wood, A.; Giersig, M.; Mulvaney, P. Fermi Level Equilibration in Quantum Dot–Metal Nanojunctions. *J. Phys. Chem. B* **2001**, *105* (37), 8810–8815. <https://doi.org/10.1021/jp011576t>.
- (10) Choi, Y.; Koo, M. S.; Bokare, A. D.; Kim, D.; Bahnemann, D. W.; Choi, W. Sequential Process Combination of Photocatalytic Oxidation and Dark Reduction for the Removal of Organic Pollutants and Cr(VI) Using Ag/TiO₂. *Environ. Sci. Technol.* **2017**, *51* (7), 3973–3981. <https://doi.org/10.1021/acs.est.6b06303>.
- (11) Cai, T.; Liu, Y.; Wang, L.; Zhang, S.; Ma, J.; Dong, W.; Zeng, Y.; Yuan, J.; Liu, C.; Luo, S. “Dark Deposition” of Ag Nanoparticles on TiO₂: Improvement of Electron Storage Capacity To Boost “Memory Catalysis” Activity. *ACS Appl. Mater. Interfaces* **2018**, *10* (30), 25350–25359. <https://doi.org/10.1021/acsami.8b06076>.
- (12) Lin, C.-Y.; Lai, Y.-H.; Balamurugan, A.; Vittal, R.; Lin, C.-W.; Ho, K.-C. Electrode Modified with a Composite Film of ZnO Nanorods and Ag Nanoparticles as a Sensor for Hydrogen Peroxide. *Talanta* **2010**, *82* (1), 340–347. <https://doi.org/10.1016/j.talanta.2010.04.047>.
- (13) Rajaraman, T. S.; Parikh, S. P.; Gandhi, V. G. Black TiO₂: A Review of Its Properties and Conflicting Trends. *Chemical Engineering Journal* **2020**, *389*, 123918. <https://doi.org/10.1016/j.cej.2019.123918>.
- (14) Chen, X.; Liu, L.; Yu, P. Y.; Mao, S. S. Increasing Solar Absorption for Photocatalysis with Black Hydrogenated Titanium Dioxide Nanocrystals. *Science* **2011**, *331* (6018), 746–750. <https://doi.org/10.1126/science.1200448>.
- (15) Naldoni, A.; Allieta, M.; Santangelo, S.; Marelli, M.; Fabbri, F.; Cappelli, S.; Bianchi, C. L.; Psaro, R.; Dal Santo, V. Effect of Nature and Location of Defects on Bandgap Narrowing in Black TiO₂ Nanoparticles. *J. Am. Chem. Soc.* **2012**, *134* (18), 7600–7603. <https://doi.org/10.1021/ja3012676>.

- (16) Åsbrink, S.; Magnéli, A. Crystal Structure Studies on Trititanium Pentoxide, Ti_3O_5 . *Acta Cryst* **1959**, *12* (8), 575–581. <https://doi.org/10.1107/S0365110X59001694>.
- (17) Andersson, S.; Collén, B.; Kruuse, G.; Kuylenstierna, U.; Magnéli, A.; Pestmalis, H.; Åsbrink, S. Identification of Titanium Oxides by X-Ray Powder Patterns. *Acta Chem. Scand.* **1957**, *11*, 1653–1657. <https://doi.org/10.3891/acta.chem.scand.11-1653>.
- (18) Wierzbicka, E.; Domaschke, M.; Denisov, N.; Fehn, D.; Hwang, I.; Kaufmann, M.; Kunstmann, B.; Schmidt, J.; Meyer, K.; Peukert, W.; Schmuki, P. Magnéli Phases Doped with Pt for Photocatalytic Hydrogen Evolution. *ACS Appl. Energy Mater.* **2019**, *2* (12), 8399–8404. <https://doi.org/10.1021/acsaem.9b02053>.
- (19) Li, X.; Zhu, A. L.; Qu, W.; Wang, H.; Hui, R.; Zhang, L.; Zhang, J. Magnéli Phase Ti_4O_7 Electrode for Oxygen Reduction Reaction and Its Implication for Zinc-Air Rechargeable Batteries. *Electrochimica Acta* **2010**, *55* (20), 5891–5898. <https://doi.org/10.1016/j.electacta.2010.05.041>.
- (20) Domaschke, M.; Zhou, X.; Wergen, L.; Romeis, S.; Miehlich, M. E.; Meyer, K.; Peukert, W.; Schmuki, P. Magnéli-Phases in Anatase Strongly Promote Cocatalyst-Free Photocatalytic Hydrogen Evolution. *ACS Catal.* **2019**, *9* (4), 3627–3632. <https://doi.org/10.1021/acscatal.9b00578>.
- (21) Naldoni, A.; Altomare, M.; Zoppellaro, G.; Liu, N.; Kment, Š.; Zbořil, R.; Schmuki, P. Photocatalysis with Reduced TiO_2 : From Black TiO_2 to Cocatalyst-Free Hydrogen Production. *ACS Catal.* **2019**, *9* (1), 345–364. <https://doi.org/10.1021/acscatal.8b04068>.
- (22) Tang, C.; Zhou, D.; Zhang, Q. Synthesis and Characterization of Magnéli Phases: Reduction of TiO_2 in a Decomposed NH_3 Atmosphere. *Materials Letters* **2012**, *79*, 42–44. <https://doi.org/10.1016/j.matlet.2012.03.095>.
- (23) Arif, A. F.; Balgis, R.; Ogi, T.; Iskandar, F.; Kinoshita, A.; Nakamura, K.; Okuyama, K. Highly Conductive Nano-Sized Magnéli Phases Titanium Oxide (TiO_x). *Sci Rep* **2017**, *7* (1), 3646. <https://doi.org/10.1038/s41598-017-03509-y>.

- (24) Malik, H.; Sarkar, S.; Mohanty, S.; Carlson, K. Modelling and Synthesis of Magnéli Phases in Ordered Titanium Oxide Nanotubes with Preserved Morphology. *Sci Rep* **2020**, *10* (1), 8050. <https://doi.org/10.1038/s41598-020-64918-0>.
- (25) Fujiwara, K.; Deligiannakis, Y.; Skoutelis, C. G.; Pratsinis, S. E. Visible-Light Active Black TiO₂-Ag/TiO_x Particles. *Applied Catalysis B: Environmental* **2014**, *154–155*, 9–15. <https://doi.org/10.1016/j.apcatb.2014.01.060>.
- (26) Bletsa, E.; Merkl, P.; Thersleff, T.; Normark, S.; Henriques-Normark, B.; Sotiriou, G. A. Highly Durable Photocatalytic Titanium Suboxide–Polymer Nanocomposite Films with Visible Light-Triggered Antibiofilm Activity. *Chemical Engineering Journal* **2023**, *454*, 139971. <https://doi.org/10.1016/j.cej.2022.139971>.
- (27) Solakidou, M.; Georgiou, Y.; Deligiannakis, Y. Double-Nozzle Flame Spray Pyrolysis as a Potent Technology to Engineer Noble Metal-TiO₂ Nanophotocatalysts for Efficient H₂ Production. *Energies* **2021**, *14* (4), 817. <https://doi.org/10.3390/en14040817>.
- (28) Gelderman, K.; Lee, L.; Donne, S. W. Flat-Band Potential of a Semiconductor: Using the Mott–Schottky Equation. *J. Chem. Educ.* **2007**, *84* (4), 685. <https://doi.org/10.1021/ed084p685>.
- (29) van de Krol, R.; Goossens, A.; Schoonman, J. Mott-Schottky Analysis of Nanometer-Scale Thin-Film Anatase TiO₂. *J. Electrochem. Soc.* **1997**, *144* (5), 1723–1727. <https://doi.org/10.1149/1.1837668>.
- (30) Stoll, S.; Schweiger, A. EasySpin, a Comprehensive Software Package for Spectral Simulation and Analysis in EPR. *Journal of Magnetic Resonance* **2006**, *178* (1), 42–55. <https://doi.org/10.1016/j.jmr.2005.08.013>.
- (31) García de Abajo, F. J.; Howie, A. Retarded Field Calculation of Electron Energy Loss in Inhomogeneous Dielectrics. *Phys. Rev. B* **2002**, *65* (11), 115418. <https://doi.org/10.1103/PhysRevB.65.115418>.
- (32) Palik, E. D. *Handbook of Optical Constants of Solids*; Academic Press, 1998.

- (33) Koutsouroubi, E. D.; Vamvasakis, I.; Drivas, C.; Kennou, S.; Armatas, G. S. Photochemical Deposition of SnS₂ on Graphitic Carbon Nitride for Photocatalytic Aqueous Cr(VI) Reduction. *Chemical Engineering Journal Advances* **2022**, *9*, 100224. <https://doi.org/10.1016/j.ceja.2021.100224>.
- (34) Matsumoto, Y. Energy Positions of Oxide Semiconductors and Photocatalysis with Iron Complex Oxides. *Journal of Solid State Chemistry* **1996**, *126* (2), 227–234. <https://doi.org/10.1006/jssc.1996.0333>.
- (35) Wang, S.; Zhang, J.; Gharbi, O.; Vivier, V.; Gao, M.; Orazem, M. E. Electrochemical Impedance Spectroscopy. *Nat Rev Methods Primers* **2021**, *1* (1), 41. <https://doi.org/10.1038/s43586-021-00039-w>.

Chapter 7

Concluding Remarks & Future Research Perspectives

In this thesis, emphasis was given on the study of the underlying photo-induced physicochemical mechanisms that occur in the presence of plasmonic/semiconducting nanomaterials. Flame spray pyrolysis (FSP) was employed for the synthesis of core@shell nanoaggregates (Ag@SiO_2) and distorted/suboxide interfaces ($\text{Ag/TiO}_x/\text{TiO}_2$) controlling precisely particle characteristics and composition. The plasmon-driven phenomena were categorized and thoroughly reviewed (**Chapter 1**) as: phenomena outside (light scattering), inside (hot carriers) the particle and in the particle-particle interface (thermal effects, hot spots, charge transfer). Following that, the plasmon-induced bulk temperature rise due to illuminated plasmonic Ag@SiO_2 nanoaggregates was monitored by tuning the interparticle Ag-Ag distance (**Chapter 3**). Furthermore, the fractal dimension (the parameter that describes the dendritic shape of flame-made aggregates) was inserted in the theoretical frame of thermoplasmonics, verifying the experimentally observed collective thermal effects.

Following the control and understanding of the photothermal mechanism, the hot-carrier generation and activity was studied in redox reactions. On this regard, a novel methodology for the detection of the short-lived hot electrons was developed using electron paramagnetic resonance (EPR) spectroscopy and the Cr^{6+} photo-reduction as a chemical probe for the first time in literature (**Chapter 4**). The population of photo-excited hot electrons was quantified in physical units (moles/gr) and correlated to the interparticle

distance, in a similar manner to photothermal mechanism. In terms of environmental remediation, the plasmon-enhanced reduction of toxic Cr^{6+} ions to inert Cr^{3+} under sunlight was observed and the contribution of each plasmon mechanism was thoroughly investigated.

In the last section, the plasmonic/semiconducting interface was studied in flame-made nanocomposites. NaTaO_3 nano-perovskites of controlled characteristics were synthesized using FSP for the first time in literature and the photo-stimulated electron/hole dynamics were explored utilizing EPR spectroscopy (**Chapter 5**). Characterizing Ag/NaTaO_3 nanostructures, no decisive evidence was provided, that Ag strongly interacts to NaTaO_3 (eg. defects, distortions). However, when Ag was coupled to TiO_2 particles inside the flames, the formation of crystalline TiO_x suboxide phases (Magneli) was introduced in the $\text{Ag}-\text{TiO}_2$ contact (**Chapter 6**). This plasmonic/semiconducting distorted interface provided superior photo-induced electron storage in surface active sites and high visible-light activity. These traits improved drastically the “dark” photocatalysis of Cr^{6+} reduction, in the terms of day-and-night photocatalysis.

In summary, in this thesis, the plasmon-driven events in flame-made nanomaterials were extensively controlled by the scalability FSP provides, with emphasis being given to the photophysical events in a plasmonic/semiconducting interface (electron excitation and transfer). These underlying photophysical mechanisms were utilized in terms of plasmonic catalysis, using the Cr^{6+} reduction as the chemical-reaction probe.

Regarding the future research perspectives, this thesis established that the plasmonic particle interface (neighboring metallic particles, adsorbed molecules or attached semiconductors) can be engineered accordingly regarding the desired application. The field of plasmonic catalysis is moving towards hybrid nanomaterials, where the plasmonic component amplifies the light energy and the non-plasmonic component that extracts this energy in the form of electronic excitations to drive selective plasmonic chemistry. Moreover, the need for the industrial production of such nanomaterials promotes the single-step and scalable process of flame spray pyrolysis for the synthesis of plasmonic/semiconducting robust nanoensembles. For the case of $\text{Ag}@\text{SiO}_2$ nanoaggregates, this thesis provided evidence of amplified hot-electron generation and plasmon-enhanced redox reactions (**Chapter 4**), thus they can be employed in boosting

more complex chemical reactions, such as sunlight-driven CO₂ reduction and H₂ production.

For the case of black Ag/TiO₂ nanocomposites, one pathway for further investigation is the detection and activity of the photo-excited holes (eg. ROS generation). The photo-excited holes can be either high-energy d-band holes or near-fermi sp-band holes. The utilization and detection of these less-mobile d-band holes. Moreover, the interfacial Magneli nano-islands have been reported to promote oxygen reduction reaction (ORR), replacing the conventional carbon as the conductive substrate, thus the black Ag/TiO₂ nanostructures can be involved to electrocatalysis as well. Lastly, the detected electron storage in the Ag/TiO₂ interface, investigated in this thesis, can be utilized in the photo-induced enhanced Raman scattering (PIERS), a novel protocol where the efficiency of surface-enhanced Raman spectroscopy (SERS) in the presence of plasmon/semiconductor is mainly attributed to the charge transfer between the semiconductor and the adsorbed chemical species, rather than the electric-field enhancement, the typical SERS enhancement mechanism. On this regard, FSP enables the in situ fabrication of SERS substrates above the flame, promoting the hot-spot homogeneity and film robustness.

Appendix A: Evaluation of Ag⁺ Leaching and UV-Vis/EPR Analysis of Ag@SiO₂/Cr system

Caution! Contact with skin and inhalation must be avoided. Cr⁶⁺ compounds are human carcinogens, and Cr⁵⁺ complexes are mutagenic and potentially carcinogenic. However, Cr³⁺ is less toxic form of chromium and an essential micronutrient for several organisms.

Sample preparation: Ag⁰@SiO₂ NPs were added in deoxygenated Milli-Q water and dispersed using a cup-horn sonicator (Sonic-V500), for 5 minutes in dark at 24 °C (RT). Then, appropriate volumes of stock solutions of 1 mM potassium dichromate (K₂Cr₂O₇), i.e., 2 mM of Cr⁶⁺, and 4 mM oxalic acid (C₂H₂O₄) were added to the aqueous Ag⁰@SiO₂ particle suspensions under continuous magnetic stirring. Three particle concentrations were studied: 80, 240 and 500 mg L⁻¹. Cr⁶⁺ was quantified using the well-established diphenylcarbazide (DPC) method by UV-Vis spectroscopy.^{1,2} The absorbance at 541 nm from the Cr⁶⁺-DPC complex was used to quantify Cr⁶⁺ in the solution.³ Before each UV-Vis measurement, the solution pH was adjusted to 3, by adding small amounts of HNO₃.

The optimal pH value (= 3) was carefully selected taking into consideration the following factors: pH values < 4 provide better EPR {Cr⁵⁺-oxalate} signals in accordance with Farrell *et al.*⁴ and Dos Santos *et al.*⁵ To avoid unwanted solubilization of the SiO₂, pH = 3 was chosen. This was confirmed by ensuring linear behavior of Cr⁶⁺-DPC calibration curves for four different pHs (1.6, 2.5, 3.5, and 4.5), shown in Figure A3. Accordingly, pH = 3.0 ± 0.2 was chosen for the present study.

Irradiation experiments were conducted using an arc xenon lamp (Oriel model 6293; 1000 W) and a 90⁰-beam turning mirror (Model Oriel 62245). This allowed a convenient overhead irradiation of the reaction suspension (Figure A1). Infrared irradiation was filtered by a cylindrical water-filter positioned in front of the lamp. Sample temperature was continuously monitored using a digital thermometer probe (Delta Ohm HD8601P) and a thermal camera (Fluke TiS40). During each irradiation experiments, 200 µL aliquots from

the sample were transferred to 5 mm o.d. quartz EPR tubes (Wilmad-LabGlass), frozen immediately at 77 K, and studied by EPR.

Arrhenius Study: To examine the contribution of thermal effects, Cr photo-reduction was examined under bulk heating of the sample in the range 25–60 °C. For each temperature, the Cr⁶⁺ photoreduction kinetics was recorded and the initial kinetic rates (*k*) were estimated. From the Arrhenius equation (eq. A1) the $\ln k$ vs. (1/T) (eq. A2) were plotted

$$k = A e^{-E_a/RT}, \quad (\text{eq. A1})$$

$$\ln k = (-E_a/R) \times (1/T) + \ln A, \quad (\text{eq. A2})$$

where A is a pre-exponential factor, R the gas constant and T the absolute temperature.⁶ From the slope of the plot { $\ln k$ vs. (1/T)}, the activation energy E_a can be calculated.

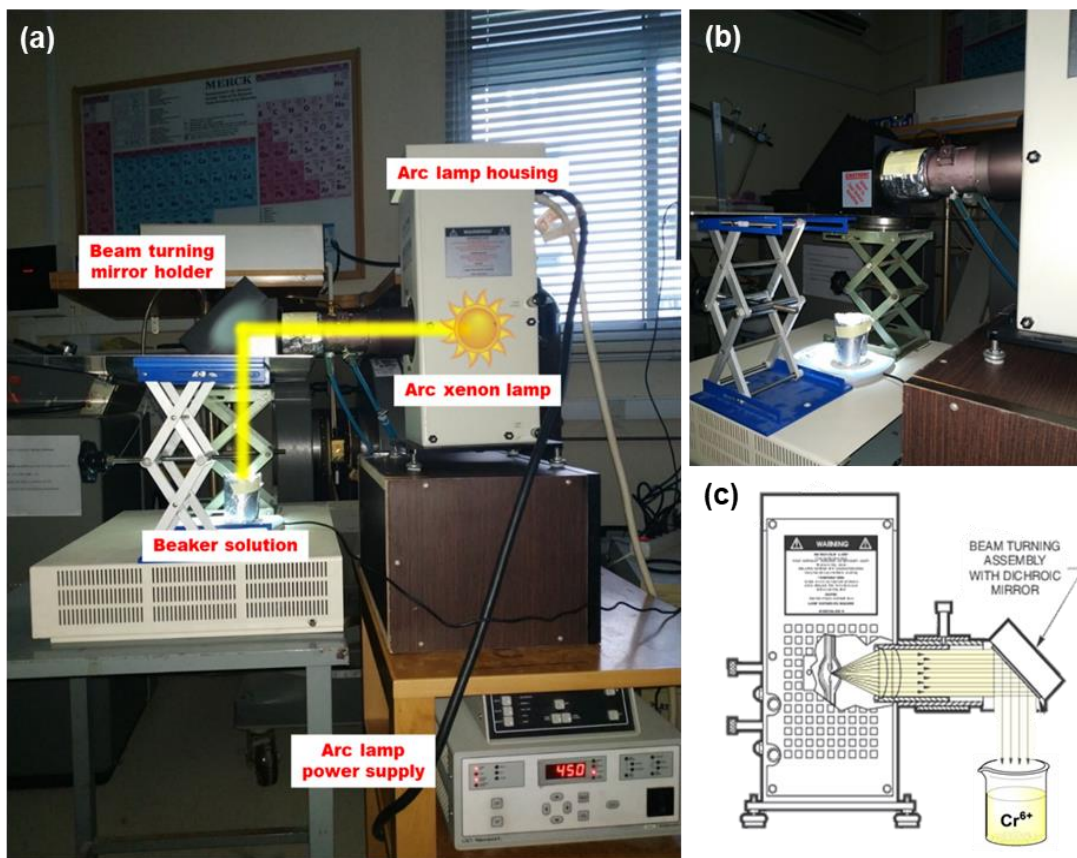


Figure A.1. (a) Experimental illumination set-up consisting of the arc xenon lamp (Oriel Mercury-Xenon Lamp; Model 6293, 1000 W) and the beam turning mirror holder (Model 62245). All the experiments were performed with lamp power of 450 W. (b) Side view of

the set-up. (c) Schematic figure of beam turner attached to the lamp housing condenser (F/1 fused silica lens) irradiating the $[Ag^0@SiO_2/\{Cr^{6+}\text{-oxalate}\}]$ solution.

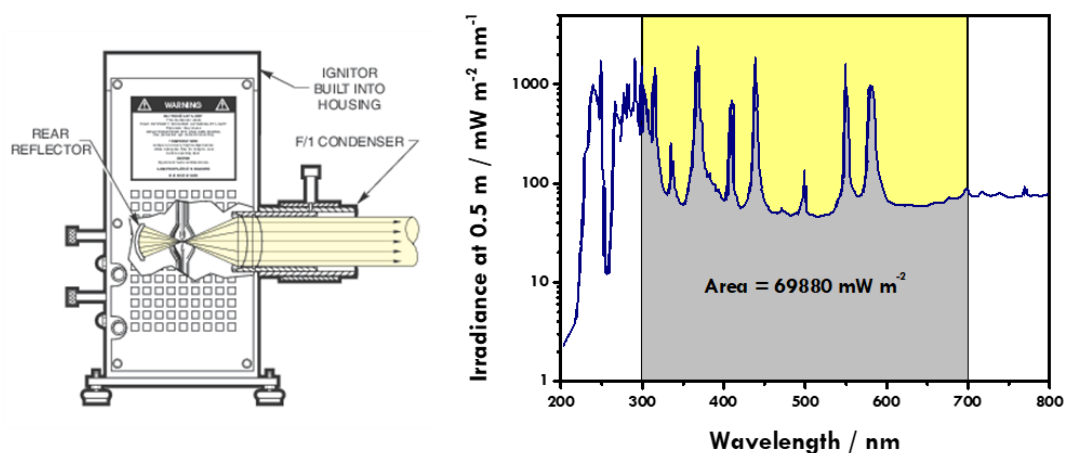


Figure A.2. (a) The 66921 Arc Lamp Housing (450-1000 W) with a F/1 fused silica condenser. (b) Typical spectral irradiance of the Oriel Mercury-Xenon Arc Lamp (model: 6293, 1000 W).

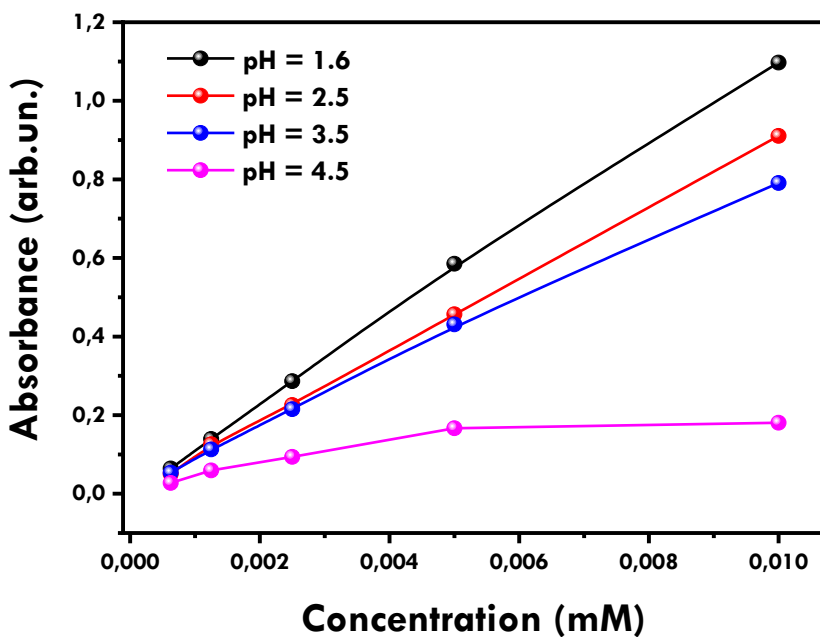


Figure A.3. UV-Vis calibration curves for standard concentration of Cr^{6+} -DPC evaluating the pH effect.

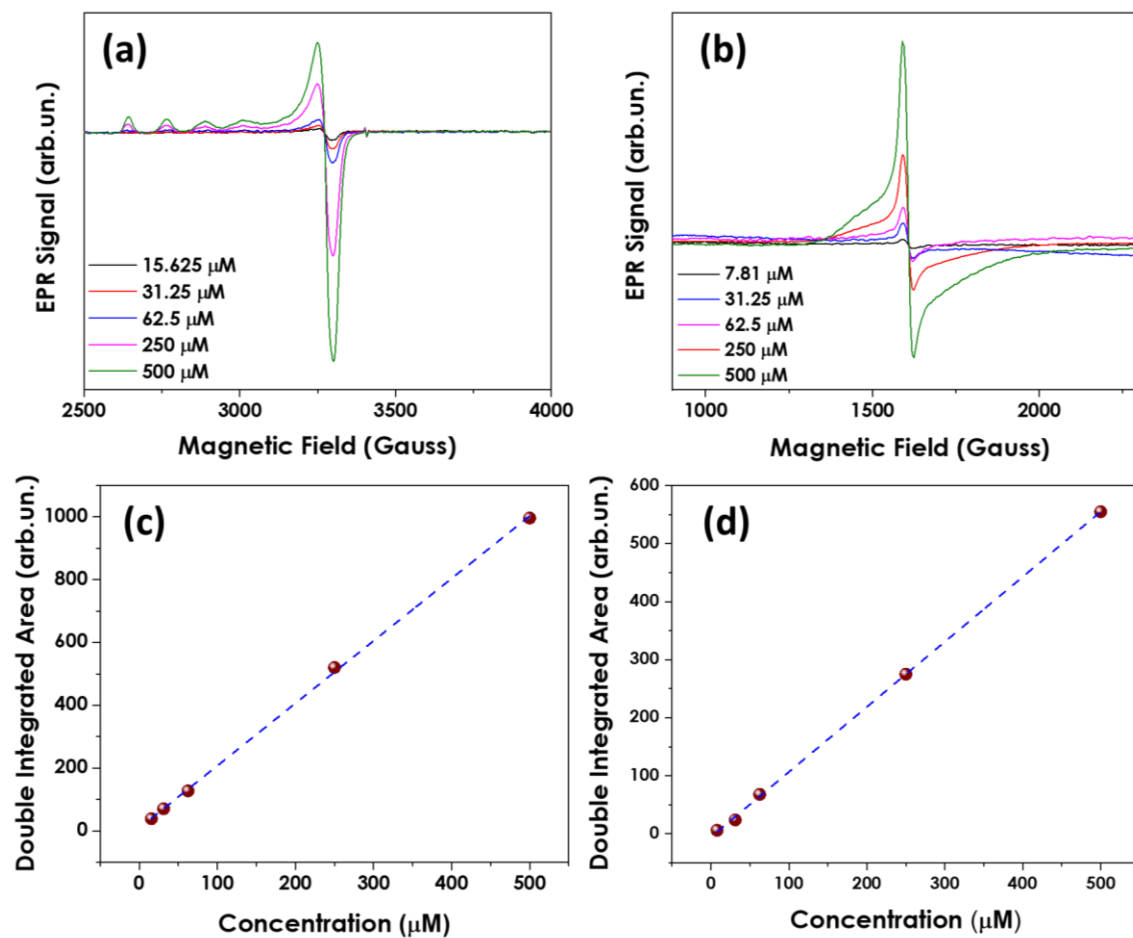


Figure A.4. EPR signals of (a) Cu²⁺ nitrate and (b) Fe³⁺-EDTA as spin standards and (c, d) the calibration curves, respectively.

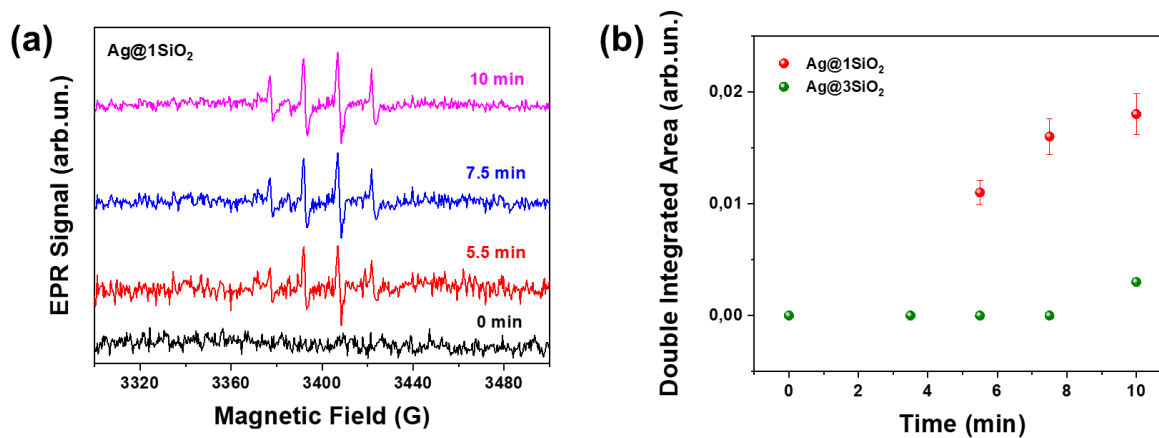


Figure A.5. EPR signals of DMPO-OH adduct of (a) Ag@1SiO₂ NPS varying illumination time. (b) Double integrated area of EPR signals vs. time.

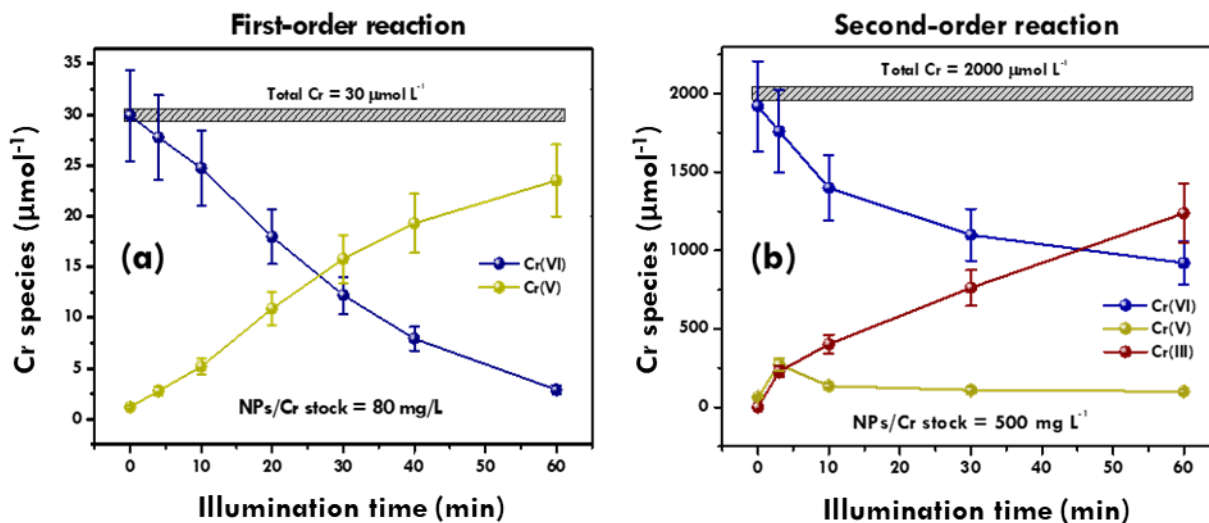


Figure A.6. Cr species (hot-electron concentration) as a function of the illumination time, using the Ag@1SiO₂ NPs. (a) First-order reaction with NP concentration of 80 mg L⁻¹. (b) Second-order reaction with NP concentration of 500 mg L⁻¹. The total chromium concentration is attributed with a grey plateau. In every measurement, the Cr⁶⁺ sum with the population of Cr⁵⁺ and Cr³⁺ matches the total chromium, with an error of 5%.

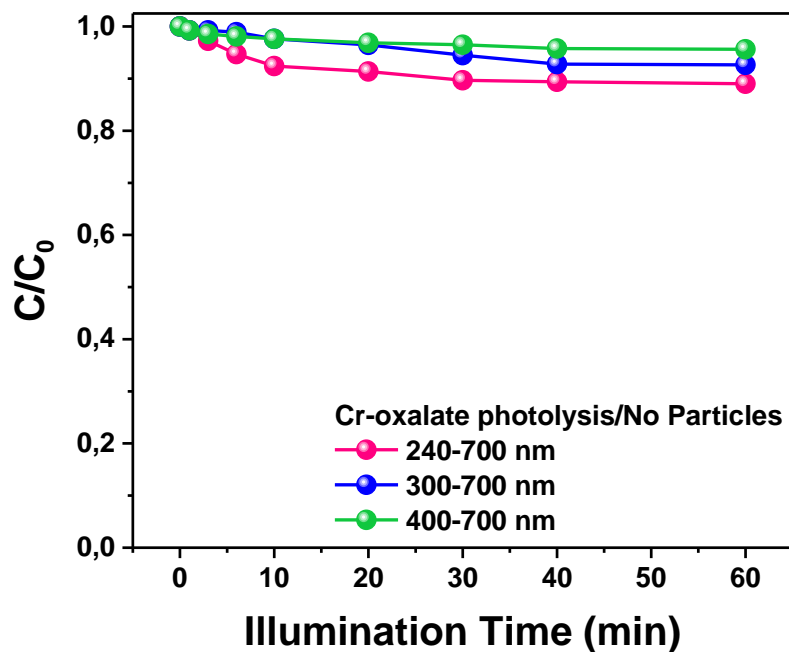
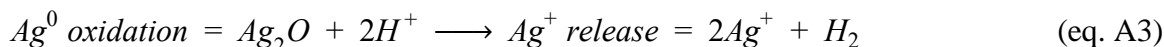


Figure A.7. Kinetics of {Cr⁶⁺-oxalate} reduction due to photolysis, by varying the excitation-wavelengths. UV light < 300 nm caused a non-zero photolysis (~10%). At > 300 nm direct photolysis is negligible.

Release of Ag⁺ ions: Ag-ion leaching was monitored using an Ag ion selective electrode (Thermo Scientific ISE) attached to an ion meter (JENWAY 3345). The electrode was calibrated using silver nitrate (AgNO₃) standard in aqueous solutions (Figure B8), at various concentrations (0.1–1000 ppm). The detection limit was 1 ppm at pH = 3. Eventual oxidation of non-coated Ag particles by Cr⁶⁺ or adventitious O₂ can result in Ag⁺ leaching according to the (eq. A3)^{7,8}



The SiO₂ encapsulation on the Ag⁰ NPs ensures that the layer prevents Ag-oxidation and Ag⁺ release. To verify this assumption, the Ag⁰@SiO₂ were tested for Ag⁺ leaching using an Ag⁺ selective electrode (Thermo Scientific ISE) attached to an ion meter (JENWAY 3345). 4 mM oxalic acid and 1 mM potassium dichromate dissolve in Millipore water. 1.5 g L⁻¹ Ag⁰@SiO₂ NPs were added to the solution and dispersed by the cup-horn sonicator,

using a total power of 100 W for 5 minutes. 2.3 M KNO_3 is added in both calibration and testing of NPs just a minute before the measurement ensuring the required ionic strength. The samples are tested after irradiation and mimic the experimental conditions. Figure A.9 shows the measured release of Ag^+ ions for the Ag^0/SiO_2 NPs and co-agglomerated (non-coated) Ag/SiO_2 (for reference). As expected, the non-coated Ag/SiO_2 NPs exhibit a significant amount of leaching (60 ppm at the very first minutes of measurement), indicating the existence of non-coated Ag particles. In the core@shell Ag^0/SiO_2 the Ag^+ release was significantly lower, see Figure A.9. The ultrathin shell of $\text{Ag}@1\text{SiO}_2$ allows the dissolution of < 20 ppm within 60 minutes under irradiation. Thicker SiO_2 shell ($\text{Ag}@5\text{SiO}_2$) release < 10 ppm Ag ions in an hour. To take this into account in our analysis we have assumed that the observed release of Ag^+ ions correspond to Cr^{6+} reduction, thus these value account for $< 13\%$ of the observed the Cr-reduction due to plasmonic hot electrons.

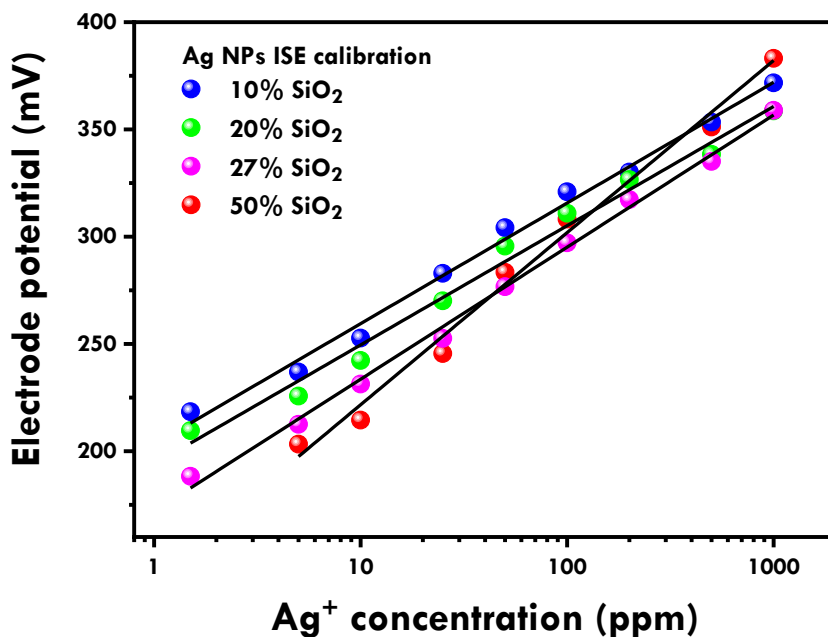


Figure A.8. Ag ion-selective electrode calibration of {Cr-oxalate} solution at pH = 3.

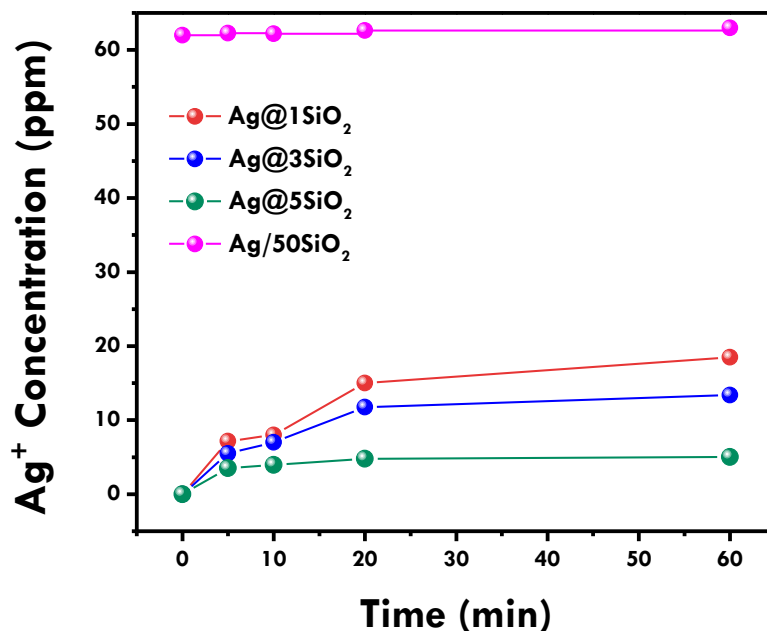


Figure A.9. Ag⁺ leaching versus time of Ag@XSiO₂ and Ag/50SiO₂ NPs adjusted for 0.5 g L⁻¹ NP concentration.

References

- [1] Stover, N. M., *Journal of the American Chemical Society*, **1928**, 50(9), 2363–2366.
- [2] Sanchez-Hachair, A., Hofmann, A., **2018**, 21(9), 890–896.
- [3] Liu, L., Leng, Y., Lin, H. *Microchimica Acta*, **2016**, 183(4), 1367–1373.
- [4] Farrell, R. P., Lay, P. A., Levina, A., Maxwell, I. A., Bramley, R., Brumby, S., Ji, J.-Y. *Inorganic Chemistry*, **1998**, 37(13), 3159–3166.
- [5] Dos Santos, V. C. G., Salvado, A. D. P. A., Dragunski, D. C., Peraro, D. N. C., Tarley, C. R. T., Caetano, J., **2012**, 35(8), 1606–1611.
- [6] Arrhenius, S.. *Zeitschrift Für Physikalische Chemie*, **1889**, 4(1). doi:10.1515/zpch-1889-0116.
- [7] Peretyazhko, T. S., Zhang, Q., Colvin, V. L.. *Environmental Science & Technology*, **2014**, 48(20), 11954–11961.

- [8] Zhou, W., Liu, Y.-L., Stallworth, A. M., Ye, C., Lenhart, J. J.. Environmental Science & Technology, **2016**, 50(22), 12214–12224.

Curriculum Vitae

Personal Information

Name: Constantinos Moularas

Date of Birth: 23/05/1994

E-mail: k.moularas@uoi.gr

Academic Track

BSc (2012-2016), Physics Department, University of Ioannina, Greece

MSc (2016-2018), Department of Physics, University of Ioannina, Greece

Thesis: *Flame Spray Pyrolysis Engineering of Hybrid Plasmonic SiO₂@Ag⁰Nanoparticles and Study of their Photothermal Efficiency.*

Supervisor: Prof. Dr. Yiannis Deligiannakis

PhD (2018-), Department of Physics, University of Ioannina, Greece

Thesis: *Photophysical and Catalytic Study of Plasmonic-Semiconducting Nanomaterials Developed by Flame Spray Pyrolysis Technology*

Supervisor: Prof. Dr. Yiannis Deligiannakis

Research Experience

(2016) Internship, Photovoltaic Systems, "Helios Products Katsouras", Ioannina, Greece

(2017-2018) L'Oreal, Engineering of colored nanoparticles by Flame Spray Pyrolysis

(2018-2019) TITAN A.E., Production of nano-Alite (tri-calcium silicate) by Flame Spray Pyrolysis technology

Publications

- (1) **Moularas, C.**; Georgiou, Y.; Adamska, K.; Deligiannakis, Y. Thermoplasmonic Heat Generation Efficiency by Nonmonodisperse Core-Shell Ag⁰@SiO₂ Nanoparticle Ensemble. *Journal of Physical Chemistry C* **2019**.
- (2) Henning, D. F.; Merkl, P.; Yun, C.; Iovino, F.; Xie, L.; Mouzourakis, E.; **Moularas, C.**; Deligiannakis, Y.; Henriques-Normark, B.; Leifer, K.; Sotiriou, G. A. Luminescent CeO₂:Eu³⁺ Nanocrystals for Robust in Situ H₂O₂ Real-Time Detection in Bacterial Cell Cultures. *Biosensors and Bioelectronics* **2019**, 132, 286–293.

- (3) Psathas, P.; Georgiou, Y.; **Moularas, C.**; Armatas, G. S.; Deligiannakis, Y. Controlled-Phase Synthesis of Bi₂Fe₄O₉ & BiFeO₃ by Flame Spray Pyrolysis and Their Evaluation as Non-Noble Metal Catalysts for Efficient Reduction of 4-Nitrophenol. *Powder Technology* **2020**.
- (4) Fragou, F.; **Moularas, C.**; Adamska, K.; Deligiannakis, Y.; Louloudi, M. Mn(II)-Based Catalysts Supported on Nanocarbon-Coated Silica Nanoparticles for Alkene Epoxidation. *ACS Applied Nano Materials* **2020**, *3* (6), 5583–5592.
- (5) Tada, S.; Otsuka, F.; Fujiwara, K.; **Moularas, C.**; Deligiannakis, Y.; Kinoshita, Y.; Uchida, S.; Honma, T.; Nishijima, M.; Kikuchi, R. Development of CO₂-to-Methanol Hydrogenation Catalyst by Focusing on the Coordination Structure of the Cu Species in Spinel-Type Oxide Mg_{1-x}Cu_xAl₂O₄. *ACS Catal.* **2020**, *10* (24), 15186–15194.
- (6) Belles, L.; **Moularas, C.**; Smykała, S.; Deligiannakis, Y. Flame Spray Pyrolysis Co₃O₄/CoO as Highly-Efficient Nanocatalyst for Oxygen Reduction Reaction. *Nanomaterials* **2021**, *11* (4), 925.
- (7) **Moularas, C.**; Psathas, P.; Deligiannakis, Y. Electron Paramagnetic Resonance Study of Photo-Induced Hole/Electron Pairs in NaTaO₃ Nanoparticles. *Chemical Physics Letters* **2021**, *782*, 139031.
- (8) Diamantis, S. A.; Pournara, A. D.; Koutsouroubi, E. D.; **Moularas, C.**; Deligiannakis, Y.; Armatas, G. S.; Hatzidimitriou, A. G.; Manos, M. J.; Lazarides, T. Detection and Sorption of Heavy Metal Ions in Aqueous Media by a Fluorescent Zr(IV) Metal–Organic Framework Functionalized with 2-Picolylamine Receptor Groups. *Inorg. Chem.* **2022**, *61* (20), 7847–7858.
- (9) Gemenetzi, A.; **Moularas, C.**; Belles, L.; Deligiannakis, Y.; Louloudi, M. Reversible Plasmonic Switch in a Molecular Oxidation Catalysis Process. *ACS Catal.* **2022**, *12* (16), 9908–9921.
- (10) **Moularas, C.**; Dimitriou, C.; Georgiou, Y.; Evangelakis, G.; Boukos, N.; Deligiannakis, Y. Electron Paramagnetic Resonance Quantifies Hot-Electron Transfer from Plasmonic Ag@SiO₂ to Cr⁶⁺/Cr⁵⁺/Cr³⁺. *J. Phys. Chem. C* **2023**, *127* (4), 2045–2057.
- (11) Psathas, P.; **Moularas, C.**; Smykała, S.; Deligiannakis, Y. Highly Crystalline Nanosized NaTaO₃/NiO Heterojunctions Engineered by Double-Nozzle Flame Spray Pyrolysis for Solar-to-H₂ Conversion: Toward Industrial-Scale Synthesis. *ACS Appl. Nano Mater.* **2023**, *6* (4), 2658–2671.
- (12) Agrafioti, K.A.; Panagiotopoulos, N.T.; **Moularas, C.**; Deligiannakis, Y.; Prouskas, C.; Soukouli, P.P.; Evangelakis, G. Development of Ti-based nanocomposite oxide thin films with CuO and Nb₂O₅ additions suitable for catalytic applications. *Thin Solid Films* **2023**, *775*, 139864.
- (13) **Moularas, C.**; Dimitriou, C.; Belles, L.; Zindrou, A.; Armatas, G.; Deligiannakis, Y. Flame-made Black Ag/TiO₂@TiO_x: Understanding the Visible-light Activity of Interfacial Magneli Islands in Electron Storage. (IN PREPARATION)

Presentations to National and International Conferences

Poster presentations

- (i) **Plasmonic Heating Efficiency by Core-Shell Ag⁰@SiO₂ Nanoparticles**,
C. Moularas, V. Tsikourkitoudi, E. Mouzourakis and Y. Deligiannakis, *14th International Conference on Nanosciences and Nanotechnologies 2017*, July 2017, Greece
- (ii) **Photocatalytic OH⁻ Radical Generation by Ag-Based Nanostructures (SiO₂@Ag₃PO₄, SiO₂@Ag⁰) Engineered by Flame Spray Pyrolysis**,
C. Moularas, Y. Georgiou, Y. Deligiannakis, *15th Panhellenic Symposium of Catalysis*, October 2018, Greece
- (iii) **Engineering of flame-made plasmonic/semiconducting nanocatalysts: a study of plasmon-induced carrier dynamics and interfacial electron transfer**,
C. Moularas, A. Zindrou, C. Dimitriou and Y. Deligiannakis, *16^o Panhellenic Symposium of Catalysis*, 20-22 October 2022, Chania, Greece

Oral presentations

- i. **Gas-phase engineering of Tantalum-based nano-ensembles for photocatalytic applications**,
C. Moularas, P. Psathas & Y. Deligiannakis, *4th International Symposium Gas-phase Synthesis of Functional Nanomaterials*, October 2020, Duisburg, Germany.
- ii. **Hot Carrier Harvesting: Distinguishing the Plasmon-induced Mechanisms in Photocatalytic Processes**,
C. Moularas, C. Dimitriou, Y. Georgiou, Y. Deligiannakis, *Young Scientists Online Conference: Minerals Resources-Environment-Chemical Engineering*, February 2021, Greece
- iii. **Hot Electron Harvesting in Plasmonic Nanoaggregates**.
C. Moularas, C. Dimitriou, Y. Georgiou, N. Boukos, Y. Deligiannakis, *XXXV Panhellenic Conference on Solid State Physics and Materials Science*, 26-29 September 2021, Athens, Greece
- iv. **Engineering of Flame-made Plasmonic-Semiconducting Nanocatalysts: A Study of the Photo-induced Carrier Dynamics and Interfacial Electron Transfer**.
Moularas, C. Dimitriou, C. Zindrou, A. Deligiannakis, Y., *9th World Congress on Particle Technology*, 18-22 September 2022, Madrid, Spain

Funding Research Projects

A. Human Resources Development, Education and Lifelong Learning (2020-2021)

Development of Reducing Suboxic Nanophotocatalysts by Flame Spray Pyrolysis

B. Reinforcement of the Research and Innovation Infrastructure (2021-2023)

Center of Research, Quality Analysis of Cultural Heritage Materials and Communication of Science